Alma Mater Studiorum · Università di Bologna

Scuola di Scienze
Dipartimento di Fisica e Astronomia "Augusto Righi"
Laurea Magistrale in Astrofisica e Cosmologia

Investigating High-Energy Emission in Young Radio Galaxies

Relatore:
Prof. Cristian Vignali

Laureando:
Ettore Bronzini

Correlatore:
Dr. Giulia Migliori

Sessione IV
Anno Accedemico 2020-21

This Thesis work was carried out as part of the research activities of the Istituto di Radioastronomia - Istituto Nazionale di Astrofisica (IRA-INAF) *in Bologna*

Alla mia famiglia,
per questo sogno realizzato

Abstract

Some of the most intriguing questions about the physics and the evolution of radio galaxies are related to the early stages of their life. The so-called *Compact Symmetric Objects* (CSOs), defined to be those with radio lobe emission on both sides of an active nucleus and an overall size less than about one kpc, are thought to represent the first stage in the evolutionary path of radio galaxies.

CSOs are considered a perfect test bench to study the accretion and ejection processes in the early-born radio galaxies and, in view of their compact dimensions, to investigate the interaction between the expanding radio source and the host galaxy (*AGN feedback*). In fact, an alternative *scenario* ascribes the compactness of CSOs to an extremely dense interstellar medium of the host galaxy, which can slow down or even completely halt the radio source expansion.

Due to their compact angular sizes ($\lesssim 1-2''$), CSOs were originally studied in the radio band and at low redshifts ($z \lesssim 1$). However, in the last two decades, an increasing number of these sources has also been detected and studied in X-rays.

Past studies of CSOs have shown that a significant, sometimes even dominant, fraction of their emission is released at high energies. There are two main hypotheses for the origin of the X-ray emission in these sources. It is possible that it is primarily produced by the accretion disk and corona via thermal Comptonization. However, theoretical models predict that the compact jets and lobes can be the sites of production of X-ray-to-γ-ray emission via inverse Compton of synchrotron and nuclear photons (e.g. the infrared photons of the dusty torus, the UV photons coming from the disk).

Unveiling the nature of X-ray emission is fundamental to constrain the physical parameters of CSOs (e.g. the accretion and jet power), hence to predict their evolution. In addition, X-rays are important to determinate how these sources release energy in the surrounding medium, so to study the feedback between the central CSO and its host galaxy. Finally, X-rays probe the environment of CSOs through the detection of intrinsic obscuring medium, which could potentially frustrate the jet expansion.

For this Thesis work, a mini-sample of three CSOs has been selected based on their detection in the X- and γ-ray band: 1718-649, 1146+596, and 1843+356. The aim of this work is to investigate the origin of the high-energy emission in these objects, infer their physical properties using the broadband spectral energy distribution (SED), and

understand the role of the ambient medium in their evolution.

The detection in γ-rays is a smoking gun of a non-thermal high-energy component, which can help in discriminating between an accretion *vs.* ejection origin of the X-ray emission.

The X-ray study made use of all the *Chandra*, XMM-*Newton*, and *Swift* data of the sample sources. In particular, for two of the three sources, 1718-649 and 1146+596, *NuSTAR* observations were available, which gave us the possibility to study the $>$ 10 keV spectrum, hence overcoming any possible issues due to obscuration. Interestingly, only another CSO, the heavily obscured OQ+208, was detected at energies higher than 10 keV (Sobolewska et al. 2019a).

Thanks to the high quality of the X-ray data, in the first part of my study I was able to (i) characterize the spectral properties of the unresolved X-ray emission associated with the CSOs; (ii) investigate the hot gaseous components co-spatial with the CSOs; (iii) measure the intrinsic obscuration of the X-ray emission, hence probe the presence of dense gas.

In the second part of my investigation, I considered the broadband emission of two of the targets against theoretical models for the non-thermal emission of lobes and jets. Modeling of the radio-to-γ-ray emission has provided estimates of the physical parameters of the young sources (e.g. magnetic field, particle contents, etc.) and of the total jet power, allowing me to make prediction on the fate of the sources.

In the future, new broad-band X-ray data for a larger sample of CSOs would be essential to fully establish the nature and the origin of their high-energy emission, as well as characterize the role of ambient medium in their evolution.

Sommario

Alcuni degli interrogativi più intriganti relativi alla fisica e all'evoluzione delle radiogalassie sono inerenti alle prime fasi della loro vita. A tal proposito, si ipotizza che i cosiddetti *Compact Symmetric Objects* (CSOs), ossia le sorgenti caratterizzate da emissione radio da lobi su entrambi i lati di un nucleo attivo e con una dimensione complessiva inferiore a circa 1 kpc, rappresentino la prima fase del percorso evolutivo delle radiogalassie.

I CSO, date le loro dimensioni compatte, sono considerati un banco di prova ideale per studiare i processi di accrescimento ed emissione nelle radiogalassie giovani e per comprendere l'interazione tra la sorgente radio in espansione e la galassia ospite (*AGN feedback*).

Proprio per le loro ridotte dimensioni angolari ($\lesssim 1 - 2''$), queste sorgenti sono state originariamente studiate in banda radio e a basso redshift ($z \lesssim 1$). Solo negli ultimi due decenni, un numero crescente di queste sorgenti è stato rivelato e studiato anche in banda X.

Studi condotti su CSOs hanno mostrato come una frazione significativa di emissione, talvolta anche dominante, sia generata alle alte energie. Esistono due ipotesi principali per spiegare l'origine dell'emissione X da queste sorgenti. È possibile che tale emissione sia prodotta per Comptonizzazione termica dal disco di accrescimento e dalla corona. Altri modelli teorici, invece, prevedono che i getti e i lobi compatti possano produrre radiazione in banda X e γ tramite Compton inverso sui fotoni prodotti sia per sincrotrone sia provenienti dal nucleo (per esempio i fotoni infrarossi del toro di polvere o i fotoni UV prodotti dal disco).

Svelare la natura dell'emissione X è fondamentale per determinare i parametri fisici di queste sorgenti (come, per esempio, la potenza dell'accrescimento e quella del getto) e per predire la loro evoluzione. In aggiunta, lo studio dell'emissione X è importante per determinare come queste sorgenti rilascino energia nell'ambiente circostante, al fine di studiare il *feedback* tra il CSO e la galassia ospite. Infine, l'emissione in banda X permette di studiare l'ambiente dove si trovano i CSOs attraverso lo studio delle densità di colonna del mezzo oscurante, che possono, in linea di principio, limitare l'espansione del getto.

In questa tesi è stato selezionato un campione di tre CSO sulla base della loro emis-

sione in banda X e γ: 1718-649, 1146+596 e 1843+356. L'obiettivo di questo lavoro è consistito nello studiare l'origine dell'emissione ad alta energia in questi oggetti, nel ricavare le proprietà fisiche dalla loro distribuzione spettrale di energia (SED) e nel comprendere il ruolo che ricopre il mezzo ambiente nella loro evoluzione.

La rivelazione in banda γ conferma la presenza di una componente che emette tramite processi non termici ad alta energia e che può aiutare a individuare l'origine dell'emissione in banda X tra processi di accrescimento o eiezione.

Per lo studio in banda X sono stati utilizzati tutti i dati delle sorgenti del campione, presi con i telescopi *Chandra*, XMM-*Newton* e *Swift*. Inoltre, per due delle tre sorgenti, 1718-649 e 1146+596, erano disponibili anche le osservazioni del telescopio *NuSTAR*, che hanno fornito l'opportunità di studiare lo spettro delle sorgenti ad energie maggiori di 10 keV, superando quindi i possibili problemi legati all'oscuramento. Solo un altro CSO, particolarmente oscurato, OQ+208, è stato rivelato ad energie maggiori di 10 keV (Sobolewska et al. 2019b).

Data l'alta qualità dei dati analizzati in banda X, nella prima parte del mio studio è stato possibile (i) caratterizzare le proprietà spettrali dell'emissione X associata alle CSO non risolte; (ii) studiare l'emissione termica da gas caldo co-spaziale con i CSO; (iii) misurare l'oscuramento intrinseco dell'emissione X e quindi provare la presenza di gas denso.

Nella seconda parte del lavoro, è stata considerata l'emissione in banda larga di due sorgenti del campione, che è stata modellata con l'emissione non termica di lobi e getti. La modellizzazione dell'emissione dal radio fino alla banda γ ha fornito stime dei parametri fisici delle radio sorgenti giovani (come per esempio il campo magnetico, il contenuto di particelle..) e della potenza totale del getto, che mi hanno permesso di effettuare predizioni sul destino delle sorgenti.

Nuove osservazioni per un campione più numeroso di CSO a banda larga in banda X potrebbero fornire informazioni essenziali per la completa comprensione della natura e dell'origine dell'emissione ad alta energia, nonché caratterizzare il ruolo del mezzo ambiente nella loro evoluzione.

Contents

Chapter 1

Active Galactic Nuclei

In this chapter I discuss the main properties of active galactic nuclei, the physics behind these objects and the importance of their study. I start with a general description of what active galactic nuclei are (Section 1.1); then I move on the main components of these objects (Section 1.2); after this, I describe the AGN classification from the radio and optical point of view and how these classifications are integrated in the context of unified models (Section 1.3); I conclude with the spectral properties of active galactic nuclei (Section 1.4). The main references for this chapter are Beckmann and Shrader 2012; Netzer 2013; Padovani et al. 2017.

1.1 What AGN are

It is commonly accepted that almost every galaxy hosts a supermassive black hole (SMBH, $\mathcal{M}_\bullet = 10^6 - 10^{10}\,\mathcal{M}_\odot$) in its center (e.g. Kormendy and Richstone 1995; Binney and Tremaine 2008; Kormendy and Ho 2013).

The presence of a SMBH can be inferred in few different ways: for instance, studying the kinematic effects on the nearby stars or gas. However, these methods fail quickly at high distances ($\gtrsim 250\,\mathrm{Mpc}$) and indirect methods are needed. These methods are based on the evidence that some observable quantities correlate in some way with the central BH mass: for instance, the existence of SMBH mass - bulge scaling relations (Kormendy and Richstone 1995; Magorrian et al. 1998; Ferrarese and Merritt 2000; Gebhardt et al. 2000).

The strong direct evidence for the existence of these black holes is a recent result: after an intense observation campaign, the EVENT HORIZON TELESCOPE (EHT) Collaboration revealed the shadow of M87, shown in Figure 1.1. Black holes are expected to reveal a dark shadow caused by gravitational light bending and photon capture at the event horizon. They have resolved the central compact radio source as an asymmetric bright emission ring: it is consistent with expectations for the shadow of a Kerr black hole (see Section 1.2.1 for further details) as predicted by the theory of General Relativity (hereafter GR) (Einstein 1916), which is the theory of gravitation assumed in this work. The asymmetry in brightness in the ring can be explained in terms of

Figure 1.1: The first image of a black hole obtained by EVENT HORIZON TELESCOPE observations of the center of the galaxy M87. The image shows a bright ring formed as light bends in the intense gravity around a BH which mass is about $6.5 \times 10^9 \mathcal{M}_\odot$. This long-sought image provides the strongest evidence to date for the existence of supermassive black holes and opens a new window onto the study of black holes, their event horizons, and gravity. Credits: Event Horizon Telescope Collaboration et al. 2019.

relativistic beaming of the emission from a plasma rotating close to the speed of light around a black hole (Event Horizon Telescope Collaboration et al. 2019).

The vast majority of these SMBH, including SgrA*, the SMBH at the center of the Milky Way, is silent or in a very low state of activity, while only a small fraction is active: these are called *Active Galactic Nuclei* (AGN). The main difference between these two classes of objects lies in the efficiency in converting accreted material into radiation: the former are very low or not at all efficient, whereas the latter are extremely high efficient (see Section 1.2.1 for further details).

The main observed features of AGN can be summarized as follows (e.g. Cimatti, Fraternali, and Nipoti 2019):

- very high bolometric luminosities, up to $\mathcal{L} \approx 10^{48}\,\mathrm{erg/s}$;
- non-stellar UV-optical continuum;
- strong X-ray emission and possibly γ-rays;
- non-thermal radio emission with a wide range of luminosities;
- broad permitted emission lines with Full-Width at Half Maximum (FWHM) $\gtrsim$ several $10^3\,\mathrm{km/s}$;
- narrow (FWHM $\lesssim 10^3\,\mathrm{km/s}$) emission lines (forbidden and permitted[1]);

[1] *Forbidden lines* (e.g. [OII], [OIII]) are produced by highly improbable transitions in lab, occurring

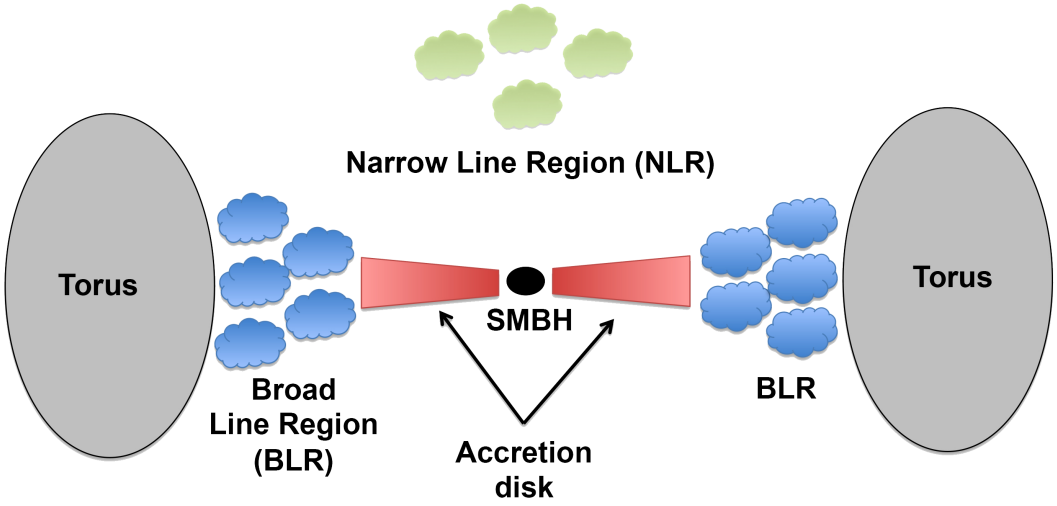

Figure 1.2: Schematic representation of the main components of an AGN according to the AGN paradigm. Credits: Ricci 2011.

- emission of relativistic plasma jets departing from the nucleus with velocities near the speed of light;
- time variability of the continuum and broad emission-line luminosities on a wide range of timescales (from minutes to years).

1.2 Main components in AGN

The AGN are thought to have an extremely complex structure. Since the discovery of the first quasars (QSOs, Schmidt 1963), an enormous number of models have been developed in order to describe the observational properties of AGN on scales of pc up to hundreds of kpc. Currently, after more than five decades, the so-called *AGN paradigm* is the commonly accepted model. A sketch of it is shown in Figure 1.2 and the characteristic scale lengths and densities of AGN components are listed in Table 1.1. In the sections below, I describe the main components in an AGN, starting from the innermost regions up to the outer scales.

1.2.1 The central supermassive black hole

A SMBH inhabits the center of its host galaxy and is the engine of the AGN.

According to the *no-hair theorem*, every black hole (hereafter BH) can be described in terms of three fundamental parameter: the mass ($\mathcal{M}_\bullet$), the spin ($\mathcal{J}$) and the charge ($\mathcal{Q}$) (Misner, Thorne, and Wheeler 1973). For simplicity, the BH is generally assumed to be neutral ($\mathcal{Q} = 0$), so the BH can be described in terms of its mass and spin: the

only at low density of the gas. In contrast, emission lines are called *permitted lines* when the probability of the associated transitions is very high.

Table 1.1: AGN components: location and typical density.

Component	Distance in r_g	Density $\left[\mathrm{cm}^{-3}\right]$
Hot corona	3-10	$\sim 10^8$
Accretion disk	tens	$\sim 10^{15}$
BLR	$10^4 - 10^5$	$\sim 10^{10}$
Torus	$10^5 - 10^6$	$10^3 - 10^6$
HIG	$\sim 10^6$	$10^3 - 10^5$
NLR	$10^7 - 10^8$	$10^3 - 10^5$

Notes. The distance is expressed in units of the gravitational radius, defined by Equation 1.1. BLR stands for *Broad Line Region*, HIG for *Highly Ionized Gas* (also known as *warm absorber*), NLR for *Narrow Line Region*. Adapted from Netzer 2013.

latter can span between 0, a non-rotating BH described by the Schwarzchild metric, and 1, a maximum rotating BH described by the Kerr metric.

For a BH of a given mass $\mathcal{M}_\bullet$, it is possible to define a characteristic scale length, the *gravitational radius* r_g, as follows

$$r_g = \frac{G\mathcal{M}_\bullet}{c^2} \simeq 1.5 \times 10^{13} \mathcal{M}_8 \,\mathrm{cm}, \tag{1.1}$$

where G is the gravitational constant, $\mathcal{M}_8$ is the BH mass expressed in units of $10^8 \mathcal{M}_\odot$ and c is the speed of light in vacuum.

Another characteristic scale-radius of BHs is the so-called *Schwarzschild radius* (r_S), which is the innermost radius only the photons can escape from. In literature, it is generally referred as $r_s = 2r_g$.

Moreover, another fundamental scale-radius of a BH is the so-called *Innermost Stable Circular Orbit* (hereafter ISCO). In order to describe the properties of a ISCO, a useful quantity has to be defined: the *spin parameter* of a BH is defined by

$$a = \frac{\mathcal{J}c}{G{\mathcal{M}_\bullet}^2}. \tag{1.2}$$

Through the definition of a, according to the GR, it is possible to introduce the *event horizon radius*

$$r_\pm = r_g \left[1 \pm \left(1 - a^2\right)^{1/2}\right]. \tag{1.3}$$

For a stationary BH ($a = 0$), the event horizon radius is given by the Schwarzschild radius, $r_+ \equiv r_S = 2r_g$, whereas for extreme BHs with $a = 1$, the event horizon radius is $r_+ = r_g$. At radii lower than the ISCO, the particle loses its orbital motion and fall directly into the event horizon.

The ISCO can be computed by the event horizon radius (e.g. McClintock et al. 2011): for a Schwarzschild BH $r_{\mathrm{ISCO}} = 6r_g$, and for a rapidly-rotating Kerr BH ($a = 0.998$) $r_{\mathrm{ISCO}} = 1.24r_g$. In general, for Kerr BHs $1 \leq r_{\mathrm{ISCO}} \leq 6r_g$, where the exact value depends on a.

The value of r_{ISCO} is fundamental because it determines the fraction of the grav-

itational potential energy that is converted to electromagnetic radiation during the accretion: it can be shown that the faster the BH rotates, the higher the efficiency in converting accreted into energy in the BH is.

Accretion onto black holes

For a BH of mass $\mathcal{M}_\bullet$ and radius R, the gravitational potential energy released by accretion of a mass m onto its surface is

$$E_{\rm acc} = \frac{G\mathcal{M}_\bullet \mathcal{M}}{R} \tag{1.4}$$

and this energy is expected to be released mainly in the form of electromagnetic radiation[2]. The $\mathcal{M}_\bullet/R$ ratio defines the compactness of the accreting object: the more compact it is, the more energy can be released, hence BHs are expected to be the most powerful emitters. Moreover, for a fixed value of compactness, the *accretion luminosity*, which is the luminosity that can be radiated as a consequence of accretion, is simply obtained by deriving Equation (1.4):

$$\mathcal{L}_{\rm acc} = \frac{G\mathcal{M}_\bullet \dot{\mathcal{M}}}{R}, \tag{1.5}$$

where $\dot{m}$ is the rate at which the matter is accreted. With the definition of the Schwarzschild radius, the accretion luminosity (Equation (1.5)) can be written as

$$\begin{aligned} \mathcal{L}_{\rm acc} &= 2\eta \frac{G\mathcal{M}_\bullet \dot{\mathcal{M}}}{r_S} \\ &= \eta \dot{\mathcal{M}} c^2, \end{aligned} \tag{1.6}$$

where the η parameter is the efficiency in converting accreted material into energy in the BH. It can be shown that for a Schwarzschild BH $\eta = 0.057$, whereas for a Kerr one $\eta = 0.321$.

The Eddington limit At high luminosities, the accretion rate may be controlled by the radiation pressure: in the process of accretion and subsequent emission of radiation, the force of gravity of the infalling matter must be taken into account on the one hand and the radiation pressure force on the other.

Consider a steady spherically symmetrical accretion of fully ionized hydrogen on a central point source with mass $\mathcal{M}_\bullet$. Let define r as the distance between the accretor and a particle of this gas. The radiation pressure force acting on this gas particle is

$$f_{\rm rad} = \frac{N_e \sigma_T}{4\pi r^2 c} \int_0^\infty \mathcal{L}_\nu d\nu = \frac{N_e \sigma_T}{4\pi r^2 c} \mathcal{L}, \tag{1.7}$$

[2]Equation (1.4) is valid for all accreting objects. If the accreting body is a neutron star with radius $R \simeq 10\,$km and mass $\mathcal{M}_\bullet \simeq 1\,\mathcal{M}_\odot$, then $\Delta E_{\rm acc.} \simeq 10^{20}$erg/g. For comparison, consider the energy that could be extracted from the mass m by nuclear fusion reactions. The maximum is obtained if the material is initially hydrogen and the major contribution comes from the burning of hydrogen to helium. This yields an energy release $\Delta E_{\rm nucl.} = 0.007mc^2 \simeq 6 \times 10^{18}$erg/g (e.g. Frank, King, and Raine 2002).

where N_e is the electron density, σ_T is the Thomson cross section, $\mathcal{L}_\nu$ is the monochromatic luminosity and $\mathcal{L}$ is the bolometric luminosity. The gravitational force per particle is

$$f_g = \frac{G\mathcal{M}_\bullet \mu m_p N_e}{r^2}, \tag{1.8}$$

where μ is the mean molecular weight (mean number of protons and neutrons per electron; about 1.17 for a fully ionized solar composition gas) and m_p is the mass of the proton. The accretion can proceed as long as $f_g > f_{\rm rad}$. The limiting requirement for accretion, $f_g = f_{\rm rad}$, leads to the definition of *Eddington luminosity*:

$$\mathcal{L}_{\rm Edd} = \frac{4\pi c G \mathcal{M}_\bullet \mu m_p}{\sigma_T} \simeq 1.5 \times 10^{38} \left(\frac{\mathcal{M}_\bullet}{\mathcal{M}_\odot}\right) \ {\rm erg/s}, \tag{1.9}$$

where the factor 1.5×10^{38} depends on the exact value of μ and was calculated for solar metallicity gas. The value of $\mathcal{L}_{\rm Edd}$ defined in this way is the maximum luminosity allowed for objects that are powered, over a long period of time, by a steady-state accretion. In reality, it is known that this limit can be violated, due to non-spherical geometry and various kinds of instabilities. Several classes of objects seem to show a super-Eddington state and luminosities, including AGN (e.g. Lanzuisi et al. 2016; Tsai et al. 2018).

The definition of $\mathcal{L}_{\rm Edd}$ in Equation (1.9) takes into account only one source of opacity, the Compton scattering, which is appropriate for a fully ionized plasma. More realistic situations may involve partly neutral gas and hence much higher opacity. Here the effective $\mathcal{L}_{\rm Edd}$ can be significantly smaller than the value defined in Equation (1.9).

Another fundamental parameter associated with the Eddington luminosity is the *Eddington accretion rate*, $\dot{\mathcal{M}}_{\rm Edd}$, which is the accretion rate required to produce a total luminosity of $\mathcal{L}_{\rm Edd}$,

$$\dot{\mathcal{M}}_{\rm Edd} = \frac{\mathcal{L}_{\rm Edd}}{\eta c^2} \simeq 3\mathcal{M}_8 \left[\frac{\eta}{0.1}\right]^{-1} \mathcal{M}_\odot/{\rm yr}, \tag{1.10}$$

and the BH *growth rate* is $\dot{\mathcal{M}}\,(1-\eta)$: the higher the efficiency in converting accreted material into energy is, the slower the BH mass growth is.

1.2.2 The accretion disk

Accretion processes around BHs involve rotating gas flow. Therefore, the accretion flow structure is determined by solving a set of four conservation equations: the conservation of vertical momentum, the conservation of mass, the conservation of energy and the conservation of angular momentum. Four solutions are currently known. In these solutions, viscosity transports angular momentum outward, allowing the accretion gas to spiral in toward the BH. Hence, viscosity acts a source of heat that is radiated away.

Assuming that thermal conduction and the vertical advection of energy are negli-

gible, and defining $q_{\rm adv}$ as the net energy advection rate per unit volume, the energy equation can be expressed as follows

$$q_{\rm adv} = q_+ - q_-, \tag{1.11}$$

where q_+ and q_- are the volume heating and cooling rates, respectively. Equation (1.11) allows a simple classification of the possible solutions depending on which of the three terms is negligible compared to the remaining two:

- $q_{\rm adv} \ll q_+ \approx q_-$
  Cooling-dominated accretion flows including the standard solution (Shakura and Sunyaev 1973) and the Shapiro, Lightman and Eardley solution. Most of the viscous heat energy is radiated ($\mathcal{L}_{\rm rad} \approx 0.1\dot{M}c^2$).

- $q_- \ll q_{\rm adv} \approx q_+$
  Advection-dominated accretion flows (hereafter ADAFs), including slim disks. Most of the heat energy is retained in the gas ($\mathcal{L}_{\rm rad} \ll 0.1\dot{M}c^2$ and $\mathcal{L}_{\rm adv} \approx 0.1\dot{M}c^2$).

- $q_+ \ll q_- \approx q_{\rm adv}$
  Cooling flows, including low angular momentum settling solutions and optically thin Bondi accretion.

Standard model

A schematic representation of the Shakura and Sunyaev accretion disk is shown in the top panel of Figure 1.3.

Disks that are geometrically thin - $H \ll R$, where H and R are the thickness and the radius of the disk, respectively - and optically thick - each element of the disk radiates as a black-body - belong to this type of solutions. In reality, energy is dissipated locally in the disk through viscosity, which acts as a dynamical friction. This implies that the temperature of the disk is a function of radius and it follows

$$T(r) = \left[\frac{3G\mathcal{M}\dot{\mathcal{M}}}{8\pi\sigma_T r^3} f(r)\right]^{1/4}, \tag{1.12}$$

where $\mathcal{M}$ is the disk mass, $\dot{\mathcal{M}}$ is the accretion rate, and

$$f(r) = 1 - \left(\frac{r_{\rm ISCO}}{r}\right)^{1/2}. \tag{1.13}$$

Since $r_{\rm ISCO} \simeq r_S$, if $r \gg r_{\rm ISCO}$, Equation (1.12) becomes

$$T(r) = \left[\frac{3G\mathcal{M}\dot{\mathcal{M}}}{8\pi\sigma_T r_S^3}\right]^{1/4} \left(\frac{r}{r_S}\right)^{-3/4}, \tag{1.14}$$

which describes the radial dependence of the temperature in a standard accretion disk.

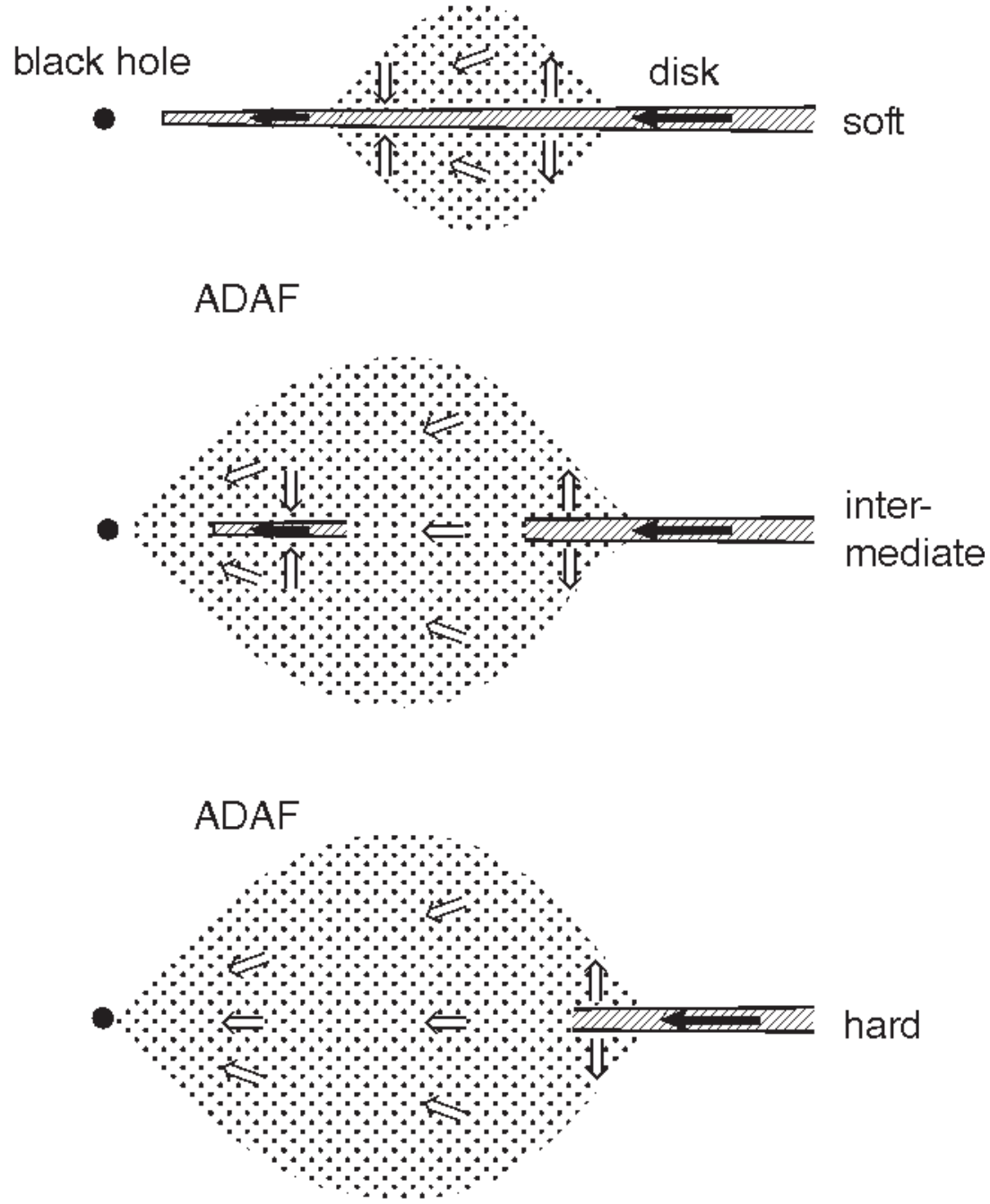

Figure 1.3: Accretion flow in soft, intermediate and hard spectral state (with decreasing mass flow rate). *Top panel*: in the soft state accretion occurs via the disk, some gas is evaporated to a coronal flow, but re-condenses onto the disk; in the inner region only the disk flow exists, which causes the soft spectrum. *Middle panel*: in the intermediate state the ADAF and an inner disk contribute to the spectrum. *Bottom panel*: in the hard state only the hot ADAF contributes to the spectrum. Credits: Meyer, Liu, and Meyer-Hofmeister 2007.

From Equation (1.14), assuming $r_S \ll r$, it can be shown that

$$T(r) \simeq 2.1 \times 10^5 \mathcal{M}_8^{-1/4} \left(\frac{\dot{\mathcal{M}}}{\dot{\mathcal{M}}_{\rm Edd}}\right)^{1/4} \frac{r}{r_S}^{-3/4} \,{\rm K} \tag{1.15}$$

$$\propto \mathcal{M}^{-1/4} \left(\frac{\dot{\mathcal{M}}}{\dot{\mathcal{M}}_{\rm Edd}}\right)^{1/4}, \tag{1.16}$$

where $\mathcal{M}_8$ is the mass of the accreting object in units of $10^8\,\mathcal{M}_\odot$. As extensively discussed in Section 1.4.3, due to the different masses, this emission peaks in the UV band for AGN, whereas in soft X-rays in black hole binaries.

ADAF solution

A schematic representation of the ADAF accretion disk is shown in the bottom panel of Figure 1.3.

Disks that are geometrically thick - $H \gg R$ - and optically thin - each element of the disk does not radiate as a black-body - belong to this type of solution. Since cooling ($\Lambda(T)$) is a function of electron number density (N_e)

$$\Lambda(T) \propto N_e^2, \tag{1.17}$$

a low-density gas, typical of optically thin accretion disks, is unable to cool efficiently: ions and electrons are thermally decoupled and Coulomb collisions between them are slower and less efficient in sharing the total kinetic energy. As a consequence, the viscous energy is stored in it as thermal energy instead of being radiated.

In ADAF, most of the gravitational energy locally deposited in the disk by viscous processes is stored as internal energy of the ions, because of their larger mass and because the electrons cool more efficiently. Hence, the ions temperature is much higher than the electrons one. If the innermost regions have a low enough density and the cooling is inefficient, the gas does not cool and reaches very high temperature: as a result, the disk inflates. The bottom panel of Figure 1.3 shows the increase in the disk thickness.

1.2.3 The hot corona

As discussed in Section 1.4.4, many hard X-ray spectra show a sharp rollover around 100 keV (e.g Fabian et al. 2015). In order to explain this observational feature, models predict the presence of a rarefied compact region above the accretion disk (not shown in Figure 1.2): the *hot corona*. Reverberation studies in many cases constrain the distance between the corona and central BH to lie in the range of $\sim 3 - 10\, r_g$ (Fabian et al. 2009; De Marco et al. 2011; Kara et al. 2013; Cackett et al. 2014; Emmanoulopoulos et al. 2014; Uttley et al. 2014; Kara et al. 2016). Thanks to its low density ($n \simeq 10^8\,{\rm cm}^{-3}$, this region is able to keep very high temperatures ($T \simeq 10^8 - 10^9\,{\rm K}$).

Nowadays, the hot corona accurate location is still debated, as well as its formation and geometry around geometrically thin accretion disks (Stern et al. 1995; Reynolds

and Nowak 2003).

1.2.4 The broad line region

Immediately beyond the hot corona, there is a clumpy dense region of gas named *Broad Line Region* (BLR, see Table 1.1). The BLR gas reprocesses the optical/UV light coming from the disk through permitted lines, while the forbidden lines are all collisionally suppressed due to the high density of the clouds ($n \simeq 10^{10}\,\mathrm{cm}^{-3}$). The motion of these clouds around the SMBH, at velocity of about $10^3 - 10^4\,\mathrm{km/s}$, leads to the broadening of the line profiles, from which this region takes its name, that can be used to estimate the velocity of these clouds, hence the SMBH mass.

1.2.5 The torus

In the context of the *Unified Model* (see Section 1.3), an important role is played by the *torus*: the obscuring torus is composed primarily of gas and dust. However, its exact nature, origin and structure, either smooth (Fritz, Franceschini, and Hatziminaoglou 2006) or clumpy (Nenkova et al. 2008; Hönig and Kishimoto 2010), is still matter of debate. Recently, more complex two-phase torus (Siebenmorgen, Heymann, and Efstathiou 2015; Stalevski et al. 2016) or wind model (Hönig and Kishimoto 2017) have also been proposed to explain observational data. It is commonly accepted that this structure has extremely high column densities ($N_H \simeq 10^{22} - 10^{24}\,\mathrm{cm}^{-2}$): for this reason, few optical and UV photons can reach the observer when the line of sight (hereafter LOS) intercepts it, as discussed in Section 1.3.2. For higher column density ($N_H \gtrsim 10^{25}\,\mathrm{cm}^{-2}$), even the X-ray emission can be heavily absorbed (see Section 1.4.4 for further details).

1.2.6 The narrow line region

The farthest ingredient in the AGN paradigm is the *Narrow Line Region*: it is composed by clouds with extremely low densities and temperatures ($T \simeq 10^3 - 10^4\,\mathrm{K}$). Due to its low densities and high distance from the central SMBH, this region emits forbidden narrow lines (e.g. [OII], [OIII], [SII], [SIII]), with typical broadening of $200 \lesssim \Delta v \lesssim 1000\,\mathrm{km/s}$. Being the NLRs external to the torus, these emission lines never undergo significant extinction, regardless of the LOS.

It is the only AGN region to be spatially resolved in the optical band, where ionization cones rather than a spherical distribution can be appreciated, suggesting an axisymmetric structure rather than a spherical one, as it can be magnificently admired in the Hubble Space Telescope images of NGC 5252 (Morse et al. 1998).

1.2.7 The jets and lobes

About 10% of AGN shows the presence of extended radio emission. This is associated with two types of structures: the *jets* and the *lobes*.

Jets are collimated *outflows* and are always ultra-relativistic on parsec scale. If large-scale magnetic fields are present, jets can derive their power from the rotation of either the BH via the Blandford and Znajek 1977 effect or the rotation of the accretion disk via the Blandford and Payne 1982 mechanism (see Davis and Tchekhovskoy 2020 for a review on the jet formation, evolution and stability). The main parameters are the BH angular frequency (Ω) and the magnetic field (B). The twisting of the magnetic field lines, tied to the rotation of the BH, can lead to highly collimated jets.

If jets are still ultra-relativistic on kpc-Mpc scales, their interaction with the surrounding medium (i.e. the *intergalactic medium* or the *intercluster medium*) leads to the formation of extended (from several kpc up to Mpc) radio structures: the lobes. As shown in the left panel of Figure 1.6, radio lobes are typical quasi-symmetric structures: they are generated by diffusion of jets plasma in the ambient medium, which emits synchrotron radiation. Due to the high values of the *Mach number*[3], shocks form at the ends of jets. These shocks create *hot-spots*: these are re-acceleration sites for electrons. Hot spot spectra are generally consistent with synchrotron-self Compton (hereafter SSC)) emission but a significant number appeared to have a larger X-ray intensity than predicted. In these sources, more complex scenarios have to be invoked.

Jets can dominate all the electromagnetic spectrum: indeed, the radiation is strongly Doppler-boosted in these structures. By the definition of the *Doppler factor*

$$\delta(\beta, \vartheta) = \frac{1}{\gamma(1 - \beta\cos\vartheta)}, \tag{1.18}$$

where

$$\gamma = \frac{1}{\sqrt{1 - \frac{v^2}{c^2}}} = \frac{1}{\sqrt{1 - \beta^2}} \tag{1.19}$$

is the Lorentz factor, $\beta = v/c$ is the bulk velocity and ϑ is the angle between the jet axis and the LOS, it is possible to evaluate the observed flux density in the assumption of intrinsic power law spectrum ($\mathcal{S}'_{\nu'} = K \times (\nu')^{-\alpha}$):

$$\mathcal{S}_\nu = \delta^{3+\alpha}\mathcal{S}'_{\nu'}, \tag{1.20}$$

where α is called *spectral index*. For high values of the Doppler factor ($\delta \gtrsim 10$, e.g. Celotti and Ghisellini 2008), which correspond to high values of β and small values of ϑ, the observed flux is strongly boosted. A cartoon of the jet structure is shown in the top panel of Figure 1.4. As it possible to notice, it seems that the jets are not composed of a continuous flow of relativistic plasma, but rather they should be organized into different superluminal compact structures: the *knots*. Accretion and collimation regions are indicated, as well as all the other AGN components. Bottom panel in Figure 1.4 shows the jet emission regions and the corresponding energy bands: the shorter

[3]In fluid dynamics, the *Mach number* is defined as the ratio of the velocity of a fluid to the velocity of sound in that fluid. For Mach numbers larger than one, shock wave patterns develop on the moving body because of compression of the surrounding fluid. In the astrophysical context, shocks waves have Mach numbers up to several 10^2: these values are typically reached in supernovae explosions (or SNe) (Müller 2020).

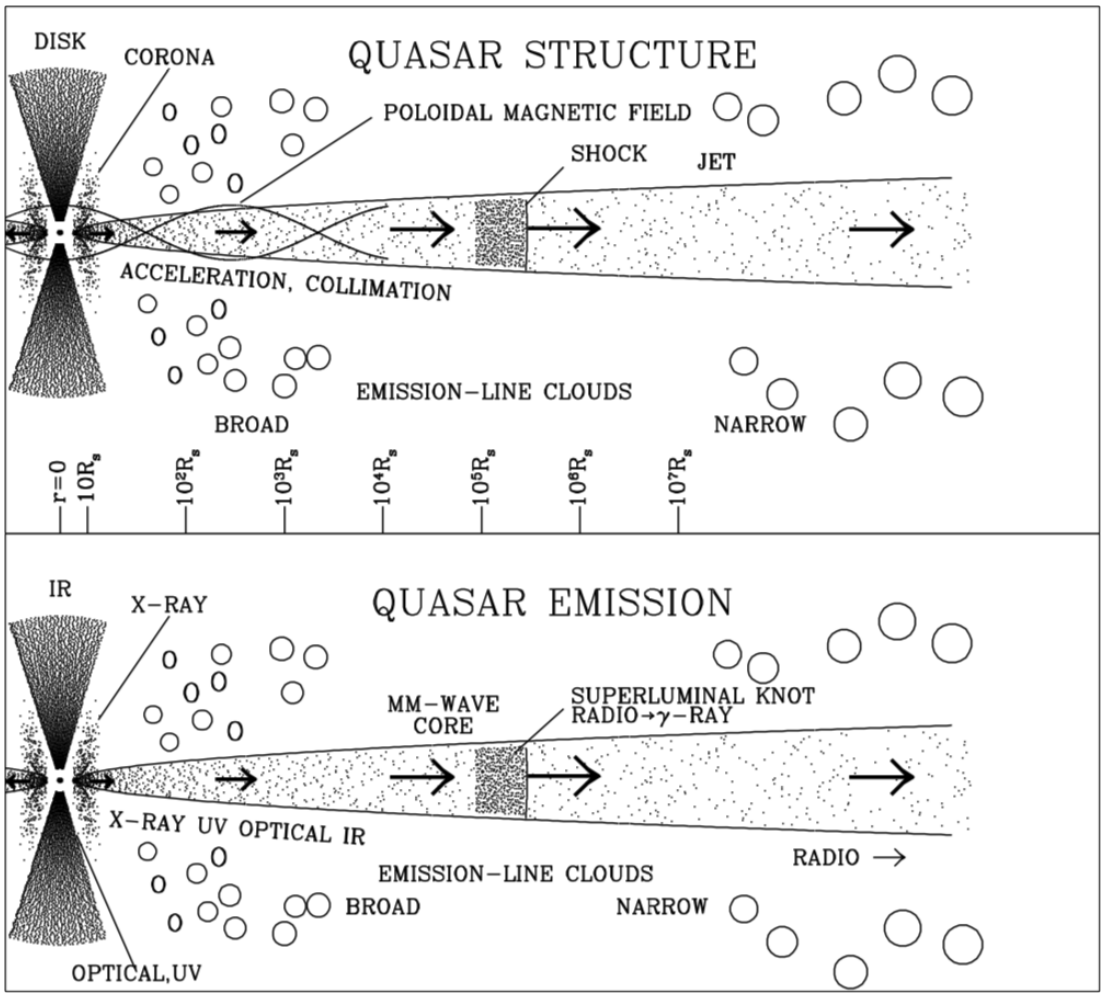

Figure 1.4: Cartoon of the physical structure and emission regions of a radio-loud AGN, excluding the extended radio lobes. The density of the dots in the disk, corona, and jet very roughly indicates the density of plasma (*top panel*) or intensity of emission (*bottom panel*) in a reference frame in which there is no beaming. Note the logarithmic length scale beyond $10\,r_S$, where r_S is the Schwarzschild radius. Only a single superluminal knot is shown; usually there are several. Credits: Marscher 2005.

the wavelength, the more internal the emitting region, hence X-rays trace the jet base. In addition, superluminal knots produce emission from radio band up to γ-rays via SSC.

1.3 AGN unification

A large number of classes and sub-classes has been introduced to classify the observational properties of AGN (e.g. Padovani et al. 2017). AGN emit over the entire electromagnetic spectrum. As a consequence, classifications are often based on features in each spectral band. Therefore, the classification of AGN is complex and based on many different methods (Tadhunter 2008) such as the presence or absence of broad emission lines in the optical spectra, the radio morphology, the variability, the luminosity or the spectral shape. In general, from the observational point of view, a source

can be classified as an AGN if it satisfies at least one of the following points (Netzer 2013):

- it contains a compact nuclear region emitting significantly beyond what is expected from stellar processes typical of host galaxy;
- it shows the clear signature of a non-stellar continuum emission in its center;
- its spectrum contains strong emission lines with line ratios that are typical of excitation by a non-stellar radiation field;
- it shows line and/or continuum variations.

In order to explain the large diversity of observed AGN properties with a small number of physical parameters, a *Unified Model* has been proposed (Antonucci 1993; Urry and Padovani 1995; Urry 2003; Tadhunter 2008). The basic idea of this model is that the major observed differences between AGN spectra are related to the inclination of the AGN structure with respect to the LOS. Hence, these schemes are usually referred as *unification by inclination* and the general view of an AGN in this context is shown in Figure 1.5, which is described in the following sections. In particular, I describe the two AGN classifications based on their radio and optical properties, and how these classifications are included in the context of unified models.

1.3.1 Radio classification

The main emission process that is responsible for the radiation observed in AGN in the radio band is synchrotron emission, produced by the interaction between charged particles (e.g. electrons) and strong magnetic fields. Even though synchrotron emission is also present in the so-called *normal* galaxies, the AGN radio emission results to be much higher: this effect is called *radio excess* and radio emitting AGN are classified as *radio galaxies* (RGs).

An essential parameter for the radio classification is the *radio loudness* (or R). It is defined as the ratio between the radio emission measured at 5 GHz and the optical flux in the B band (centered at 4400 Å):

$$R = \frac{\mathcal{F}_{5\,\mathrm{GHz}}}{\mathcal{F}_B}. \tag{1.21}$$

If it is larger than 10, the source is classified as *Radio-Loud* (RL); otherwise, it is classified as *Radio-Quiet* (RQ) (Kellermann et al. 1989). Statistical studies on radio galaxies pointed out that the vast majority of them, about 90%, are RQ (e.g. Padovani et al. 2017). In addition, the RL galaxies are generally hosted by giant ellipticals (Matthews, Morgan, and Schmidt 1964), while the RQ ones preferentially reside spiral hosts (Wilson and Colbert 1995; Floyd et al. 2004). A more recent definition of radio loudness was given by Terashima and Wilson 2003:

$$\log R_X = \frac{\nu\mathcal{L}_\nu\,(5\mathrm{GHz})}{\mathcal{L}_X}, \tag{1.22}$$

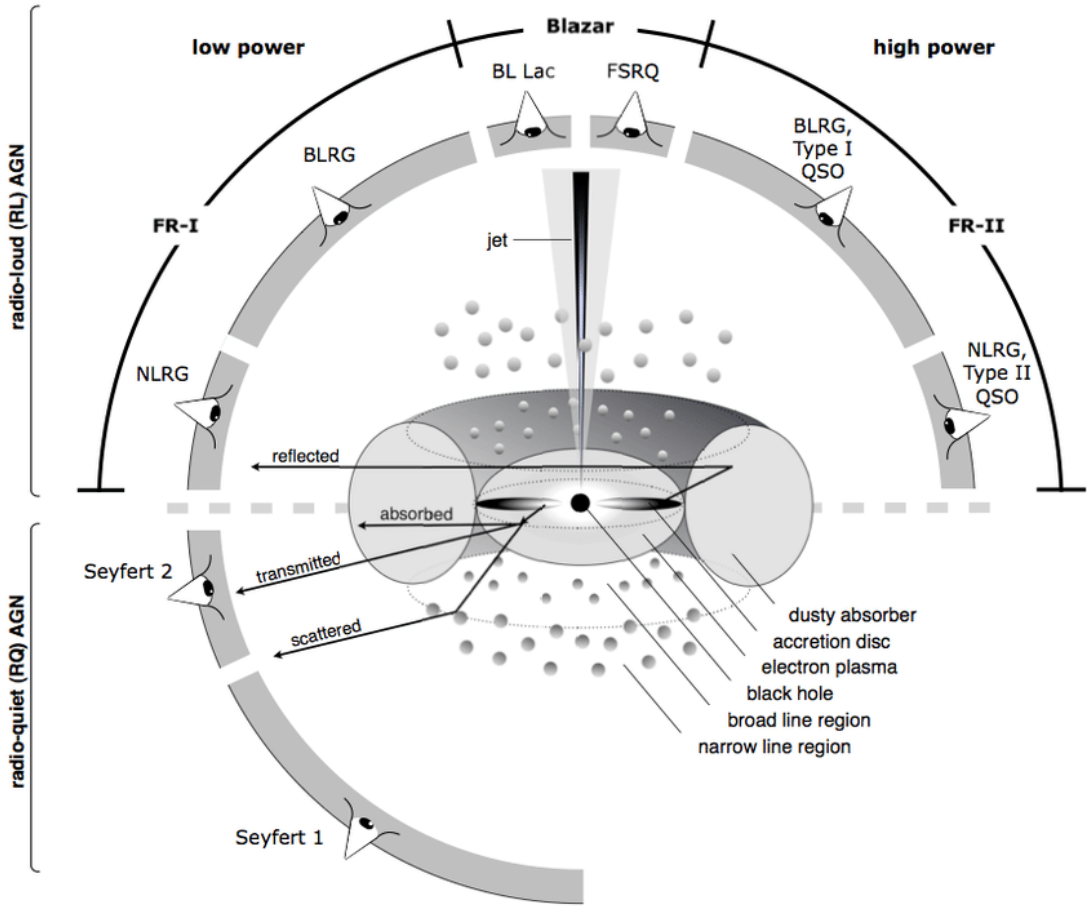

Figure 1.5: Schematic representation of the AGN phenomenon in the unified scheme. The type of object observed depends on the viewing angle, whether or not the AGN produces a significant jet emission, and how powerful the central engine is. Note that radio-loud objects are generally thought to display symmetric jet emission. Adapted from Beckmann and Shrader 2012. Image credits: M. L. Menzel.

where $\mathcal{L}_X$ is the X-ray luminosity measured in the $2-10\,\mathrm{keV}$ energy range. If R_X is less than or equal to -4.5, the source is defined RQ, otherwise RL.

Radio-Loud AGN

Several morphologies of jets are observed in radio images of RL AGN: Figure 1.6 shows the VLA view at 1.4 GHz of 3C 31 (left panel) and 3C 219 (right panel). The morphology of the two sources, as well as the intrinsic power, is different. For this reason, RL galaxies are split into two sub-classes (FRI and FRII) based on their radio power and morphology (Fanaroff and Riley 1974).

- FRI radio galaxies
  Their radio morphology is similar to the one of 3C 31. Jets are ultra-relativistic at pc scale. However, it is thought that jets launching opening angles in this class of sources are larger than the ones in FRII: as a consequence, jets decelerate and become sub-relativistic on scales of hundred of pc to kpc. Hence, radio jets

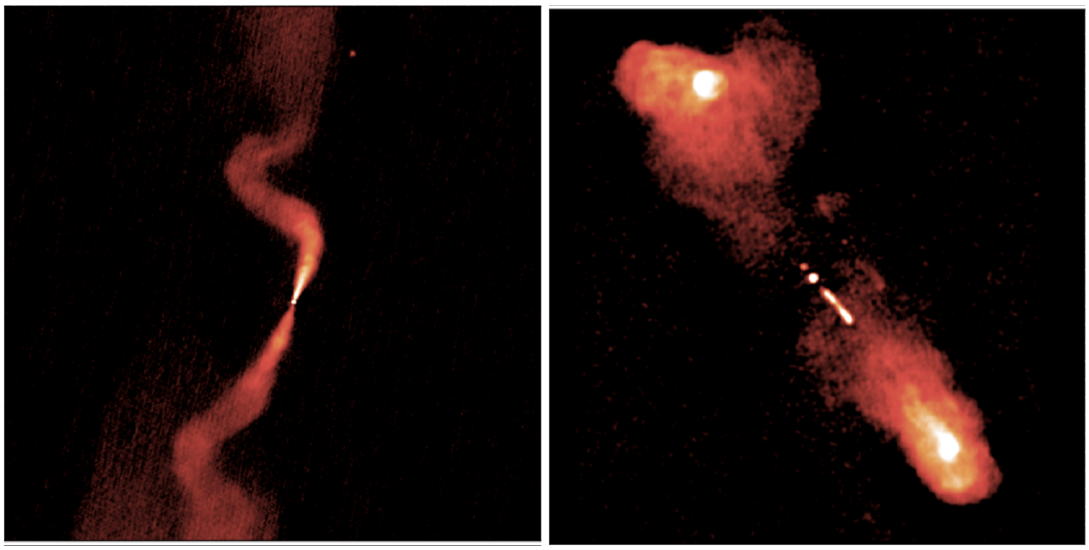

Figure 1.6: VLA views at 1.4 GHz of the Fanaroff-Riley class I radio galaxy 3C 31 (*left panel*) and the Fanaroff-Riley class II radio galaxy 3C 219 (*right panel*). Credits: Hardcastle and Croston 2020 and references therein.

are not able to produce strong shocks in their interaction with the surrounding medium and end with a *plume*-like morphology. In addition, FRI RGs have low radio luminosities ($\mathcal{L}_{178\,\mathrm{MHz}} < 2 \times 10^{25}\,\mathrm{W/Hz/sr}$) that decreases moving from the inside to the outside along the jets. All these effects lead to an important characteristic of FRI radio images: both radio jets are usually clearly detectable and FRI appears jet-dominated (*edge-darkened*).

- FRII radio galaxies
  Their radio morphology is similar to the one of 3C 219. Jets are ultra-relativistic at pc scale and at least moderately relativistic and supersonic at kpc one. Hence, radio jets are able to produce strong shocks in their interaction with the surrounding medium and end with extended radio lobes. In addition, FRII RGs have high radio luminosities ($\mathcal{L}_{178\,\mathrm{MHz}} > 2 \times 10^{25}\,\mathrm{W/Hz/sr}$). As a consequence of high jet speed, hence of beaming effects, the source appears one-sided in radio maps: the incoming jet flux is boosted, whereas the outcoming is strongly de-beamed, generally undetectable, according to Equation (1.20), and FRII appears lobe-dominated (*edge-brightened*).

1.3.2 Optical classification

The AGN optical classification is based on the presence and properties of optical emission lines, and can be adopted both for RQ and RL AGN. In this classification, AGN are divided in three main classes, described below.

- Type 1 AGN
  Optical spectra of AGN that belong to this class are characterized by weak narrow (FWHM $\simeq 10^2\,\mathrm{km/s}$) and strong broad (FWHM $\simeq 10^3 - 10^4\,\mathrm{km/s}$) emission lines. The narrow ones are essentially forbidden and produced in the NLR,

whereas the broad one are produced in the dense clouds of the BLR. With reference to Figure 1.5, RQ *Seyfert 1* and *non-jetted QSOs*, as well as low-power *Broad Lines Radio Galaxies* (BLRGs) and high-power *Type 1 QSOs* RL AGN belong to this category.

- Type 2 AGN
  In the optical band, Type 2 AGN show a week continuum and only narrow emission lines (FWHM $\simeq$ several 10^2 km/s). Indeed, broad lines emitted in the BLR are completely extincted by the dusty torus. Moreover, as extensively discussed in Section 1.4.4, obscuration effects can significantly impact on the X-ray observed spectra. X-ray photons interact with the torus through photoelectric absorption[4] and Compton scattering[5]. These effects can work simultaneously but in different bands. Indeed, the former operates typically at energies lower than 10 keV and the latter at higher energies. The Compton scattering reduces the photon energy which, below a certain threshold, can be absorbed by metals via photoelectric effect. The result is that the higher is the hydrogen column density (N_H), the higher are the energies at which the X-ray spectrum is absorbed. Based on the amount of hydrogen colum density along the LOS, a source is defined

  - *unabsorbed*, if $N_H \lesssim 10^{21}\,\mathrm{cm}^{-2}$;
  - *Compton-thin*, if $N_H \sim 10^{21} - 10^{24}\,\mathrm{cm}^{-2}$;
  - *mildly Compton-thick*, if $N_H \sim 10^{24} - 10^{25}\,\mathrm{cm}^{-2}$;
  - *heavily Compton-thick*, if $N_H \gtrsim 10^{25}\,\mathrm{cm}^{-2}$.

  As shown in Figure 1.5, this class of AGN involves RQ *Seyfert 2*, and low-power *Narrow Lines Radio Galaxies* (NLRGs) and high-power *Type 2 QSOs* RL AGN.

- Type 3 AGN
  Optical spectra of Type 3 AGN show low-ionization emission lines, weak optical continuum, and the dominant emission is associated to the host galaxy.

Furthermore, it is clear that, in the context unified model, the central engine of both Type 1 and Type 2 AGN is exactly the same. However, in addition to this classification, RL AGN present another sub-class due to the presence of the radio jets. Indeed, when the viewing angle between the LOS and the jet axis is small ($\vartheta < 10°$), the entire electromagnetic spectrum is dominated by jet emission, due to strong beaming effects (see Section 1.4.5 for further details) and the source is classified as a *Blazar*. Both high-power (*Flat Spectrum Radio Quasars*, FSRQ) and low-power (*BL Lac*) blazars are compact in radio images and show a non-thermal spectrum from the radio band

[4]The *photoelectric absorption* consists in the ejection of a bound electron from an atom by the absorption of a photon with energy higher than the ionization potential of that atom.

[5]The *Compton scattering* is an inelastic collision between an assumed stationary electron and a photon, which provides energy to the electron. The photon shifts to longer wavelengths because it loses energy via the interaction

up to γ-rays, typical flat radio spectra, large polarization, and strong variability. Generally, FSRQs can show emission lines over-imposed on a strong continuum, while BL Lac has a featureless optical continuum[6].

Additionally, Laing et al. 1994 proposed a different optical classification of radio galaxies, based on the excitation modes in the NLR. They split radio galaxies into *High-Excitation Radio Galaxies* (HERGs) and *Low-Excitation Radio Galaxies* (LERGs): LERGs are those characterized by [OIII] equivalent width < 10Å and/or [OII/OIII] ratios > 1, whereas HERGs have greater equivalent widths of [OIII] and consequently lower [OII/OIII] ratios. More recently, Buttiglione et al. 2010 proposed a new criterion based on the excitation index (EI[7]) to distinguish the classes: LERGs have $EI < 0.95$ and HERGs $EI > 0.95$. This classification plays an essential role in the study of RL AGN: indeed, FRIIs are generally associated to HERGs and FRIs to LERGs, which means that it is possible to use optical properties and data to investigate the power of the central source. Hence, it is almost natural to consider the nuclear engine as the main driver of the FRI-FRII dichotomy. However, this one-to-one correspondence (FRI-LERGs *vs.* FRII-HERGs), based on the study of powerful sources with Jy flux densities is probably a simplification (Grandi et al. 2021).

In this context, it is clear that the unified model previously discussed fails in describing the general properties of AGN, because it does not take into account the different accretion modes of the central SMBH. For this reason, it was recently suggested that AGN can be split in two major groups based on the accretion efficiency on the central source, which is reflected in the HERG/LERG classification: HERGs accrete efficiently and their energy output is mainly in the form of electromagnetic radiation, whereas LERGs are characterized by inefficient accretion flows and the majority of the energetic output is released in bulk kinetic form through radio jets. The former is called *radiative-mode* and it is characterized by standard accretion disks, whereas the latter *jet-mode* and is characterized by an ADAF solution. Both modes are shown in Figure 1.7.

1.4 AGN across the electromagnetic spectrum

Due to the complexity of AGN structure and emission processes in act, the only way to fully characterize a source is to study its broad-band emission, from the radio up to the γ-ray band. To this goal, the *spectral energy distribution* (hereafter SED) is studied and modelled: it describes the radiative output of a source as a function of frequency and is highly informative on the frequency range where most of the power is emitted. The SEDs of normal (i.e. without AGN) galaxies is the sum of three main components (e.g. Cimatti, Fraternali, and Nipoti 2019):

- the radiation from stars
- the radiation from diffuse matter

[6] However sometimes weak lines can be present in optical spectra.

[7] $EI = \log([\text{OIII}]/H\beta) - 1/3\,(\log([\text{NII}]/\text{H}\alpha) + \log([\text{SII}]/H\alpha) + \log([\text{OI}]/H\alpha))$

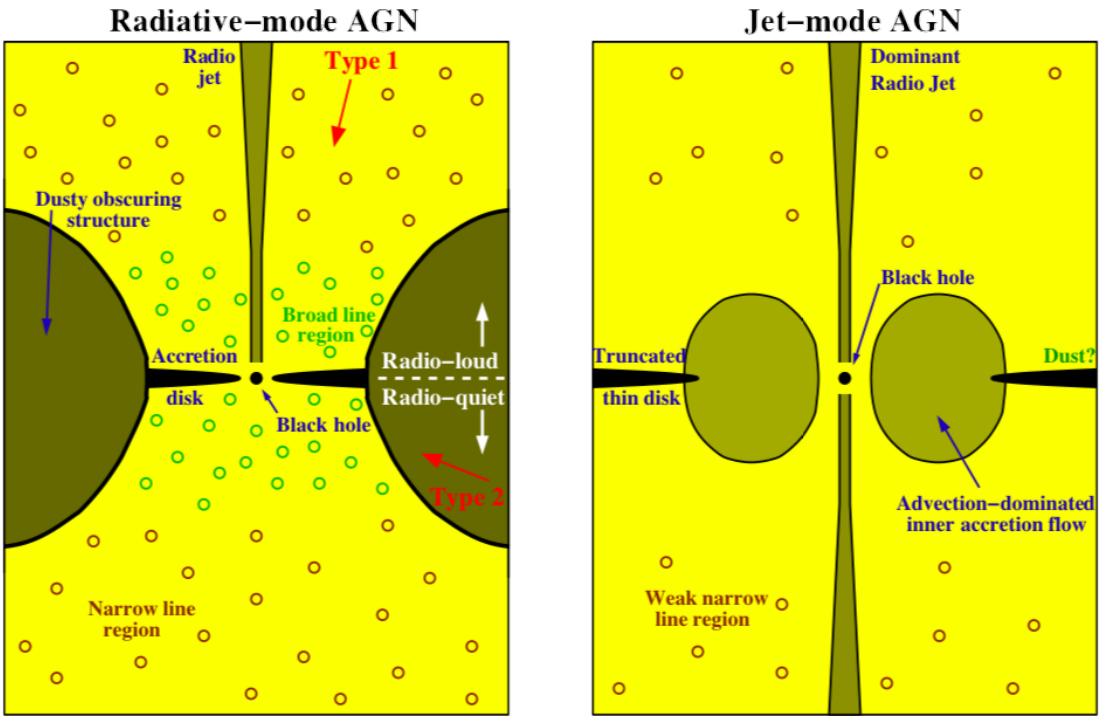

Figure 1.7: The revised unified model of Active Galactic Nuclei (not to scale). *Left panel*: radiative-mode AGN with a geometrically-thin, optically-thick accretion disk reaching in to the radius of the innermost stable orbit around the central SMBH. An obscuring torus is present: if the LOS intercepts it, the source is named Type 2 AGN, whereas if the accretion disk and the BLR is directly visible, it is named Type 1 AGN. A small percentage of AN also shows extended radio jets. In jet-mode AGN (*right panel*), the thin accretion disk is replaced in the inner regions by an ADAF. At larger radii there may be a transition to an outer (truncated) thin disk. The majority of the energetic output of these sources is released in bulk kinetic form through radio jets. Radiative emission is less powerful, but can weakly ionize the surrounding medium (LINERs) especially where the truncation radius of the thin disk is relatively low. Credits: Heckman and Best 2014.

- the radiation from dust grains

If an AGN is present, it can dominates the entire spectrum of the host. Figure 1.8 shows sketch of the AGN SED for a non-jetted QSO, a high-synchrotron peaked blazar (HSP) and a low-synchrotron peaked blazars (LSP). The latter two are sub-classes of the blazars family and the difference lies in the peak frequency and intensity of the synchrotron emission (see Section 1.4.5 for further details). In the following, I describe the principal mechanisms and origin of electromagnetic emission in AGN from radio band up to γ-rays.

1.4.1 Radio emission

As previously discussed, the radio emission from an RL AGN is produced by synchrotron radiation. In contrast, in RQ AGN the absence of luminous jets allows to probe radio emission from a wide range of possible mechanisms, from the host galaxy kpc scale down to the innermost region near the SMBHs: star formation, AGN driven

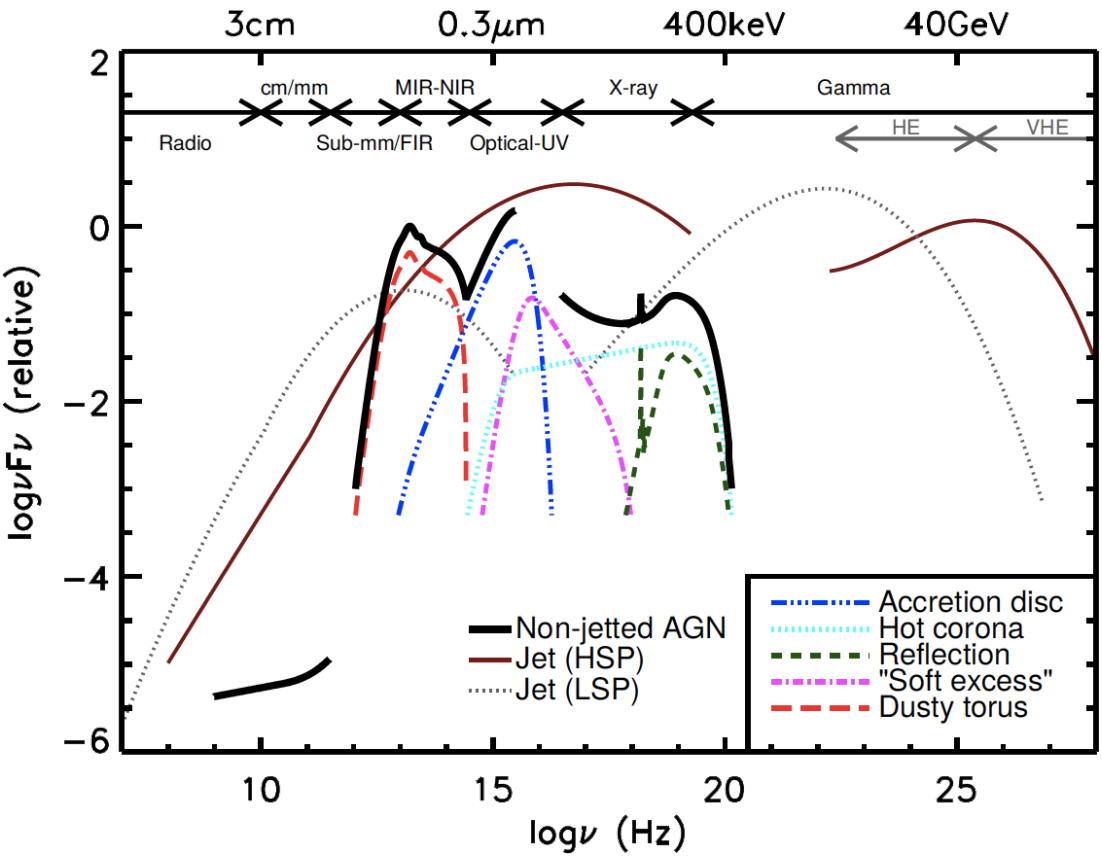

Figure 1.8: A schematic representation of an AGN spectral energy distribution (SED), loosely based on the observed SEDs of non-jetted quasars (e.g. Elvis et al. 1994; Richards et al. 2006. The black solid curve represents the total emission and the various coloured curves (shifted down for clarity) represent the individual components. The intrinsic shape of the SED in the mm-far infrared (FIR) regime is uncertain; however, it is widely believed to have a minimal contribution (to an overall galaxy SED) compared to star formation (SF), except in the most intrinsically luminous quasars and powerful jetted AGN. The primary emission from the AGN accretion disk peaks in the UV/optical region. The jet SED is also shown for a high synchrotron peaked blazar (HSP, based on the SED of Mrk 421) and a low synchrotron peaked blazar (LSP, based on the SED of 3C 454.3). Adapted from Harrison 2014. Image credits: C. M. Harrison.

wind, free-free emission from photo-ionized gas, low-power jet, and the innermost accretion disk coronal activity (Panessa et al. 2019).

In both cases, RQ and RL AGN show nuclear point-like synchrotron emission from the compact nucleus with flat, typically < 0.5, spectral indices[8]. Moreover, RL AGN show an additional and dominant emission component coming from the extended structures: the spectral index is $\alpha \sim 0.5$ for the lobes and $\alpha \sim 0.7$ for the jets.

1.4.2 Infrared emission

Infrared emission has a thermal origin: dust reprocesses UV/optical light and re-emits it in infrared band, peaking at $10 - 30\,\mu$m. According to the AGN paradigm (see

[8]In this work, the spectral index is defined as $S_\nu \propto \nu^{-\alpha}$, where S_ν is the spectral flux density usually measured in Jansky.

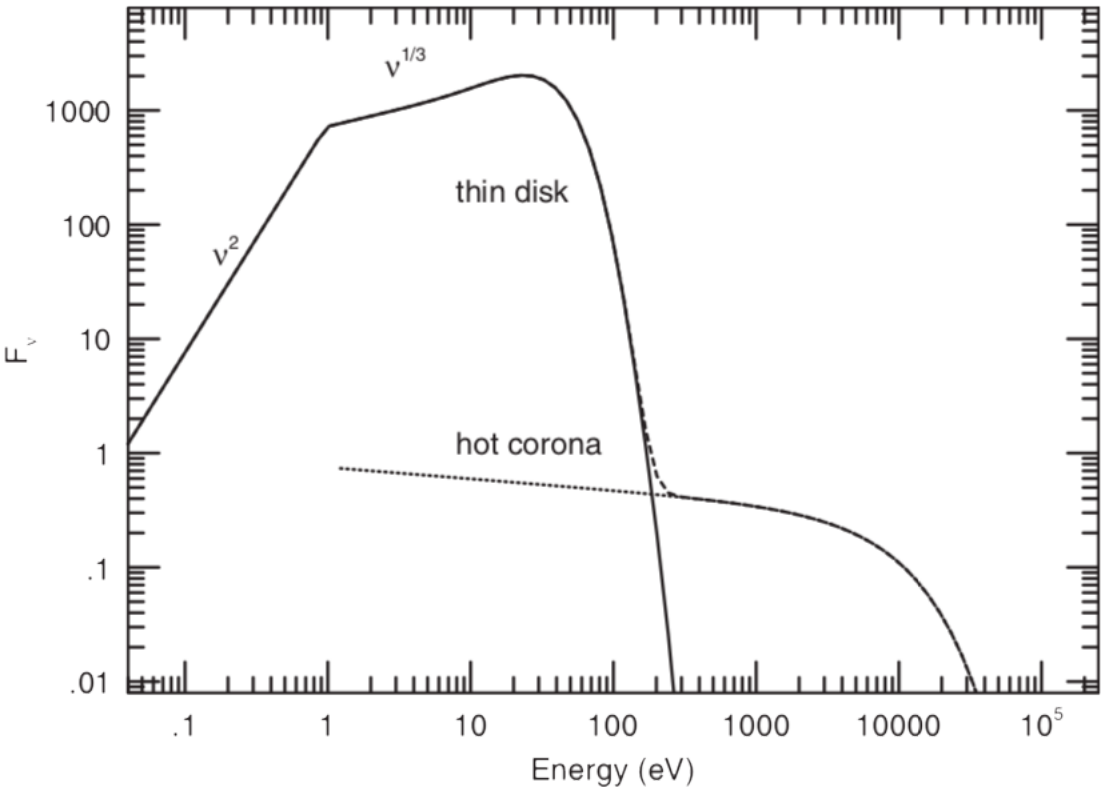

Figure 1.9: A schematic of a combined disk-corona spectrum. The maximum temperature of the geometrically thin, optically thick accretion disk is $T_{\max} = 10^5$ K, and its outer boundary temperature is determined by the conditions at the self-gravity radius[10]. The disk is surrounded by an optically thin corona with $T_{\rm cor} = 10^8$ K. Credits: Netzer 2013.

Section 1.2), the dust region is associated with the obscuring torus and the UV/optical photons come from the accretion disk: the dust acts as a grey body[9]. In addition to this, another thermal component produced by the reprocessing of the star light by cold dust is often present peaking around 100 µm.

In addition, at lower wavelengths the dust can reach its sublimation temperature ($T \approx 1000 - 2000$ keV) and produce a minimum at $\lambda \approx 1 - 2$ µm.

1.4.3 Optical/UV emission

The optical/UV radiation is thought to be produced by the accretion disk surrounding the central SMBH. Equation (1.14) implies that in a Shakura-Sunyaev accretion disk each radial layer has a different temperature and emits as a black-body: the overlap of the spectra emitted by each layer produces the observed multi black-body spectrum which is often referred as the *Big Blue Bump*, peaking in the optical/UV band. The spectrum emitted by a standard Shakura-Sunyaev accretion disk is shown in Figure 1.9.

[9] In realistic situations, the emission of a pure black-body is attenuated by scattering and absorption: the system is thus called a *grey body*. The spectrum emitted by a grey body is $Q_\nu \mathcal{B}_\nu$, where Q_ν is the efficiency factor for emission and $\mathcal{B}_\nu(T) = \left(2h\nu^3/c^2\right) / \left[\exp\left(h\nu/kT\right) - 1\right]$ is the Planck function for black-body radiation, at a given temperature T. For a pure black-body, $Q_\nu = 1$.

If the disk is optically thick, each element of the disk surface radiates roughly as a blackbody with temperature $T(r)$ (Equation (1.14)), the emitted spectrum is

$$I(\nu) = B_\nu [T(r)] = \frac{2h\nu^3}{c^2} \frac{1}{\exp[h\nu/kT(r)] - 1}. \tag{1.23}$$

The locally emitted (one side) monochromatic luminosity of the disk is defined as

$$d\mathcal{L}_\nu = 2\pi r (\pi B_\nu) dr \tag{1.24}$$

and the total monochromatic luminosity is

$$\begin{aligned} \mathcal{L}_\nu &= \int_{r_{\rm in}}^{r_{\rm out}} d\mathcal{L} \\ &= 2 \times \frac{4\pi^2 h\nu^3}{c^2} \int_{r_{\rm in}}^{r_{\rm out}} \frac{r}{\exp[h\nu/kT(r)] - 1} dr, \end{aligned} \tag{1.25}$$

where the multiplying factor 2 is to account for both surfaces of the disk. The integral can be evaluated by making the substitution $x = h\nu/kT$ and noting that $T \propto \nu/x \propto r^{-3/4}$. Thus $rdr \propto \nu^{-8/3} x^{5/3} dx$, which allows the integration between $r_{\rm in}$ and $r_{\rm out}$. If $r_{\rm out} \gg r_{\rm in}$, the spectral shape over a certain frequency range is given by

$$\mathcal{L}_\nu \propto \dot{\mathcal{M}}^{2/3} \mathcal{M}^{2/3} \nu^{1/3}, \tag{1.26}$$

where I used of the temperature dependence on the mass and the accretion rate (Equation (1.14)).

The simple schematic $\nu^{1/3}$ dependence of $\mathcal{L}_\nu$ holds only over a limited energy band because of the physical boundaries of the disk. The outer boundary imposes a minimal disk temperature and a typical frequency associated with this temperature, $\nu_{\rm out}$. Below this frequency, the spectrum resembles a black-body with a frequency dependence of $\mathcal{L}_\nu \propto \nu^2$. At the inner boundary, there is an inner temperature and a typical associated inner frequency, $\nu_{\rm in}$. Beyond this frequency, $\mathcal{L}_\nu$ drops exponentially with a functional dependence corresponding to the maximum disk temperature.

The part of the SED that shows the $\mathcal{L}_\nu \propto \nu^{1/3}$ dependence is important because it can give important estimates of $\dot{\mathcal{M}}$ from direct measurements of $\mathcal{L}_\nu$.

1.4.4 X-ray emission

The X-ray band ($\sim 0.1 - 100\,$keV) is fundamental to unveil the properties of the inner region of the AGN, including the hot corona. AGN X-ray spectra are generally the result of a complex interplay between thermal and non-thermal components, asi shown in Figure 1.10.

In the following sections, I describe the origin of each of these components, starting from the primary X-ray emission.

[10]The *self-gravity radius* is the location where the local gravity exceeds the vertical component of the central BH gravity and the disk becomes unstable.

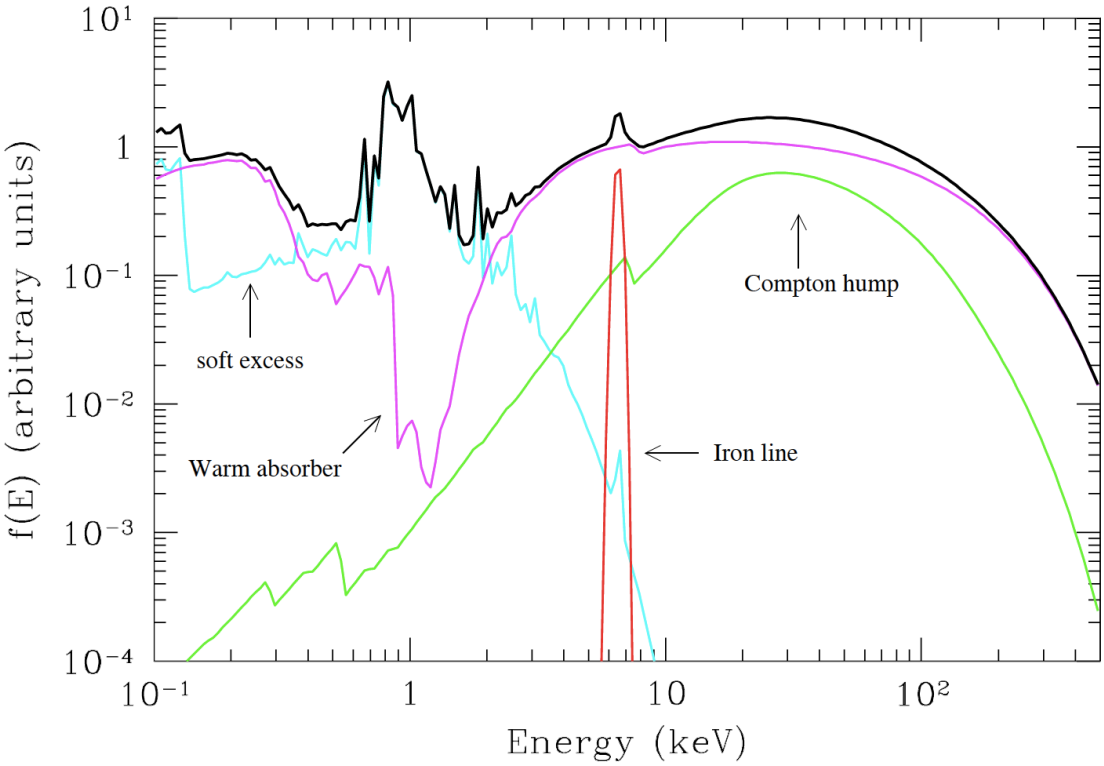

Figure 1.10: Average total spectrum (thick black line) and main components (thin grey lines) in the X-ray spectrum of a type I AGN. The main primary continuum component is a power law with a high-energy cut-off at $E \simeq 100 - 300\,\mathrm{keV}$, absorbed at soft energies by warm gas with $N_H \simeq 10^{21} - 10^{23}\mathrm{cm}^{-2}$. A cold reflection component is also shown. The most relevant narrow feature is the iron $K\alpha$ emission line at 6.4 keV. Finally, a *soft excess* is shown, due to thermal emission of a Compton thin plasma with temperature $kT \simeq 0.1 - 1\,\mathrm{keV}$. Credits: Risaliti and Elvis 2004.

The primary emission

The primary power law emission in X-rays is thought to be produced in the hot corona via thermal Comptonization of seed UV-photons coming from the accretion disk. Due to its low density, this region does not radiate as a black-body (optically thin gas) and it is able to keep very high temperatures ($T \approx 10^8 - 10^9\,\mathrm{K}$), as discussed in Section 1.2.3. It can be shown that the emitted spectrum by thermal Comptonization follows

$$\mathcal{F}_E \propto E^{-\Gamma(kT,\tau)} \exp\left(-\frac{E}{E_c\,(kT,\tau)}\right), \tag{1.27}$$

where Γ is the *photon index*[11], T is the temperature of the corona, k is the Boltzmann constant, τ is the plasma optical depth, E_c is the cut-off energy, and a Maxwellian distribution of electron energies is assumed. The exact relation between the spectral index and the optical depth depends on the geometry of the scattering region. Moreover, it can be shown that the mean energy gained from photons per collision is

$$\frac{\Delta E}{E} \approx \left(\frac{4kT}{mc^2}\right), \tag{1.28}$$

[11] The photon index Γ is in relation with the spectral index α as follows $\Gamma = \alpha + 1$.

for $E \ll kT$. After $N = \max\left(\tau + \tau^2\right)$ collisions, the final photons energy (E_f) is

$$E_f = E_i e^y \tag{1.29}$$

where E_i is the initial energy and $y = (\Delta E/E)\, N$ is the *Compton parameter*.

As photons approach the electron thermal energy ($E_c \simeq kT$), they no longer gain energy from scattering and a sharp rollover is expected in the spectrum. The observed high-energy spectral cut-off yields information about the temperature of the underlying electron distribution.

A single power law of the type $\mathcal{F}_\nu \propto E^{-\Gamma}$, where Γ is the photon index, fits well the intrinsic spectrum of many Type 1 and Type 2 AGN over the energy range $0.2 - 20$ keV. Typical values of Γ are $1.8 - 2.0$, both for low-luminosity Seyfert galaxies and high-luminosity quasars. RL AGN tends to have a flatter spectrum (Γ between 1.5 and 1.7). This is thought to be due to the additional hard component emitted by inverse-Compton scattering of the electron in the jets with the radio-synchrotron photons, but this is not fully established (Zamorani et al. 1981; Wilkes and Elvis 1987; Worrall et al. 1987).

The soft excess

An excess of X-ray emission below 1 keV, the so-called *soft excess*, is detected in a large fraction of Type 1 AGN. However, it is probably the least understood feature in X-ray spectra: indeed, in the last two decades, several attempts were done to unveil the nature of this emission and different models have been proposed (i.e. a disk reflection model, Crummy et al. 2006; a complex absorption model, Sobolewska and Done 2006). However, only recent results suggested that the intensity of the soft excess appears to positively correlate with the photon index as well as with the accretion rate, whereas there is no correlation with the BH mass or link with reflection (Boissay, Rozenn, Ricci, Claudio, and Paltani, Stéphane 2016; Gliozzi and Williams 2019): the most plausible explanation is the presence of a warm Comptonization component (e.g. Petrucci et al. 2018).

Warm absorber

An important fraction of Type 1 AGN ($\sim$ 50%) shows an absorption feature in the soft X-ray band (< 2 keV) (Nandra and Pounds 1994): it is due to the presence of a out-flowing ionized gas ($T \simeq 10^4 - 10^5$ keV) along the LOS. Typically, out-flowing velocities are about $10^2 - 10^3$ km/s (Kaspi et al. 2002; Netzer et al. 2002) and the location of the gas is still debated: different pieces of evidence place it between $0.1 - 10$ pc far from the central AGN (Netzer 2013).

Compton hump and Iron line

The hot corona isotropically up-scatters UV/optical photons coming from the disk: about 50% of them arrives to the observer and the other half goes back to the accretion

disk. An important fraction of these high-energy photons are then reflected through Compton scattering by the disk, producing a bump at $20 - 40$ keV: the so-called *Compton hump*.

The other high-energy photons, instead, are absorbed by metals present in the accretion disk through photoelectric absorption[12]: the consequent ejection of an electron in the inner atom shells can lead to line emission (*fluorescent lines*). This process is important at X-ray energies where lines of this type, most notably Fe Kα and Kβ lines, in the $6.4 - 9.0$ keV energy range are occasionally observed. The flourescence effiency (Y), the so-called *fluorescence yield*, which is the probability of a radiative de-excitation, is $Y \approx Z^4 / \left(Z^4 + 33^4\right)$, where Z is the atomic number. Thanks to its abundance and large atomic number, iron is the element with the highest production of flourescence photons. When an AGN is heavily obscured, a plethora of fluorescence emission lines appears as a consequence of the continuum suppression.

The detection and the study of iron lines produced in the innermost regions of the accretion disks are fundamental tools also to test the GR theory: the sum of the special relativity effects, through transverse Doppler shift and beaming effects, and the GR ones, through gravitational redshift, warps the line profile from the Newtonian expected shape (Fabian et al. 2000). Moreover, the line profile depends on the inner disk radius, hence on the BH spin, the inclination of the disk, and the emissivity profile[13]. However, at least another alternative model which does not include the Fe Kα line has been proposed to explain the observed feature at 6.4 keV (Miller, Turner, and Reeves 2008): the model combines highly ionized disks and several systems of large-column-density clouds that partially obscure the primary power law sources and the reflected radiation.

1.4.5 Gamma-ray emission

RL AGN, typically blazars, can also produce very high-energy emission in γ-ray band. γ-ray emission can be produced only in non-thermal processes occurring in the relativistic jets. Blazars are the dominant class of active galaxies in the γ-ray sky due to beaming effects (see Section 1.2.7; Hartman et al. 1999; Mattox and Ormes 2002; Massaro, Thompson, and Ferrara 2015; Abdollahi et al. 2020. Figure 1.8 shows two type of jetted sources: the *high synchrotron peaked blazar* (HSP, dark red line) and the *low synchrotron peaked one* (or LSP, dotted light grey line). HSP SED peaks at around $50\,\text{MeV} - 10\,\text{TeV}$, whereas LSP SED at around $100\,\text{MeV} - 100\,\text{GeV}$. Moreover, the related synchrotron peak level is different: HSP low-energy peak is in the IR-X-ray band

[12] The *photoelectric absorption* consists in the ejection of a bound electron from an atom by the absorption of a photon with energy higher than the ionization potential of that atom.

[13] The observed profile depends on the line emissivity pattern across the disk since every ring produced a somewhat different (local) profile. In many disk models, the assumed line emissivity pattern is modeled by a simple power law where the emitted line flux per unit area at an angle i and distance r from the BH is given by

$$\varepsilon(i, r) = f(i)\, r^{-\beta}. \tag{1.30}$$

The dependence of the disk line profiles on the emissivity index β is such that larger β results in a smaller emission region closer to the ISCO. This increases the importance of GR effects and results in broader lines that extends further into lower energies.

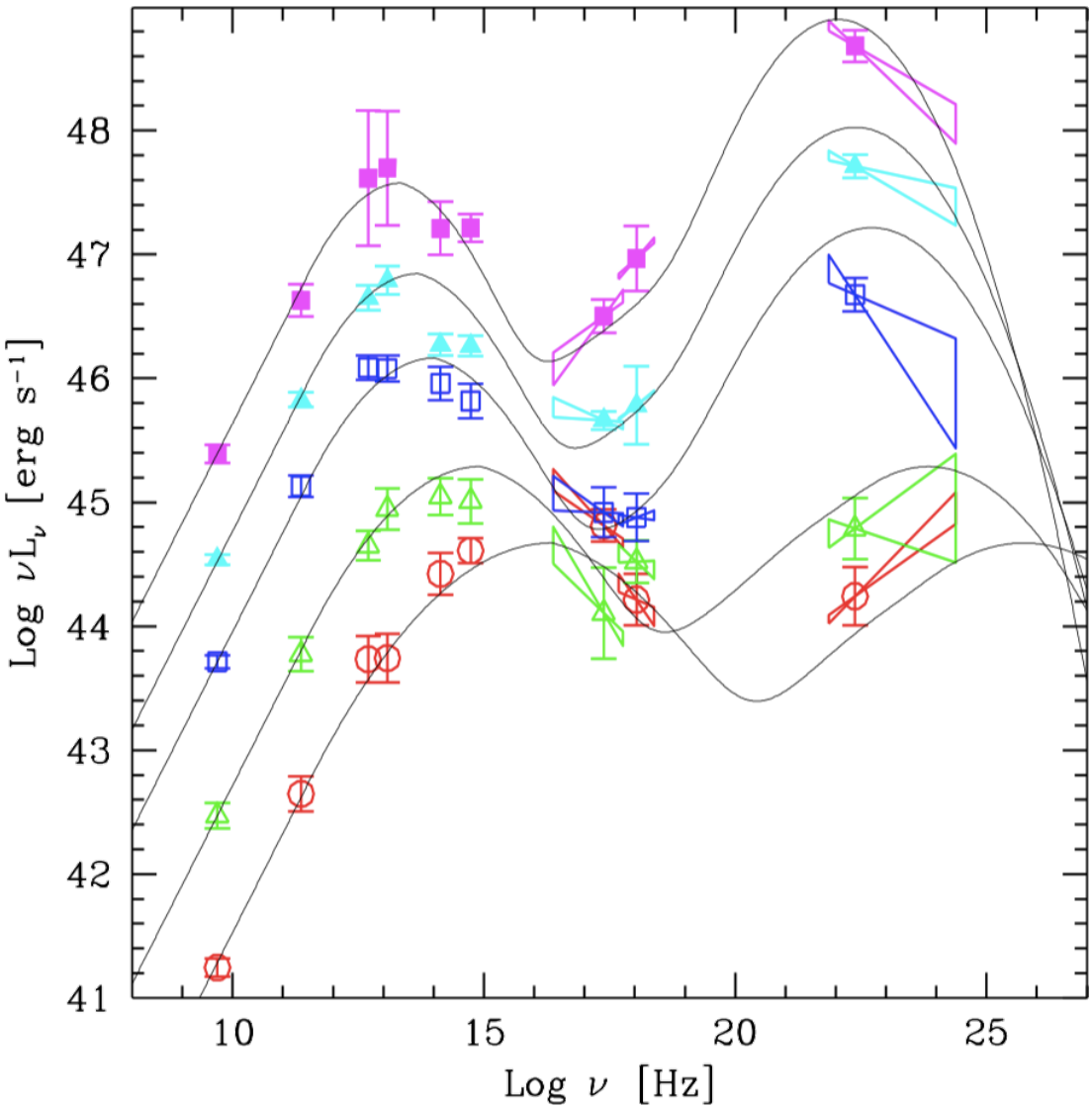

Figure 1.11: The original blazar sequence (Fossati et al. 1998; Donato et al. 2001), constructed with the 126 blazars belonging to complete (flux limited) radio and X–ray samples of blazars at those times. Credits: Donato et al. 2001.

and its intensity is comparable to the γ-ray one; LSP low-energy peak is at lower energies with respect to the HSP one and its intensity is much lower ($\sim 1-2$ orders of magnitude) than the γ-ray one. These observational characteristics are directly related to the source properties and produce the so-called *Blazar sequence* (Fossati et al. 1998; Donato et al. 2001), shown in Figure 1.11. The relation between the two peaks lies in the intensity of the magnetic field: the higher the magnetic field strength, the higher the synchrotron energy peak, the lower the number of electron available for the IC scattering, because many electrons reach very high-energies and do not gain energy from IC scattering anymore. Hence, LSP should have lower magnetic fields, and IC and SSC are the main processes in act. This explanation assumes a *leptonic model* of the jets (e.g. Maraschi, Ghisellini, and Celotti 1992): both electrons and positrons are the emitting relativistic particle population. In the *hadronic model* (e.g. Böttcher et al. 2013), the emitting particles are mostly relativistic protons and electrons: high-energy pro-

tons loose energy through either synchrotron emission (Aharonian 2000) or through photon-meson interactions (Mannheim 1993). General energy budget considerations seem to show that the total luminosity of pure leptonic models falls short of the observed luminosity in several well-studied cases, thus electron-positron pairs cannot be the sole source of the observed γ-ray radiation, and some combinations of the two types were also considered.

Chapter 2

Young radio galaxies

In this chapter I discuss the main properties of young radio galaxies and their role in the context of the RGs life-cycle. I start with a general description of what young radio galaxies are (Section 2.1; then I discuss the nature of these sources (Section 2.2), and their high-energy emission in X- and γ-ray bands (Sections 2.3 and 2.4, respectively); I then conclude presenting the sample selected for this work and the aim of this project (Section 2.5). The main references for this chapter are Siemiginowska 2009; Orienti 2016; Sobolewska et al. 2019b; O'Dea and Saikia 2021.

2.1 What YRGs are

What triggers the AGN activity is still a matter of debate. Hydrodynamic simulations suggest that when two gas-rich galaxies merge, the cold gas previously retained in each galaxy looses its angular momentum and inflows to the center, triggering the AGN activity (e.g. Gaspari, Brighenti, and Temi 2012; Gaspari, Ruszkowski, and Oh 2013).

The radio activity in extended RGs typically lasts for $10^7 - 10^8$ years (e.g. Jamrozy et al. 2005; Parma et al. 2007; Harwood et al. 2017). After this period, the so-called *active phase*, the sources enter in the *relic phase*, which typically lasts for 10^9 years: the nuclear activity stops and the radio core disappears, as well as the jets and the hotspots. Despite this, the radio lobes may still remain detectable for a long time if they are subject only to radiative losses. However, in the life-cycle of radio activity of these sources, the most important role seems to be played by the early stages of their life, when the radio activity has been just triggered. These sources are named *Young Radio Galaxies* (YRGs) and *Young Radio Quasars* (YRQs), where the distinction follows the extended radio sources classification: in the former, the angle between the jet axis and the LOS is greater 10°, for the others it is smaller. Both classes are referred to as *Young Radio Sources* (YRSs).

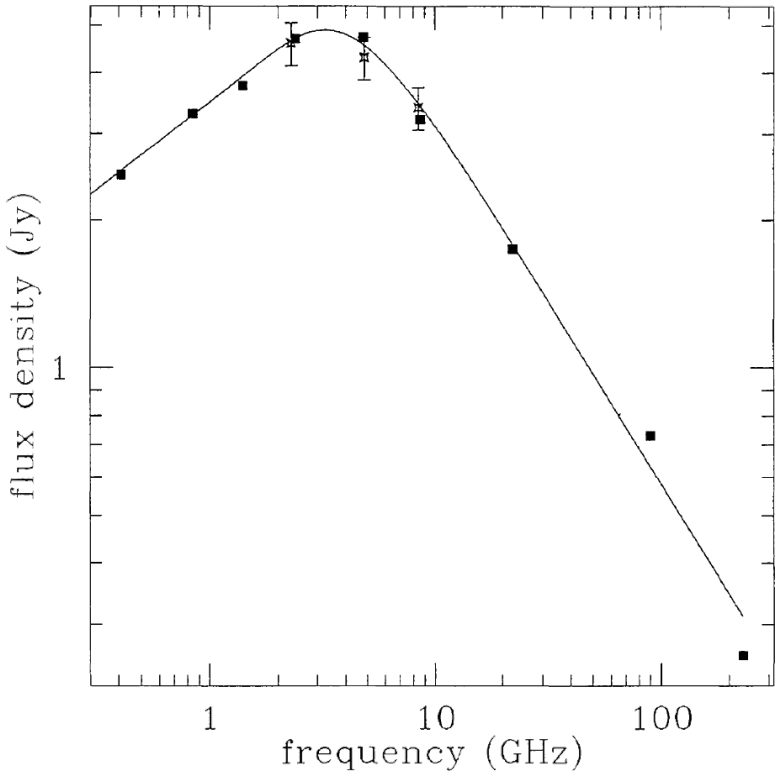

Figure 2.1: Radio spectrum of 1718-649. Total flux densities from single-dish and synthesis (MOST and ATCA) observations are shown as filled squares between 408 MHz and 230 GHz. VLBI flux densities from SHEVE observations are shown as open stars with errorbars between 2.3 and 8.4 GHz. Finally, the solid line fitted to the total flux densities is from free-free absorption model of Bicknell, Dopita, and O'Dea 1997.

2.1.1 The CSS and PS radio sources

The *Compact steep spectrum* (CSS) and *peaked spectrum* (PS) radio sources are powerful $\left(P_{1.4\,\mathrm{GHz}} > 10^{25}\,\mathrm{W/Hz}\right)$ and compact objects with angular sizes not exceeding $1-2''$ (e.g. Orienti 2016). Intrinsically compact sources are not generally dominated by their nuclear or radio core emission and are believed to represent the early stages of evolution of radio AGN, while some may be confined to small sizes by interstellar medium (hereafter ISM, O'Dea and Saikia 2021). The main peculiarity of these sources is the convex synchrotron spectrum in the radio band, as shown for 1718-649 in Figure 2.1.

In the CSS, the spectrum peaks at around 100 MHz, while PS sources, which peak in the GHz band, are divided in two sub-classes: the *GHz-Peaked-Spectrum* (GPS) sources are selected to have their radio flux density peak around 1 GHz, while sources that peak above 5 GHz are called *High Frequency Peakers* (HFPs) (Dallacasa et al. 2000). Above the peak frequency, the spectrum is steep, with a spectral index $\alpha \sim 0.7$. However, very recently, Pallavi et al. 2022 studied a sample of heavily obscured quasars observed by both WISE, in the infrared band, and NVSS, in the radio band: they found steeper high-frequency spectral indices ($\alpha \approx 1$) which correlate, weakly, with the ratio of MIR photon energy density to magnetic energy density, suggesting that the spectral steepening could arise from IC scattering off the intense MIR photon field. In addition, the PS tend to have projected linear sizes less than 500 pc, while CSS sources

tend to have sizes between 500 pc and 20 kpc (e.g. Fanti et al. 1990; O'Dea and Saikia 2021).

From the morphological point of view, VLBI imaging surveys (e.g. Wilkinson et al. 1994; Peck et al. 2000) found evidences for a new class of compact radio sources, the so-called *Compact Symmetric Objects* (CSOs), defined to be those with radio lobe emission on both sides of an active nucleus and an overall size less than about 1 kpc (O'Dea and Saikia 2021).

Because of their extremely compact linear sizes, YRGs can be spatially resolved and studied in a limited range of redshifts: they all belong to the local universe ($z \lesssim 1$), with few exceptions (e.g. B30935+428A at $z \simeq 1.29$). Instead, thanks to beaming effects, YRQs can be studied up to higher redshifts (e.g. J144516.46+095836.0 at $z \simeq 3.54$).

The turnover in the radio spectrum of CSS and PS sources likely requires an absorption mechanism (e.g. de Kool and Begelman 1989; Tingay and Kool 2003). Statistical analysis of CSS/PS samples pointed out an empirical anti-correlation between the peak frequency and the linear size (O'Dea and Baum 1997). This has been interpreted either in terms of synchrotron-self absorption, hereafter SSA, related to the compact dimension of the sources (e.g. Snellen et al. 2000; Orienti and Dallacasa 2008; Fanti 2009) or due to free-free absorption, hereafter FFA, from an ionized medium enshrouding the radio emission (e.g. Bicknell, Dopita, and O'Dea 1997; Callingham et al. 2015; Tingay et al. 2015).

2.2 The nature of YRSs

There are three main *scenarios* to explain the nature of PS and CSS sources.

1. The *Youth scenario*: the PS sources might be very young radio galaxies which will evolve into CSS sources and finally become large radio galaxies (e.g. Fanti et al. 1995; Snellen et al. 2000; Perucho 2016; Patil et al. 2020). Strong supports to this *scenario* came from the measurements of the hotspot separation velocities (typically $0.05\,c \lesssim v_h \lesssim 0.80\,c$) based on radio monitoring campaigns of selected targets over years (Taylor et al. 2000; Giroletti and Polatidis 2009) as well as the estimates of the radiative ages using multi-frequency radio spectra (Murgia 2003; Nagai et al. 2006).

2. The *Frustration scenario*: the PS and CSS sources might be compact because they are confined by interaction with dense clouds in the host galaxy ISM (e.g. van Breugel, Miley, and Heckman 1984; O'Dea, Baum, and Stanghellini 1991; Dicken et al. 2012). However, the total gas mass required to confine a radio source is still uncertain and depends on the mass and distribution of the individual dense clouds, though rough estimates are that masses of at least 10^9 to $10^{10}\,\mathcal{M}_\odot$ (De Young 1993; Carvalho 1994; Carvalho 1998; O'Dea 1998). Simulations suggest that in sufficiently dense environments ($n_e \simeq 300\,\mathrm{cm}^{-3}$), jets can remain frus-

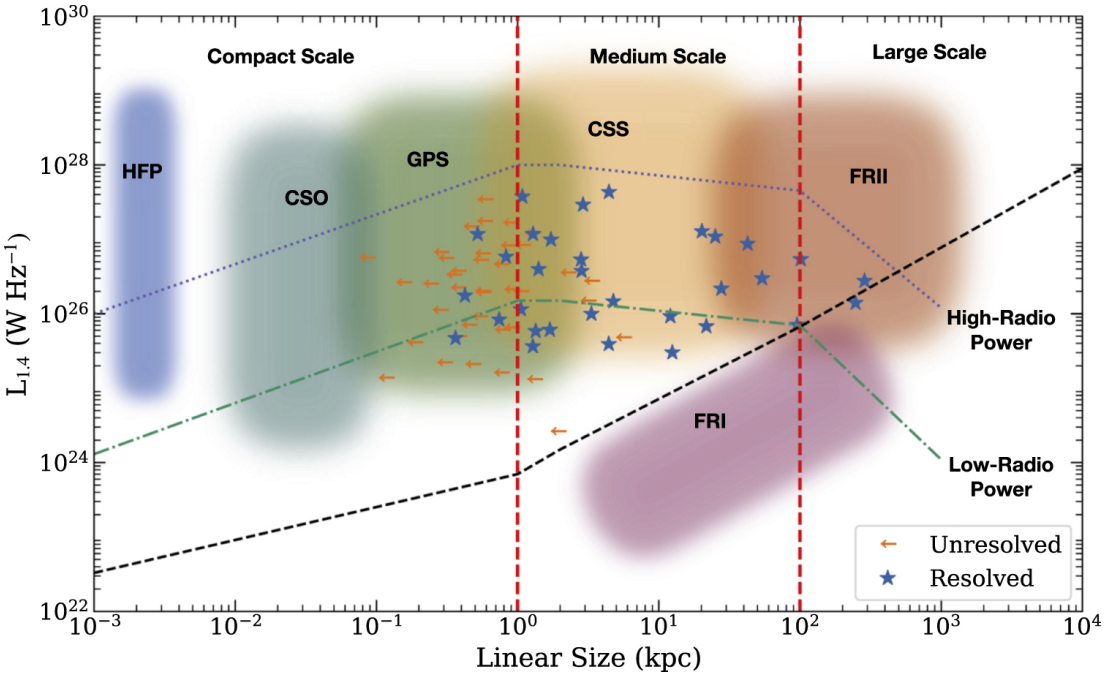

Figure 2.2: Radio luminosity measured at 1.4 GHz as a function of largest linear source extent. Blue stars represent resolved sources and orange arrows indicate unresolved sources from Patil et al. 2020. The colored boxes represent the parameter space occupied by different radio populations compiled by An and Baan 2012. The purple dotted and green dash-dotted lines are the evolutionary tracks followed by high-(HRP) and low-radio power (LRP) sources, respectively, based on the model given in An and Baan 2012. The vertical red dotted lines divide the entire plane into three broad size scales. The HFP, CSO, and GPS sources are on the compact scales ($<$ 1 kpc), CSS and a minority of FRI/FRII sources fall into the medium scales ($\sim 1 - 100$ kpc), and FRI/II sources are the large scale populations ($>$ 100 kpc). The black dashed line is the boundary between the stable and turbulent jet flows. Credits: Patil et al. 2020.

trated for 1 to 2 Myr (e.g. Bicknell and Sutherland 2006; Wagner and Bicknell 2011).

3. The PS sources might be transient or intermittent sources . In particular, radiation pressure instabilities in accretion disks may provide the timescales needed for intermittent activity (Czerny et al. 2009). In this scenario, activity lasts for $\sim 10^3 - 10^4$ yr and episodic activities are separated by $\sim 10^4 - 10^6$ yr (Czerny et al. 2009; Wu 2009; Siemiginowska et al. 2010). Jet disruption is another was of producing short-lived radio sources (e.g. De Young 1991; Higgins, O'Brien, and Dunlop 1999; Wiita 2004; Sutherland and Bicknell 2007; Wagner and Bicknell 2011; Mukherjee et al. 2016; Bicknell et al. 2018; Mukherjee et al. 2018a,b).

For the vast majority of the sources, the first *scenario* is the most plausible and is in agreement with observational data: PS and CSS sources are compact because they are young.

2.2.1 The YRSs evolution

In the context of the *Youth scenario*, an essential role is played by the luminosity evolution of the source (Figure 2.2). In the first stages of evolution, the radio source expands within the relatively dense medium at the centre of its host galaxy. The interaction with an in-homogeneous ISM manifests in the disturbed morphologies observed in the lobes of a large fraction ($\sim$ 50%) of CSOs (Saikia et al. 2003). According to theoretical predictions, in this first phase the radiative losses dominate over the adiabatic ones, leading to higher hotspots pressure (Bicknell, Saxton, and Sutherland 2003; Jeyakumar et al. 2005). Therefore, CSOs (and GPSs) are expected to be radio luminous (see Figure 2.2).

When the source reaches kiloparsec scales and expands out of the galaxy in the intergalactic medium, the adiabatic losses become dominant and the source's radio luminosity begins declining. This scenario establishes a relation between the source's linear size, age and radio luminosity.

However, there are observational evidences for a more complex evolutionary path of radio galaxies. In fact, flux-density limited catalogues shows an excess (15%-30%, depending on the frequency) of CSS and GPS radio sources, even if it is assumed a decrease of luminosity in extended sources. In particular, if CSS and GPS are $10^3 - 10^4$ years old and giant RGs are $10^7 - 10^8$ years old, the expected fraction would be 0.01%. A possible explanation could be that a large fraction of sources in these catalogues are short-lived objects, which may never become extended RGs.

This finds support also in the results reported by Kunert-Bajraszewska et al. 2010, who found a clear distinction between high-power and low-power sources: the former seem to follow the evolutionary path shown in Figure 2.2, whereas the latter could represent a short-lived objects with a different fate.

2.3 X-ray emission from CSOs

GPS sources are generally faint in X-rays ($\mathcal{L}_{2-10\,\mathrm{keV}} \lesssim$ few $10^{43}\,\mathrm{erg/s}$, Tengstrand et al. 2009) and, for the majority of the targets, only snapshot ($\sim 5\,\mathrm{ks}$) observations have been performed. Given their typical angular sizes ($< 2''$), CSOs are too compact to be resolved by any X-ray telescope and they appear as point-like in X-ray images. The X-ray observations have unveiled that CSOs can be surrounded by diffuse, thermal ($0.6 - 0.8\,\mathrm{keV}$) emission at the scales of the host galaxy (e.g. Guainazzi et al. 2006; Beuchert et al. 2018).

In general, X-ray spectra of PS and CSO galaxies can be described by an absorbed power-law with photon indices in the range $\Gamma \simeq 1.4 - 1.7$ (Siemiginowska et al. 2016). The absorbing column in the PS and CSO galaxies lies in the range $N_H \simeq 10^{21} - 10^{24}\,\mathrm{cm}^{-2}$.

There are two main hypotheses for the origin of the X-ray emission in PS and CSOs. It is possible that the it is produced primarily by the accretion disk and corona (e.g. Tengstrand et al. 2009). However, it is also possible that the X-ray emission is pro-

duced in the jets or lobes of the radio source via IC on the seed photons (i.e. the infrared photons of the dusty torus or the UV photons coming from the disk, Stawarz et al. 2008; Ostorero et al. 2010). Unveiling the nature of X-ray emission in CSOs is essential to constrain the physical parameters of these source (e.g. the accretion and the jet power), hence to predict their evolution. In addition, X-rays are important to determinate how these sources release energy in the surrounding medium (if in radiative or mechanical form), hence to study the feedback between CSOs and their host galaxies.

Combining X-ray data and their radio properties offers a unique view of CSOs: as discussed in Section 2.2, high radio luminosities are expected in the first phase when the radio source is clearing its way out of the galaxy. In these conditions, X-rays provide estimates of the total equivalent hydrogen column densities of the sources. Sobolewska et al. 2019b identified CSOs with moderately-to-high intrinsic hydrogen column densities ($N_H > 10^{23}\,\mathrm{cm}^{-2}$). These sources appear to be characterized by smaller sizes in comparison with CSOs having the same luminosity at 5 GHz but low intrinsic columns ($N_H \lesssim 10^{22}\,\mathrm{cm}^{-2}$). This finding suggests that a dense medium in X-ray obscured CSOs may be able to confine the radio jets: the more one source is obscured in X-rays, the smaller its linear size. Alternatively, X-ray obscured CSOs could be brighter in the radio band than their unobscured counterparts because the high-density environments ensure high accretion rates and, possibly, high jet powers.

2.4 Gamma-ray emission from YRSs

According to theoretical models, γ-ray emission can be produced in the jets and lobes of young radio sources (Stawarz et al. 2008; Ostorero et al. 2010; Kino and Asano 2011; Migliori et al. 2014). For the case of CSOs, the model presented in Stawarz et al. 2008 predicts a significant isotropic non-thermal emission in the $0.1 - 100$ GeV band produced in the radio lobes, however, within a wide range from $\sim 10^{41}$ erg/s up to $\sim 10^{46}$ erg/s depending on the source parameters. In this scenario, the non-thermal, high-energy emission may even dominate the total radiative output of the source and, as such, it is crucial for constraining the total energetic of the expanding source.

However, these predictions still await for validation, as currently only a handful of YRGs have been detected in γ-rays by *Fermi*/LAT (see Migliori et al. 2016; Principe et al. 2020, 2021). Principe et al. 2021 performed a γ-ray study of a large ($\sim$ 160) sample of young radio galaxies and quasars. They concluded that young quasars and radio galaxies appear to have distinct γ-ray properties. On the one hand, the former are luminous (generally $\mathcal{L}_{0.1-1000\,\mathrm{GeV}} \simeq 7 - 9 \times 10^{45}$ erg/s, up to $\mathcal{L}_{0.1-1000\,\mathrm{GeV}} \simeq 5 \times 10^{46}$ erg/s), typically variable and share the same location as blazar sources in the Γ_γ *vs.* γ-ray luminosity plot (see Figure 2.4). This strongly favors a jet origin for their γ-ray emission. On the other hand, young radio galaxies are γ-ray faint, not significantly variable and have photon index and γ-ray luminosities (generally $\mathcal{L}_{0.1-1000\,\mathrm{GeV}} \simeq 0.9 - 1.1 \times 10^{44}$ erg/s, up to $\mathcal{L}_{0.1-1000\,\mathrm{GeV}} \simeq 1 \times 10^{45}$ erg/s) similar to

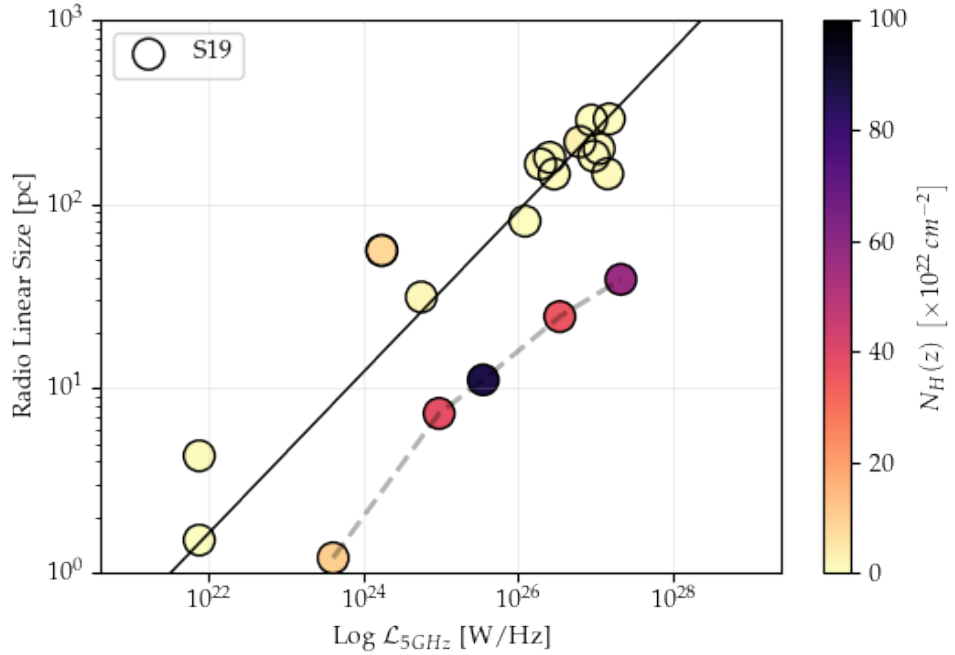

Figure 2.3: Luminosity at 5 GHz *vs*. radio source size for CSOs observed with *Chandra* and/or XMM-*Newton*. Color coding indicates the intrinsic equivalent hydrogen column density measured from the X-ray spectra. Solid line marks the relation fitted to the CSO data of Tremblay et al. 2016. Dashed line connects CSOs with intrinsic $N_H > 10^{23}\,\mathrm{cm}^{-2}$. Data from Sobolewska et al. 2019b and reference therein. Adapted from Sobolewska et al. 2019b.

misaligned sources. Such features are in principle compatible with an origin of the γ-ray emission (or a fraction of it) in the lobes.

2.5 The sample

The high-energy emission can be a significant, even dominant, fraction of the total radiative output of YRSs. Establishing its origin is crucial to constrain the parameters of the expanding radio source and its impact on the environment.

In X-rays, it is hard to disentangle the contribution of the jet- and lobe-related non-thermal emission from the contribution related to the accretion processes. A detection in γ-rays can be instrumental, as at these energies the disk-corona component is expected to rapidly drop in intensity.

For this Thesis work, a mini-sample of three YRGs (with a GPS classification based on the radio spectrum) has been selected based on their detection in the X-ray and γ-ray band (Migliori et al. 2016; Abdollahi et al. 2020; Principe et al. 2020, 2021). The goals of this study are

1. to investigate the nature of their X-ray and high-energy emission;

2. to infer their physical parameters using the broadband (radio-to-γ-ray) SED;

Table 2.1: Basic correspondences found for the sample sources

source	z	scale [kpc/arcsec]	d_L [Mpc]	References
1718-649	0.014	0.305	64.8	Meyer et al. 2004
1136+596	0.011	0.228	48.0	de Vaucouleurs et al. 1991
1843+356	0.763	7.613	4881	Wójtowicz et al. 2020

Notes. d_L is the luminosity distance that corresponds to the redshift z of the source. The online tool written by Wright 2006 to evaluate the corresponding scales and d_L was used.

3. to probe the environment in which the sources are expanding.

All the sample sources belong to the local Universe ($z \lesssim 1$), as well as the vast majority of YRSs known (e.g. Principe et al. 2021): a larger redshifts, also VLBI techniques fail to resolve these sources due to their extreme compactness and the consequent sample selections are biased by this effect.

Figure 2.4 shows the γ-ray photon index *vs.* γ-ray luminosity: all the sources with known redshift contained in the fourth catalog of γ-ray AGN (4LAC, The *Fermi*/LAT collaboration et al. 2020) including 1718-649 (alias NGC 6328) and 1146+596 (alias NGC 3894) are shown. From this figure, it is clear that, even if these two sources are both classified as CSOs with comparable linear sizes and kinematic ages, their γ-ray spectral properties are quite different. From the one hand, 1718-649 has a steep photon index in γ-ray band, comparable to those of FSRQs. From the other band, 1146+596 has a flat photon index, comparable to those of BL Lacs. This could be due to the different origin of γ-rays in these sources: γ-ray emission in 1718-649 is probably originated in *mini*-radio lobes of the sources (Migliori et al. 2016; Sobolewska et al. 2021), whereas they probably have jets-origin in 1146+596 (Principe et al. 2020). Interestingly, this could be related to their radio morphologies (see Figures 2.5 and 2.6): 1718-649 shows mini lobes and no clear detection of jets, while 1146+596 exhibits a jet (more collimated) structure, as discussed in the following sections.

2.5.1 1718-649

The galaxy NGC 6328 hosts 1718-649, the most studied CSO in the local Universe, at a redshift $z \simeq 0.0144$ (Meyer et al. 2004) and a kinematic age of about 100 years (Giroletti and Polatidis 2009). The central SMBH has a mass of about $3 \times 10^8 \mathcal{M}_\odot$ (Wójtowicz et al. 2020) and the AGN is classified as a LINER (Filippenko 1985). The main properties of the source and its host are listed in Table 2.2.

NGC 6328 shows an elliptical morphology and is classified as a S0 galaxy (Lauberts 1982; Maccagni et al. 2014); however, the host can also be classified as a SAB(s)ab galaxy, due to the prominent nuclear bulge surrounded by spiral arms of very low surface brightness (de Vaucouleurs et al. 1991; Maccagni et al. 2014). In particular, spectroscopic observations in the mid-infrared band showed features typical of star-

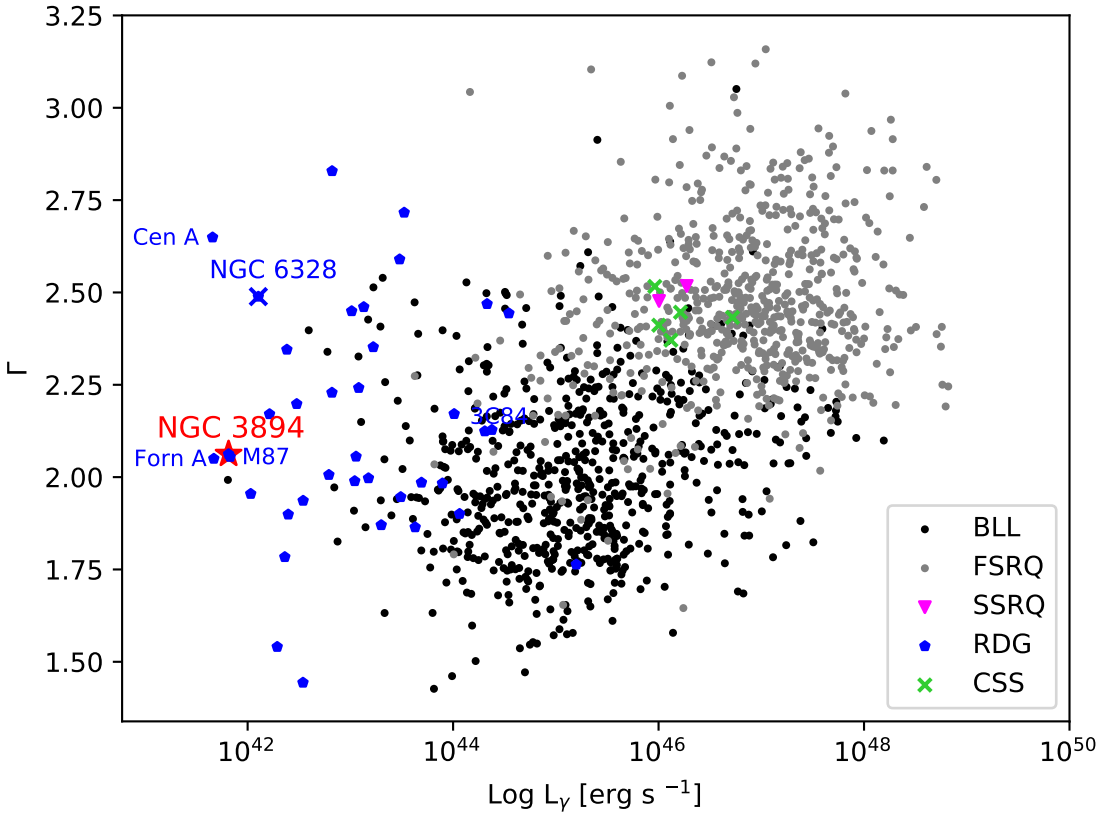

Figure 2.4: Diagram of the γ-ray luminosity *vs.* spectral index for the extragalactic sources with known redshift included in the fourth catalog of γ-ray AGN (4LAC, The *Fermi*/LAT collaboration et al. 2020). The young radio galaxies 1718-649 (alias NGC 6328) and 1146+596 (alias NGC 3894) are also labeled in the plot. Credits: Principe et al. 2020.

forming gas and AGN gas illumination (SFR $\simeq 0.8 - 1.9 \mathcal{M}_\odot$/yr, Willett et al. 2010). The high-quality optical spectra of NGC 6328 obtained by Filippenko 1985 show that high-density ($10^6 - 10^7$ cm^{-3}) clouds exist within $\sim$ 500 pc of the nucleus and that photo-ionization is the most favored mechanism responsible for the strong optical emission lines: this points to the presence of a contribution from a non-stellar power law continuum that might be associated with weak nuclear emission is present.

VLBI images at 22 GHz unveiled the morphology of 1718-649 (right panel in Figure 2.5), which is only 2 pc extended: the CSO displays two mini lobes, while the core remains undetected even at 22 GHz (Tingay et al. 1997; Tingay and Kool 2003; Angioni et al. 2019). Radio monitoring has measured a velocity separation of the two lobes of $\sim 0.07c$ (Giroletti and Polatidis 2009). Radio observations in the $2.1 - 9.0$ GHz frequency range show a spectrum peaking at $\sim$ 3.25 GHz (Tingay et al. 2015). Recent observations of the source with Australia Telescope Compact Array (ATCA) and Murchison Widefield Array (MWA) allowed Tingay et al. 2015 to conclude that the turnover in the radio band produced by an in-homogeneous free-free absorption model (Bicknell, Dopita, and O'Dea 1997).

Left panel in Figure 2.5 shows the *Chandra* image of 1718-649 in the $0.3 - 7$ keV energy range; the contours of the host galaxy in the optical badn are also shown. From

Table 2.2: Basic properties of 1718-649 and its host

Parameter	Symbol	Value	Unit	Ref.
Morphological type		S0/SABab III		(1, 2)
Radio continuum center α (J2000)	RA	$17^{\mathrm{h}}\,23^{\mathrm{m}}\,41.09^{\mathrm{s}}$		(3)
Radio continuum center δ (J2000)	DEC	$-65^{\circ}\,00'\,37''$		(3)
Redshift	z	0.0144		(4)
Age	τ_j	100	yr	(5)
Linear radio size	LS	2	pc	(5)
Hotspot separation velocity	v_h	0.07	c	(5)
Radio turnover frequency	ν_p	3.25	GHz	(6)
Galactic column density	$N_{H,\,\mathrm{Gal}}$	5.9×10^{20}	cm^{-2}	(7)

References: (1) Lauberts 1982; (2) de Vaucouleurs et al. 1991; (3) Cutri et al. 2003; (4) Meyer et al. 2004; (5) Giroletti and Polatidis 2009; (6) Tingay et al. 2015; (7) HI4PI Collaboration et al. 2016.

this figure, it is clear that the X-rays are produced in the nuclear region of the host galaxy, from a spatially unresolved region.

The case of 1718+649 illustrates well the relevance of a γ-ray detection to understand the origin of the high-energy emission in young radio sources.

Sobolewska et al. 2021 performed for the first time modeling of the radio-to-γ-ray SED of 1718+659. The γ-ray detection supports a non-thermal, high-energy component. At the same time, the symmetric morphology rules out significant beamed emission from a jet. Therefore, Sobolewska et al. 2021 applied the dynamic and radiative model by Stawarz et al. 2008 to investigate the emission of the mini-lobes. They show that, in the framework of this model, the γ-ray emission is reproduced by IC of the UV photons from an accretion disk off energetic electrons in the *mini*-radio lobes.

The interpretation of the X-ray emission is instead less solid. The $0.5 - 10\,\mathrm{keV}$ flux could be produced via IC scattering of the infrared ambient photons in the radio lobes.

However, the X-ray data are equally compatible with X-ray emission from a weak X-ray corona or a radiatively inefficient accretion flow and the authors argue that observations at $> 10\,\mathrm{keV}$ could help to solve the degeneracy between the two scenarios. Based on the modeling, Sobolewska et al. 2021 could derive estimates of important physical parameters of the source. A moderate departure from energy equipartition conditions, with the particles' energy density dominating over the magnetic field, is required to reproduce the high-energy emission.

The model infers a jet kinetic power of $\mathcal{L}_{\mathrm{kin}} \simeq 2.2 \times 10^{42}\,\mathrm{erg/s}$, in agreement with estimates obtained with other methods. Based on this, 1718-649 could be classified as a low-power source, suggesting that it is likely to evolve as a FR-I radio galaxy.

2.5.2 1146+596

The galaxy NGC 3894 (left panel in Figure 2.6) hosts 1146+596, a well studied CSO and the nearest of the studied sample, at a redshift $z \simeq 0.0107$ (van den Bosch et al. 2015)

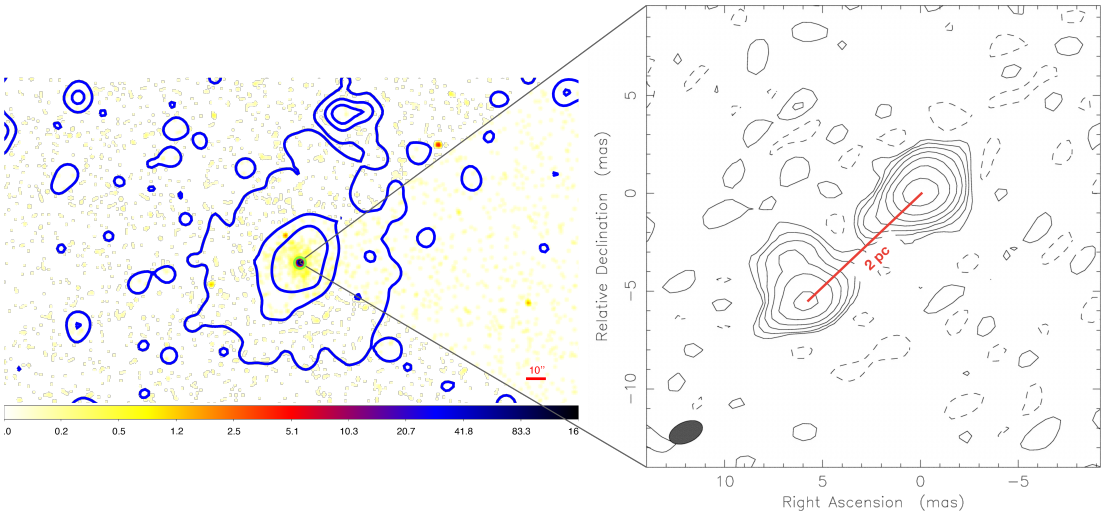

Figure 2.5: *Left panel*: *Chandra* image of 1718-649 in the $0.3 - 7$ keV energy range. A smoothing Gaussian filter ($\sigma = 1.5$ pixels, native pixel size) is applied for graphical reasons. Optical DSS contours (at $5\,\sigma$ in the IIIaJ band, centered at 4860 Å) of the host galaxy are shown in blue. *Right panel*: first VLBI image of 1718-649 at 22 GHz. The peak flux density in the image is 0.34 Jy/beam, contour levels are -1%, 1%, 2%, 4%, 8%, 16%, 32%, and 64% of peak, and beam size is $1.8 \times 1.05\,\mathrm{mas}^2$ at 66.1°. Credits: Tingay and Kool 2003.

and a kinematic age of about 60 years (Principe et al. 2020). The central SMBH has a mass of about $2 \times 10^9\,\mathcal{M}_\odot$ (Balasubramaniam et al. 2021) and the AGN is classified as a LINER (Gonçalves and Serote Roos 2004). The main properties of the source are listed in Table 2.3.

NGC 3894 shows an elliptical/lenticular morphology and is classified as a E4-5 galaxy (de Vaucouleurs et al. 1991). Although its optical continuum is dominated by starlight, this galaxy's radio and far-infrared continuum suggests the presence of an active nucleus (Condon and Broderick 1988). Spectroscopic observations carried by Kim 1989 show the presence of a dust lane and ionized gas along the galaxy's major axis; the gas kinematics are rather peculiar, exhibiting non-circular motions.

Top right pane in Figure 2.6 shows the *Chandra* image of the innermost region of NGC 3894 in the $0.3 - 7$ keV energy range. Bottom right panel in Figure 2.6 shows how the source look like in multi-epoch VLBA images at 8.4 GHz. From the morphological point of view, it has a quasi-symmetric structure, with a detected core and two mini lobes at a distance of 5 pc moving apart at about $0.2\,c$. However, Principe et al. 2020 showed that the two lobes speeds are different: $v_{\mathrm{app,\,NW}} \simeq 0.13\,c$ and $v_{\mathrm{app,\,NW}} \simeq 0.06\,c$. In addition, the radio spectrum peaks at about 5 GHz and was suggested that the most plausible mechanism responsible for the radio turnover is the SSA (Taylor, Wrobel, and Vermeulen 1998).

The first X-ray detection of the central point-like source was reported by Balasubramaniam et al. 2021. They found that the core spectrum is best-fitted by a combination of an ionized thermal plasma with the temperature of $\simeq 0.8^{+0.1}_{-0.1}$ keV, and a moderately absorbed power law component (photon index $\Gamma = 1.4^{+0.4}_{-0.4}$ and hydrogne column den-

Table 2.3: Basic properties of 1146+596 and its host

Parameter	Symbol	Value	Unit	Ref.
Morphological type		E4-5		(1)
Radio continuum center α (J2000)	RA	$11^{\rm h}\,48^{\rm m}\,36^{\rm s}$		(1)
Radio continuum center δ (J2000)	DEC	$-59^\circ\,24'\,56.43''$		(1)
Redshift	z	0.0107		(2)
Age	τ_j	60	yr	(3)
Distance of the radio lobes	LS	5	pc	(3)
Hotspot separation velocity	v_h	0.2	c	(3)
Radio turnover frequency	ν_p	5	GHz	(3)
Galactic column density	$N_{H,\,\rm Gal}$	1.86×10^{20}	$\rm cm^{-2}$	(4)

References: (1) de Vaucouleurs et al. 1991; (2) van den Bosch et al. 2015; (3) Principe et al. 2020: (4) HI4PI Collaboration et al. 2016.

Table 2.4: Basic properties of 1843+356

Parameter	Symbol	Value	Unit	Ref.
Radio continuum center α (J2000)	RA	$18^{\rm h}\,45^{\rm m}\,35^{\rm s}$		(1)
Radio continuum center δ (J2000)	DEC	$+35^\circ\,41'\,16.72''$		(1)
Redshift	z	0.763		(2)
Age	τ_j	180	yr	(1)
Distance of the radio lobes	LS	22.6	pc	(1)
Hotspot separation velocity	v_h	0.59	c	(1)
Radio turnover frequency	ν_p	2	GHz	(3)
Galactic column density	$N_{H,\,\rm Gal}$	6.7×10^{20}	$\rm cm^{-2}$	(4)

References: (1) Polatidis and Conway 2003; (2) Vermeulen et al. 1996; (3) Wójtowicz et al. 2020; (4) HI4PI Collaboration et al. 2016.

sity $N_H = 2.4^{+0.7}_{-0.7} \times 10^{22}\,\rm cm^{-2}$. Interestingly, they also suggested the detection of the iron Kα line at $6.5^{+0.1}_{-0.1}\,\rm keV$. Moreover, they found evidences of extended soft X-ray emission produced by the thermal component on the scale of the host galaxy, while the hard X-ray emission originates within the unresolved core.

Furthermore, 1146+596 has been detected in γ-rays with a strong significance of $\sigma \simeq 9.7$, and no significant variability has been observed in the γ-ray flux on a yearly time-scale (Principe et al. 2020). The γ-ray spectrum is modeled with a flat power law ($\Gamma = 2.0^{+0.1}_{-0.1}$) and a flux on the order of $2.2 \times 10^{-9}\,\rm photons/s/cm^{-2}$.

2.5.3 1843+356

1843+356 is the least studied CSO in the sample, no optical classification is available in literature (Wójtowicz et al. 2020). In addition, it is the farthest, $z \simeq 0.763$ (Vermeulen et al. 1996), and oldest, $\tau_j \simeq 180$ yrs (Polatidis and Conway 2003) source of the sample. From the morphological point of view, it has two lobes at a distance of 22.6 pc moving apart at about 0.6 c (Polatidis and Conway 2003), and the radio spectrum peaks around

2 GHz (Wójtowicz et al. 2020).

Stanghellini et al. 1993 observed a very faint host ($m_r \simeq 22$) with the NORDIC OPTICAL TELESCOPE (NOT) and the Gunn r filter ($\lambda_{ref} = 6497$ Å). The main properties of the source are listed in Table 2.4.

The first X-ray detection of the source was reported by Siemiginowska et al. 2016, even if the statistics was extremely low (about 11 net counts). It has also a marginal detection ($\sigma \simeq 3.3$) in γ-rays (Principe et al. 2021).

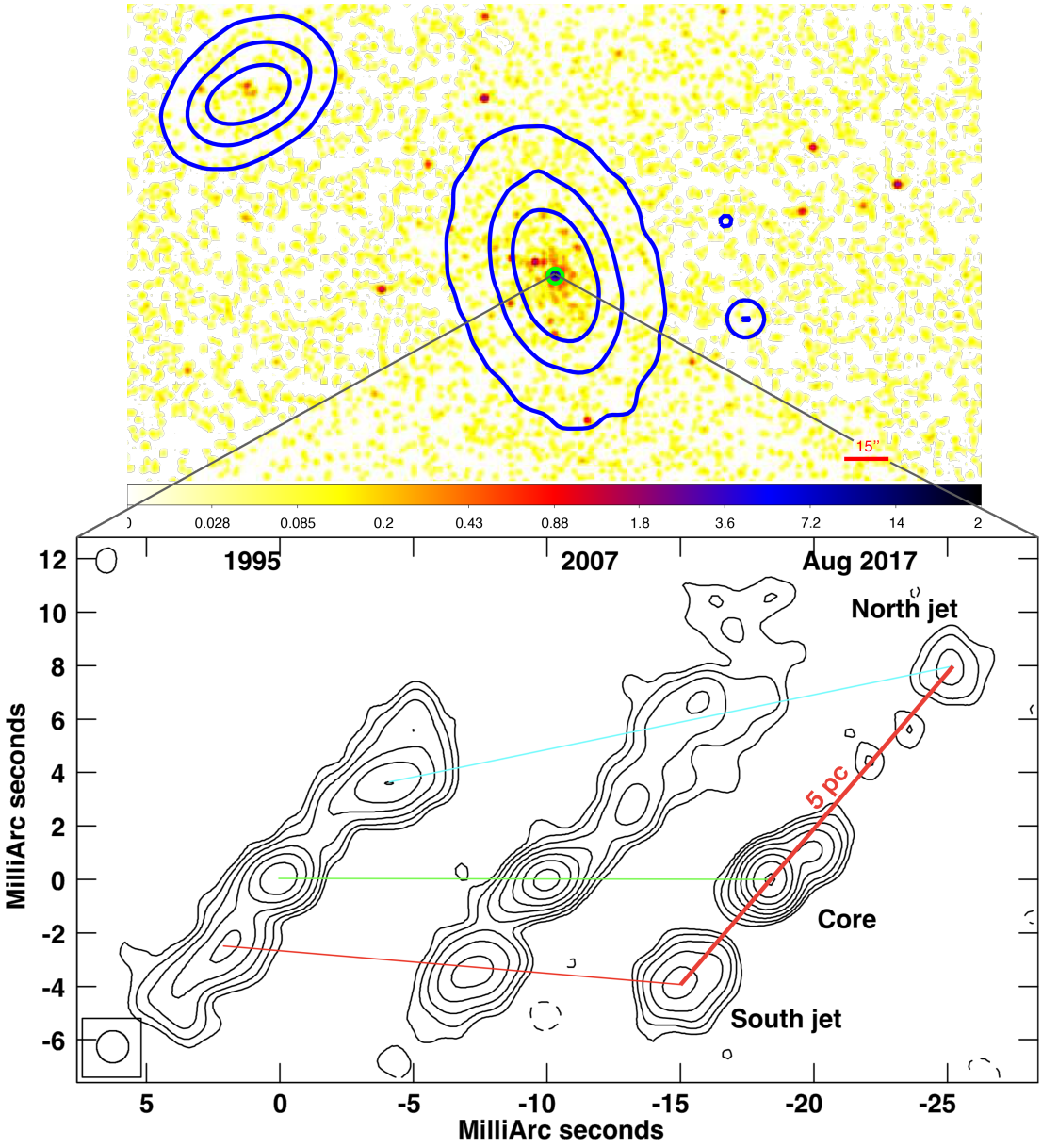

Figure 2.6: *Top panel*: *Chandra* image of 1146+596 in the $0.3-7$ keV energy range. A smoothing Gaussian filter ($\sigma = 1.5$ pixels, native pixel size) is applied for graphical reasons. Optical DSS contours (at 5σ in the 103aE band, centered at 6450 Å) of the host galaxy are shown in blue. The optical contours of NGC 3895 are also shown (top left). *Bottom panel*: comparison of three VLBA epochs at 8.4 GHz in 1995, 2007, and August 2017 (left to right). Images are spaced horizontally by a distance proportional to the time separation. Contours are traced at $\pm(1, 2, 3, 8, 16, \dots) \times 1.5$ mJy/beam. The colored lines trace the central position of the NW jet (light blue), SE jet (red), and core (green), respectively. All the images are convolved with the same circular beam (shown in the bottom left corner), whose full width at half-maximum is 1.2 mas. Credits: Principe et al. 2020.

Chapter 3

Instruments for High-Energy Astrophysics

In this chapter I discuss the general properties of X-ray telescopes (Section 3.1); then I present the main properties of *Chandra*, XMM-*Newton*, and *NuSTAR* and their importance for this work (Sections 3.2, 3.3, 3.4). The main references for this chapter are Trümper and Hasinger 2008, Seward and Charles 2010 and the user's manual of each telescope.

3.1 X-ray telescopes

Due to the opacity of the Earth's atmosphere at X-rays, telescopes working in this band ($\Delta E \simeq 0.1 - 100\,\mathrm{keV}$) have to be placed in orbit.

It is important to remember that X-ray wavelengths are very short and comparable to the atomic dimensions, and the photon energies comparable to the binding energies of the electrons in atoms. For this reason, X-ray photons requires a characteristic technique to be focused: the grazing incidence reflection. In other words, an X-ray photon can be reflected by a material if its incidence angle with respect to the mirror plane is lower than a critical angle (ϑ_c). It can be shown that, far from the fluorescent edges of the reflecting material, the critical grazing angle (ϑ_c) is a function of the reflecting material density (ρ) and the incident photon energy (E), as follows

$$\vartheta_c \propto \frac{\sqrt{\rho}}{E}. \tag{3.1}$$

Hence, for a fixed grazing angle, the higher the material density, the higher the energies reflected. In addition, for a chosen material, it is easier to reflect low-energy photons thanks to the higher values of ϑ_c.

As the German physicist Hans Wolter elaborated, the solution for X-ray optics is an optical system of at least two mirrors. He described three configurations of two-mirror systems, each with a pair of different figures of revolution in a co-focal arrangement. They are mostly called Wolter-1, Wolter-2, and Wolter-3. Both Wolter-1 and Wolter-2

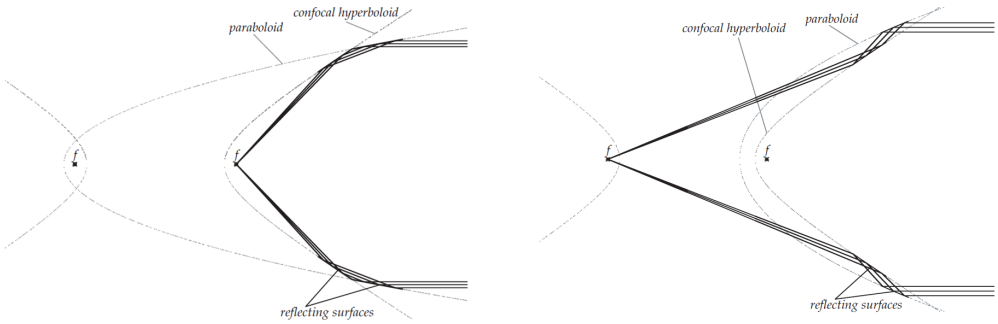

Figure 3.1: *Left panel*: Scheme of Wolter-1 (*left panel*) and Wolter-2 (*right panel*) optics. Adapted from Trümper and Hasinger 2008.

configurations are composed of a paraboloid and a hyperboloid (see Figure 3.1). A Wolter-3 system consists of a paraboloid plus an ellipsoid.

Wolter-1 geometry is the configuration adopted in X-ray telescopes because it guarantees the minimum focal length for a given aperture and allows to nest together many co-focal mirror shells, in order to maximize the *Effective Area*. This is related to the capability of a telescope plus detector system to collect photons, and is a function of the energy of incident photon (E), the off-axis angle (ϑ) and the positional coordinates on the detector (x, y):

$$A_{eff}\left(E, \vartheta, x, y\right) = A_g \times R\left(E\right) \times V\left(E, \vartheta\right) \times QE\left(E, x, y\right), \tag{3.2}$$

where A_g is the geometrical area of the telescope, $R\left(E\right)$ is the mirror reflectivity, $V\left(E\right)$ is the *vignetting* and $QE\left(E, x, y\right)$ is the *quantum efficiency* of the detector. In particular, R is the fraction of photons reflected by the mirrors, V is linked to the fraction of photons lost as a function of the off-axis angle[1] and QE is the fraction of photons that succeed in producing a signal on the detector and is independent from optics. Note that the effective area strongly depends on the energy of the incident photon, since three quantities out of four in Equation (3.2) depend on it. The effective area can also be related to the optical parameters

$$A_{eff} \approx f^2 \times \vartheta_c^2 \times R^2, \tag{3.3}$$

where f represents the focal length. In the specific case of Wolter-1 geometry, the focal length is an inverse function of the incidence angle, as follows

$$f = \frac{R}{\tan 4\vartheta}, \tag{3.4}$$

so the smaller the angle, the larger the focal length. For this reason, X-ray telescopes are generally long structures, from few up to several meters (see Table 3.1).

[1] moving away from the optical axis of the detector, a fraction of photons is lost, and this fraction is larger at increasing off-axis angle.

Table 3.1: X-ray telescopes parameters.

Mission	Nested shells	Effective area	Focal length [m]	Max energy [keV]	On-axis resolution† [arcsec]
Chandra	4	800 cm^2 @ 0.25 keV 400 cm^2 @ 5.0 keV 100 cm^2 @ 8.0 keV	10	10	0.5
XMM-*Newton*	58	1800 cm^2 @ 0.15 keV 1500 cm^2 @ 1.0 keV 350 cm^2 @ 10 keV	7.5	12	6.0
NuSTAR	133	850 cm^2 @ 9.0 keV 60 cm^2 @ 78 keV	10	79	16

Notes. † values of the Full Width at Half Maximum (FWHM).
All telescopes adopt a Wolter-1 focusing systems. *Chandra* values are listed for the HRMA in the 24^{th} Cycle.

3.1.1 Angular and spectral resolution

The *angular resolution* of a telescope corresponds to the minimum angular distance that must separate two objects in order to recognize them as two distinct sources. In other words, it is a quantitative measurement of the capability of an instrument in resolving two close sources.

Related to this, a fundamental quantity to take into account when building a telescope is the *Point Spread Function* (PSF): it describes the shape of a point-like source in the detector and is a measure of the angular resolution. The PSF in X-rays is a function of the incoming photon and off-axis angle. It is sharper in the central region of the detector and significantly broadens as the off-axis angle increases. Figure 3.2 shows how the same source looks for the three different detectors on board the XMM-NEWTON telescope (see Section 3.3 for more details): in general, the PSF shape can be approximated by a Gaussian.

In relation to this, the angular resolution is often replaced by the concept of *encircled energy fraction* (EEF): it is the fraction of photons collected within a given aperture or extraction radius. It is also referred to as the bi-dimensional PSF. The EEF of *Chandra*/ACIS-S, XMM-*Newton*/pn, and *NuSTAR*/FPMA are shown in Figures 3.3a, 3.3b, and 3.3c, respectively. From the comparison of them, it is clear that *Chandra* is the one with the best angular resolution (see also Section 3.2): about 90% of X-ray photons in the $0.3 - 7$ keV energy range are collected within a circular region of radius $2''$. With XMM-*Newton*/pn, this fraction is reached with a radius of about $30''$ ($50''$) for photons with energy of 1.5 keV (5 keV). *NuSTAR*, instead, has a much less sharp PSF and about 60% of incident photons in the $3 - 79$ keV energy range are collected within a circular region of radius $50''$.

In addition to this, an important parameter is the *spectral resolution*: it is the least difference in energy that two photons can have to be detected as two photons of different energy. When a photon of a given energy is collected, it frees a charge carrier

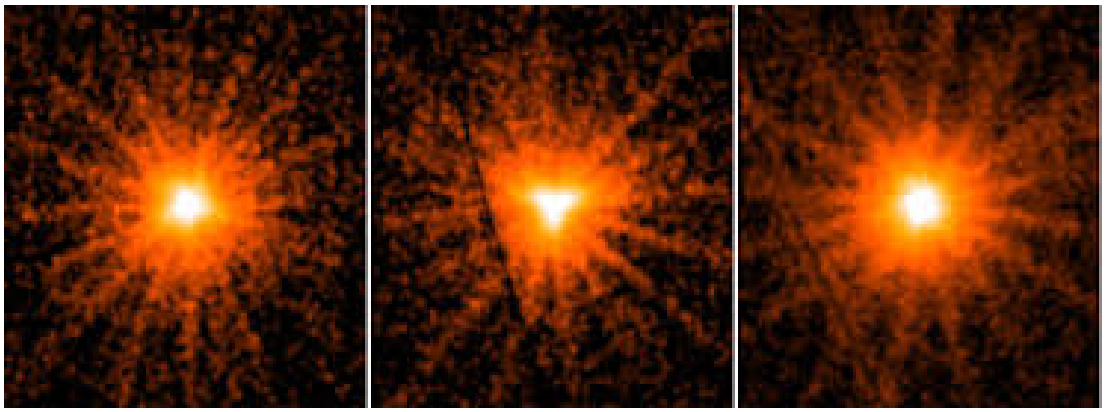

Figure 3.2: PSFs of the three EPIC detectors (MOS1 *left*, MOS2 *centre*, pn *right*) for the same non-piled-up source from the same observation (2XMM J130022.1+282402, ObsID 0204040101, revolution 823). The images are in the $0.2 - 10$ keV band with binning $1.1'' \times 1.1''$, and are very lightly smoothed, to accentuate the features. The star-like pattern is created by the spider which supports the 58 co-axial Wolter 1 mirrors of the telescope and the shape of the PSF core is slightly different for all cameras (see Section 3.3. Credits: Read et al. 2011.

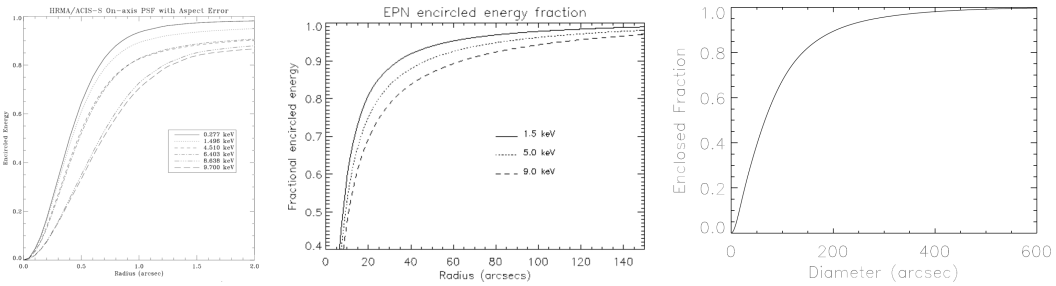

(a) (b) (c)

Figure 3.3: Encircled energy fraction as a function of angular radius (on-axis) for *Chandra*/ACIS-S (*Panel (a)*, from the *Chandra* Proposers' Observatory Guide), XMM-*Newton*/pn (*Panel (b)*, from XMM-*Newton* Users Handbook), and *NuSTAR* (*Panel (c)* from Harrison 2014).

in the detector via photoelectric absorption. The signal produced by a single carrier is too low to be appreciable, hence it has to be amplified. It can be done thank to amplification circuits: the process of charge carrier generation is usually Poissonian and the spectral resolution is defined as follows:

$$R_P = \frac{\Delta\lambda}{\lambda} = \frac{\text{FWHM}}{H_0} = \frac{2.35\sigma}{KN} = \frac{2.35K\sqrt{N}}{KN} = \frac{2.35}{\sqrt{N}}. \tag{3.5}$$

For a non purely Poissonian distribution, a correction factor F, called *Fano factor*, has to be taken into account and the Equation (3.5) becomes

$$R_F = 2.35\sqrt{\frac{F}{N}}. \tag{3.6}$$

Related to this, the *resolving power* (in some literature *spectral resolving power*) is usually used and it is defined as the precision with which the energy of an incident photon can be determined. It can be written as

$$R = \frac{E}{\Delta E}, \tag{3.7}$$

where E is the energy of the incident photon and ΔE is the broadening of the signal from the detector because of the statistical fluctuations in the number of charge carriers produced. As discussed in Section 1.4.4, the Kα iron line at 6.4 keV is one of the most important features in X-ray spectra; at these energies, the typical resolving power of for X-ray CCD spectroscopy is $E/\Delta E \simeq 40$.

3.1.2 Signal-to-Noise Ratio

Another fundamental quantity to consider during the data analysis is *Signal-to-Noise Ratio* (or SNR, in some literature also S/R): it is a measure of the source counts with respect to the background counts

$$\text{SNR} = n_\sigma = \frac{c_s}{\sqrt{c_s + c_{bkg}}}, \tag{3.8}$$

where c_s are the source counts and c_{bkg} are the background counts. In real X-ray observations, the source counts are obtained subtracting the background counts to the total counts extracted from a region containing the source: in other words, $S = (S + B) - B$. Assuming to be in Poisson regime, the error becomes

$$\sigma_S^2 = \sigma_{S+B}^2 + \sigma_B^2 = \left(\sqrt{S+B}\right)^2 + (B)^2 = S + B + B = S + 2B, \tag{3.9}$$

so

$$\text{SNR} = \frac{S}{\sigma_S} = \frac{S}{\sqrt{S+2B}} \tag{3.10}$$

Related to this, the *sensitivity* (S_{min}) of the instrument can also be defined as the

minimum detectable flux and, for a fixed SNR, it is expressed by

$$S_{\min} = \mathrm{SNR} \times \sqrt{\frac{B_1/A + \Omega B_2}{AT}}, \tag{3.11}$$

where A is the area of the detector, Ω is the solid angle subtended by the beam of the telescope on the sky, T is the exposure time, B_1 and B_2 are the instrumental and cosmic background[2], respectively.

There are to ways to improve the sensitivity of an instrument: reducing the background or increasing the effective area. The former approach was adopted by *NASA* for the *Chandra* telescope (see Section 3.2); the latter was adopted by *ESA* for the XMM-NEWTON telescope (see Section 3.3).

3.1.3 Pile-up

Another fundamental parameter which is related to the detectors in X-ray telescopes is the *pile-up*: it affects observations when the source count rate is too high with respect to the read-out time of the CCDs.

Pile-up occurs on X-ray CCDs when two or more photons hit the detector at the same place between two read-outs. In that case they are counted as one and their energies are summed. Pile-up thus affects both flux measurements and spectral characterization of bright sources. The results consist in an increase in amplitude, a reduction of detected events, a spectral hardening of continuum and a distortion of PSF (see Ballet 2003 for further details). Correcting for pile-up can be challenging, hence observations are usually set up properly to minimize such effect in case of bright targets.

3.2 *Chandra*

The *Chandra X-ray Observatory* was launched by *NASA*'s Space Shuttle Columbia in July 1999. A labelled sketch of the *Chandra* spacecraft is shown in Figure 3.4 and its main properties are listed in Table 3.1.

When *NASA* decided to send its own X-ray telescope into space, the primary goal was to improve the sensitivity compared to telescopes that were already at work. For this reason, scientists designed a telescope with four shells of very high-quality mirrors in order to increase the SNR. The result has been a telescope with a moderate effective area ($\sim 700\,\mathrm{cm}^2$ at 1.5 keV, $\sim 400\,\mathrm{cm}^2$ at 5 keV), but with a excellent spatial resolution (FWHM $\simeq 0.5''$ on-axis) and a very low level of the background, thanks to the very sharp PSF.

In particular, *Chandra* has a single focusing telescope Wolter-1 type, consisting of 4 high-quality paraboloid mirror shells associated with 4 hyperboloid ones: the so-called *High-Resolution Mirror Assembly* (or HRMA). The iridium-coated mirrors direct photons to four instruments which, however, cannot operate simultaneously:

[2]The cosmic background is produced by all the unresolved X-ray sources in the FOV of the telescope.

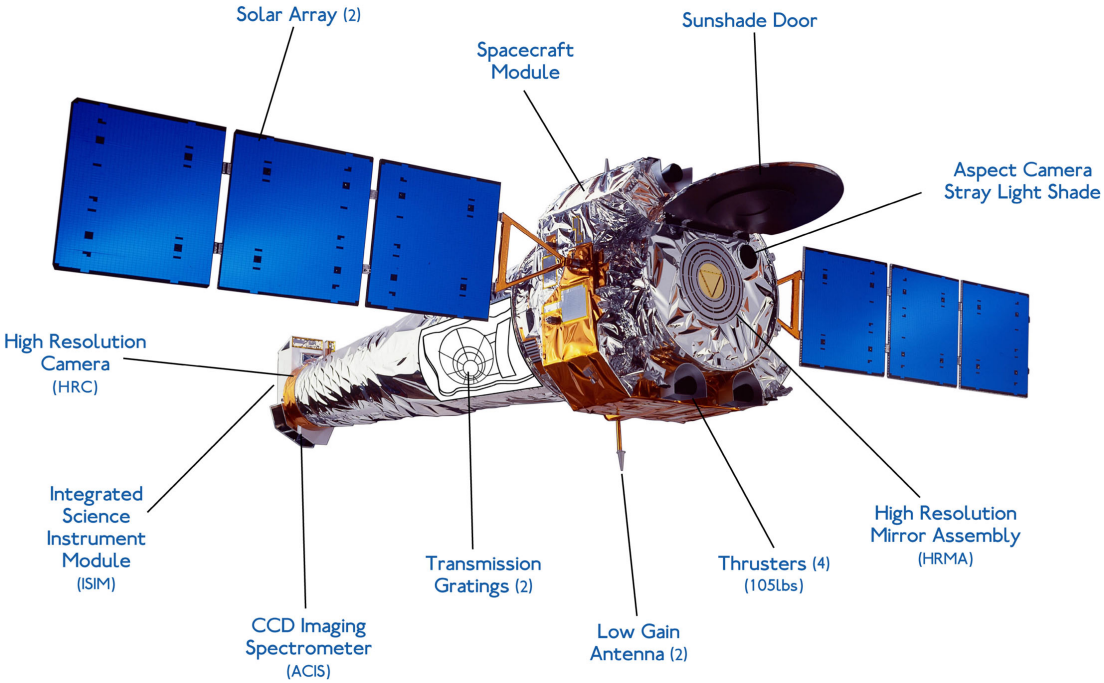

Figure 3.4: Labelled sketch of the *Chandra* spacecraft. Credits: NASA/CXC/NGST.

- The *Advanced CCD Imaging Spectrometer* (or ACIS).
  It consists of 10 CCDs and can be used either for imaging or for spectral studies. The CCDs, each composed by 1024×1024 pixels, are divided into two arrays:

  1. ACIS-I: a 2×2 array of 4 CCDs. ACIS-I is comprised of front-illuminated (FI) CCDs;
  2. ACIS-S: a 1×6 array of 6 CCDs. ACIS-S is comprised of 4 FI and 2 back-illuminated (BI) CCDs.

  ACIS allows to reach the best FWHM on-axis, about $0.5''$, for a X-ray telescope. In general ACIS-S configuration is preferred for single objects, while ACIS-I is preferred for surveys. This is because the ACIS-I configuration guarantees a larger field of view with a good angular resolution.

- The *High resolution camera* (or HRC).
  The HRC is a micro-channel plates detector with two instruments: HRC-I and HRC-S. Its spatial resolution is about $0.4''$ and the temporal resolution is about 16 ms. The HRC-I configuration is optimized for imaging, the HRC-S for spectroscopy.

- The *High* and *Low Energy Transmission Grating* (or HETG and LETG).
  HETG allows for high-resolution spectroscopy at energies between 0.4 and 10 keV. Its energy resolution ranges from 800 (at 1.5 keV) to 200 (at 6 keV). The LETG have a resolving power larger than 1000 at energies from 0.07 to 0.2 keV.

As discussed in Section 2.3, YRGs are too compact to be resolved by X-ray fa-

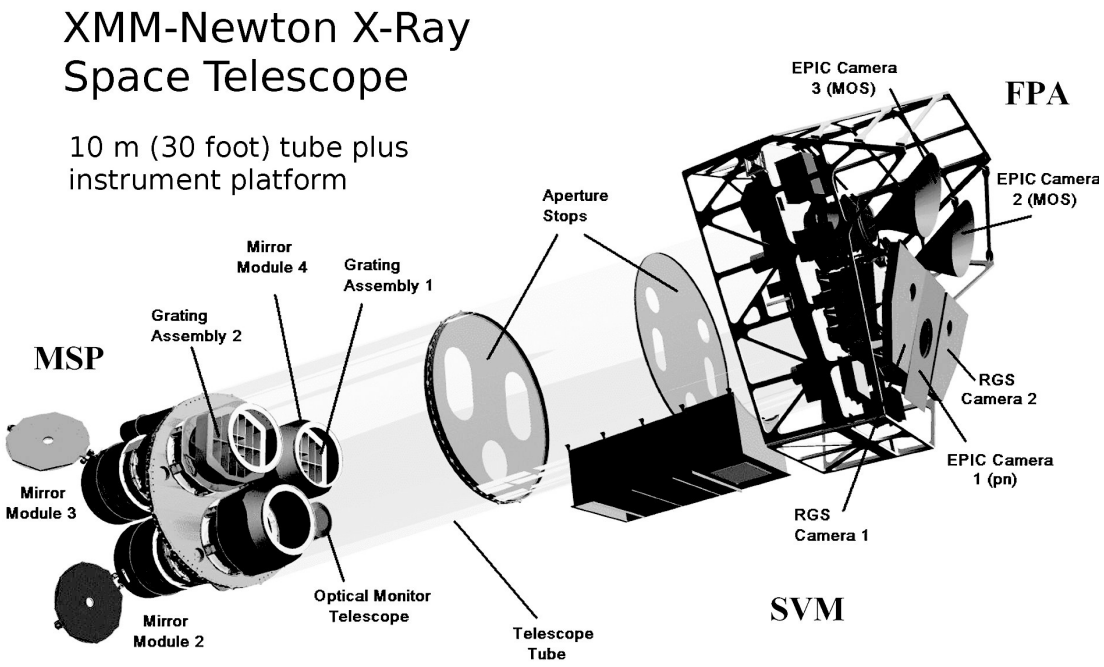

Figure 3.5: Labelled sketch of the XMM-*Newton* spacecraft. Credits: ESA/XMM-*Newton*

cilities. However, *Chandra*/ACIS-S observations allowed me to perform spatially resolved studies of the X-ray emission from the host galaxies of 1718-649 and 1146+596.

3.3 XMM-*Newton*

XMM-*Newton* was launched by *ESA*'s Ariane 5 in December 1999. A sketch of the XMM-*Newton* spacecraft is shown in Figure 3.5 and its main properties are listed in Table 3.1.

When *ESA* decided to send its own X-ray telescope into space, the primary goal was to improve the sensitivity compared to telescopes that were already at work. For this reason, scientists designed a telescope with 58 nested shells in order to increase the effective area. The result has been a telescope with a larger effective area ($\sim 1800\,\mathrm{cm}^2$ at 150 eV, $\sim 1500\,\mathrm{cm}^2$ at 2 keV, and $\sim 350\,\mathrm{cm}^2$ at 10 keV), but with a worse angular resolution (FWHM $\simeq 6''$ on-axis) and an higher level of the background with respect to *Chandra*.

XMM-*Newton* carries two distinct types of telescope: three Wolter-1 type X-ray telescopes, with different X-ray detectors in their foci, consisting of 58 nested gold-coated shells, and a 30 cm optical/UV telescope with a micro-channel plate pre-amplified CCD detector in its focal plane. Thus, XMM-*Newton* offers simultaneous access to two windows of the electromagnetic spectrum: X-ray and optical/UV. XMM-*Newton* provides the following three types of science instrument:

Table 3.2: XMM-*Newton* parameters.

#	Parameter	EPIC MOS	EPIC pn
(1)	Bandpass	$0.15 - 12\,\mathrm{keV}$	$0.15 - 12\,\mathrm{keV}$
(2)	Orbital target visibility	$5 - 135\,\mathrm{ks}$	$5 - 135\,\mathrm{ks}$
(3)	Sensitivity	$\sim 10^{-14}\,\mathrm{erg/s/cm^2}$	$\sim 10^{-14}\,\mathrm{erg/s/cm^2}$
(4)	Field of View (FOV)	$30'$	$30'$
(5)	PSF (FWHM/HEW)	$5''/14''$	$6''/15''$
(6)	Pixel size	$40\,\mu\mathrm{m}$ ($1.1''$)	$150\,\mu\mathrm{m}$ ($4.1''$)
(7)	Timing resolution	1.75 ms	0.03 ms
(8)	Spectral resolution	$\sim 70\,\mathrm{eV}$ @ $1\,\mathrm{keV}$	$\sim 80\,\mathrm{eV}$ @ $1\,\mathrm{keV}$
		$\sim 150\,\mathrm{eV}$ @ $6.4\,\mathrm{keV}$	$\sim 150\,\mathrm{eV}$ @ $6.4\,\mathrm{keV}$

Notes. The orbital target visibility is the total time available for science per orbit. XMM-*Newton* science observations can only be performed outside the Earth's radiation belts. Partially adapted from XMM-*Newton* Users Handbook.

- The *European Photon Imaging Camera* (EPIC).
  Three CCD cameras for X-ray imaging, moderate resolution spectroscopy - with respect to the RGS one -, and X-ray photometry; the two different types of EPIC camera, MOS and pn. XMM-*Newton* carries 2 MOS cameras and one pn. They offer the typical resolving power of CCDs ($E/\Delta E \simeq 40$ at 6.4 keV) and operate in the $0.3 - 10\,\mathrm{keV}$ band.

- *Reflection Grating Spectrometer* (RGS).
  Two essentially identical spectrometers for high-resolution X-ray spectroscopy and spectro-photometry. Limited in working in the $0.3 - 2.5\,\mathrm{keV}$ energy range, these high-resolution spectrometers have much lower effective area ($\sim 100\,\mathrm{cm^2}$ at 0.8 keV) than the EPIC camera instruments, in favour of excellent resolving power ($E/\Delta E \simeq 200 - 800$).

- *Optical Monitor* (OM).
  It is used for optical/UV ($\lambda \simeq 180 - 600\,\mathrm{nm}$) imaging and grism spectroscopy ($E/\Delta E \simeq 180$).

The three EPIC cameras and the two detectors of the RGS spectrometers reside in the focal planes of the X-ray telescopes, while the OM has its own telescope. There are in total six science instruments on board XMM-*Newton*, which can work simultaneously.

Table 3.2 summarizes the main parameters of the EPIC detector, which are the ones I used in this work. The properties of pn and MOS detector are quite similar. The main differences are the pixel, the timing resolution, and the effective areas: MOS detectors have smaller pixel and higher timing resolution than pn ones. However, the effective areas of the two MOS cameras are lower than that of the pn, because only $\sim$ 50% of the incoming radiation falls onto these detectors, and the other half goes to RGS. In general, XMM-*Newton* mirrors are most efficient in the energy range $0.3 - 2.5\,\mathrm{keV}$, with a maximum at about 1.5 keV and a pronounced edge near 2 keV (the Au M edge).

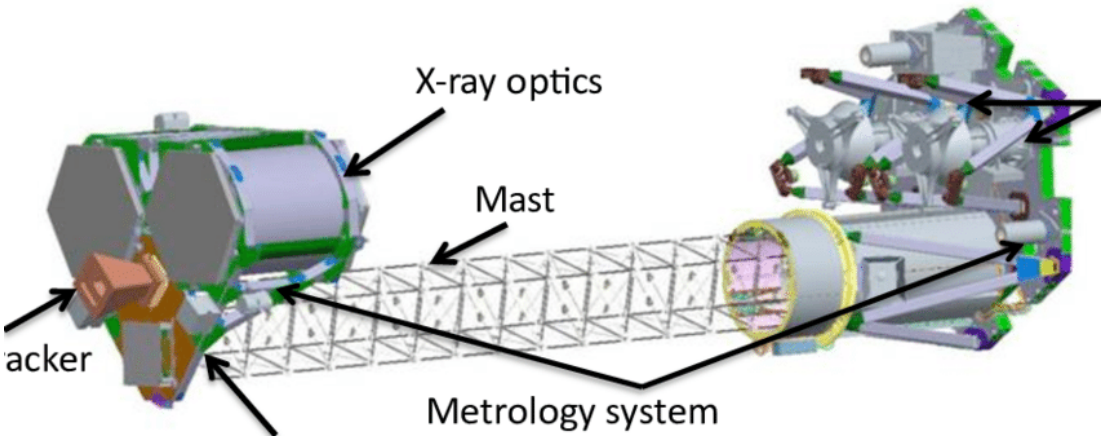

Figure 3.6: Labelled sketch view of the *NuSTAR* spacecraft. Credits: NASA/JPL-Caltech.

As discussed in Chapter 4, XMM-*Newton* was essential for this work: it allowed me to perform high-resolution spectral studies.

3.4 *NuSTAR*

As discussed in Sections 3.2 and 3.3, *Chandra* and XMM-*Newton* are complementary instruments, which give the opportunity to carry out high-quality X-ray studies from both the morphological and spectroscopic point of view. However, their energy covering range is quite small, limited to the $\sim 0.3 - 10$ keV. As a consequence, a large energy range of the electromagnetic spectrum ($10 - 100$ keV) could not be investigated until the launch of *NuSTAR*.

The *Nuclear Spectroscopic Telescope ARray* (*NuSTAR*) was launched on Pegasus XL rocket on March 2012. It is a NASA Small-class Explorer mission led by the California Institute of Technology (Caltech), which is responsible for the overall direction of the mission, with NASA's Jet Propulsion Laboratory providing project management.

It represents the first focusing hard X-ray ($3 - 79$ keV) satellite in orbit. A sketch of the *NuSTAR* spacecraft is shown in Figure 3.6 and its main properties are listed in Table 3.1.

The *NuSTAR* observatory consists of two co-aligned hard X-ray telescopes pointed at celestial targets by a three axis stabilized spacecraft based on Orbital Science's LeoStar-2 bus which provides power, data handling, storage, and transmission, and attitude control (ACS) functions. The reflection of hard photons is possible using multi-layer optics, that use different density material allowing the reflection of photons with higher energies. In particular, the coating materials vary as a function of the graze angle and have been designed to optimize the broadband energy response and FoV. The inner 89 shells are coated with depth-graded Pt/C multilayers that reflect efficiently below the Pt K-absorption edge at 78.4 keV. The outer 44 shells are coated with depth-grade W/Si multilayers that reflect efficiently below the W K-absorption edge at 69.5 keV. Consequently, the effective area is approximately 850 cm^2 at 9 keV

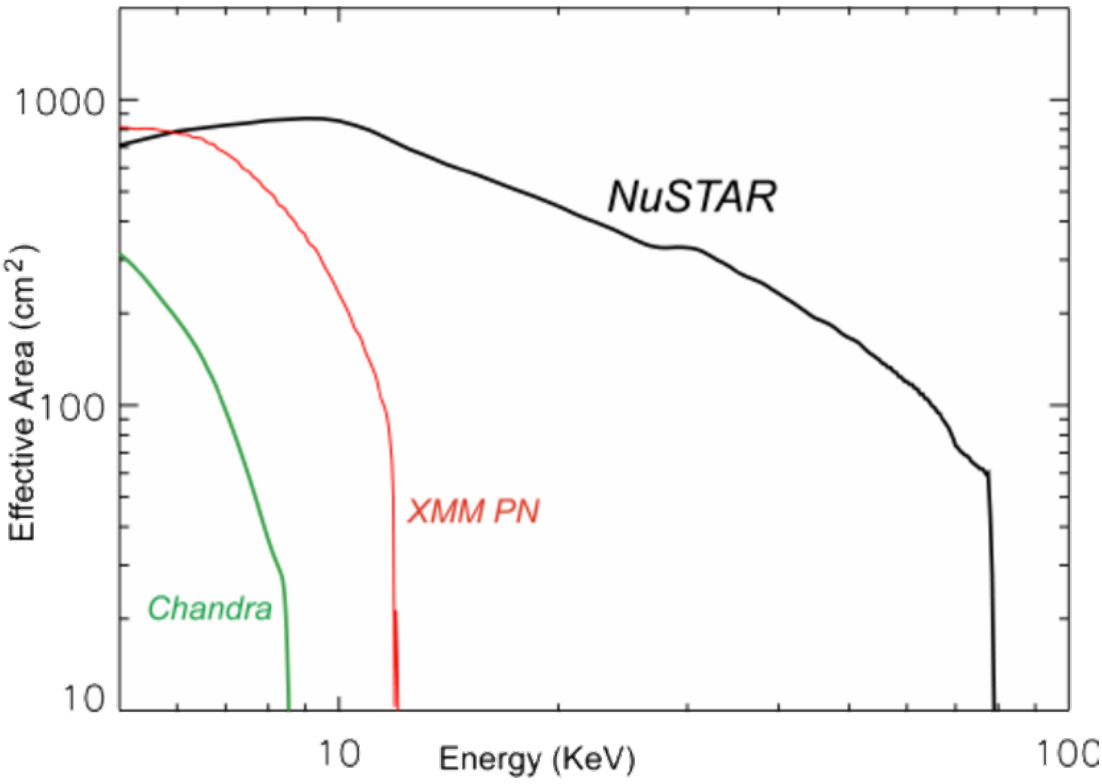

Figure 3.7: Effective area for different X-ray telescopes. Credits: Harrison et al. 2010.

adn 60 cm^2 at 78 keV, with an on-axis resolution of FWHM $\simeq 16''$.

Instead of having a CCD, as it is for *Chandra* and XMM-*Newton*, *NuSTAR* is characterized by a CzT detector, with a pixel size corresponding to $12.3''$, which reflects on a different spectroscopic resolution. The spectral response varies in the range $\Delta E \sim 0.4 - 1.0$ keV between $6 - 60$ keV.

As discussed in Chapter 4, *NuSTAR* was essential for this work: it allowed me to extend the X-ray working band, with respect to the *Chandra* and XMM-*Newton* ones, and to study X-ray spectra not affected by the obscuration contamination.

3.5 Conclusions

In conclusion, X-ray photons are challenging to be focused and telescopes have to use the grazing incidence to focus them. Each telescope is designed to perform different types of analysis: thanks to its unprecedented angular resolution, *Chandra* is the best observatory to make spatial resolved studies; XMM-*Newton*, instead, is the ideal telescope to obtain high-quality spectra, thanks to its higher effective area (about three times higher than the *Chandra* one in the $0.3 - 2$ keV band); for latest, *NuSTAR* was the first telescope to cover the hardest X-ray band (nominally, up to 79 keV), allowing to investigate sources limiting the bias against obscuration. When used in combination with *Chandra* and XMM-*Newton* observations, *NuSTAR* data are particularly useful in constraining the continuum emission of a source. As a consequence, *NuSTAR* data can significantly help the X-ray analysis of obscured or mildly-obscured sources be-

low 10 keV. However, I highlight that, for many astrophysical sources, the SNR of the observations generally allows to analyzed sources spectra up to $\sim 25 - 40$ keV. In particular, in the context of YRSs, Sobolewska et al. 2019a reported the first *NuSTAR* observation of a YRG (OQ+208, $z \simeq 0.0766$) up to about 30 keV.

Figure 3.7 shows a comparison of the effective area as a function of energy for the three main telescopes discussed above: *Chandra* ACIS in green, XMM-*Newton* pn in red and *NuSTAR* in black. The high effective area of XMM-*Newton* is limited to a small energy range, whereas *NuSTAR* covers a much broader band, allowing studies without precedent.

In this Master thesis research work, I used all the three telescopes described above: this gave me the opportunity to fully establish the X-ray properties of the studied sample achieving the maximum information available.

Chapter 4

X-ray analysis

In this chapter I describe the steps necessary to reduce and analyze the X-ray data available for the three targets of my study. The analysis involves all available data taken with *Chandra*, XMM-*Newton*, *NuSTAR* and *Swift*, listed in Table 4.1. First, I briefly outline the data reduction and calibration methods. Then, I outline the techniques of imaging and spectral analysis that were carried out. The aim of this analysis is to characterize the X-ray properties of the source sample from the spatial and spectral point of view.

Throughout the work, I used the most recent estimate of the cosmological parameters (Planck Collaboration et al. 2020): $\Omega_m = 0.315$, $\Omega_\Lambda = 0.685$ and $H_0 = 67.4\,\mathrm{km/s/Mpc}$. By assuming a flat ΛCDM cosmology with these parameters, I found the correspondences listed in Table 2.1.

4.1 Data reduction

Data reduction is a process that consists in applying the latest calibrations to the raw data of the telescopes, in order to make them readable and analyzable with data analysis software. In general, specific threads are available, that are different for each satellite. However, sometimes it is necessary to apply specific tasks depending on the quality data.

4.1.1 *Chandra*

For each target, I retrieved the available *Chandra* observations from the archive. To reduce and analyze *Chandra* data, `CIAO v.4.13`[1] (Fruscione et al. 2006) and `CALDB v.4.9.4` software packages were used.

Data reduction was carried out following standard steps. I started checking that all *Chandra* observations were carried out in `VFAINT` mode. Then, the task `chandra_repro` was used to reprocess the event file and apply the latest calibration files. I verified

[1] `https://cxc.cfa.harvard.edu/ciao/`

Table 4.1: Archival and proprietary observations used in this work.

Source (1)	Telescope (2)	ObsID. (3)	Date (4)	Exp. [ks] (5)	Ref. (6)
1718-649	*Chandra*	12849	2010-11-09	4.78	(1, 2)
	Chandra	16070†	2014-06-20	15.9	(2)
	Chandra	16623†	2014-06-23	33.0	(2)
	XMM-*Newton*	0784530201	2017-03-05	32.0	(2)
	XMM-*Newton*	0804520301	2018-03-08	40.0	—
	XMM-*Newton*	0845110101	2020-03-27/29	140.7	—
	NuSTAR	60601020002	2020-08-27	68.9	—
	Swift	00031815001	2010-09-16/09-17	5.11	—
	Swift	00031815004	2015-05-28/06-06	21.2	—
	Swift	00089109001	2020-08-25/26	5.13	—
1146+596	*Chandra*	10389	2010-07-20/21	38.5	(3)
	NuSTAR	60601019002	2020-08-02/03	77.4	—
1843+356	*Chandra*	12850	2010-10-26	4.78	(1)
	XMM-*Newton*	0822350201	2018-05-08/09	80.9	—

Notes. (1) Source ID, (2) telescope name, (3) observation ID, (4) date of the observation, (5) nominal exposure time, (6) reference corresponding to work presenting the datasets. †The two observations belong to the same observation, which was split due to technical reasons. Hence, I will analyze them as a single dataset.
References: (1) Siemiginowska et al. 2016; (2) Beuchert et al. 2018; (3) Balasubramaniam et al. 2021.

that the observations were unaffected by periods of high-flares, therefore the exposure times of the final, cleaned files are basically unchanged (see values in Table 4.1).

For each observation, I produced images in the broad ($0.3-7\,\mathrm{keV}$), soft ($0.3-2\,\mathrm{keV}$) and hard ($2-7\,\mathrm{keV}$) energy bands. The task `specextract` was used to obtain the source and background spectra. The source spectra were extracted from circular regions: for point-like source I adopted a radius of $2.5''$. For the background spectrum, several regions free from sources on the same chip of each of the target were tested in order to maximize the SNR: for 1718-649 and 1146+596, I selected two circular regions of radius $20''$ and $30''$ each, while for 1843+356 an annulus region centered on the source was chosen. I grouped data at 20 and 15 counts per bin for 1718-649 (ObsID. 16070 and 16623) and for 1146+596, respectively, in order to apply the χ^2 statistics.

4.1.2 XMM-*Newton*

I used `SAS v.19.1.0`[2] software package to reprocess XMM-*Newton* data.

First, I generated event files for each EPIC camera using the task `emproc` and `epproc` for the MOS and the pn, respectively. Due to the highly eccentric orbit of the telescope, XMM-*Newton* observations are generally affected by high-levels of back-

[2] `https://www.cosmos.esa.int/web/xmm-newton/sas/`

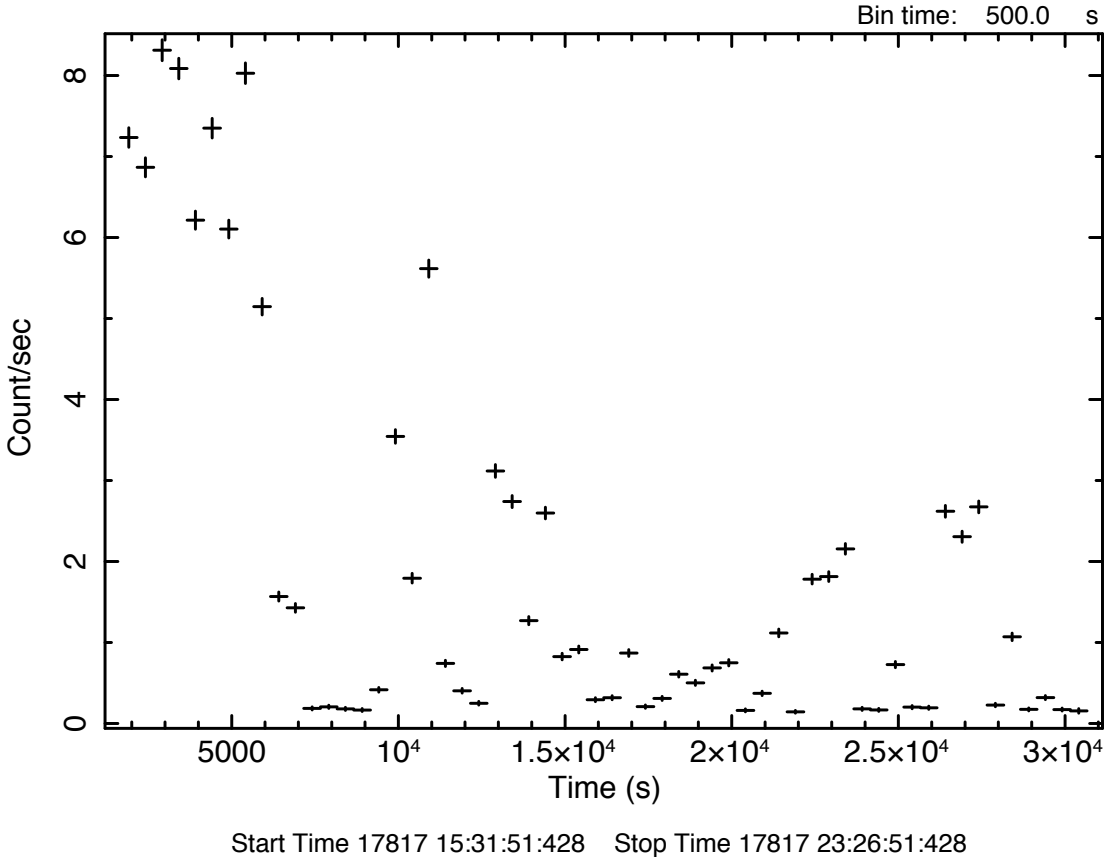

Figure 4.1: 1718-649 high-energy ($\Delta E = 10 - 12$ keV) light-curve of XMM-*Newton*/pn obtained from ObsID. 0784530201. A time interval of 500 s has been chosen for this light-curve.

ground (see Figure 4.1): indeed, when the telescope passes through the Earth's magnetosphere, it interacts with high-energy particles. This produces a signal at energies higher than 10 keV, where the XMM-*Newton* effective area is low and only background events are expected at these energies. Hence, I extracted the source light-curve in the $10 - 12$ keV energy range from the event file of each observation, in order to filter the flaring particle background.

In the case of 1718-649, I filtered data according to the standard routine: for each observation, I selected a maximum count rate over which the observation is considered affected and dominated by the flaring background. The initial and final duration for each observation and instrument are listed in Table 4.2, as well as the selected filtering rate. I grouped data of all observations at 20 count per bin.

For all XMM-*Newton* observations of 1718-649, the SNR is maximized using a circular region centered on the source. The radii of these regions depend on the observation and the detector, and are listed in Table 4.4: for the pn detector, a circular region of radius 25″ was chosen for each observation, while for MOS detectors a circular region of radius of 20″ or 25″ was chosen depending on the specific observation. Three different background shapes - single circular, double circular, annulus - were tested and I selected a single circular regions to extract the background spectrum. I then grouped data at 20 counts per bin in order to apply the χ^2 statistics.

Table 4.2: XMM-*Newton* filtering rates of 1718-649.

ObsID.	Detector	T_i [ks]	T_f [ks]	Rate [cts/s]
(1)	(2)	(3)	(4)	(5)
0784530201	pn	26.5	14.1	0.50
″	MOS1	30.2	25.4	0.20
″	MOS2	30.2	27.0	0.35
0804520301	pn	33.9	28.3	0.35
″	MOS1	38.1	37.2	0.17
″	MOS2	38.1	37.4	0.24
0845110101	pn	122.7	108.0	0.40
″	MOS1†	133.2	121.6	0.15
″	MOS2†	133.4	121.0	0.22

Notes. (1) Observation ID, (2) EPIC detector, (3-4) duration of the observation before and after the filtering procedure is applied, (5) rate at which light curves were filtered in the $10-12$ keV energy range.
†Due to the long duration of the observation, nominally 140 ks, the `emproc` task splits EPIC MOS observations into two sub-observations. I listed and analyzed only the longest sub-observations for the MOS1 and MOS2 (the other ones, few ks-long, were not included: $T_{i,\,\mathrm{MOS1}} = 4.2$ ks, $T_{i,\,\mathrm{MOS2}} = 4.0$ ks).

In the case of 1843+356, due to the high level of background in the XMM-*Newton* observation, I used a different approach: for this source, the `espfilt` thread was used. This tool performs a GTI filtering of EPIC event files and generates soft proton contamination-filtered products, including clean event lists and GTI files. In fact, the high level of the background in the XMM-*Newton* observation makes observation unusable if the same method adopted for 1718-649 was used. The source spectrum was then extracted from a circular region of radius 15″ centered on the source.

4.1.3 *NuSTAR*

To reduce and analyze *NuSTAR* data, `HEASoft v.6.28` and `NuSTARDAS v.2.0.0`[3] and `CALDB v.20211202`[4] software packages were used.

First, I ran the `nupipeline` for data calibration and screening. This process consists in processing data to produce calibrated event files and then in filtering and cleaning them according to some criteria based on specified instrument parameters.

Then, I extracted the scientific products of both instruments on-board *NuSTAR*, including spectra, with the specific task `nuproducts`. The source spectra were extracted from circular regions of radius $r_{src} = 30''$ centered on the source. For the background spectrum, a free-from-source circular region of radius $r_{bkg} = 90''$ was chosen. The spectra were extracted in the full working energy range $3-79$ keV. However, the background dominates the source signal at energies higher than 19 keV: for this reason, I performed the spectral analysis in the $3-19$ keV energy range. Then, I grouped

[3] `https://heasarc.gsfc.nasa.gov/docs/nustar/analysis/`
[4] `https://heasarc.gsfc.nasa.gov/docs/heasarc/caldb/nustar/`

data of each instrument on-board *NuSTAR* at 20 and 15 counts per bin for 1718-649 and 1146+596, respectively.

4.2 Spatial analysis

YRGs have too compact angular sizes ($< 1 - 2''$, Orienti 2016) to be spatially resolved by X-ray telescopes. However, thanks to their proximity, spatial analyses on extended X-ray emission, if present, can be performed thanks to the excellent angular resolution of *Chandra*. Each source of the sample was observed by *Chandra* at least one time. However, due to the extremely low available statistics of 1843+356 (see Table 4.4), no spatial studies could be conducted.

Siemiginowska et al. 2016 and Balasubramaniam et al. 2021 suggested the presence of extended X-ray emission in 1718-649 and 1146+596, respectively. Hence, I made use of `CIAO v.4.13 Sherpa v.14`[5] to study the surface brightness profiles of these sources.

The *Chandra* images of 1718-649 and 1146+596 in the broad ($0.3 - 7$ keV), soft ($0.3 - 2$ keV), intermediate ($2 - 5$ keV), and hard ($5 - 7$ keV) energy bands are shown in Figures 4.2 and 4.3, respectively. In both figures, the central source is the CSO and the green circular region of radius $r_{src} = 2.5''$ contains all the source radio structure. Beyond the point-like emission, which contains most of the nuclear X-ray emission, the images in the soft energy band suggest the presence of extended emission.

To reveal it, I simulated the *Chandra* PSF (Carter et al. 2003): in this regard, I have made use of the Chandra Ray Tracer (`ChaRT`[6]) online tool. I uploaded to `Chart` the spectrum of the sources for which a spatial study was performed (see Section 4.2: each spectrum was fitted with an absorbed power law model in the $0.3 - 7$ keV energy range. In particular, I asked for 50 PSF simulations, each of the nominal duration of the observation. From each simulation, I obtained a set of rays, which were then projected onto the detector plane with the `MARX v.5.5.1`[7] software (Davis et al. 2012). Then, I used the task `dmmerge` to merge the simulations.

4.2.1 1718-649

I excluded from the analysis a field source which is present in the images at RA: $17^h\,23^m\,42^s$, Dec: $-65^\circ\,00'\,23''$.

Then, I started modeling the radial profile data assuming a point-like source: indeed, a simple **const1d+psf1** model, where **const1d** is a constant model mimicking the background emission and **psf1** is the simulated PSF, was used to fit the data. The level of the background was measured from two circular free-from-source regions and fixed to 0.019 cts/pixel^2. Figure 4.4a shows the best-fit model in red and its individual components. From this, there is a relevant excess of the residuals up to about 25

[5] `https://cxc.cfa.harvard.edu/sherpa/`
[6] `http://cxc.harvard.edu/chart/`
[7] `https://space.mit.edu/cxc/marx/`

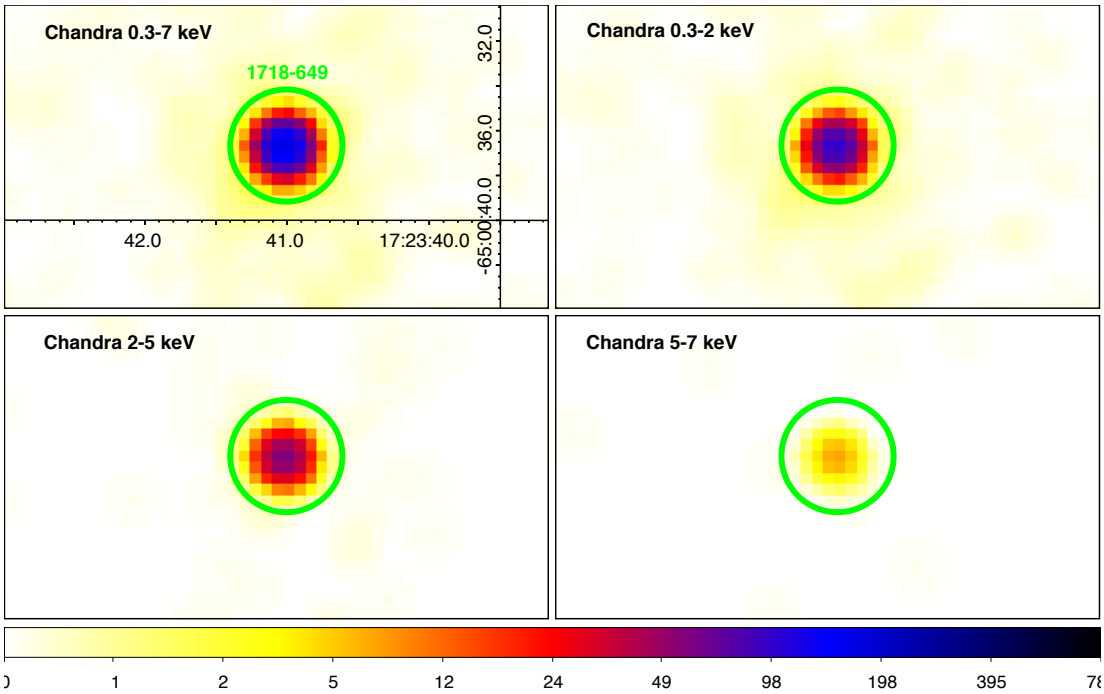

Figure 4.2: *Chandra*/ACIS-S image of 1718-649 from the longest observation (ObsID. 16623) in the $0.3-7.0$ keV energy range (*upper left panel*), the soft band $0.3-2.0$ keV (*upper right panel*), the medium band $2.0-5.0$ keV (*bottom left panel*) and the hard band $5.0-7.0$ keV (*bottom right panel*). The green circle represents the $2.5''$ extraction region of the source spectrum. A Gaussian smoothing filter ($\sigma = 1.5$ pixels, native pixel size) was applied for graphical reasons.

pixels: this suggests the presence of a diffuse component. For this reason, I added a **beta1d** component to the model: this model has been proposed, for the first time, to describe the gas density profile in galaxy clusters[8]. This is a Lorentz model with a varying power law, and its analytical expression is

$$f(x) = A\left[1 + \left(\frac{x - x_{pos}}{r_0}\right)\right]^{\frac{1}{2}-3\beta}, \tag{4.1}$$

where x_{pos} is the reference point of the profile, A the maximum value of the model at $x = x_{pos}$, and r_0 the core radius. The value of x_{pos} was set frozen to 0, which means that the maximum value of the model is reached at the source position.

Figure 4.4b shows the best-fit model in red and its individual components. All the other parameters have been left free to vary, and the best-fit parameters are listed in Table 4.3.

The difference between the source profile and the simulated PSF is much smaller than in the previous case. My results are in agreement with those reported in Siemiginowska et al. 2016 for the profile extracted from a previous shorter (4.8 keV) *Chandra* observation: they found $\beta > 0.55$, which is in agreement with $\beta > 0.82$ that I found

[8]In the context of self-gravitating Simple Isothermal Sphere (SIS) models, the gas density profile can be described by what is called a β *model*, that is valid if the potential well is associated to a King profile for the dark matter.

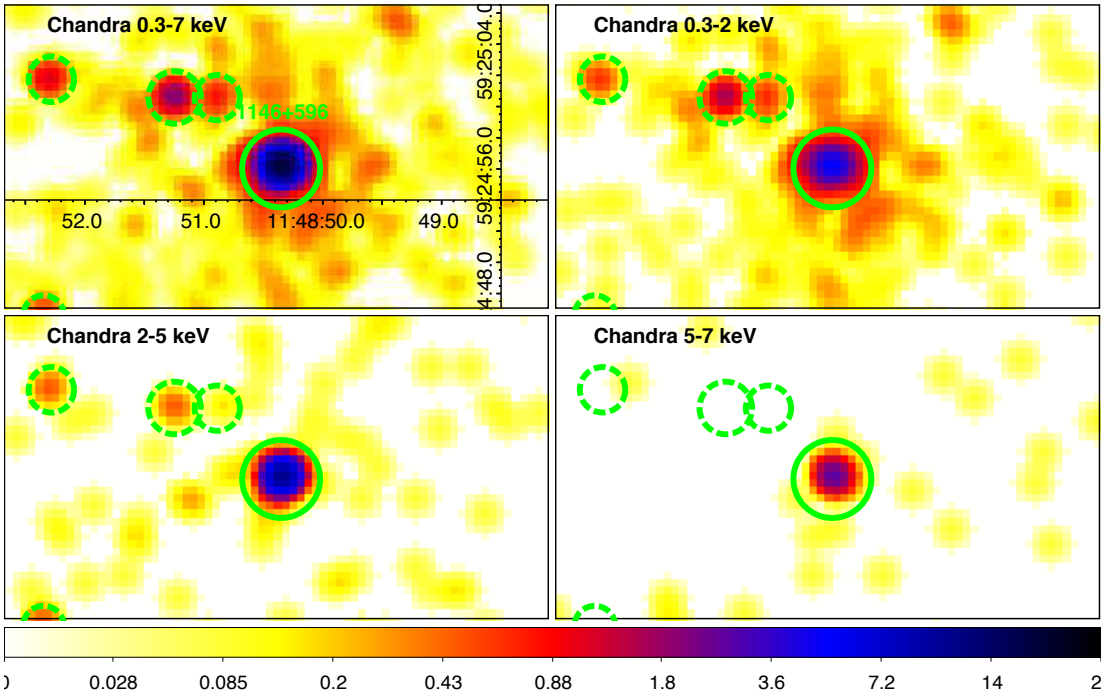

Figure 4.3: *Chandra* / ACIS-S image of 1146+596 (ObsID. 10389) in the $0.3-7.0$ keV energy range (*upper left panel*), the soft band $0.3-2.0$ keV (*upper right panel*), the medium band $2.0-5.0$ keV (*bottom left panel*) and the hard band $5.0-7.0$ keV (*bottom right panel*). The green circle represents the $2.5''$ extraction region of the source spectrum, whereas the green dashed circles represent 4 different sources I excluded for the surface brightness profile study. A Gaussian smoothing filter ($\sigma = 1.5$ pixels, native pixel size) was applied for graphical reasons.

Table 4.3: The best-fit parameters of the radial profile study of 1718-649.

psf1	**beta1d**		
ampl $\left[\times 10^{-2}\right]$	r_0	β	$A\ \left[\times 10^{-1}\right]$
$1.48^{+0.08}_{-0.08}$	67^{+9}_{-57}	> 0.82	$3.60^{+3.12}_{-0.97}$

Notes. A **const1d+psf1+beta1d** model was used to fit the surface brightness profile. The x_{pos} and the value of the constant background were frozen to 0 and 0.019 cts/pixel^2, respectively.

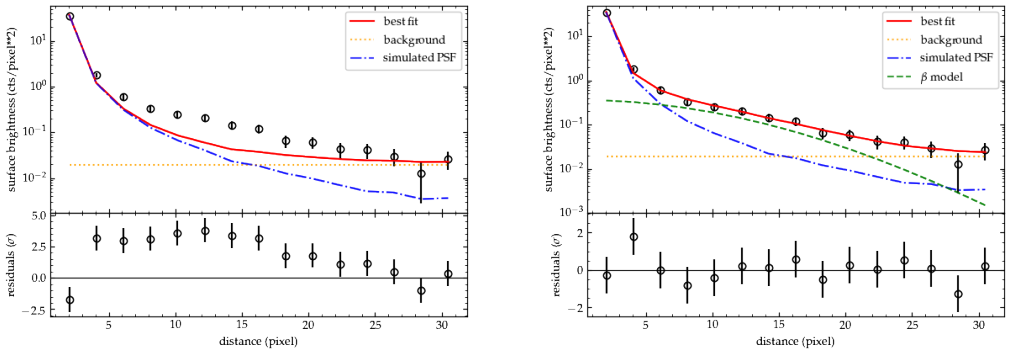

(a) (b)

Figure 4.4: X-ray surface brightness profile of 1718-649. The horizontal dotted orange line is the constant background, the blue long dashed curve represents the *Chandra* simulated PSF and the green dashed curve represents the β model ($\beta > 0.82$ from the fit). The simulation was performed assuming an absorbed power law model for the source in the $0.3 - 7$ keV energy range. The extended X-ray emission is evident up to about 25 pixel ($\simeq 12.5''$).

from the analysis of the longest observation. It is possible that there is a second diffuse emitting component: it is present up to about 25 pixels ($\simeq 12.5''$) and emits in soft X-rays ($\Delta E = 0.3 - 2$ keV). From optical observations (see Figure 2.5), since $12.5''$ correspond to 3.8 kpc at $z = 0.0144$, this component is extended up to the host galaxy scales.

4.2.2 1146+596

Following the same approach as for 1718-649, I began fitting a simple **const1d+psf1** model, where **const1d** is a constant model and **psf1** is the simulated PSF, was used to fit the data. The green dashed circles in Figure 4.3 identify 4 different sources I excluded during the surface brightness profile study. Each panel in Figure 4.5 shows the surface brightness profile of the source in different energy bands: Figure 4.5a is in the $0.3 - 7$ keV energy range, Figure 4.5b is still in $0.3 - 7$ keV energy range but without excluding any source, Figure 4.5c is in the $0.3 - 2$ keV and Figure 4.5d is in the $2 - 7$ keV.

As it evident from the figure, even if the 4 contaminating sources are excluded, the presence of extended emission is evident both from images and from residuals at least up to 20 pixels. From optical observations (see Figure 2.6), since $20''$ correspond to 4.6 kpc at $z = 0.011$, this component is extended up to the host galaxy scales. In addition, from Figure 4.5c, it is clear that this emission affects the soft-band, whereas the intermediate-hard one is well fitted by the simulated PSF (Figure 4.5d). These results are in agreement with those reported in Balasubramaniam et al. 2021, who suggested the presence of X-ray emission up to 30 pixels.

Furthermore, in analogy to the analysis carried out for 1718-649, I tried to model the excess in the $0.3 - 7$ keV energy range by adding a β component to the model:

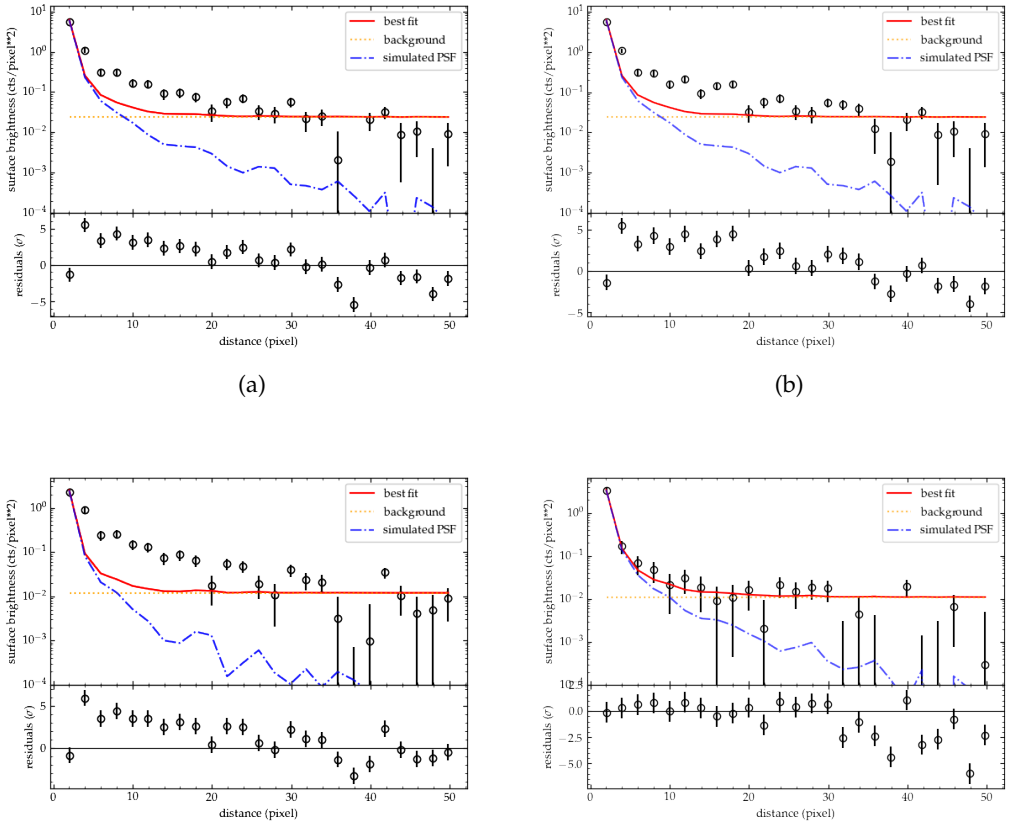

(a) (b)

(c) (d)

Figure 4.5: X-ray surface brightness profile of 1146+596. In each panel, the horizontal dotted orange line is the constant background and the blue long dashed curve represents the *Chandra* simulated PSF. The simulation was performed assuming an absorbed power law model for the source in different energy ranges: *top left panel* is in the $0.3-7$ keV energy range, the *top right* one is still in $0.3-7$ keV energy range but without excluding any source, the *bottom left* one is in the $0.3-2$ keV and the *bottom right* one is in the $2-7$ keV. The excess, which can be observed in the residuals related to the extended emission, is evident at least up to 20 pixels ($\simeq 10''$).

however, due to the less smooth radial profile of the source between 20 and 30 pixels with respect to the 1718-649 one, I was not able to model the extended emission with this component.

In conclusion, extended X-ray emission is present up to 25 and 20 pixels in 1718-649 and 1146+356, respectively, and these results are in agreement with those in literature (Siemiginowska et al. 2016; Beuchert et al. 2018 for 1718-649 and Balasubramaniam et al. 2021 for 1146+596).

4.3 Spectral analysis

For the spectral analysis, I used `Xspec v.12.11.1`[9] (Arnaud 1996) and χ^2 fitting statistics to analyze background-subtracted data, whereas `Sherpa` and Cstat (Cash 1979) fitting statistics to analyze the unbinned ones. In both cases, the Levenberg-Marquardt minimization technique was adopted. All the errors are listed at a 90% level of confidence for one significant parameter (Avni 1976). To evaluate the statistical significance for the addition of a model component, the Fisher test (Fisher 1922) was adopted. I highlight that this is not the most accurate method to evaluate the significance of the addition of a model component: however, it is sufficiently accurate for the purposes of this work.

4.3.1 1718-649

Chandra

The *Chandra*/ACIS-S image of 1718-649 in the $0.3 - 7\,\mathrm{keV}$ energy range is shown in Figure 4.2. As previously mentioned, for the unresolved emission of the CSO, the radius of the source region was set to $r_{src} = 2.5''$. I also performed a spectral analysis of the extended emission unveiled by the surface brightness profile study. For this study, I enlarged the extraction region radius to $15''$.

Central AGN emission Firstly, I analyzed each observation individually. In ObsID. 16070 and 16623 the number of counts allowed grouping of the data in bins of 20 counts each and I could therefore use the χ^2 fitting statistics. Because of the limited statistics, the spectrum of Obs 12849 was not binned and I made use of the Cstat fitting statistics. When the χ^2 fitting statistics was adopted, I analyzed the background-subtracted data; when the Cstat one is adopted, the background should not be subtracted from the data and was modeled simultaneously with the source. However, thanks to the extremely low level of the background in *Chandra* observations, the Cstat fitting statistics can be used to fit the unbinned data even if their are background-subtracted (e.g. Zappacosta et al. 2020).

For each observation, I started modeling the spectrum with a simple power law model (model I), **phabs**×**powerlaw** in `Xspec` nomenclature. The analytic model is

$$M(E) = \exp\left[-N_{H,\,\mathrm{Gal}}\sigma(E)\right] \times K \times E^{-\Gamma}, \tag{4.2}$$

where $N_{H,\,\mathrm{Gal}}$ is the Galactic column density (see values in Tables 2.2, 2.3 measured in cm^{-2}, $\sigma(E)$ is the photoelectric cross-section (not including Thomson scattering), K is the power law normalization measured in photons/s/cm^2 at 1 keV, Γ is the photon index of the power law.

The fit was not satisfactory for ObsID. 16070 and ObsID. 16623: in particular, negative residuals were present and significant to more than $5\,\sigma$ in the soft energy band

[9] `https://heasarc.gsfc.nasa.gov/docs/xanadu/xspec/`

Table 4.4: 1718-649 counts and SNR.

Telescope (1)	ObsID. (2)	Det. (3)	Ext. reg. (4)	Tot. cts (5)	Net cts (6)	SNR (7)
Chandra	12849	ACIS-S	2.5″	208 ± 14	207.6 ± 14.4	10
Chandra	12849	ACIS-S	15″	208 ± 14	207.6 ± 14.4	10
Chandra	16070	ACIS-S	2.5″	1094 ± 33	1093.3 ± 33.0	23
Chandra	16070	ACIS-S	15″	1235 ± 35	1208.0 ± 35.3	34
Chandra	16623	ACIS-S	2.5″	2739 ± 52	2737.5 ± 52.3	37
Chandra	16623	ACIS-S	15″	3070 ± 55	3014.3 ± 55.5	54
XMM-*Newton*	0784530201	pn	25″	2161 ± 46	1994 ± 44.7	43
XMM-*Newton*	0784530201	MOS1	20″	753 ± 27	704.8 ± 26.5	26
XMM-*Newton*	0784530201	MOS2	20″	1050 ± 32	993.3 ± 31.5	31
XMM-*Newton*	0804520301	pn	25″	4018 ± 63	3668.4 ± 60.6	58
XMM-*Newton*	0804520301	MOS1	25″	1699 ± 41	1537.6 ± 39.2	37
XMM-*Newton*	0804520301	MOS2	25″	1673 ± 41	1547.5 ± 39.3	38
XMM-*Newton*	0845110101	pn	25″	15515 ± 125	14323.9 ± 119.7	115
XMM-*Newton*	0845110101	MOS1	25″	5537 ± 74	5077.4 ± 71.3	68
XMM-*Newton*	0845110101	MOS2	25″	5505 ± 74	5075.6 ± 71.2	68
NuSTAR	60601020002	FPMA	30″	674 ± 26	381.5 ± 19.5	15
NuSTAR	60601020002	FPMB	30″	686 ± 26	380.0 ± 19.5	15
Swift	00031815001	XRT	35.4″	59 ± 8	55.6 ± 7.5	7
Swift	00031815004	XRT	35.4″	270 ± 16	254.6 ± 16.0	16
Swift	00089109001	XRT	35.4″	58 ± 8	54.3 ± 7.4	7

Notes. (1) Telescope name, (2) observation ID, (3) detector name, (4) radius of the circular region used to extract the source spectrum, (5) source plus the background counts in the extraction region of the source spectrum, (6) source counts in the extraction region of the source spectrum, (7) signal to noise ratio computed using Equation (3.8).

($\Delta E < 2$keV). For this reason, I considered a second absorbing component which should represent the absorbing material along the LOS in the proximity of the source. Hence, I used the redshifted photoelectric absorbing component (**zphabs**, in `Xspec` nomenclature): the analytical model (model II) is

$$M(E) = \exp\left[-N_{H,\mathrm{Gal}}\sigma(E)\right] \times \exp\left[-N_H\sigma\left(E(1+z)\right)\right] \times K \times E^{-\Gamma}, \tag{4.3}$$

where N_H the intrinsic column density of the source measured in cm^{-2}. The best-fit parameters are listed in Table A.1. Figures 4.6a and 4.6c show the unfolded spectra from ObsID. 16070 and ObsID. 16623, respectively, fitted with model II. In addition, for each observation, Figure A.1 shows the folded spectrum fitted with model II on the left side, and the contours plot are on the right side. These show the confidence contours of $1\,\sigma$, $2\,\sigma$, and $3\,\sigma$ on the two parameters N_H and Γ. The cross in cyan represents the values of the best-fit parameters. Due to the low statistics of ObsID. 12849, I obtained only an upper limit for N_H, whereas the presence of this absorbing material is suggested by ObsdID. 16070 and ObsID. 16623, with values of $N_H = 1.74^{+1.11}_{-1.01} \times 10^{21}\,\mathrm{cm}^{-2}$ and $N_H = 2.47^{+0.51}_{-0.47} \times 10^{21}\,\mathrm{cm}^{-2}$, respectively. The spectra are now fitted in a more accu-

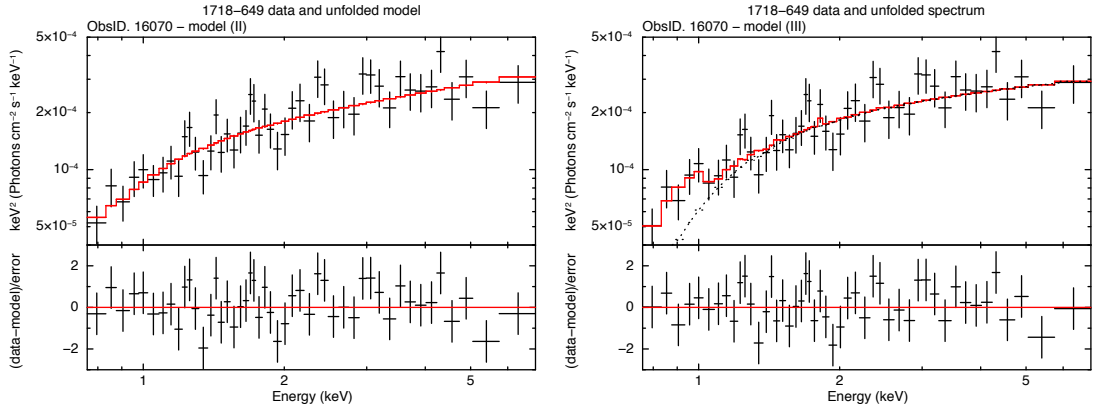

(a) χ^2/d.o.f. = 40.4/45 (b) χ^2/d.o.f. = 38.3/43

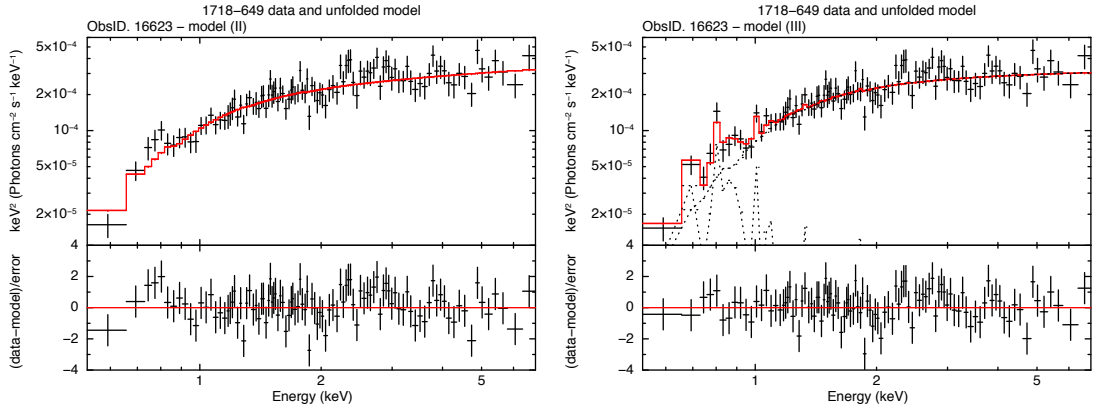

(c) χ^2/d.o.f. = 98.3/100 (d) χ^2/d.o.f. = 89.1/98

Figure 4.6: *Chandra*/ACIS-S spectra fitted with model II (**phabs**×**zphabs**×**powerlaw**, in `Xspec` nomenclature, *left panels*) and model III (**phabs**×(**zphabs**×**powerlaw**+**mekal**), in `Xspec` nomenclature, *right panels*) in the $0.3-7$ keV energy range obtained from ObsID. 16070 and ObsID. 16623. The red solid line is the total model, while the dotted curves are the single components of the model. Spectra are extracted from a circular region of radius 2.5″ centered on the source and data are grouped at 20 counts per bin. To make spectra clearer, data are also graphically rebinned.

rate way, with a reduced χ^2[10] close to 1, even if some residuals are present at energies less then 1 keV.

The radial-profile study suggested the presence of a diffuse emission in the soft band ($0.3-2$ keV): this could be associated to the hot gas, typically found in the ISM of giant ellipticals (e.g. Fabbiano 2019). This component may also affect the source spectrum extracted from the central region and, for this reason, I added a thermal component (**mekal**, in `Xspec` nomenclature; Mewe, Gronenschild, and van den Oord 1985; Mewe, Lemen, and van den Oord 1986; Liedahl, Osterheld, and Goldstein 1995). The model (model III) used to fit data was **phabs**×(**zphabs**×**powerlaw**+**mekal**). The best-fit parameters, listed in Table A.1, remain unconstrained for ObsID. 12849, due to the small available statistics. Figures 4.6b and 4.6d show unfolded spectra from ObsID.

[10]The reduced χ^2 is the ratio of the χ^2 to the degrees of freedom (d.o.f.). The closer it is to one, the more the model is a good representation of the data.

16070 and ObsID. 16623, respectively, fitted with model III. However, the addition of this component does not improve the fit in statistically a significant way: from the Fisher test, the significance of this addition is $1.0\,\sigma$ and $2.7\,\sigma$ for ObsID. 16070 and ObsID. 16623, respectively.

Since ObsID. 16070 and ObsID. 16623 belong to the same observation, which was split due to technical reasons, and no short-term variability arose from the study of the source light curves, I performed a simultaneous fit between the data-set, in order to place better constrains the best-fit parameters. I modeled the emission with model II and model III and the best-fit parameters are listed in Table 4.5. From model III, I found $N_H = 2.02^{+0.40}_{-0.38} \times 10^{21}\,\mathrm{cm}^{-2}$ and $\Gamma = 1.86^{+0.13}_{-0.12}$, which are better constrained with respect to those obtained from the single observation fit.

Even if assuming model III produces lower residuals in the residuals below 1 keV with respect to the one obtained assuming model II, the addition of the thermal component does not improve the fit in a statistically significant way: from the Fisher test, from the Fisher test, the significance of this addition is $2.8\,\sigma$. The main explanation is that the statistics related to this component is too low to produce an appreciable signal when the source spectrum is extracted from a circular region of radius $r_{src} = 2.5''$. This is in agreement with the results obtained during the modeling of the surface brightness profile: near the central source, the emission is dominated by the point-like emission and the β model is sub-dominant.

Extended emission In order to better constrain the physical properties of the diffuse emission, I also studied the spectrum extracted from a region of radius $r_{src} = 15''$ centered on the source. In light of the results obtained from the analysis of the point-like source spectra, I started modeling data from an absorbed power law model (model II). The best-fit parameters are listed in Table A.2. Figures 4.7a and 4.7c show the unfolded spectra from ObsID. 16070 and ObsID. 16623, respectively, fitted with model II. In addition, for each observation, Figure A.2 shows the folded spectrum fitted with model II on the left side, while the contour plots are on the right side.

Also in this case, due to the low statistics of ObsID. 12849, I obtained only an upper limit for N_H, whereas the presence of this second absorbing material is suggested by ObsdID. 16070 and ObsID. 16623, with values of $N_H = 2.06^{+0.87}_{-0.79} \times 10^{21}\,\mathrm{cm}^{-2}$ and $N_H = 2.02^{+1.02}_{-0.43} \times 10^{21}\,\mathrm{cm}^{-2}$, respectively. Also for the extended emission, relevant residuals at energies less then 1 keV.

Following the same considerations made for the point-like fitting spectra, I added a **mekal** component and fitted spectra with model III. Also in this case, the best-fit parameters, listed in Table A.2, remain unconstrained for ObsID. 12849, due to the small available statistics. Figures 4.7b and 4.7d show unfolded spectra from ObsID. 16070 and ObsID. 16623, respectively, fitted with model III. In contrast with what I found from the study of the point-like emission, it was possible to constrain the properties of the thermal component for both observations. However, the temperature found from the fit are quite different: of ObsID. 16070 I found $kT = 0.81^{+0.23}_{-0.17}\,\mathrm{keV} \Rightarrow T = 9.40^{+2.67}_{-1.97} \times 10^6\,\mathrm{K}$, while for ObsID. 16623 $kT = 0.49^{+0.10}_{-0.10}\,\mathrm{keV} \Rightarrow T = 5.69^{+1.16}_{-1.16} \times 10^6\,\mathrm{K}$,

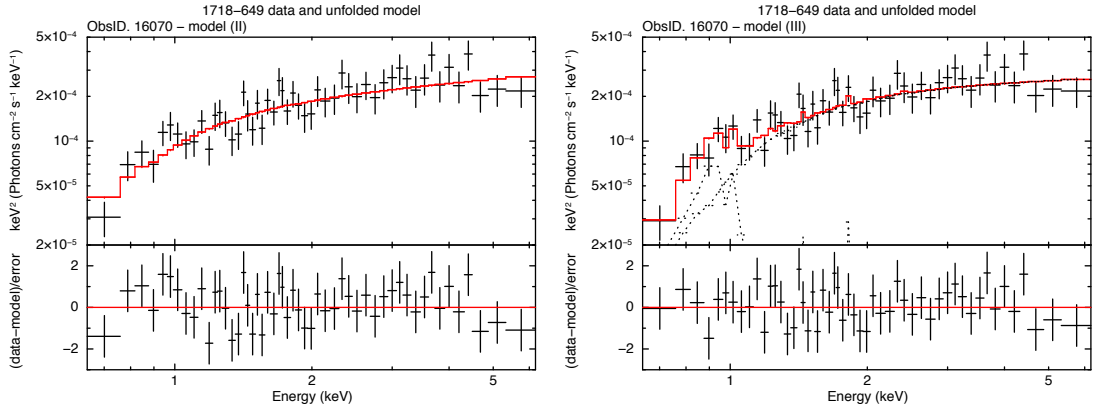

(a) $\chi^2/\text{d.o.f.} = 47.9/49$

(b) $\chi^2/\text{d.o.f.} = 40.2/47$

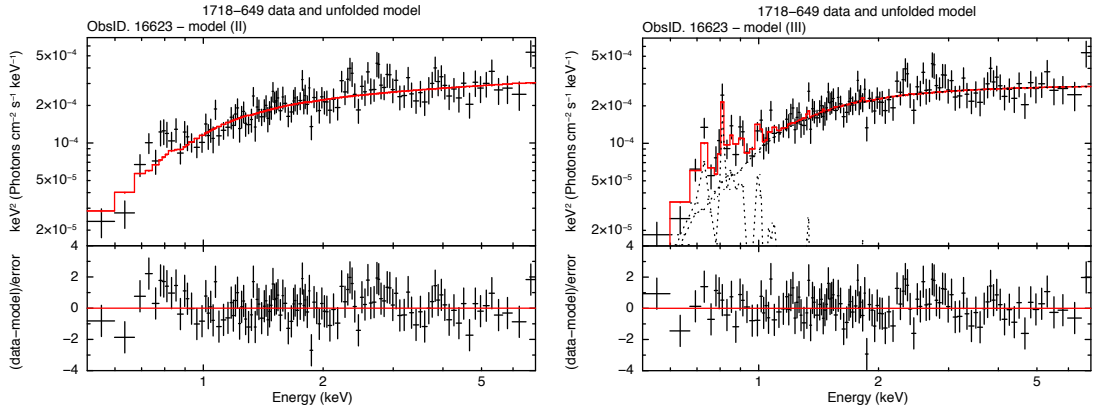

(c) $\chi^2/\text{d.o.f.} = 110.8/115$

(d) $\chi^2/\text{d.o.f.} = 97.6/113$

Figure 4.7: *Chandra*/ACIS-S spectra fitted with model II (**phabs**×**zphabs**×**powerlaw**, in `Xspec` nomenclature, *left panels*) and model III (**phabs**×**(zphabs**×**powerlaw**+**mekal)**, in `Xspec` nomenclature, *right panels*) in the $0.3-7\,\text{keV}$ energy range obtained from ObsID. 16070 and ObsID. 16623. The red solid line is the total model, whereas the dotted curves are the single components of the model. Spectra are extracted from a circular region of radius 15″ centered on the source centroid and data are grouped at 20 counts per bin. To make spectra clearer, data are also graphically rebinned.

and they are consistent at $2.4\,\sigma$. I attributed this difference to the different available statistics between the two observations (see Table 4.4). In contrast with the results obtained from the analysis of the point-like emission, the addition of the thermal component improves the fit in a significantly way for ObsID. 16623: from the Fisher test, the significance of this addition is $3.5\,\sigma$. However, it is not significant for ObsID. 16070 ($2.4\,\sigma$)

Moreover, by analogy with the analysis of the point-like emission, I performed a simultaneous fit between the two data-set assuming model II and model III. Thanks to the increase of the statistics in the soft-band ($0.3-2\,\text{keV}$) the addition of the thermal component improves the fit and this improvement is significant at $3.5\,\sigma$, according to the Fisher test. The best-fit parameters of both models are listed in Table 4.5. In particular, the source is Compton-thin, with an equivalent hydrogen column density of $N_H = 3.73^{+1.38}_{-1.07} \times 10^{21}\,\text{cm}^{-2}$ and a photon index of $\Gamma = 1.91^{+0.14}_{-0.12}$.

Table 4.5: *Chandra*/ACIS-S best-fit parameters of the joint fit of ObsID. 16070 and ObsID. 16623.

Ext. reg.	Model	**cons_1**	**cons_2**	**zphabs**	**powerlaw**		**mekal**		χ^2/d.o.f.
	#			$N_H\ [\times 10^{21}\,\mathrm{cm}^{-2}]$	Γ	norm $[\times 10^{-4}]$	kT [keV]	norm $[\times 10^{-5}]$	
(1)	(2)	(3)	(4)	(5)	(6)	(7)	(8)	(9)	(10)
2.5″	(II)	1 (frozen)	$1.20^{+0.08}_{-0.07}$	$2.32^{+0.44}_{-0.42}$	$1.74^{+0.09}_{-0.09}$	$1.74^{+0.19}_{-0.17}$	—	—	140.7/147
2.5″	(III)	1 (frozen)	$1.20^{+0.08}_{-0.07}$	$3.96^{+1.29}_{-1.11}$	$1.86^{+0.13}_{-0.12}$	$2.05^{+0.38}_{-0.30}$	$0.50^{+0.13}_{-0.13}$	$1.20^{+0.58}_{-0.65}$	131.1/145
15″	(II)	1 (frozen)	$1.21^{+0.07}_{-0.07}$	$2.02^{+0.40}_{-0.38}$	$1.80^{+0.09}_{-0.08}$	$1.80^{+0.18}_{-0.17}$	—	—	160.5/166
15″	(III)	1 (frozen)	$1.22^{+0.07}_{-0.07}$	$3.73^{+1.38}_{-1.07}$	$1.91^{+0.14}_{-0.12}$	$2.10^{+0.40}_{-0.29}$	$0.56^{+0.09}_{-0.11}$	$1.43^{+0.68}_{-0.65}$	147.1/164

Notes. (1) Radius of the circular region used to extract the source spectrum, (2) model fit, (3-4) multiplying constant components necessary to take into account the differences in normalization of the two observations, (5) intrinsic hydrogen column density, (6-7) photon index and normalization of the power law emission component, (8-9) temperature and normalization of the collisionally ionized thermal plasma, (10) ratio of the χ^2 fitting statistics to degrees of freedom. Both models include Galactic hydrogen column density $N_{H,\mathrm{Gal}} = 5.90 \times 10^{20}\,\mathrm{cm}^{-2}$, and the thermal component assumes solar abundance. The normalizations are photons/keV/cm^2/s at 1 keV for the power law component, and $10^{-14}\,(1+z)^2\,n_e n_H V/4\pi d_L^2$, assuming uniform ionized plasma with electron and H number densities n_e and n_H, respectively, and volume V, all in cgs units, for the thermal component.

In conclusion, the addition of the thermal component is statistically significant when the source spectrum is extracted from a circular region of radius $r_{src} = 15''$ and well fits the soft band $0.3 - 2\,\mathrm{keV}$ of the spectrum.

XMM-*Newton*

As previously mentioned, the radii of the extraction regions depend on the observation and the detector, and are listed in Table 4.4. The source counts and the SNR values for each detector and all observations are listed in Table 4.4: in particular, notice that the source counts from the EPIC pn longest observation (ObsID. 0845110101) are more than 4.5 times higher than the corrisponding ACIS-S one (ObsID. 16623). This would provide important information on the presence and the nature of the extended component, thanks to the better spectral resolution of the EPIC pn detector than ACIS-S one.

I analyzed the source spectrum for each observation and detector: I modeled the source emission in energy ranges in which its signal was higher than the background one. Figure 4.8 shows the XMM-*Newton*/pn image of 1718-649 in the $0.35 - 8.5\,\mathrm{keV}$ energy range. The green circle represents the $25''$ extraction region of the source spectrum, which includes the extended emission of the source revealed during the spatial study.

Chandra analysis indicated the presence of an intrinsic absorbing component and extended emission. However, the best-fit parameters are not well constrained due to the low available statistics. Hence, I started fitting data with model II. The best-fit parameters for pn and MOS detector are listed in Table 4.6 and A.3, respectively, where different energy ranges were chosen in order to maximize the source signal. Figure 4.9a shows the unfolded spectrum from ObsID. 0845110101 fitted with model II. In addition, for each observation, Figure A.3 shows the folded spectrum fitted with model II on the left side, whereas the contours plot are on the right side.

As shown in Figure 4.9a, and also from Figure A.3, there is a clear discrepancy between the model and the data in the soft energy band ($0.3 - 2\,\mathrm{keV}$) in each observation: the spectral shape suggests the presence of a second emitting component. For this reason, I fitted data with model III, by analogy with what was carried out during *Chandra* spectral analysis. Also in this case, the addition of the thermal component improves the fit in a statistically significant way: from the Fisher test, the significance of this addition is larger than 5σ for all the observations. The best-fit parameters for pn and MOS detector are listed in Table 4.6 and A.3, respectively. Figure 4.9b shows the unfolded spectrum from ObsID. 0845110101 fitted with model III. For each observation, Figure A.4 shows the spectrum fitted with model II on the left side, while the contours plot are on the right side. Thanks to this addition, the residuals decreases significantly and the reduced χ^2 is closer to 1.

From the analysis of XMM-*Newton*/pn data, it was found $N_H = 0.67^{+0.38}_{-0.35} \times 10^{21}\,\mathrm{cm}^{-2}$ from ObsID. 0784530201, $N_H = 0.92^{+0.23}_{-0.22} \times 10^{21}\,\mathrm{cm}^{-2}$ from ObsID. 0804520301 and $N_H = 0.89^{+0.15}_{-0.14} \times 10^{21}\,\mathrm{cm}^{-2}$ from ObsID. 0845110101. These values are in tension with

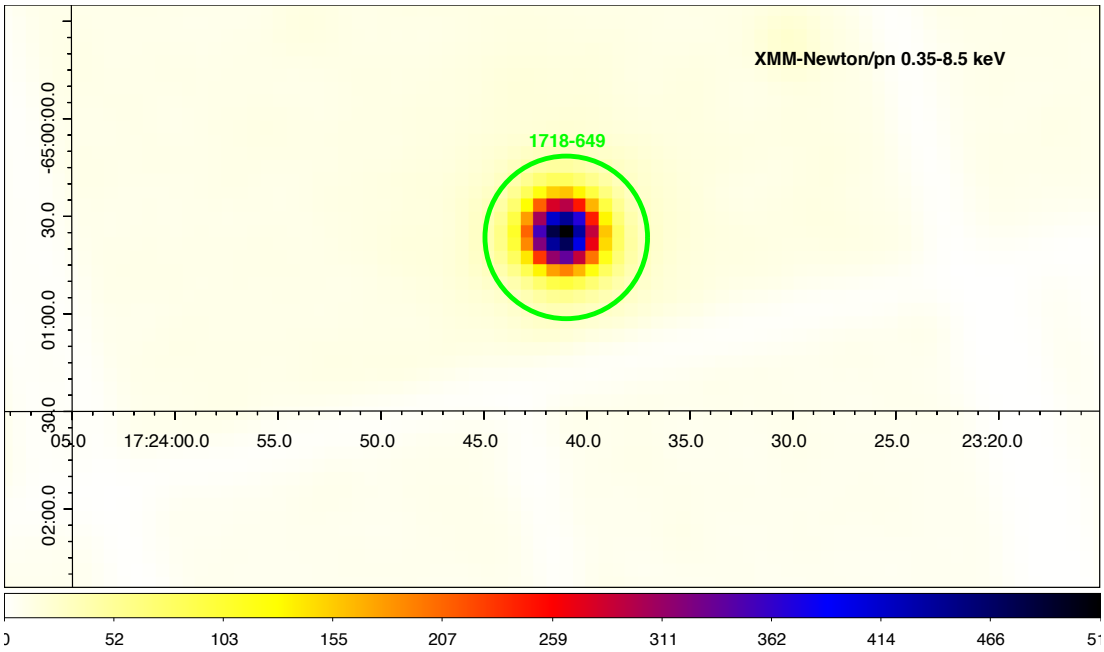

Figure 4.8: XMM-*Newton*/pn image of 1718-649 from the longest observation (ObsID. 0845110101) in the $0.35 - 8.5\,\mathrm{keV}$ energy range. The green circle represents the $25''$ extraction region of the source spectrum. A Gaussian smoothing filter ($\sigma = 1.5$ pixels, native pixel size) was applied for graphical reasons.

the one obtained from the simultaneous fit of two longest *Chandra* observations at $3.9\,\sigma$, $3.7\,\sigma$ and $3.8\,\sigma$, respectively. This difference is statistically significant and suggests a variability on years scale of the intrinsic column density of 1718-649, as it was also suggested by Beuchert et al. 2018. From this analysis, I also obtained new estimates for the photon index of the primary power law of the source: from ObsID. 0784530201 I found $\Gamma = 1.61^{+0.13}_{-0.13}$, from ObsID. 0804520301 $\Gamma = 1.72^{+0.10}_{-0.10}$ and from ObsID. 0845110101 $\Gamma = 1.73^{+0.05}_{-0.05}$. These values are consistent with the one obtained from the simultaneous fit of two longest *Chandra* observations at $2.7\,\sigma$, $1.9\,\sigma$ and $2.1\,\sigma$, respectively. Hence, no significant ($> 3\,\sigma$) spectral variability was found.

In conclusion, the presence of a thermal component is essential to reproduce the observed spectra. The most plausible explanation for which this addition is statistically significant for XMM-*Newton*/pn and not for *Chandra* is the different duration of the observations of the two telescopes. In addition, the higher effective area below 2 keV of the former with respect to the latter allows to collect more enough soft photons to produce a well defined signal.

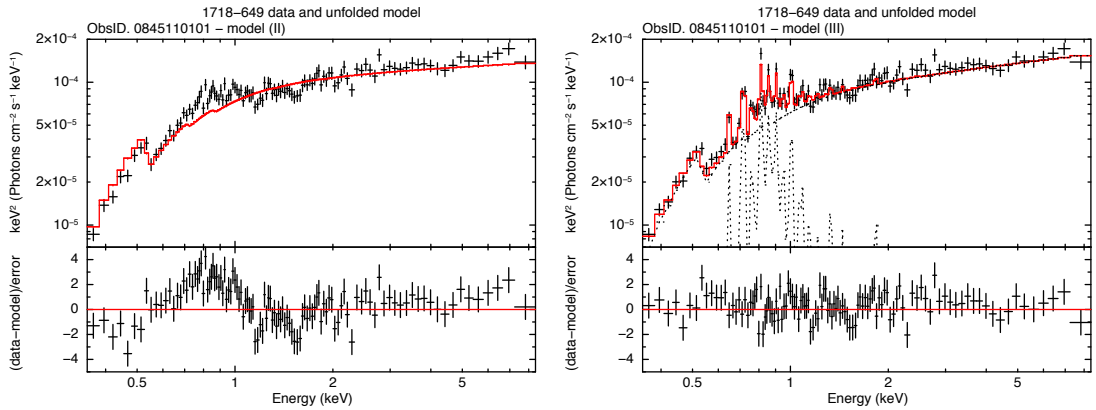

(a) χ^2/d.o.f.=666.6/482 (b) χ^2/d.o.f.=477.7/480

Figure 4.9: XMM-*Newton*/pn spectrum fitted with model II (**phabs**×**zphabs**×**powerlaw**, in `Xspec` nomenclature, *left panel*) and model III (**phabs**×(**zphabs**×**powerlaw**+**mekal**), in `Xspec` nomenclature, *right panel*) in the $0.35 - 8.5$ keV energy range obtained from ObsID. 0845110101. The red solid line is the total model, while the dotted curves are the single components of the model. Spectra are extracted from a circular region of radius $25''$ centered on the source and data are grouped at 20 counts per bin. To make spectra clearer, data are also graphically rebinned.

Table 4.6: 1718-649 XMM-*Newton*/ best-fit parameters

Model	ObsID	energy range	**zphabs**	**po**		**mekal**		χ^2/d.o.f.
#		[keV]	N_H $[\times 10^{21}\,\mathrm{cm}^{-2}]$	Γ	norm $[\times 10^{-4}]$	kT [keV]	norm $[\times 10^{-5}]$	
(1)	(2)	(3)	(4)	(5)	(6)	(7)	(8)	(9)
(II)	0784530201	$0.3-9.5$	$0.82^{+0.30}_{-0.28}$	$1.80^{+0.12}_{-0.11}$	$1.06^{+0.12}_{-0.11}$	—	—	117.3/94
(III)	0784530201	$0.3-9.5$	$0.67^{+0.38}_{-0.35}$	$1.61^{+0.13}_{-0.13}$	$0.83^{+0.13}_{-0.11}$	$0.83^{+0.19}_{-0.13}$	$1.71^{+0.55}_{-0.55}$	87.8/92
(II)	0804520301	$0.3-8.5$	$0.92^{+0.23}_{-0.22}$	$1.85^{+0.09}_{-0.09}$	$1.02^{+0.09}_{-0.08}$	—	—	173.9/169
(III)	0804520301	$0.3-8.5$	$0.88^{+0.28}_{-0.26}$	$1.72^{+0.10}_{-0.10}$	$0.88^{+0.10}_{-0.09}$	$0.66^{+0.18}_{-0.11}$	$0.93^{+0.29}_{-0.30}$	146.6/167
(II)	0845110101	$0.35-8.5$	$0.86^{+0.11}_{-0.11}$	$1.87^{+0.04}_{-0.04}$	$1.05^{+0.04}_{-0.04}$	—	—	666.6/482
(III)	0845110101	$0.35-8.5$	$0.89^{+0.15}_{-0.14}$	$1.73^{+0.05}_{-0.05}$	$0.88^{+0.05}_{-0.05}$	$0.60^{+0.04}_{-0.05}$	$1.25^{+0.16}_{-0.16}$	477.7/480

Notes. (1) Model fit, (2) observation ID, (3) energy range, (4) intrinsic hydrogen column density, (5-6) photon index and normalization of the power law emission component, (7-8) temperature and normalization of the collisionally ionized thermal plasma, (9) ratio of the χ^2 fitting statistics to degrees of freedom. Both models include Galactic hydrogen column density $N_{H,\mathrm{Gal}} = 5.90 \times 10^{20}\,\mathrm{cm}^{-2}$, and the thermal component assumes solar abundance. The normalizations are photons/keV/cm^2/s at 1 keV for the power law component, and $10^{-14}\,(1+z)^2\,n_e n_H V/4\pi d_L^2$, assuming uniform ionized plasma with electron and H number densities n_e and n_H, respectively, and volume V, all in cgs units, for the thermal component.

Swift

I also analyzed the spectra obtained by SWIFT/XRT. I used the SWIFT/XRT products online builder[11] to build the products of the observations, including spectra. Due to the small available statistics (see Table 4.4), I used ungrouped data and adopted the Cstat fitting statistics. Since the level of the background is sufficiently low, I analyzed the background-subtracted data. In the light of the *Chandra* and XMM-*Newton* results, I fitted data with model II. The best-fit parameters are listed in Table A.5. Figure A.5 shows the folded spectra on the left side and confidence contours on the right side. From these, it is possible to notice that relative errors of the best-fit parameters are higher than those using data from the other telescopes: as a consequence, the *Swift*/XRT best-fit parameters are not well constrained and I did not used them for further analyses.

NuSTAR

Figure 4.10 shows the *NuSTAR* image of 1718-649 of both instruments in the $3 - 19\,\mathrm{keV}$. The green circle represents the $30''$ extraction region of the source spectrum.

I started analyzing data-set of each instrument on-board *NuSTAR* individually. Due to the *NuSTAR* energy working range, the expected emission should not be affected by obscuration effects. Hence, I modeled each spectrum with model I. The best-fit parameters are listed in Table A.4. Photon indices and power law normalizations are consistent at $2.1\,\sigma$ and $1.6\,\sigma$, respectively. For this reason, I made a simultaneous fit of the two data-set in order to increase the available statistics and better constrain the best-fit parameter consequently. The best-fit parameters are listed in Table A.4. Figure 4.11 shows the folded spectrum fitted with model I: the FPMA data and best-fit curve are in green, whereas the FPMB ones are in red. The resulting photon index ($\Gamma = 2.08^{+0.17}_{-0.17}$) is in tension with XMM-*Newton*/pn ones at $3.6\,\sigma$ for ObsID. 0784530201, $3\,\sigma$ for ObsID. 0804520301 and $3.2\,\sigma$ for ObsID. 0845110101: these differences are statistically significant and have to be investigated.

Long-term variability

Since the source was observed several times over the 10-year window of observations, for each of these I measured the source flux assuming the best-fit model obtained from the analysis. The goal of this study was double: to point out if the source presents a long-term variability and, consequently, to select observations in which it is in the same state to perform a simultaneous fit of them.

The unabsorbed source fluxes for each model component in the three energy bands - broad ($0.3 - 10\,\mathrm{keV}$), soft ($0.3 - 2\,\mathrm{keV}$), total ($2 - 10\,\mathrm{keV}$) - are listed in Table 4.7. In Figure 4.12, I plotted the total fluxes as a function of time. The measured fluxes seem to point to some level of flux variability over the 10-year window of observations:

[11] `https://www.swift.ac.uk/user_objects/`

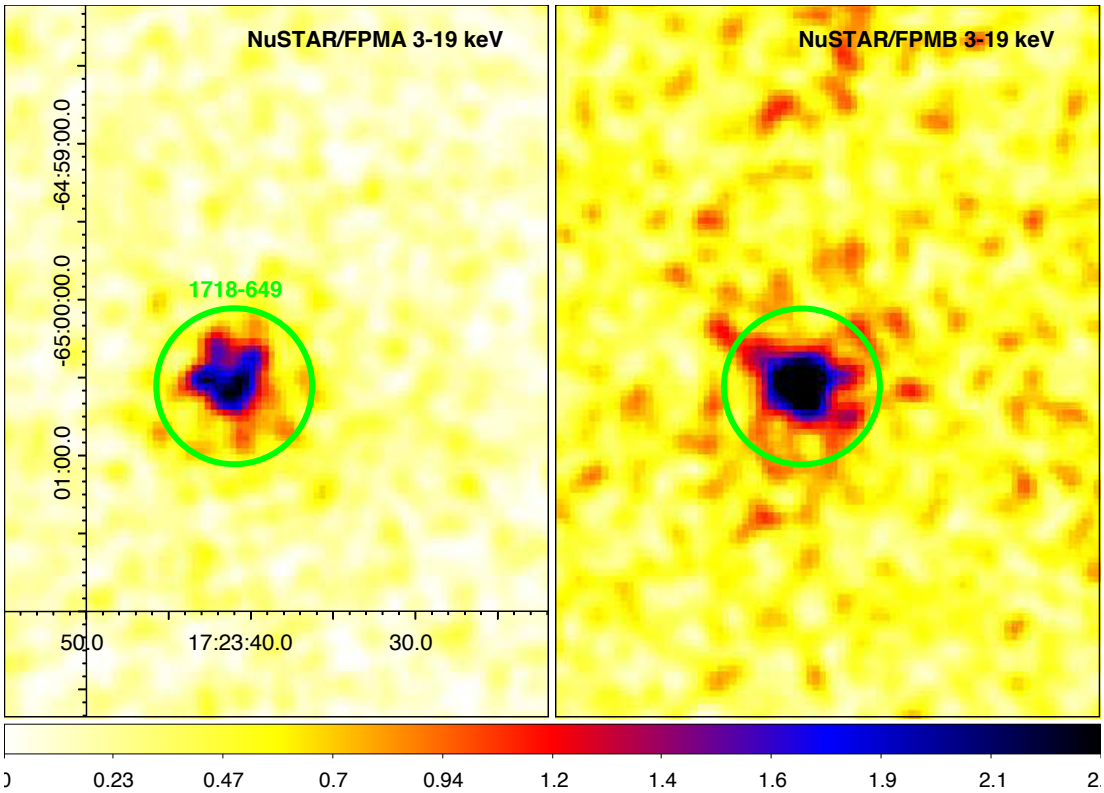

Figure 4.10: *NuSTAR* FPMA (*left panel*) and FPMB (*right panel*) image of 1718-649 in the $3-19$ keV energy range. The green circular region has a radius of $30''$ and was used to extract the source spectrum. A Gaussian smoothing filter ($\sigma = 1.5$ pixels, native pixel size) was applied for graphical reasons.

specifically, I observe an increase by about a factor of 2 of the flux in 2014 in comparison with the other epochs. This is in agreement with Beuchert et al. 2018, who pointed out this variability for the very first time.

In light of these results, I performed a simultaneous fit between XMM-*Newton*/pn and *NuSTAR* data and I did not used *Chandra*/ACIS-S data.

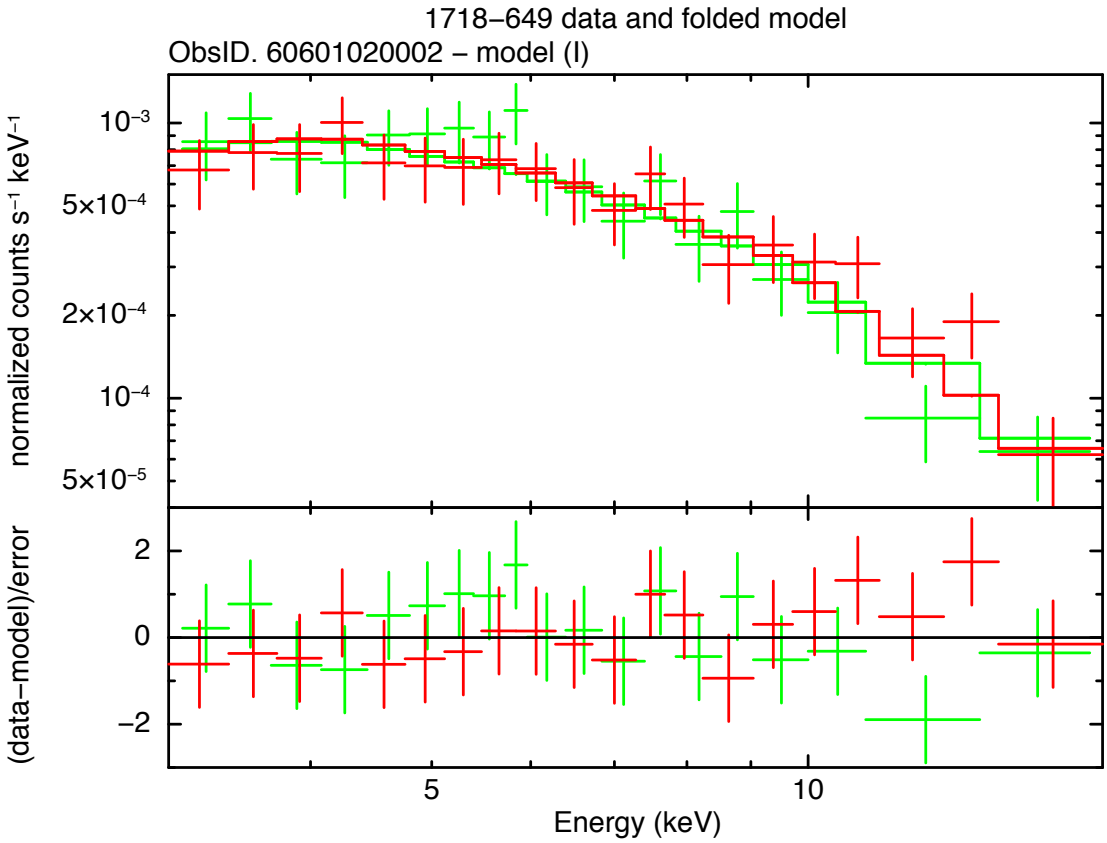

Figure 4.11: *NuSTAR* FPMA, in green, and FPMB, in red, spectra fitted with model I (**phabs**×**powerlaw**, in `Xspec` nomenclature) in the $3-19$ keV energy range obtained from ObsID. 60601020002 (χ^2/d.o.f. $= 23.6/36$). Spectra are extracted from a circular region of radius $30''$ centered on the source centroid.

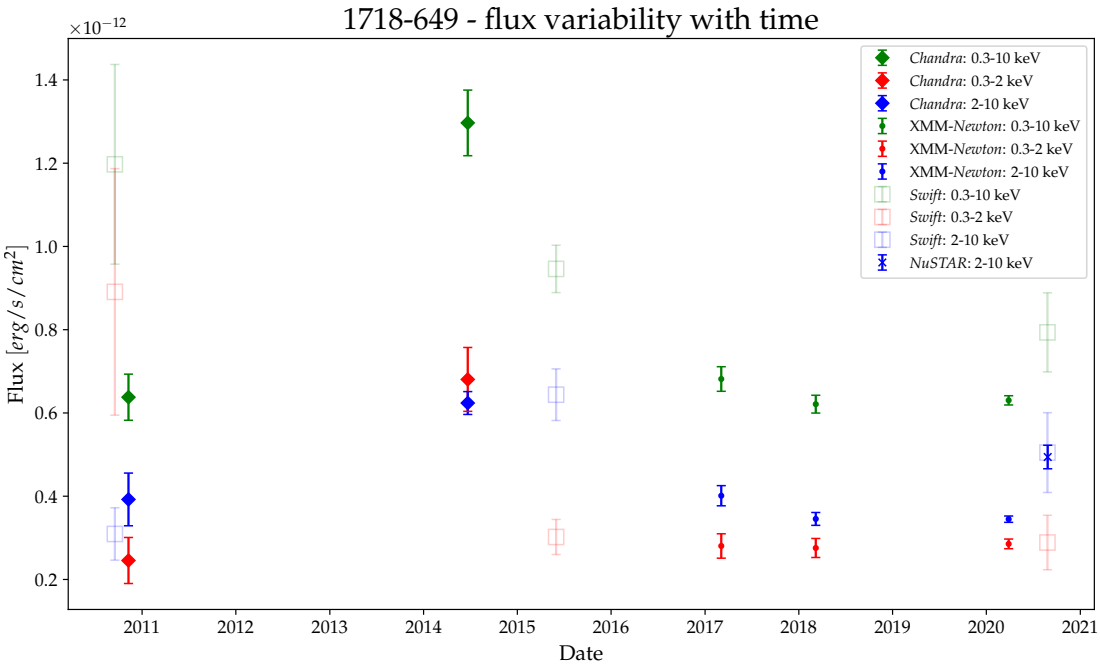

Figure 4.12: Unabsorbed X-ray fluxes in three energy bands ($0.3-10$ keV in green, $0.3-2$ keV in red, $2-10$ keV in blue): *Chandra*/ACIS fluxes are the diamonds, XMM-*Newton*/pn ones are the small filled circles, SWIFT/XRT ones are the empty squares and *NuSTAR* one is the star. Fluxes are obtained adopting the best-fit model derived from the X-ray analysis. 1718-649 seems to have a long-term variability: in particular, the flux of the source in 2014 is more than twice the value of 2010, which is consistent with the XMM-*Newton* more recent ones.

Table 4.7: 1718-649 unabsorbed fluxes

Telescope	Det.	ObsID.	Model #	$\log_{10}\mathcal{F}_{0.3-10\,\mathrm{keV}}$		$\log_{10}\mathcal{F}_{0.3-2\,\mathrm{keV}}$		$\log_{10}\mathcal{F}_{2-10\,\mathrm{keV}}$	
				powerlaw	**mekal**	**powerlaw**	**mekal**	**powerlaw**	**mekal**
(1)	(2)	(3)	(4)	(5)	(6)	(7)	(8)	(9)	(10)
Chandra	ACIS-S	12849	(II)	$-12.20^{+0.06}_{-0.06}$	—	$-12.61^{+0.18}_{-0.12}$	—	$-12.41^{+0.12}_{-0.12}$	—
Chandra	ACIS-S	16070 - 16623	(III)	$-11.90^{+0.04}_{-0.04}$	$-13.39^{+0.14}_{-0.21}$	$-12.19^{+0.08}_{-0.07}$	$-13.39^{+0.14}_{-0.21}$	$-12.21^{+0.03}_{-0.03}$	$-15.21^{+0.22}_{-0.30}$
XMM-*Newton*	pn	0784530201	(III)	$-12.19^{+0.02}_{-0.03}$	$-13.40^{+0.11}_{-0.14}$	$-12.62^{+0.07}_{-0.07}$	$-13.42^{+0.11}_{-0.14}$	$-12.40^{+0.04}_{-0.04}$	$-14.82^{+0.19}_{-0.28}$
XMM-*Newton*	pn	0804520301	(III)	$-12.22^{+0.02}_{-0.02}$	$-13.61^{+0.12}_{-0.16}$	$-12.60^{+0.05}_{-0.05}$	$-13.62^{+0.12}_{-0.16}$	$-12.46^{+0.03}_{-0.03}$	$-15.21^{+0.34}_{-0.31}$
XMM-*Newton*	pn	0845110101	(III)	$-12.22^{+0.01}_{-0.01}$	$-13.47^{+0.05}_{-0.06}$	$-12.60^{+0.03}_{-0.03}$	$-13.48^{+0.05}_{-0.06}$	$-12.46^{+0.02}_{-0.02}$	$-15.20^{+0.10}_{-0.13}$
NuSTAR	FPMA-FPMB	60601020002	(I)	—	—	—	—	$-12.31^{+0.04}_{-0.04}$	—
Swift	XRT	00031815001	(II)	$-11.92^{+0.50}_{-0.24}$	—	$-12.05^{+0.60}_{-0.44}$	—	$-12.51^{+0.23}_{-0.24}$	—
Swift	XRT	00031815004	(II)	$-12.02^{+0.06}_{-0.06}$	—	$-12.52^{+0.15}_{-0.13}$	—	$-12.19^{+0.09}_{-0.09}$	—
Swift	XRT	00089109001	(II)	$-12.10^{+0.15}_{-0.13}$	—	$-12.54^{+0.39}_{-0.26}$	—	$-12.30^{+0.20}_{-0.22}$	—

Notes. (1) Telescope name, (2) detector, (3) observation ID, Col(4) the model fit, (5-6) logarithmic value of the unaborbed fluxes of the **powerlaw** and **mekal** components in the $0.3-10\,\mathrm{keV}$ energy range, (7-8) logarithmic value of the the unaborbed fluxes of the **powerlaw** and **mekal** components in the $0.3-2\,\mathrm{keV}$ energy range, respectively, (9-10) logarithmic value of the the unaborbed fluxes of the **powerlaw** and **mekal** components in the $2-10\,\mathrm{keV}$ energy range, respectively.

XMM-*Newton* – *NuSTAR* joint fit

To better constrain the spectral parameters, I performed a simultaneous fit of the XMM-*Newton*/pn observations and the *NuSTAR* one. I started modeling the spectrum with model III, assuming the same parameters, with the exception of normalizations, for both telescopes. The best fit parameters are listed in Table 4.8. Figure 4.13a shows the spectra of the XMM-*Newton*/pn – *NuSTAR* joint fit assuming model III and the underlying model is shown in Figure 4.13b.

The photon index value ($\Gamma = 1.74^{+0.04}_{-0.04}$) is consistent with the results obtained for the individual XMM-*Newton*/pn spectra, whereas in slight tension ($3.2\,\sigma$) with the *NuSTAR* results. The fit of model III returns a $\chi^2/\text{d.o.f.} = 762.6/784$, however I note that this result is mostly driven by the XMM-*Newton* data. Indeed, the XMM-*Newton*/ statistics in the $0.3-10$keV band (source counts $c_s \simeq 2\times10^4$) is about thirty times higher than the *NuSTAR* one in $3-19$ keV (source counts $c_s \simeq 7\times10^2$): this inevitably makes the results weigh towards the slope of the former.

However, in order to model the different value of the photon index arose from the individual analyses of XMM-*Newton* and *NuSTAR* data, I tested a broken power law (**bknpower**, in `Xspec` nomenclature). The best fit parameters are listed in Table 4.9. Figure 4.13c shows the spectra of the XMM-*Newton*/pn - *NuSTAR* joint fit assuming the broken power law model and the theoretical model is shown in Figure 4.13d. From this, I found an energy break at $E_{\rm break} = 6.61^{+0.86}_{-1.41}$ keV. At energies below this value, the primary power law is characterized by $\Gamma_1 = 1.71^{+0.04}_{-0.04}$, whereas at energies greater than $E_{\rm break}$, the photon index of the power law is $\Gamma_2 = 2.38^{+0.38}_{-0.34}$. However, I highlight that the power law model at energies higher than the $E_{\rm break}$ is driven by the FPMA instrument: excluding this, a break in the power law is not necessary and a simple power law model with $\Gamma = 1.70^{+0.06}_{-0.06}$ well fit data. The best-fit parameters are listed in Table 4.10.

In conclusion, I argue that the presence of a break in the power law spectrum is necessary if data of both instruments on-board *NuSTAR* are used. However, when data of these instruments are analyzed individually, they show a slight tension ($2.1\,\sigma$) in the photon index parameter. This could be the result of instrumental problem, which have affected the FPMA observation, producing a steeper photon index. As a consequence, I assumed a simple power law model with $\Gamma \simeq 1.74$ for further analyses (see Section 5.2.1).

Summary

To summarize, I analyzed all *Chandra*, XMM-*Newton*, *Swift*, and *NuSTAR* available observations of 1718-649.

Modeling of the brightness profile confirms the presence of diffuse emission in the $0.3-2$ keV band extended up to the host galaxy scales ($\simeq 3.8$ kpc).

I jointly fit the XMM-*Newton* observations and the Nustar observation, which allowed me to expand the spectrum energy range in $0.3-19$ keV. The best fit model is given by a power law component, with a photon index $\Gamma = 1.91^{+0.14}_{-0.12}$, and a thermal

model with a gas temperature $kT = 0.56^{+0.09}_{-0.11}$ keV. In addition, there are indications for an intrinsic absorber with a hydrogen column density of $N_H = 0.92^{+0.12}_{-0.11} \times 10^{21}$ cm^{-2}.

By exploiting the best angular resolution of *Chandra* observation, it is evident that the power law emission is related to the point-source, hence the radio source, while the thermal one to the extended, diffuse emission.

By separately fitting the XMM-*Newton* and *NuSTAR* spectra, I obtained different photon indices. Therefore I repeated the joint-analysis testing a broken power law model (plus a thermal component). For this model, I obtained $\Gamma_1 = 1.71^{+0.04}_{-0.04}$ and $\Gamma_2 = 2.38^{+0.38}_{-0.34}$ and an energy break at $E_{\rm break} = 6.61^{+0.86}_{-1.41}$ keV. However, I stress that only the fit of the FPMA spectrum returns a softer photon index, the FPMB one being in line with XMM-*Newton* results. Therefore, I argued that this spectral steepening is probably an instrumental artefact.

Finally, analysis of the individual spectra by the different observatories, covering a period of XX years, has confirmed long-term, flux variability, within a factor of 10 years, which was also reported with a smaller dataset by Beuchert et al. 2018.

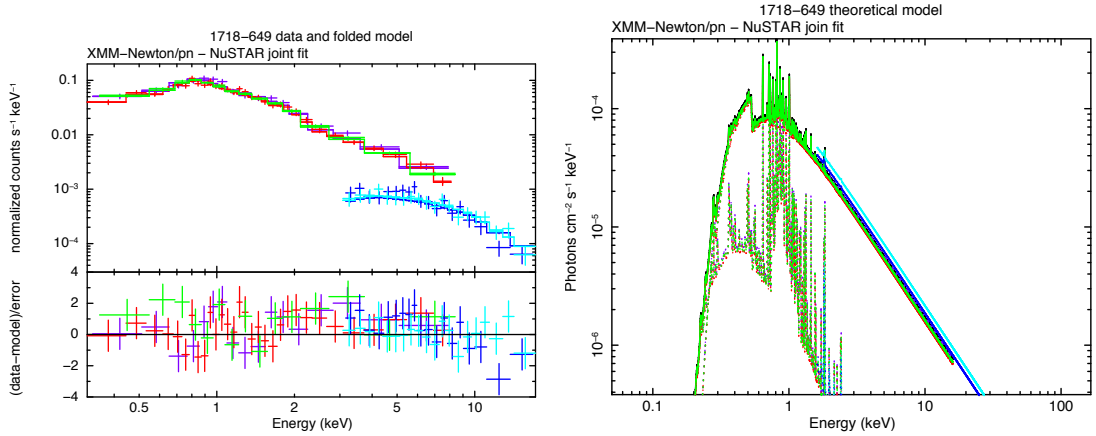

(a) χ^2/d.o.f. = 762.6/784 (b)

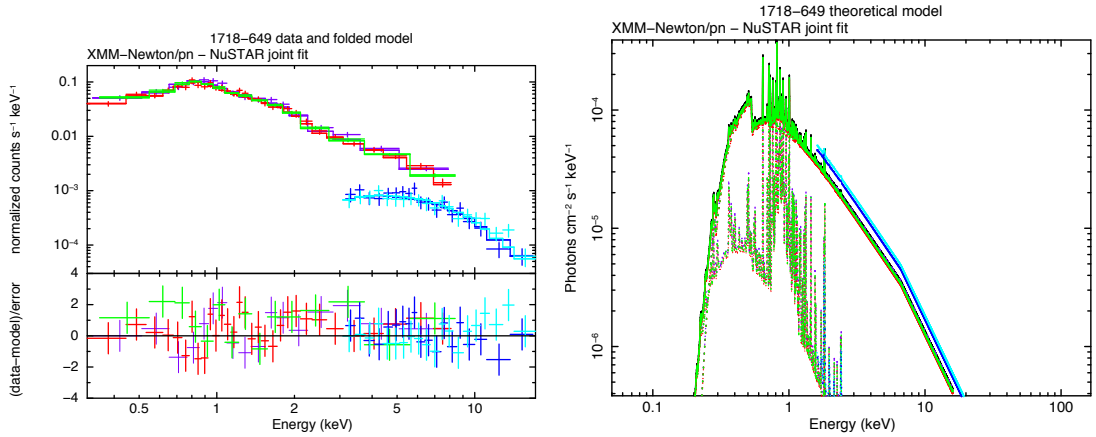

(c) χ^2/d.o.f. = 747.8/782 (d)

Figure 4.13: XMM-*Newton*/pn – *NuSTAR* spectra fitted with model **phabs**×(**zphabs**×**powerlaw**+**mekal**), in `Xspec` nomenclature, (*top left panel*) and **phabs**×(**zphabs**×**bknpower**+**mekal**), in `Xspec` nomenclature, (*bottom left panel*). *Right panels* show the corresponding theoretical models. ObsID. 0784530201, ObsID. 0804520301 and ObsID. 0845110101 pn data and model curves are in violet, red and green, respectively. ObsID. 60601020002 FPMA and FPMB data and theoretical curves are in blue and light blue, respectively. XMM-*Newton*/pn and *NuSTAR* spectra are extracted from a circular region of radius 25″ and 30″ centered on the source, respectively, and data are grouped at 20 counts per bin. To make spectra clearer, data are also graphically rebinned.

Table 4.8: 1718-649 XMM-*Newton*/pn – *NuSTAR* joint fit

zphabs	**powerlaw**		**mekal**		χ^2/d.o.f.
$N_H\ [\times 10^{21}\,\mathrm{cm}^{-2}]$	Γ	norm $[\times 10^{-4}]$	kT [keV]	norm $[\times 10^{-5}]$	
(1)	(2)	(3)	(4)	(5)	(6)
$0.91^{+0.12}_{-0.11}$	$1.74^{+0.04}_{-0.04}$	$0.94^{+0.05}_{-0.05}$	$0.63^{+0.04}_{-0.04}$	$1.22^{+0.15}_{-0.14}$	763.1/784

Notes. (1) Intrinsic hydrogen column density, (2-3) photon index and normalization of the power law emission component, (4-5) temperature and normalization of the collisionally ionized thermal plasma, (6) ratio of the χ^2 fitting statistics to degrees of freedom. XMM-*Newton*/pn and *NuSTAR* data are fitted with model III in `Xspec` nomenclature in the energy ranges specified in Tables A.3 and 4.11, respectively. The model III was multiplied by a constant function (**cons**, in `Xspec` nomenclature) to take into account the differences in normalizations between the different observations: for ObsID. 0784530201 the constant was set frozen to 1; for ObsID. 0804520301 **cons** $= 0.92^{+0.05}_{-0.04}$; for ObsID. 0845110101 **cons** $= 0.95^{+0.04}_{-0.04}$; for ObsID. 60601020002 $\mathbf{cons}_{\mathrm{FPMA}} = 1.10^{+0.13}_{-0.13}$ and $\mathbf{cons}_{\mathrm{FPMB}} = 1.27^{+0.15}_{-0.14}$. The model includes Galactic hydrogen column density $N_{H,\mathrm{Gal}} = 5.90 \times 10^{20}\,\mathrm{cm}^{-2}$, and thermal component assumes solar abundance. The normalizations are photons/keV/cm^2/s at 1 keV for the power law component, and $10^{-14}\,(1+z)^2\,n_e n_H V/4\pi d_L^2$, assuming uniform ionized plasma with electron and H number densities n_e and n_H, respectively, and volume V, all in cgs units, for the thermal component.

Table 4.9: 1718-649 XMM-*Newton*/pn – *NuSTAR* joint fit

zphabs	**bknpower**				**mekal**		χ^2/d.o.f.
$N_H\ [\times 10^{21}\,\mathrm{cm}^{-2}]$	Γ_1	$E_{\mathrm{break}}\,[\mathrm{keV}]$	Γ_2	norm $[\times 10^{-4}]$	$kT\,[\mathrm{keV}]$	norm $[\times 10^{-5}]$	
(1)	(2)	(3)	(4)	(5)	(6)	(7)	(8)
$0.84^{+0.12}_{-0.12}$	$1.71^{+0.04}_{-0.04}$	$6.61^{+0.86}_{-1.41}$	$2.38^{+0.38}_{-0.34}$	$0.92^{+0.05}_{-0.05}$	$0.63^{+0.04}_{-0.04}$	$1.26^{+0.15}_{-0.14}$	748.5/782

Notes. (1) Intrinsic hydrogen column density, (2-4) photon indices of the power law before and after the energy break, (3) energy of the break, (4) normalization of the broken power law component, (6-7) temperature and normalization of the collisionally ionized thermal plasma, (8) ratio of the χ^2 fitting statistics to degrees of freedom. XMM-*Newton*/pn and *NuSTAR* data are fitted with model **phabs**×**(zphabs**×**bknpower**+**mekal)**, in `Xspec` nomenclature in the energy ranges specified in Tables A.3 and 4.11, respectively. Model III was multiplied by a constant function (**cons**, in `Xspec` nomenclature) to take into account the differences in normalizations between the different observations: for ObsID. 0784530201 the constant was set frozen to 1; for ObsID. 0804520301 **cons** $= 0.92^{+0.05}_{-0.04}$; for ObsID. 0845110101 **cons** $= 0.95^{+0.04}_{-0.04}$; for ObsID. 60601020002 $\mathbf{cons}_{\mathrm{FPMA}} = 1.25^{+0.16}_{-0.15}$ and $\mathbf{cons}_{\mathrm{FPMB}} = 1.36^{+0.16}_{-0.15}$. The model includes Galactic hydrogen column density $N_{H,\mathrm{Gal}} = 5.90 \times 10^{20}\,\mathrm{cm}^{-2}$ and thermal component assumes solar abundance. The normalizations are photons/keV/cm^2/s at 1 keV, for the broken power law component, and $10^{-14}\,(1+z)^2\,n_e n_H V/4\pi d_L^2$, assuming uniform ionized plasma with electron and H number densities n_e and n_H, respectively, and volume V, all in cgs units, for the thermal component.

Table 4.10: 1718-649 XMM-*Newton*/pn – *NuSTAR*/FPMB joint fit

zphabs	**powerlaw**		**mekal**		χ^2/d.o.f.
$N_H\ [\times 10^{21}\,\mathrm{cm}^{-2}]$	Γ	norm $[\times 10^{-4}]$	kT [keV]	norm $[\times 10^{-5}]$	
(1)	(2)	(3)	(4)	(5)	(6)
$0.82^{+0.17}_{-0.16}$	$1.70^{+0.06}_{-0.06}$	$0.93^{0.07}_{-0.07}$	$0.76^{+0.07}_{-0.12}$	$1.18^{+0.26}_{-0.37}$	392.4/450

Notes. (1) Intrinsic hydrogen column density, (2-3) photon index and normalization of the power law emission component, (4-5) temperature and normalization of the collisionally ionized thermal plasma, (6) ratio of the χ^2 fitting statistics to degrees of freedom. XMM-*Newton*/pn and *NuSTAR*/FPMB data are fitted with model III in `Xspec` nomenclature in the energy ranges specified in Tables A.3 and 4.11, respectively. The model III was multiplied by a constant function (**cons**, in `Xspec` nomenclature) to take into account the differences in normalizations between the different observations: for ObsID. 0784530201 the constant was set frozen to 1; for ObsID. 0804520301 **cons** $= 0.92^{+0.05}_{-0.04}$; for ObsID. 0845110101 **cons** $= 0.91^{+0.05}_{-0.04}$; for ObsID. 60601020002 $\mathbf{cons}_{\mathrm{FPMB}} = 1.20^{+0.15}_{-0.14}$. The model includes Galactic hydrogen column density $N_{H,\mathrm{Gal}} = 5.90 \times 10^{20}\,\mathrm{cm}^{-2}$, and thermal component assumes solar abundance. The normalizations are photons/keV/cm^2/s at 1 keV for the power law component, and $10^{-14}\,(1+z)^2\,n_e n_H V/4\pi d_L^2$, assuming uniform ionized plasma with electron and H number densities n_e and n_H, respectively, and volume V, all in cgs units, for the thermal component.

Table 4.11: 1146+596 counts and SNR

Telescope (1)	ObsID. (2)	Det. (3)	Ext. reg. (4)	Tot. cts (5)	Net cts (6)	SNR (7)
Chandra	12850	ACIS-S	$2.5''$	378 ± 19	376.2 ± 19.4	19
Chandra	12850	ACIS-S	$10''$	596 ± 24	566.6 ± 24.4	23
NuSTAR	60601019002	FPMA	$30''$	247 ± 16	188.7 ± 13.7	12
NuSTAR	60601019002	FPMB	$30''$	215 ± 15	157.6 ± 12.6	11

Notes. (1) Telescope name, (2) observation ID, (3) detector name, (4) radius of the circular region used to extract the source spectrum, (5) source plus the background counts in the extraction region of the source spectrum, (6) source counts in the extraction region of the source spectrum, (7) signal to noise ratio computed using Equation (3.8).

4.3.2 1146+596

Chandra

The *Chandra*/ACIS-S image of 1146+596 in the $0.3 - 7$ keV energy range is shown in Figure 4.3. The spatial study has confirmed the presence of diffuse emission also for 1146+596. Therefore, I adopted the same analysis method as for 1718-649. I first performed the spectral analysis of the central point-like source within $2.5''$; then, I analyzed the one within a circular region of radius $10''$.

Central AGN emission The point-like source spectrum was studied in the $0.3 - 7$ keV energy range. I started modeling the spectrum using a simple power law model (model I). However, the fit was not satisfactory: in particular, the model underrepresented the data, leaving residuals to more than $4\,\sigma$ in the soft energy band ($\Delta E < 2$ keV).

The extended emission, which is evident in the soft band, supports the presence of thermal emission from a hot gas. Therefore, I tested a composite mode which included an **apec** component, in `Xspec` nomenclature. However, due to the compactness of the source ($LS \simeq 5$ pc, Principe et al. 2020), it is completely confined in the host galaxy: from the optical HST image 2.6, a prominent dust lane in present along the major axis of the source. This component can significantly obscure the source and its contribution has to be taken into account. In addition, if a dusty torus is present, it contributes to the source obscuration. Hence, from these considerations, an intrinsic obscuring component is expected, therefore it was included into the model. The model (model IV) used to fit the source spectrum was **phabs**$\times$**(zphabs**$\times$**powerlaw**$+$**apec)**, in `Xspec` nomenclature. The best-fit parameters are listed in Table A.6. Figure 4.14a shows the unfolded spectrum of 1146+596 fitted with this model. In addition, Figures 4.14a and A.6b show the folded spectrum and the confidence contours for the two parameters N_H and Γ, respectively. In particular, I obtained a thermal plasma at $kT = 0.84^{+0.17}_{-0.16}$ keV $\Rightarrow$ $T = 9.74^{+1.97}_{-1.86} \times 10^6$ K, an equivalent hydrogen column density of $N_H = 1.90^{+1.32}_{-1.00} \times 10^{22}\,\mathrm{cm}^{-2}$ and an usually flat photon index ($\Gamma = 1.05^{+0.67}_{-0.59}$)

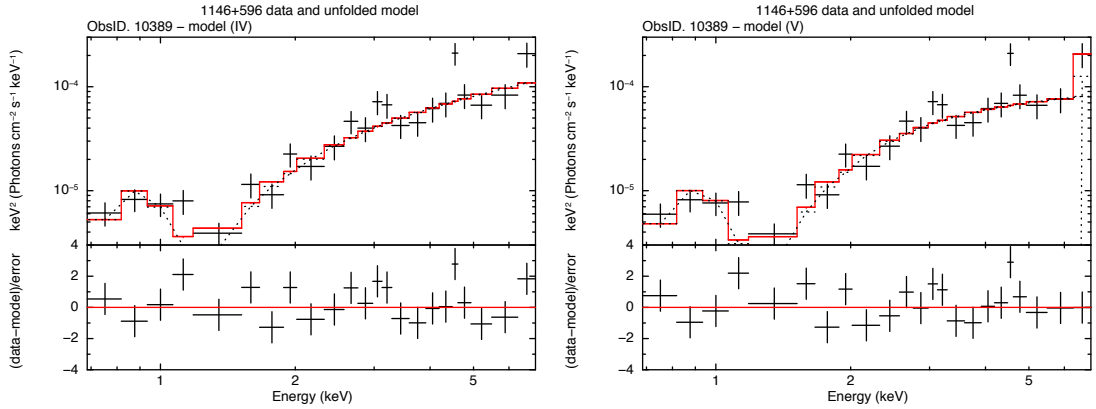

(a) χ^2/d.o.f. = 31.6/18 (b) χ^2/d.o.f. = 28.6/17

Figure 4.14: *Chandra*/ACIS-S spectrum fitted with model IV (**phabs**×**(zphabs**×**powerlaw**+**apec)**, in `Xspec` nomenclature, *left panel*) and model V (**phabs**×**(zphabs**×(**powerlaw**+**zgauss)**+**apec)**, in `Xspec` nomenclature, *right panel*) in the $0.3 - 7$ keV energy range obtained from ObsID. 10389. The red solid line is the total model, whereas the dotted curves are the single components of the model. For model V, the photon index of the power law component was set frozen to $\Gamma = 1.70$. Spectra are extracted from a circular region of radius 2.5″ centered on the source centroid.

in comparison with typical values of radio quiet/flat AGN (unless obscured, see Section 1.4.4). However, as Figure A.6b suggests, they cover a very wide range of values, hence not well constrained.

For this reason, I decided to fix the photon index to $\Gamma = 1.70$, which is the typical value of unabsorbed ($N_H \lesssim 10^{22}\,\mathrm{cm}^{-2}$) AGN (Burlon et al. 2011) and is equal to the main value found by Siemiginowska et al. 2016 for a sample of CSOs. The best-fit parameters are listed in Table A.6. However, I noticed a statistically significant positive residuals, more than $2\,\sigma$, possibly pointing at the presence of narrow emission lines. In particular, the most interesting one is at energies larger than 6 keV. Hence, I modeled this component with a Gaussian line (**zgauss**, in `Xspec` nomenclature): the model used (model V) to fit the data was **phabs**×**(zphabs**×**(power**+**zgauss)**+**apec)**, in `Xspec` nomenclature, where I froze the value of the sigma of the Gaussian component to 10 eV. The best-fit parameters are listed in Table A.6. Figure 4.14b shows the unfolded spectrum fitted with model V. As a consequence of this choice, the intrinsic hydrogen column density of the source increases ($N_H = 3.04^{+0.68}_{-0.55} \times 10^{22}\,\mathrm{cm}^{-2}$), while the parameters of the thermal component remain almost unchanged ($kT = 0.88^{+0.17}_{-0.15}\,\mathrm{keV} \Rightarrow T = 1.02^{+0.20}_{-0.17} \times 10^7\,\mathrm{K}$).

In addition, the excess is well modeled this narrow Gaussian component at energies $E_\ell = 6.42^{+0.69}_{-0.09}\,\mathrm{keV}$: as discussed in Section 1.4.4, this is an expected feature of AGN spectra. The other relevant excess at energies about 4.6 keV is probably an instrumental artefact (e.g. Xu et al. 2016; Cappelluti et al. 2018), as suggested by Balasubramaniam et al. 2021: this feature should be a Si escape peak. In particular, Grimm et al. 2009 argued the presence of this line at energies around 5.5 keV, an energy that

is higher than the 4.5 keV observed in the *Chandra*/ACIS-S spectra. However, this is produced by a monochromatic beam of energy 7.5 keV. Hence, for an Fe line photon with energy about 6.4 keV, this Si escape peak would be at around 4.5 keV.

Even if model V better reproduces the spectrum in the $6-7$ keV and the presence of a Gaussian line at 6.4 keV is supported by the excess around 4.5 keV, the addition of the component does not improve the fit significantly ($1.2\,\sigma$ according to the Fisher test).

Extended emission In order to investigate the physical properties of the diffuse emission, I studied the spectrum extracted from a region of radius $r_{src} = 10''$ centered on the source. I started modeling data from an absorbed power law model and a Gaussian line plus a thermal component (model V). However, no satisfactory fit could be performed, as in the case of point-like study. For this reason, following the same considerations discussed in the previous paragraph, I froze the photon index to 1.70. The best-fit parameters are listed in Table A.6. The results obtained are consistent with those of the point-like emission ($N_H = 2.70^{+0.74}_{-0.52} \times 10^{22}\,\mathrm{cm}^{-2}$ and $kT = 0.84^{+0.11}_{-0.13}$ keV). However, from Figure 4.15a, I noticed a relevant scatter in the residuals up to $3\,\sigma$ at energies below 2 keV. Hence, I tested a model with a multi-temperature gas (model VI) and fit the data with the model **phabs**×**(zphabs**×**(powerlaw**+**zgauss)**+**apec**+**apec)**, in `Xspec` nomenclature. The best-fit parameters are listed in Table A.6. Now, the two thermal components at $kT = 0.31^{+0.16}_{-0.09}\,\mathrm{keV} \Rightarrow T = 3.60^{+1.86}_{-1.04} \times 10^6\,\mathrm{K}$ and $kT = 1.21^{+0.25}_{-0.17}\,\mathrm{keV} \Rightarrow T = 1.30^{+0.29}_{-0.20} \times 10^7\,\mathrm{K}$. From Figure 4.15b, it is evident that the second thermal component appears to be necessary to model the source emission at energies lower than 2 keV. Moreover, this second thermal component improve the fit in a statistically significant way: from the Fisher test, the significance of this addition is $3.5\,\sigma$.

The single thermal component in the best-fit model arose from the study of the point-like emission ($kT \simeq 0.88\,\mathrm{keV} \Rightarrow T \simeq 1.02 \times 10^7\,\mathrm{K}$) is in agreement with the results of Balasubramaniam et al. 2021, who found $kT = 0.8^{+0.1}_{-0.1}$ keV, extracting the spectrum from a circular region of radius $5''$ centered on the source. However, I note that this gas could be the result of the superposition two emitting gas components, one warmer ($kT \simeq 0.31\,\mathrm{keV} \Rightarrow T \simeq 3.60 \times 10^6\,\mathrm{K}$) and one hotter ($kT \simeq 1.12\,\mathrm{keV} \Rightarrow T \simeq 1.30 \times 10^7\,\mathrm{K}$).

The only open question concerns the value of photon index, which I set frozen to 1.70: regarding this, since the X-ray emission in the *NuSTAR* energy range ($3-19$ keV) is not affected by the emission of these gases or by obscuring effects, the new data play a fundamental role.

I underline that Balasubramaniam et al. 2021 was able to constrain the iron line at $E_\ell = 6.5^{+0.1}_{-0.1}$ keV with $\sigma_\ell = 0.12^{+0.08}_{-0.08}$ keV, without fixing the value of the photon index ($\Gamma = 1.4^{+0.4}_{-0.4}$) and extracting the spectrum from a circular region of radius $5''$ centered on the source. However, this can be explained in terms of the binning data: they grouped data at 5 counts per bin and applied the χ^2 statistics to background-subtracted data. This choice is questionable and not in agreement with the standard conditions, i.e. a minimum grouping of 15/20 counts per bin, necessary to apply the

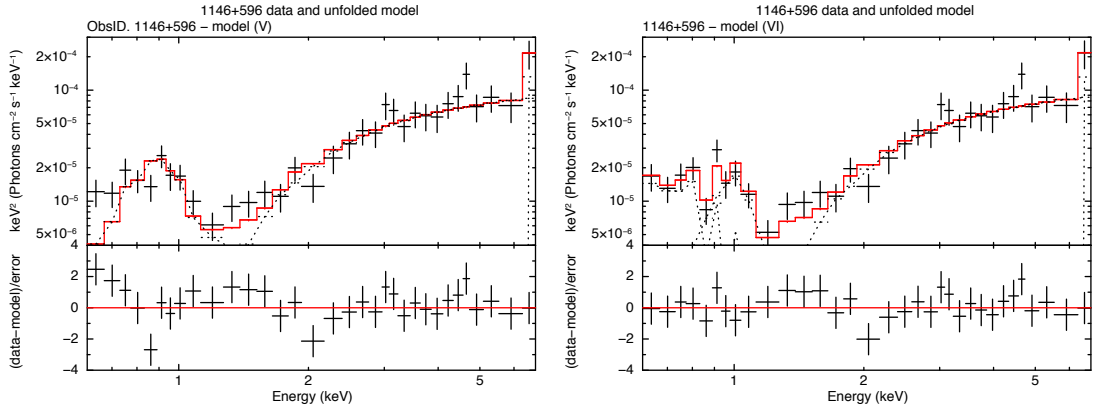

(a) χ^2/d.o.f. = 36.8/27 (b) χ^2/d.o.f. = 19.6/25

Figure 4.15: *Chandra*/ACIS-S spectrum fitted with model V (**phabs**×**(zphabs**×(**powerlaw**+**zgauss)**+**apec)**, in `Xspec` nomenclature, *left panel*) and model VI (**phabs**×**(zphabs**×(**powerlaw**+**zgauss)**+**apec**+**apec)**, in `Xspec` nomenclature, *right panel*) in the $0.3-7$ keV energy range obtained from ObsID. 10389. The red solid line is the total model, whereas the dotted curves are the single components of the model. Spectra are extracted from a circular region of radius $10''$ centered on the source.

χ^2 statistics. For this reason, I grouped data at 15 counts per bin: as a consequence, the spectral resolution decreases and this explains why the line properties are less constrained with respect to those found by Balasubramaniam et al. 2021.

NuSTAR

Figure 4.16 shows the *NuSTAR* image of 1146+596 of both instruments in the $3-19$ keV. The green circle represents the $30''$ extraction region of the source spectrum.

I started analyzing the data of both telescopes on-board *NuSTAR* individually. The best-fit parameters are listed in Table 4.14. The spectrum is well fitted by a simple power law model with a photon index of $\Gamma \simeq 1.9$. No significant signatures of emission lines, including the iron $K\alpha$, are present in the spectrum (see Figure 4.17). However, I highlight that the source net counts in the *Chandra* observation is the twice the statistics of *NuSTAR* for each instrument.

Chandra **–** *NuSTAR* **joint fit**

Assuming model VI, I performed a simultaneous fit between *Chandra*[12] and *NuSTAR* observations. I fitted the spectra without freezing the photon index value. The best-fit parameters are listed in Table 4.12. The unfolded spectrum and the theoretical model are shown in Figures 4.18a and 4.18b.

As discussed in the *Chandra* spectral analysis section, the soft band is well fitted assuming two emitting gas components, a warm one ($kT = 0.32^{+0.17}_{-0.09}$ keV $\Rightarrow T =$

[12]The *Chandra*/ACIS-S spectrum is the one extracted from a circular region of radius $10''$ centered on the source.

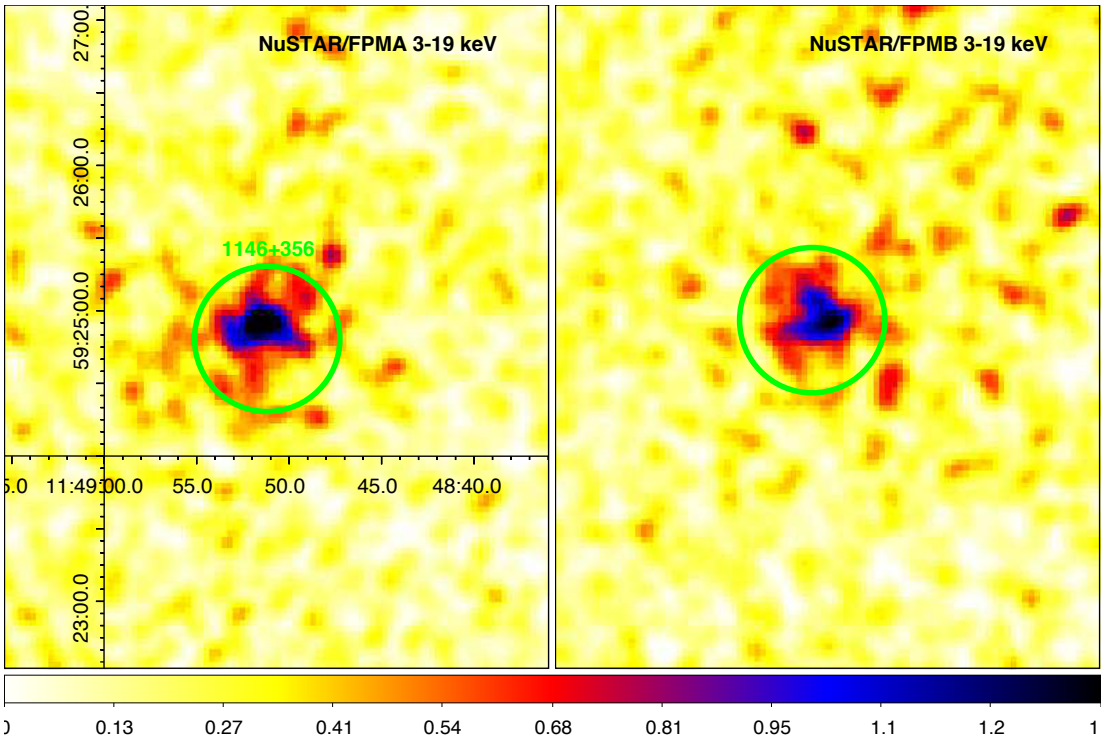

Figure 4.16: *NuSTAR*/FPMA (*left panel*) and FPMB (*right panel*) image of 1146+596 in the $3 - 19$ keV energy range. The green circular region has a radius of $30''$ and was used to extract the source spectrum. A Gaussian smoothing filter ($\sigma = 1.5$ pixels, native pixel size) was applied for graphical reasons.

$3.71^{+2.02}_{-0.99} \times 10^6$ K) and an hot one ($kT = 1.16^{+0.31}_{-0.18}$ keV $\Rightarrow T = 1.34^{+0.36}_{-0.21} \times 10^7$ K). However, thanks to the larger energy band available with the new *NuSTAR* data with respect to the *Chandra* one, now I am able to constrain the nature of this two gas components without freezing the photon index: the final estimate of the photon index is $\Gamma = 1.92^{+0.34}_{-0.33}$, with an intrinsic hydrogen column density of $N_H = 3.49^{+1.28}_{-1.04} \times 10^{22}\,\mathrm{cm}^{-2}$. The unfolded spectrum and the theoretical model are shown in Figures 4.18a and 4.18b.

In addition, since the Gaussian line appears narrow in the *Chandra* spectrum, it is possible that it is produced by reflection processes, rather than in the innermost regions of the accretion disk. For this reason, I also tested another model (model VII) where the power law component and the Gaussian line in model VI are replaced by a **pexmon** component, in `Xspec` nomenclature (George and Fabian 1991; Nandra et al. 2007): this is a model which takes into account the neutral Compton reflection with self-consistent Fe and Ni lines. Hence, I performed a joint fit of the *Chandra*/ACIS-S and *NuSTAR* spectra with model **phabs**×(**zphabs**×**pexmon**+**apec**+**apec**), in `Xspec` nomenclature. I assumed the spectra to be dominated by reflection, so the scaling factor of the reflection (**rel_refl** in `Xspec` nomenclature) was set frozen to 1. This choice is driven by the idea that narrow emission lines are produced by scattering regions nearby the central AGN. By this choice, the model assumes the presence of an isotropic source above the disk. In addition, Principe et al. 2020 constrained the inclination viewing angle of the 1146+596 in a range of $10° < \vartheta < 21°$, therefore I adopted an

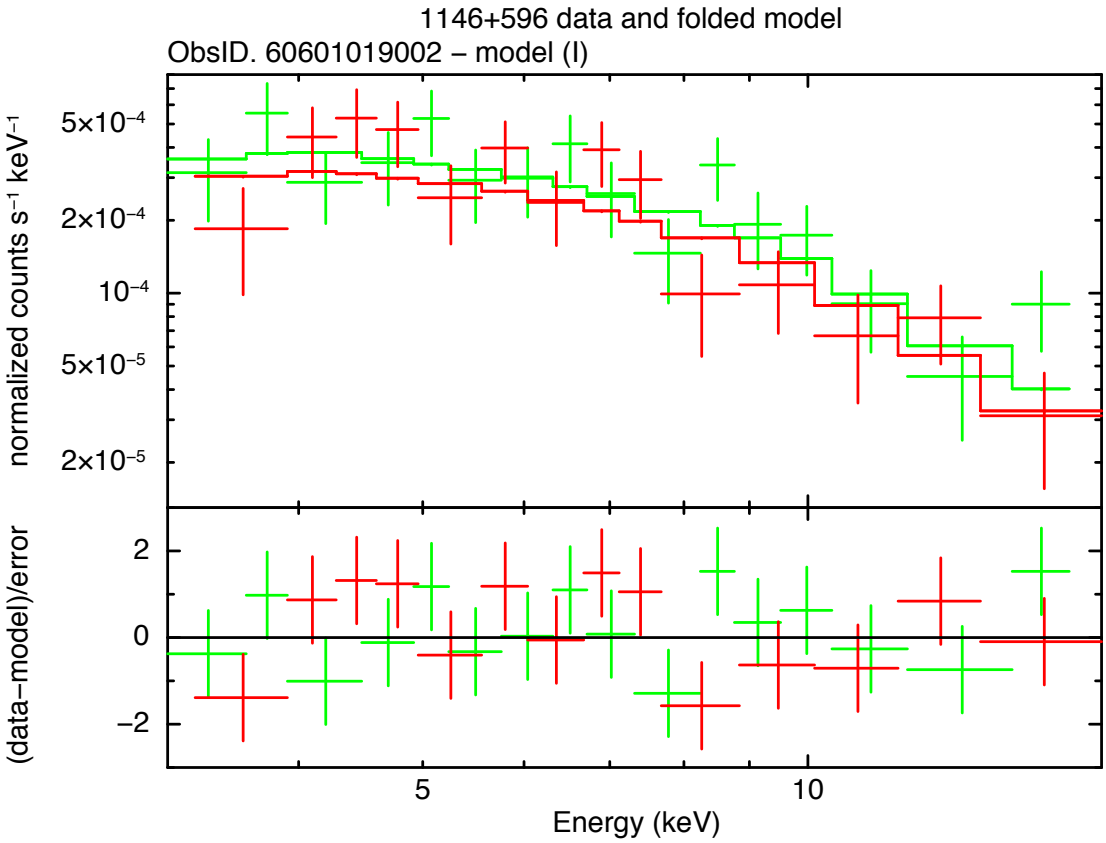

Figure 4.17: *NuSTAR* FPMA, in green, and FPMB, in red, spectra fitted with model I (**phabs**×**po**, in `Xspec` nomenclature) in the $3 - 19$ keV energy range obtained from ObsID. 60601019002 (χ^2/d.o.f. $= 27.3/27$). Spectra are extracted from a circular region of radius $30''$ centered on the source.

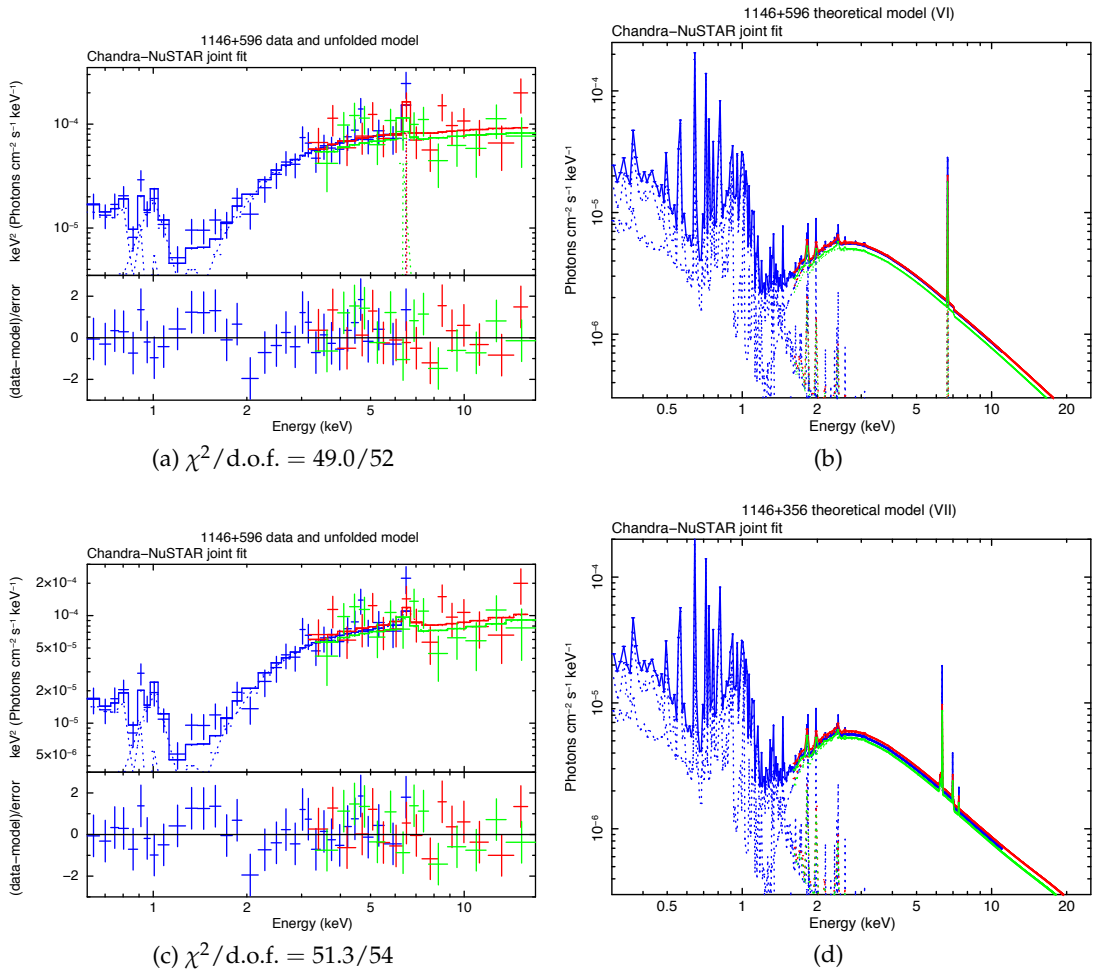

(a) $\chi^2/\text{d.o.f.} = 49.0/52$ (b)

(c) $\chi^2/\text{d.o.f.} = 51.3/54$ (d)

Figure 4.18: *Chandra*/ACIS-S and *NuSTAR* spectra of 1146+596 fitted with model VI (**phabs**×**(zphabs**×**(po**+**zgauss)**+**apec**+**apec**), in `Xspec` nomenclature, *top left panel*) and model VII (**phabs**×**(zphabs**×**pexmon**+**apec**+**apec**), in `Xspec` nomenclature, *bottom left panel*). The corresponding theoretical models are shown in *right panels*. *Chandra*/ACIS-S data and models curves are in blue, whereas *NuSTAR* FPMA and FPMB are in red and green, respectively. *Chandra*/ACIS-S and *NuSTAR* spectra are extracted from a circular region of radius 10″ and 30″ centered on the source centroid, respectively, and data are grouped at 15 counts per bin.

intermediate value $\vartheta = 15°$. The best-fit parameters are listed in Table 4.13. The unfolded spectrum and the theoretical model are shown in Figures 4.18c and 4.18d.

From the best-fit parameters, model VI and model VII are completely consistent and statistically equivalent. For this reason, since model VI assumes a less complex physical model, I assumed it for the further analyses.

Summary

To summarize, I analyzed the *Chandra* and the *NuSTAR* available observations of 1146+596.

From the spatial point of view, I confirmed the presence of extended X-ray emission in $0.3 - 2\,\mathrm{keV}$ band up to host galaxy scales ($\simeq 4.6\,\mathrm{kpc}$) suggested by Balasubramaniam et al. 2021.

The best fit model obtained by jointly fitting the *Chandra* and *NuSTAR* spectra is a composite model with an absorbed power law and two thermal components. The bulk of the emission is produced by a steep power-law ($\Gamma = 1.92^{+0.34}_{-0.33}$, $\mathcal{F}_{2-10\,\mathrm{keV}} = 2.16^{+0.07}_{-0.08} \times 10^{-13}\,\mathrm{erg/s/cm^2}$), which undergoes moderate obscuration ($N_H = 3.49^{+1.28}_{-1.04} \times 10^{22}\,\mathrm{cm^{-2}}$). This result differs from the conclusions of Balasubramaniam et al. 2021, which however were based on the *Chandra* data only. In line with Balasubramaniam et al. 2021, we find indications of a Gaussian line at $E_\ell = 6.73^{+0.24}_{-0.35}\,\mathrm{keV}$, which can be identified with $K\alpha$ iron line at 6.4 keV.

In the soft band there are indications for emission from multi-temperature gas ($kT = 0.32^{+0.17}_{-0.09}\,\mathrm{keV}$ and $kT = 1.16^{+0.31}_{-0.18}\,\mathrm{keV}$). A deeper *Chandra* observation would be necessary to investigate the spatial distribution of the thermal gaseous component.

Table 4.12: *Chandra* – *NuSTAR* joint fit

zphabs	**powerlaw**		**zgauss**		**apec**		**apec**		χ^2/d.o.f.
$N_H\,[\times 10^{22}\,\mathrm{cm}^{-2}]$	Γ	norm $[\times 10^{-5}]$	$E_\ell\,[\mathrm{keV}]$	norm $[\times 10^{-6}]$	$kT\,[\mathrm{keV}]$	norm $[\times 10^{-6}]$	$kT\,[\mathrm{keV}]$	norm $[\times 10^{-6}]$	
(1)	(2)	(3)	(4)	(5)	(6)	(7)	(8)	(9)	(10)
$3.49^{+1.28}_{-1.04}$	$1.92^{+0.34}_{-0.33}$	$7.44^{+5.70}_{-3.17}$	$6.73^{+0.24}_{-0.35}$	$0.81^{+0.88}_{-0.66}$	$0.32^{+0.17}_{-0.09}$	$6.13^{+2.66}_{-2.47}$	$1.16^{+0.31}_{-0.18}$	$5.60^{+2.99}_{-1.90}$	49.0/52

Notes. (1) Intrinsic hydrogen column density, (2-3) photon index and normalization of the power law emission component, (4-5) central energy and normalization of the Gaussian component, (6-7) temperature and normalization of the cold collisionally ionized thermal plasma, (8-9) ones of the hot one, (10) ratio of the χ^2 fitting statistics to degrees of freedom. *Chandra* and *NuSTAR* data fitted with model VI in the $0.3-19$ keV energy range. The model VI was multiplied by a constant function (**cons**, in `Xspec` nomenclature) to take into account the differences in normalizations between the different observations: for ObsID. 10389 the constant was set frozen to 1; for ObsID. 60601019002 $\mathbf{cons}_{\mathrm{FPMA}} = 1.01^{+0.29}_{-0.23}$ and $\mathbf{cons}_{\mathrm{FPMB}} = 0.90^{+0.28}_{-0.22}$. The model includes Galactic hydrogen column density $N_{H,\mathrm{Gal}} = 1.86 \times 10^{20}\,\mathrm{cm}^{-2}$ and thermal component assumes solar abundance. The normalizations are photons/keV/cm^2/s at 1 keV for the power law component, $10^{-14}\,(1+z)^2\,n_e n_H V/4\pi d_L^2$, assuming uniform ionized plasma with electron and H number densities n_e and n_H, respectively, and volume V, all in cgs units, for the thermal component, and total number of photons/cm^2/s in the line, for the Gaussian component.

Table 4.13: *Chandra – NuSTAR* joint fit

zphabs	**pexmon**		**apec**		**apec**		χ^2/d.o.f.
$N_H\ [\times 10^{22}\,\mathrm{cm}^{-2}]$	Γ	norm $[\times 10^{-5}]$	kT [keV]	norm $[\times 10^{-6}]$	kT [keV]	norm $[\times 10^{-6}]$	
(1)	(2)	(3)	(4)	(5)	(6)	(7)	(8)
$3.71^{+1.30}_{-1.03}$	$2.05^{+0.32}_{-0.31}$	$8.90^{+6.53}_{-3.63}$	$0.32^{+0.18}_{-0.09}$	$6.14^{+2.66}_{-2.48}$	$1.17^{+0.33}_{-0.19}$	$5.71^{+3.15}_{-1.19}$	51.3/54

Notes. (1) Intrinsic hydrogen column density, (2-3) photon index and normalization of the **pexmon** component, (4-5) temperature and normalization of the cold collisionally ionized thermal plasma, (6-7) ones of the hot one, (8) ratio of the χ^2 fitting statistics to degrees of freedom. *Chandra* and *NuSTAR* data fitted with model VII (**phabs**$\times$**(zphabs**$\times$**pexmon**+**apec**+**apec**), in `Xspec` nomenclature) in the $0.3-19$ keV energy range. The model VII was multiplied by a constant function (**cons**, in `Xspec` nomenclature) to take into account the differences in normalizations between the different observations: for ObsID. 10389 the constant was set frozen to 1; for ObsID. 60601019002 $\mathbf{cons}_{\mathrm{FPMA}} = 1.06^{+0.29}_{-0.23}$ and $\mathbf{cons}_{\mathrm{FPMB}} = 0.94^{+0.28}_{-0.23}$. The model includes Galactic hydrogen column density $N_{H,\mathrm{Gal}} = 1.86 \times 10^{20}\,\mathrm{cm}^{-2}$ and thermal components assumes solar abundance. The normalizations are photons/keV/cm^2/s at 1 keV for the power law component of the **pexmon** model, and $10^{-14}\,(1+z)^2\,n_e n_H V/4\pi d_L^2$, assuming uniform ionized plasma with electron and H number densities n_e and n_H, respectively, and volume V, all in cgs units, for the thermal component.

Table 4.14: 1843+356 counts and SNR

Telescope (1)	ObsID. (2)	Det. (3)	Ext. reg. (4)	Tot. cts (5)	Net cts (6)	SNR (7)
Chandra	12850	ACIS-S	2.5″	11 ± 3	10.8 ± 3.3	3
XMM-*Newton*	0822350201	pn	15″	283 ± 17	135.3 ± 11.6	8
XMM-*Newton*	0822350201	MOS1	15″	115 ± 11	64.5 ± 8.0	6
XMM-*Newton*	0822350201	MOS2	15″	127 ± 11	75.6 ± 8.7	7

Notes. (1) Telescope name, (2) observation ID, (3) detector name, (4) radius of the circular region used to extract the source spectrum, (5) source plus background counts in the extraction region of the source spectrum, (6) source counts in the extraction region of the source spectrum, (7) signal to noise ratio computed using Equation (3.8).

4.3.3 1843+356

Chandra

The *Chandra*/ACIS-S image of 1843+356 in the $0.3 - 7$ keV energy range is shown in Figure 4.19.

Because of the extremely small available statistics (see Table 4.14), I adopted the Cstat fitting statistics. Following the same considerations discussed for the *Chandra* spectral analysis of 1718-649 (see Section 4.3.1), I analyzed background-subtracted data.

I started modeling the spectrum with model I. However, due to the extremely low statistics, the photon index parameters remain unconstrained (Table 4.15). For this reason, following the same considerations made for 1146+596, I fixed the value of the photon index of the power law model to 1.70. The best-fit parameters are listed in Table 4.15. Since an obscuring component is expected in YRGs, I added a **zphabs** component and fitted the data with model II. The best-fit parameters are listed in Table 4.15. However, the statistics was too small to derive well constrained best-fit parameters and I could only use this observation as a validation of X-ray emission from 1843+356.

XMM-*Newton*

Because of the limited available statistics, I only analyzed the EPIC pn data in the $0.7 - 4$ keV energy range: at higher energies, the background signal is dominant with respect to the source one. Figure 4.20 shows the XMM-*Newton*/pn image of 1843+356 in the $0.7 - 4$ keV energy range.

I simultaneously fitted the source and background spectra and employed the Cstat fitting statistics. I adopted an absorbed power law model, with Galactic and intrinsic absorption (**xswabs**×**xszwabs**×**powlaw1d**, in `Sherpa` nomenclature) to fit the source spectrum and a double power law plus a Gaussian line (**powlaw1d**+**powlaw1d**+**gauss1d**, in `Sherpa` nomenclature) for the background one. The best-fit parameters of the source and the background spectra are listed in Table 4.16.

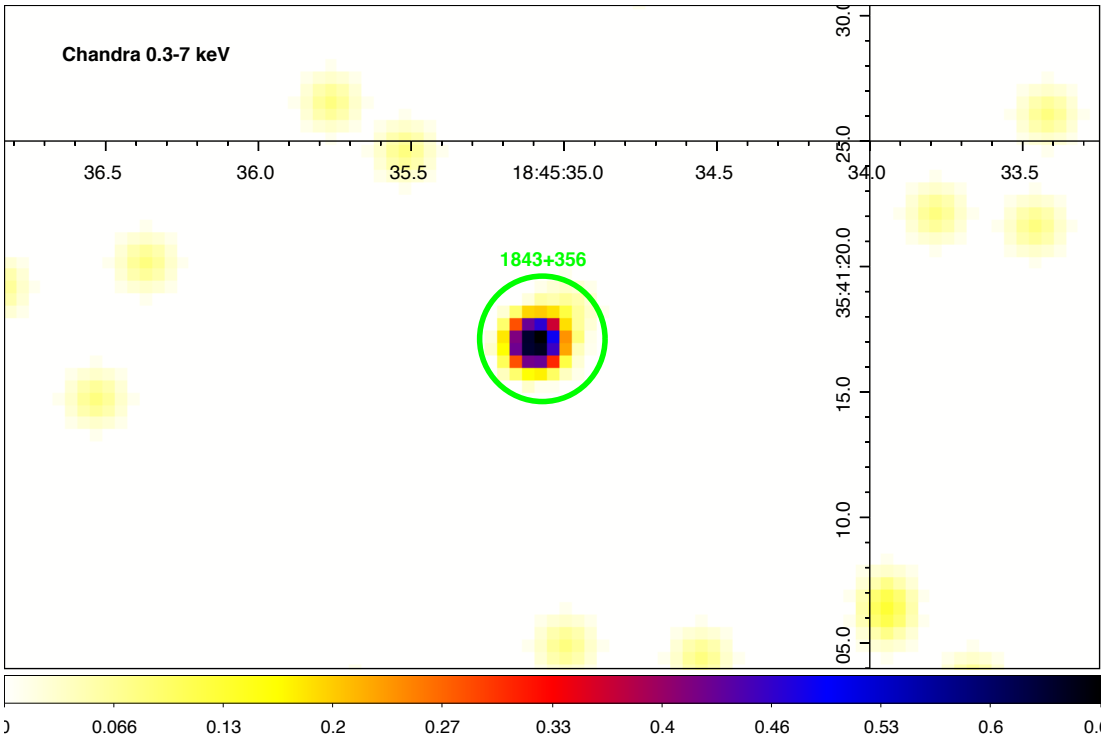

Figure 4.19: *Chandra* image of 1843+356 in the $0.3-7$ keV energy range. The green circle represents the $2.5''$ extraction region of the source spectrum. A Gaussian smoothing filter ($\sigma = 1.5$ pixels, native pixel size) was applied for graphical reasons.

Table 4.15: 1843+356 *Chandra*/ACIS-S best-fit parameters

Model	**zphabs**	**powerlaw**		Cstat/d.o.f.
#	$N_H\,[\times 10^{22}\,\mathrm{cm}^{-2}]$	Γ	norm $[10^{-6}]$	
(1)	(2)	(3)	(4)	(5)
(I)	—	$1.32^{+2.69}_{-2.42}$	< 3.78	4.4/8
(I)	—	1.70 (frozen)	$4.07^{+2.51}_{-1.78}$	10.7/9
(II)	< 3.30	1.70 (frozen)	$4.99^{+5.01}_{-2.60}$	10.3/8

Notes. (1) Model fit, (2) intrinsic hydrogen column density, Col(3-4) photon index and normalization of the power law emission component, (5) ratio of the Cstat fitting statistics to degrees of freedom. *Chandra*/ACIS-S data are fitted with model I (**phabs**×**po**, in `Xspec` nomenclature) and model II in the $0.3-7$ keV energy range. The model includes Galactic hydrogen column density $N_{H,\,\mathrm{Gal}} = 6.70 \times 10^{20}\,\mathrm{cm}^{-2}$. The normalization of the power law component is photons/keV/cm^2/s at 1 keV.

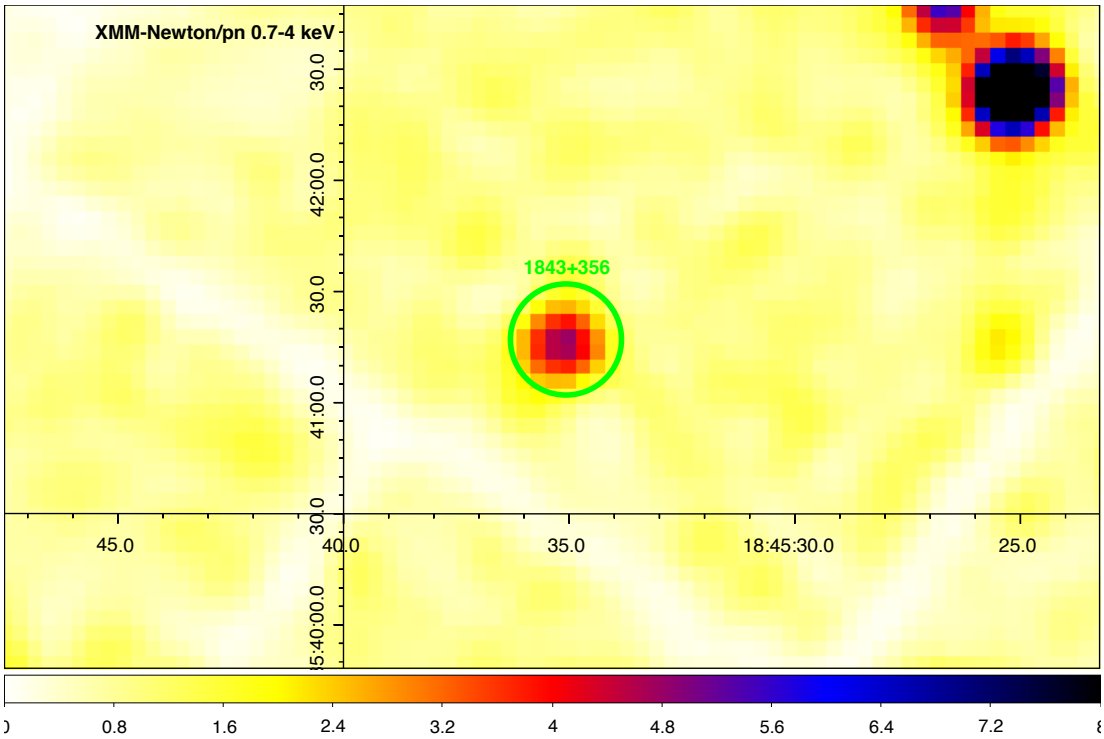

Figure 4.20: XMM-*Newton*/pn image of 1843+356 in the $0.7 - 4$ keV energy range. The green circle represents the $15''$ extraction region of the source spectrum. A Gaussian smoothing filter ($\sigma = 1.5$ pixels, native pixel size) was applied for graphical reasons.

From the fit, I derived only an upper on intrinsic equivalent column density of the source ($N_H < 1.85 \times 10^{22}\,\mathrm{cm}^{-2}$) with a very flat photon index ($\Gamma = 1.04^{+0.99}_{-0.54}$). However, since the relative error is more than 50% at $1\,\sigma$, it is plausible that the flatness of the photon index is the result of the small available statistics and an absorbing component higher than actually measures, rather than an intrinsic flatness of the source power law component. For this reason, I froze the value of the photon index in the source model at the typical value of $\Gamma = 1.70$. The best-fit parameters are listed in Table 4.16. The reduced χ^2 does not increase in a statistically significant way. However, by this choice, I was able to better constrain the intrinsic equivalent column density at a value of $N_H = 1.13^{+0.92}_{-0.73} \times 10^{22}\,\mathrm{cm}^{-2}$, suggesting the presence of an obscuring component, as expected.

Summary

To summarize, I analyzed the *Chandra* and the XMM-*Newton* available observations of 1146+596.

It was not possible to investigate the surface distribution of the X-ray emission of 1843+356 because of the low count statistic in the *Chandra* image. The source is faint also in the XMM-*Newton* observation: the spectral analysis was restricted to the $0.7 - 4$ keV energy band, beyond which the background becomes dominant. The data

[13]The `backscal` factor is defined as the ratio of the extraction area of the source spectrum to the background one.

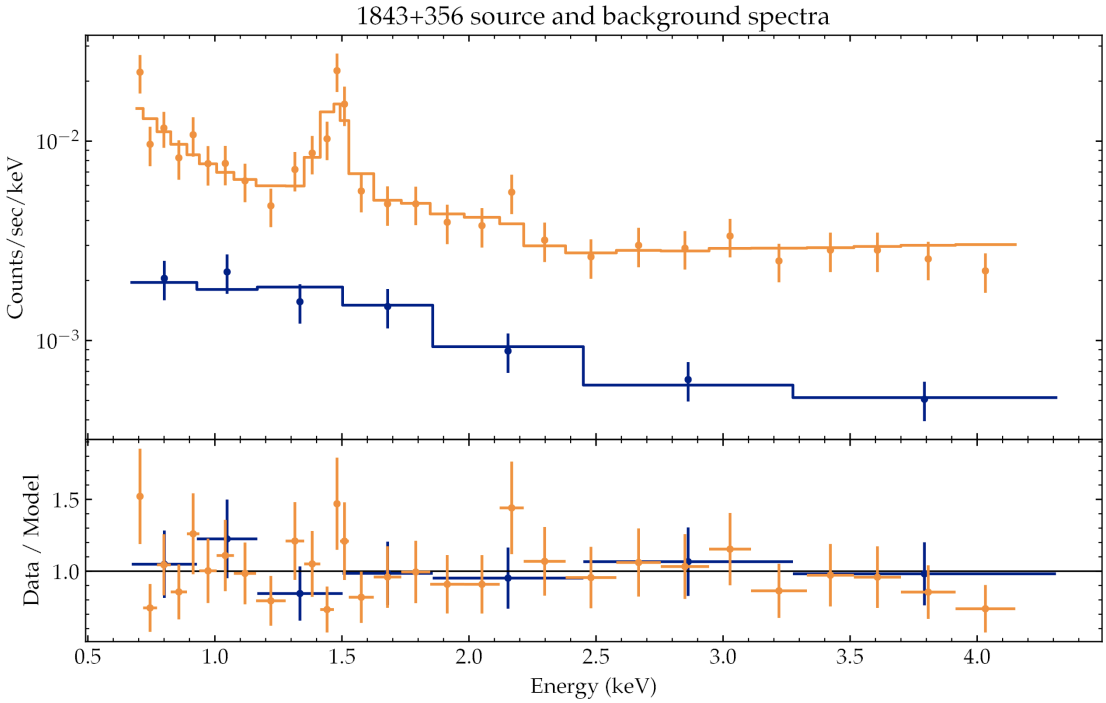

Figure 4.21: XMM-*Newton*/pn source, in blue, and background, in orange, spectra in the $0.7 - 4\,\mathrm{keV}$ energy range. For graphical reasons, background spectrum is multiplied by the `backscal` factor[13], which is equal to 2.8×10^5, and data are graphically rebinned. Source emission is fitted with a model **xswabs**×**xszwabs**×**powlaw1d**, in `Sherpa` nomenclature, whereas the background one with **powlaw1d**+**powlaw1d**+**gauss1d**, in `Sherpa` nomenclature. The fit returns Cstat/d.o.f. $= 221.3/231$. The background spectrum is well fitted with the model selected: a very steep power law is essential to fit the soft band ($0.7 - 1.5\,\mathrm{keV}$), while a slightly inverted one fits the rest of the spectrum ($1.5 - 4\,\mathrm{keV}$). In addition, the excess around 1.5 keV is well modeled with a Gaussian component, whose width σ is frozen to 10 eV: this line is consistent with the Al Kα one.

are best-fitted by an absorbed power law. The flat photon index, $\Gamma = 1.04^{+0.99}_{-0.55}$, seems to indicate obscuration by an intrinsic absorber, for which, however, only an upper limit ($N_H < 1.85 \times 10^{22}\,\mathrm{cm}^2$) could be derived. When the photon index is fixed to $\Gamma = 1.70$, i.e. a typical value for unaborbed AGN, a $N_H = 1.13^{+0.92}_{-0.73} \times 10^{22}\,\mathrm{cm}^{-2}$ is required, indicating moderate levels of obscuration. The unabsorbed energy flux of the source is $\mathcal{F}_{0.7-4\,\mathrm{keV}} \simeq 1.21 \times 10^{-14}\,\mathrm{erg/s/cm}^2$.

Table 4.16: 1843+356 XMM-*Newton*/pn best-fit parameters

Spectrum	**xszwabs**	**powlaw1d**		**bkg_powlaw1d**		**bkg_powlaw1d**		**bkg_gauss1d**		Cstat/d.o.f.
	$N_H\ [\times 10^{22}\,\mathrm{cm}^{-2}]$	Γ	norm $[\times 10^{-6}]$	Γ	norm $[\times 10^{-6}]$	Γ	norm $[\times 10^{-6}]$	E_ℓ [keV]	norm $[\times 10^{-4}]$	
(1)	(2)	(3)	(4)	(5)	(6)	(7)	(8)	(9)	(10)	(11)
source	< 1.85	$1.04^{+0.99}_{-0.55}$	$2.06^{+3.02}_{-0.75}$	—	—	—	—	—	—	221.3/231
background	—	—	—	$-0.07^{+0.39}_{-0.67}$	$4.22^{+2.12}_{-2.44}$	$4.16^{+2.95}_{-1.84}$	$4.09^{+3.36}_{-2.62}$	$1.47^{+0.02}_{-0.02}$	$1.30^{+0.44}_{-0.40}$	″
source	$1.13^{+0.92}_{-0.73}$	1.70 (frozen)	$3.67^{+1.19}_{-0.97}$	—	—	—	—	—	—	222.5/232
background	—	—	—	$-0.09^{+0.39}_{-0.65}$	$4.14^{+2.07}_{-2.34}$	$4.18^{+2.84}_{-4.92}$	$4.14^{+3.28}_{-2.60}$	$1.47^{+0.02}_{-0.02}$	$1.30^{+0.44}_{-0.40}$	″

Notes. (1) Source of the spectrum, (2) intrinsic hydrogen column density, (3-4) photon index and normalization of the power law emission component in the source model, (4-6) and (5-7) photon indexes and the normalizations of the two power law emission components in the background model, Col(9-10) central energy and normalization of the Gaussian component, (11) ratio of the Cstat fitting statistics to degrees of freedom. XMM-*Newton*/pn source and data spectra fitted with model **xswabs**×**xszwabs**×**powlaw1d** and **powlaw1d**+**powlaw1d**+**gauss1d**, in `Sherpa` nomenclature, respectively, in the $0.7 - 4\,\mathrm{keV}$ energy range. The model includes Galactic hydrogen column density $N_{H,\,\mathrm{Gal}} = 6.70 \times 10^{20}\,\mathrm{cm}^{-2}$. The normalizations are photons/keV/cm^2/s at 1 keV, for the power law components and total number of photons/cm^2/s in the line, for the Gaussian component.

Chapter 5

Discussion

In this chapter I discuss the main physical properties of the sources analyzed in this work and their ambient medium in light of the results I obtained from the X-ray analysis.

5.1 Ambient medium of YRGs

As discussed in Section 2.3, X-rays have the potential to constrain the role of ambient medium in the source expansion: the host galaxy environment can be studied in the X-ray band via detection of the hot component of the ISM and the total equivalent hydrogen column density along the LOS.

The results of the spectral analysis indicate that all the three sample sources are not particularly obscured, with intrinsic equivalent hydrogen column densities in the range from tens of $10^{20}\,\mathrm{cm}^{-2}$ up to few $10^{22}\,\mathrm{cm}^{-2}$, in agreement with the majority of YRSs reported by Sobolewska et al. 2019b.

5.1.1 X-ray absorption in CSOs

Sobolewska et al. 2019b noted that obscured and unoscured sources appeared to occupy different regions in the linear size *vs.* radio power plane (see Figure 2.3), possibly indicating a role of the ambient in the source expansion. In Figure 2.3, we updated the plot including the three CSOs analyzed in this work.

While 1146+596 lies, as expected, on the relation found for unobscured/mildly obscured sources, the other two CSOs seem instead to share the same location of obscured sources, contrary to what expected from their moderate/low column densities.

The interpretation of this result is not unique. One possibility is that the separation proposed by Sobolewska et al. 2019b is intrinsic but is biased by the small sample of CSOs considered. Alternatively, one could argue that unoscured sources can occupy any region in the plot, while oscured, and possibly frustrated sources, are confined within a specific area in the plot. One important point to stress is that the X-ray analysis cannot constrain precisely the location of the obscuring component, because of

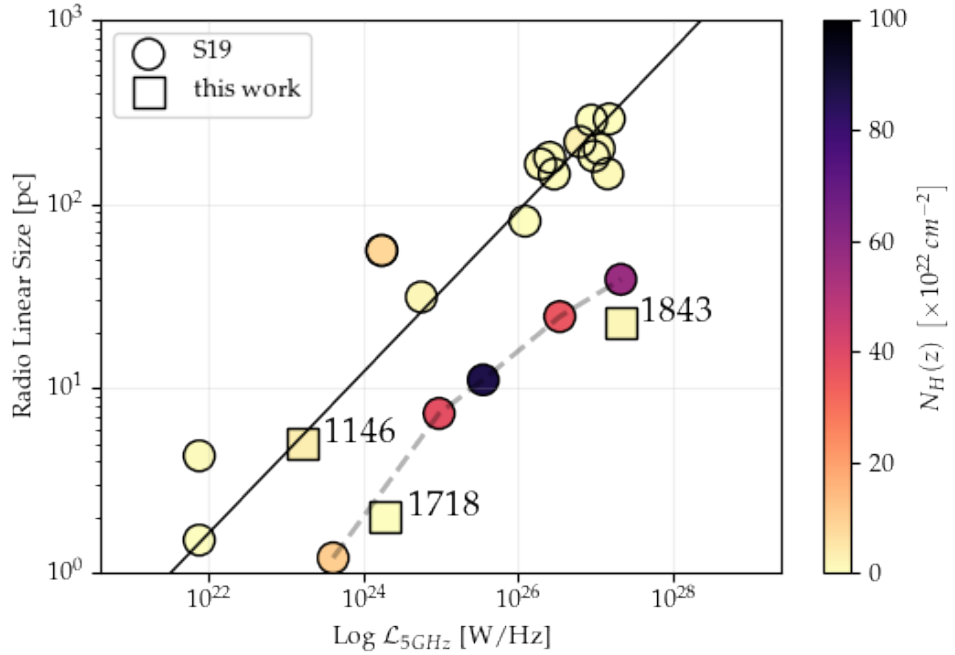

Figure 5.1: Luminosity at 5 GHz *vs*. radio source size for CSOs observed with *Chandra* and/or XMM-*Newton* proposed by Sobolewska et al. 2019b (circles), updated with the three CSOs studied in this work (squares). Color coding indicates the intrinsic equivalent hydrogen column density measured from the X-ray spectra. Solid line marks the relation fitted to the CSO data of Tremblay et al. 2016. Dashed line connects CSOs with intrinsic $N_H > 10^{23}$ cm^{-2}. Adapted from Sobolewska et al. 2019b.

the limited angular resolution of the X-ray instruments ($\sim 1''$ corresponds to 305 pc at $z \simeq 0.014$, 228 pc at $z \simeq 0.011$, and 7.6 kpc at $z \simeq 0.763$). .

In 1146+596, the optical HST images unveiled the presence of a dust lane along the major axis of the host galaxy (Perlman et al. 2001). It is possible that also the X-ray obscurer is distributed at the same scales, thus obscuring the X-ray emission without affecting the CSO's expansion.

5.1.2 Extended X-ray thermal component

In two of the three sources, 1718+649 and 1146+596, thermal emission is evident in the soft X-ray band ($0.3 - 2$ keV). The emission is extended on kiloparsec scale, thus beyond the size of the CSOs, raising the question on the origin of such emission and its relation with the presence of a young source.

In 1718-649, we measured a gas temperature of $kT \simeq 0.63$ keV. This result is only apparently in tension with the temperatures reported by Beuchert et al. 2018. In fact, they identified two emitting components, one photo-ionized gas responsible for features detected in the soft band (e.g. OVIII at ~ 0.56 keV), most-likely located at subparsec scales, and a second collisionally ionized gas with $kT \simeq 0.75$ keV. The gas temperature could result by blending of these two components, as we included a single thermal component in the spectral model.

Interestingly, in the X-ray spectrum of 1146+596 we found evidences for a two-temperature emitting gas, with a warmer component at $kT \simeq 0.32$ keV and a hotter one at $kT \simeq 1.16$ keV.

The possible presence of a multi-temperature, X-ray emitting gas in the two CSOs is interesting. Beuchert et al. 2018 relate the warmer component to photo-ionized gas by the AGN, and the hotter component to collisionally ionized gas by supernova remnants. However, the expanding radio structures could also generate shocks which impact the ISM on larger scales with respect to the linear sizes of the radio sources. Also, the continuum photo-ionizing the gas could be either the AGN emission or the non-thermal radiation from the jets and mini-lobes. A deep XMM-*Newton* observation would be needed to confirm the presence of the double thermal component in 1146+596.

5.2 Origin of high-energy emission in YRGs

In the following sections, we discuss the SED model of 1718-649 originally proposed by Sobolewska et al. 2021, two different models for the SED of 1146+596, and we discuss the γ-ray association proposed by Principe et al. 2021.

5.2.1 1718-649

The SED modeling presented in Sobolewska et al. 2021 leaves the question on the origin of the X-ray emission unsettled. In the favored model, the emission is the sum of IC/IR flux and radiation from a weak corona. The latter is needed to account for a fraction of the soft X-ray emission, while it should be sub-dominant at higher ($>$ 10 keV) energies. The deep XMM-*Newton* observation, along with the *NuSTAR* data, allowed me to refine the spectral parameters of the X-ray emission, with a photon index of $\Gamma \simeq 1.74$ and a normalization of the power law component of norm_po $\simeq 0.94 \times 10^{-4}$ photons/keV/cm^2/s.

In Figure 5.2, we plot the observed and modeled SED of 1718-649 presented in Sobolewska et al. 2021, adding the results of the joint-fit of the deep XMM-*Newton* and *NuSTAR* data. We also include the upper limit in the $20 - 40$ keV measured from the *NuSTAR* observation[1]. The improved X-ray dataset confirms the main findings of the modelization: the IC/IR is the dominant contribution. The non-thermal flux underpredicts the < 1.5 keV flux by about a factor of 2. As proposed by Sobolewska et al. 2021, this excess could be accounted for by an additional emitting component such as the corona ($\Gamma = 2.0$, $\mathcal{L}_{2-10\,\mathrm{keV}} = 6.6 \times 10^{40}$ erg/s and a high-energy cut-off at 100 keV). The model is consistent with the data at energies higher than 10 keV obtained from the *NuSTAR* observation which, unfortunately, provides only loose constraints beyond 20 keV.

[1]The upper limit was obtained using `PIMMS v.4.11a`, adopting a photon index of $\Gamma = 1.74$ and the count rate derived from the *NuSTAR* observation (1.3×10^{-3} cts/s in the $20 - 40$ keV energy range).

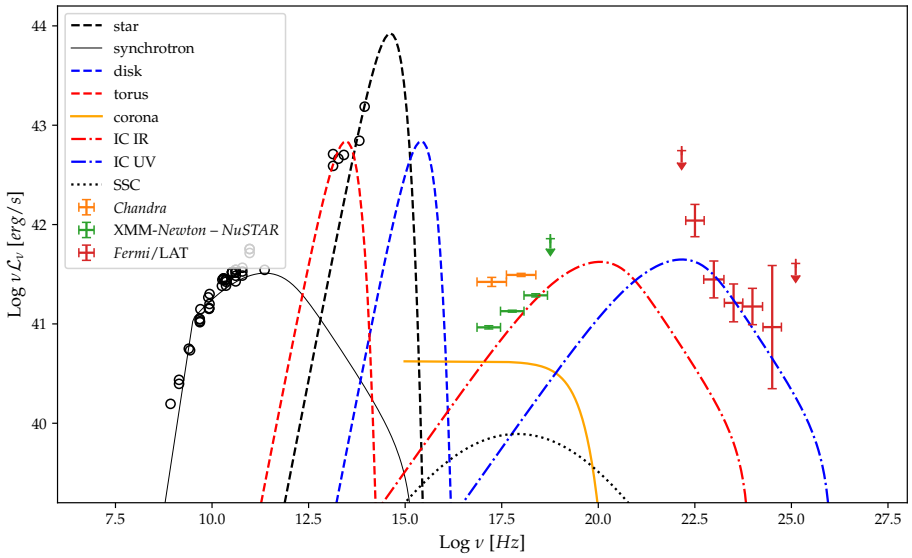

Figure 5.2: Observed broadband spectral energy distribution of 1718-649 and the best-fit theoretical model. Circles are archival data (see Sobolewska et al. 2021, for references). Orange data are *Fermi*/LAT luminosity constraints from Principe et al. 2020. Green data are XMM-*Newton* – *NuSTAR* luminosity constraints from this work, while orange data are the *Chandra* ones, both assuming a simple power law model for X-ray emission. Broadband model components are as follows: self-absorbed synchrotron radiation (solid black line), SSC (dotted black line), three black-body components representing the infrared (dashed red line), starlight (dashed black line) and accretion disk photon fields (blue dashed line), and their corresponding IC components originating from a single radio lobe. The solid orange line illustrates the contribution of a low-luminosity X-ray nuclear emission (either a weak X-ray corona or an ADAF-type emission). All the other theoretical curves are courtesy of M. Sobolewska.

To conclude, the new X-ray data provide support to the scenario of non thermal high-energy emission associated with the *mini*-lobes. If so, the inferred jet power, $\mathcal{L}_{\rm kin} \simeq 2.2 \times 10^{42}$ erg/s, leaves uncertain the capability of the source to expand beyond the host galaxy. Interestingly, Mukherjee et al. 2017 argued that jets with power $\lesssim 10^{43}$ erg/s may be too weak to break out the ISM confinement.

We finally comment on the indications from the spectral analysis of a possible break at $E_{\rm break} \simeq 6.61$ keV, with a photon index beyond the break of $\Gamma \simeq 2.38$. A second *NuSTAR* observation would be necessary to clarify whether this break is real or due to instrumental issues. We also replot the SED with the X-ray flux bins recalculated assuming that the spectral break is actually present. The IC/IR curve is still consistent with the data up to the last significantly detected bin (< 19 keV); an extrapolation of the broken power law at higher energies would require a lower IC/IR contribution. If this spectral shape is confirmed by future *NuSTAR* observations, the suggested SED model should be called into question.

5.2.2 1146+596

The broadband X-ray spectrum of 1146+596 can be described by an absorbed power-law model with $\Gamma = 1.92^{+0.34}_{-0.33}$ and $N_H = 3.49^{+1.28}_{-1.04} \times 10^{22}\,\mathrm{cm}^{-2}$ and thermal emission, that, as discussed in Section 4.3.2, is extended over galactic scales ($\simeq 4.6$ kpc). In addition, as also found by Balasubramaniam et al. 2021, we possibly detected the iron Kα line at $6.73^{+0.24}_{-0.35}$ keV (at a significance of $\sim 1.5\,\sigma$), which is likely indicative of X-ray reflection from material located in the inner kilo-parsec region of 1146+596. The spectral modeling is not conclusive on the nature of the continuum, as the model assuming a reflection-dominated spectrum is basically indistinguishable from the (phenomenological) power law model (see Section 4.3.2). The X-ray continuum could be then for non-thermal origin, related to the jets, or produced by the AGN powering the radio source.

More insights can come by the study of the observed broadband SED. To this aim, we assembled the broadband SED of 1146+596 by combining the analyzed data with those available in literature and in on-line databases[2]. The integrated γ-ray fluxes are taken from the 4FGL (Abdollahi et al. 2020); we assumed the best-fit model of Principe et al. 2020, a power law with $\Gamma \simeq 2.01$. The X-ray data-points are the fluxes measured from the spectral analysis (see Section 4.3.2). The observed SED is shown in Figure 5.3. Note that the emission of the host galaxy dominates the SED in the optical-IR band.

Similarly to the analysis carried out for 1718-649 by Sobolewska et al. 2021, in the following we explore the implications of a non-thermal origin of the high-energy emission of 1146+596 by modeling its radio-to-γ-ray emission.

While 1718-649 displays two mini-lobes, in the multi-epoch 8.4 GHz VLBA maps, the pc-extended radio structure of 1146+596 presents a jet and a counter-jet (Principe et al. 2020). Therefore, we do not apply the dynamical and radiative model of Stawarz et al. 2008, but we test instead a leptonic model for the emission of the jets. We consider the simplest, and yet informative, scenario of a jet emitting via synchrotron and SSC mechanism. For the modeling, we used the SSC numerical code developed by Tramacere et al. 2009. In the model, the emission is produced in a jet region of spherical shape and radius R' (where primed quantities indicate the jet comoving frame). The spherical volume is uniformly filled by relativistic plasma (i.e. a filling factor equal to one was assumed) and magnetic field, B'. The energy densities of relativistic leptons and magnetic field are U'_e and U'_B, respectively.

The region is moving with a bulk Lorentz factor Γ_{bulk}, and θ is the angle between the jet axis and the observer LOS. Interacting with the jet magnetic field (B), the electrons in the blob radiate via synchrotron emission. The synchrotron radiation provides the seed photons for the IC mechanism (SSC).

A broken power-law function is used to describe the energy distribution of the radiating electrons, $N(\gamma)$. The minimum, maximum and break Lorentz factors are γ_{min}, γ_{max}, and γ_{break}, respectively. The spectral indices below and above γ_{break} are $p_1 \equiv 2\alpha_1 + 1$ and $p_2 \equiv 2\alpha_2 + 1$, respectively. To summarise the input parameters of

[2] https://tools.ssdc.asi.it/SED/

Table 5.1: 1146+596 input SED models parameters

Model #	$\log_{10} R$ [cm]	δ	B [mG]	$\log_{10} \mathcal{N}$ [cm^{-3}]	s_1	s_2	$\log_{10} \gamma_{\mathrm{min}}$	$\log_{10} \gamma_{\mathrm{max}}$	$\log_{10} \gamma_{\mathrm{break}}$
(1)	(2)	(3)	(4)	(5)	(6)	(7)	(8)	(9)	(10)
1	18.3	1.3	0.6	0.02	1.9	2.9	2.5	8	5
2	18.5	1.6	1.0	0.4	1.8	3.0	1	6	4

Notes. (1) SED model, (2) emitting electron number density, (3) cross section radius of the jet, (4) Doppler factor obtained assuming $\Gamma_1 = 1.04$ and $\Gamma_2 = 1.11$ for model 1 and 2, respectively, (5) magnetic field, (6-7) slope of the electron power law distribution before and after the energy break, (8-9) minimun and maximum value of the electrons Lorentz factor, (10) electrons Lorentz factor at the break of power law fuction.

the models are $N(\gamma)$, γ_{min}, γ_{max}, γ_{break}, $p_1 \equiv 2\alpha_1 + 1$, $p_2 \equiv 2\alpha_2 + 1$, the magnetic field B, and the Doppler factor δ.

Initial estimates for some of the model input parameters could be derived from the observations. The radio observations provided us with constraints on the inclination of the jet with respect to the observer LOS and its bulk motion ($10^{\circ} \leq \vartheta \leq 21^{\circ}$, $1.04 \leq \Gamma_{\mathrm{bulk}} \leq 1.11$, Principe et al. 2020): from these, the Doppler factor is $1.3 \lesssim \delta \lesssim 1.6$. We estimated the magnetic field under the assumption of energy equipartition between B and particles from Wójtowicz et al. 2020:

$$B_{\mathrm{eq}} = [4.5 c_{12} \mathcal{L}_{\mathrm{rad}}]^{2/7} R_{\mathrm{eff}}^{-6/7}, \tag{5.1}$$

where $c_{12} \simeq 3 \times 10^7$, $R_{\mathrm{eff}} \simeq 0.18 \times LS$ is the effective radius of the lobes[3], and $\mathcal{L}_{\mathrm{rad}}$ stands for the total radio power emitted in the frequency range $0.01 - 100\,\mathrm{GHz}$, all in cgs units (see Beck and Krause 2005). Assuming that the intrinsic radio continuum is well approximated by a simple power law with a mean spectral index $\alpha \simeq 0.73$ above the frequency peak, as derived for YRGs (de Vries, Barthel, and O'Dea 1997), it yields $\mathcal{L}_{\mathrm{rad}} \simeq 7.62 \times \mathcal{L}_{5\,\mathrm{GHz}}$. With $LS = 5\,\mathrm{pc}$ and $\mathcal{L}_{5\,\mathrm{GHz}} = 1.62 \times 10^{23}\,\mathrm{W/Hz}$ (Principe et al. 2020), we found

$$B_{\mathrm{eq}} \simeq 9.9\,\mathrm{mG}, \tag{5.2}$$

where the $\mathcal{L}_{5\,\mathrm{GHz}}$ is divided by δ^4, with $\delta = 1.45$[4] in order to correct it for beaming.

The slope of the $N(\gamma)$ beyond the energy break, p_2, can be derived from the photon index of the γ-ray emission, $p_2 = 2\alpha_2 + 1 = 2\Gamma - 1$. Note that these are initial values that need to be adjusted in order for the model to match the observed SED.

SED models

We begin testing a scenario in which the jet emission accounts for both X-ray and γ-ray emission (Model 1). This model is borrowed from high-energy peaked BL Lacs

[3]The source linear size ($LS \simeq 5\,\mathrm{pc}$) was assumed as a loose upper limit for the dimension of the emitting region.

[4]We chose the mean value obtained from the constraints on the Doppler factor ($1.3 \lesssim \delta \lesssim 1.6$) reported in Principe et al. 2020).

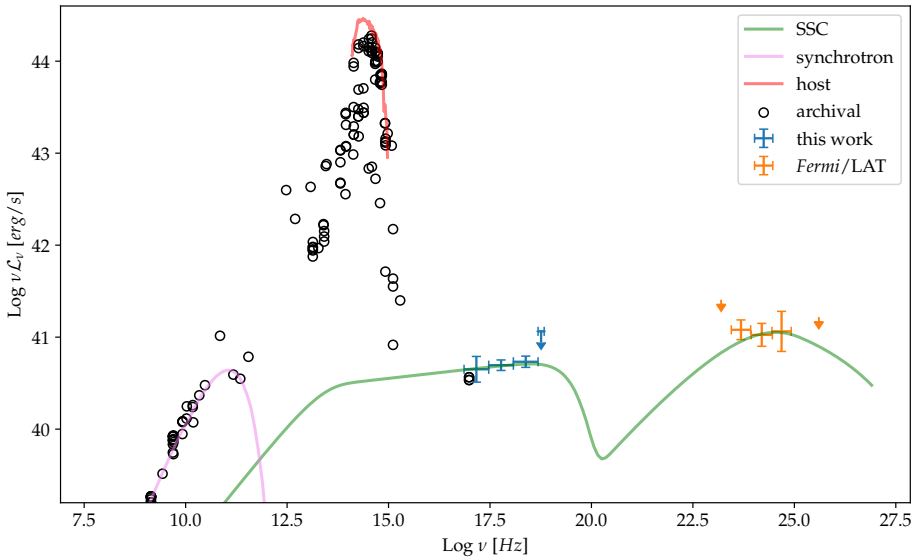

Figure 5.3: Observed broadband spectral energy distribution of 1146+596 and theoretical model 1. Circles are data from SSDC/ASI online builder tool and reference therein. Orange data are *Fermi*/LAT luminosity constraints from Principe et al. 2020. Blue data are *Chandra* – *NuSTAR* luminosity constraints from this work. Broadband model components are as follows: SSC in light green, synchrotron model in light violet (all from Tramacere et al. 2009).

(1.4.5), whose synchrotron curve peaks in the UV-X-ray band, while the γ-ray emission is attributed to SSC curve. This choice is also motivated by the fact that, in the γ-ray luminosity *vs.* photon index plot (Figure 2.4), 1146+596 is located closer to the region of γ-ray BL Lacs. Hence, in this scenario, 1146+596 could be considered as a misaligned low-power BL Lac with a mildly relativistic jet.

Model 1 is presented in Figure 5.3 and the model parameters are reported in Table 5.1. Some simple considerations can be made:

1. if we calculate the energy densities in magnetic field (U_B) and particles (U_e), we find that U_e is larger than U_B by several order of magnitudes ($U_B/U_e \simeq 3 \times 10^{-4}$), implying that the emitting region must be heavily particle dominated;

2. in order to produce the observed X-ray emission via synchrotron mechanism, a $\gamma_{\rm max} \geq 10^8$ is needed. This is an extreme value, that is not typically found even for BL Lacs detected at TeV energies (Celotti and Ghisellini 2008). Moreover, such electrons energies are not easily obtained in particle acceleration simulations (Sironi, Spitkovsky, and Arons 2013; Sironi and Spitkovsky 2014);

3. as evident in the figure, the synchrotron curve cannot account for the X-ray and radio emission at once. Therefore, in this scenario, the radio emission could be produced in a different region, which could be a larger jet region or mini-lobe (see Figure 5.3). If this second region were in equipartition conditions, its high-energy flux would be negligible.

We then considered an alternative *scenario*, in which the γ-ray emission is still due to SSC, whereas the X-ray emission is instead related to the AGN emission (model 2). As discussed in Section 2.5.2, 1146+596 harbours a LINER type AGN as 1718-649. Therefore, we assumed the same phenomenological AGN model of 1718-649 (Sobolewska et al. 2021): a disk blackbody peaking at UV frequencies and a cut-off power law function with $\Gamma = 2.0$, $E_{\text{cut-off}} = 100\,\text{keV}$. We adjusted the luminosities of these two components so to match the observed SED: this resulted in a UV luminosity of $\mathcal{L}_{\text{UV}} \simeq 9.3 \times 10^{42}\,\text{erg/s}$, which is in agreement with the upper limit of $\mathcal{L}_{\text{bol}} < 5 \times 10^{43}\,\text{erg/s}$ reported in Balasubramaniam et al. 2021, and a $2 - 10\,\text{keV}$ luminosity of $\mathcal{L}_{2-10\,\text{keV}} \simeq 7.3 \times 10^{42}\,\text{erg/s}$. Note that these parameters are typical for LINER-type AGN in X-rays (González-Martin et al. 2009), and that the X-ray emission could be explained as emission from a weak corona or a radiatively inefficient accretion flow. For completeness, we also included the emission of the putative torus, modeled as a blackbody peaking in the IR band. Model 2 is shown in Figure 5.4 and the model parameters are reported in Table 5.1. Main findings for this model are:

1. relaxing the requirement of reproducing the X-ray emission via synchrotron emission, the model allows for lower, rather standard γ_{max};

2. in this *scenario*, the radio and γ-ray emission are produced in the same region. Only slow, low-level of variability has been observed in the decade-long monitoring of the source with the Owens Valley Radio Observatory, which is in line with the lack of significant variability in the γ-ray band, i.e. *Fermi*/LAT could not be sensitive to variability of a factor of fews at these low flux levels (Principe et al. 2020);

3. the dominance of the particles over the magnetic field holds true also in this case ($U_B/U_e \simeq 8 \times 10^{-4}$), as it is an unavoidable consequence of a SSC luminosity peak comparable with the synchrotron one.

We also comment on the origin of the iron Kα line for the two models: in model 1 the line could be related to photo-ionized medium illuminated by the non-thermal X-ray continuum from the jet, while in model 2 it could originate in the accretion disk illuminated by the X-ray corona.

Estimated jet powers

Estimates of the total power carried by the jet can be inferred from the SED modeling that we have performed. The jet power ($\mathcal{L}_{\text{jet}}$) is the sum of different components:

- the kinetic power ($\mathcal{L}_{\text{kin}}$) which is the energy stored into relativistic emitting electrons ($\mathcal{L}_e$) and cold protons ($\mathcal{L}_p$). The jet transports matter. As mentioned in Section 1.4.5, jets composition is still a matter of debate. In particular, the main issue concerns the proton contribution: this is controversial, because if the emission is totally produced by electron-positrons, there are no protons; if, instead,

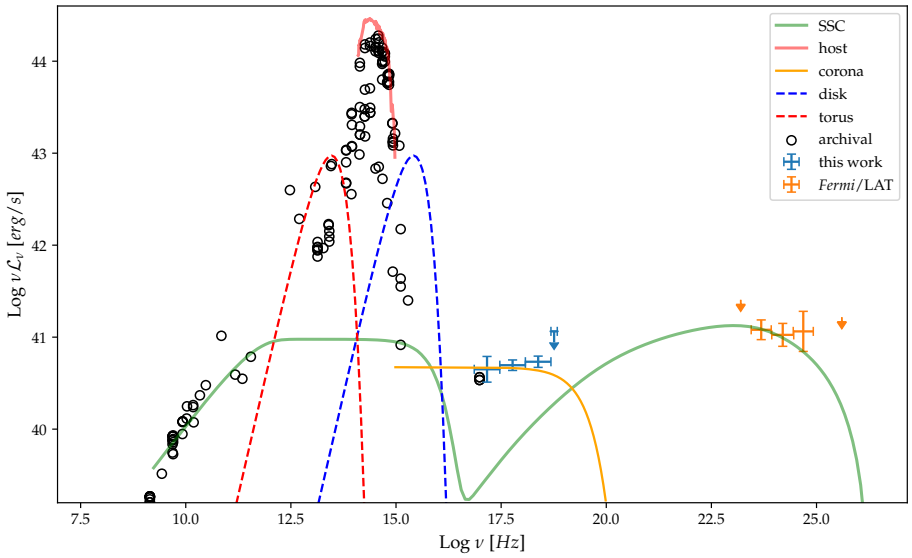

Figure 5.4: Observed broadband spectral energy distribution of 1146+596 and theoretical model 2. Circles are data from SSDC/ASI online builder tool and reference therein. Orange data are *Fermi*/LAT luminosity constraints from Principe et al. 2020. Blue data are *Chandra* – *NuSTAR* luminosity constraints from this work. Broadband model components are as follows: SSC in light green (from Tramacere et al. 2009), two black-body components representing the torus, in red, and the disk, in blue, emission. The solid orange line illustrates the contribution of a low-luminosity X-ray nuclear emission (a weak X-ray corona or an ADAF-type emission).

the emitting plasma is a electron-proton one, than there is one proton per emitting electron;

- the power carried as Poynting flux ($\mathcal{L}_B$).

A fraction of this power is dissipated in form of electromagnetic radiation, the radiative power ($\mathcal{L}_{\rm rad}$). All the previous components can be formally accounted for by writing

$$\mathcal{L}_i = \pi R^2 \Gamma^2 \beta c U_i', \tag{5.3}$$

where $U_i^{'}$ is the comoving energy density of the $i^{\rm th}$ component. Considering a plasma made of electrons and *cold* protons[5], it gives

$$U_e' = m_e c^2 \int_{\gamma_{\rm min}}^{\gamma_{\rm max}} \gamma \mathcal{N}(\gamma)\, d\gamma = \langle\gamma\rangle n_e' m_e c^2 \tag{5.4}$$

and

$$U_p' = U_e' \frac{m_p}{m_e} \frac{n_p'}{\langle\gamma\rangle n_e'}, \tag{5.5}$$

respectively, where $\langle\gamma\rangle$ is the average random Lorentz factor of the leptons, measured

[5]With the term *cold protons*, we mean that, considering a blob in jet structure, random walks of protons in it are negligible and they only contribute to the bulk motion of the blob. As a consequence, they do not provide pressure within the blob.

Table 5.2: 1146+596 jet power

Model # (1)	$\mathcal{L}_{\rm rad}$ $[\times 10^{41}\,{\rm erg/s}]$ (2)	$\mathcal{L}_e$ $[\times 10^{42}\,{\rm erg/s}]$ (3)	$\mathcal{L}_p$ $[\times 10^{42}\,{\rm erg/s}]$ (4)	$\mathcal{L}_{\rm kin}$ $[\times 10^{42}\,{\rm erg/s}]$ (5)	$\mathcal{L}_B$ $[\times 10^{39}\,{\rm erg/s}]$ (6)	$\mathcal{L}_{\rm jet}$ $[\times 10^{42}\,{\rm erg/s}]$ (7)
1	1.46	6.79	0.13	6.92	4.25	6.92
2	1.75	33.3	30.0	63.3	53.4	63.4

Notes. (1) SED model, (2) radiative power, (3) electrons kinetic power, (4) protons kinetic power, (5) total kinetic power, (8) magnetic power, (7) total jet power. For each component, the power is evaluated by Equation 5.3. $\mathcal{L}_{\rm kin}$ is the sum of $\mathcal{L}_e$ and $\mathcal{L}_p$. For $\mathcal{L}_{\rm rad}$, $\mathcal{L}_{\rm bol} = 1.40 \times 10^{42}\,{\rm erg/s}$ and $\mathcal{L}_{\rm bol} = 2.14 \times 10^{42}\,{\rm erg/s}$ are obtained for model 1 and 2, respectively, and used to evaluate $\mathcal{L}_{\rm rad}$.

in the comoving frame, n'_e and n'_p are the comoving electron and proton number densities, and $\mathcal{N}(\gamma)$ is the number density of emitting electrons. Since we considered an electron-proton jet, we fixed the ratio $n'_p/n_e\prime$ to 1. When dealing with the magnetic field it gives

$$U'_{\rm B} = \frac{B'^2}{8\pi}, \tag{5.6}$$

where B' is the magnetic field, and when dealing with the radiation it gives

$$U'_{\rm rad} = \frac{\mathcal{L}'_{\rm bol.}}{4\pi R^2 c} = \frac{\mathcal{L}_{\rm bol}}{4\pi R^2 c \delta^4}, \tag{5.7}$$

where $\mathcal{L}_{\rm bol}$ is the bolometric luminosity and δ is the Doppler factor defined by Equation (1.18).

We calculated the radiative and jet powers for both models using the formulae reported above. The results are reported in Table 5.2.

The total jet power is in the range $0.69 - 6.34 \times 10^{42}\,{\rm erg/s}$, which points to moderately low-power jets, similarly to what estimated for 1718-649 ($\mathcal{L}_{\rm jet} \simeq 2.2 \times 10^{42}\,{\rm erg/s}$) by Sobolewska et al. 2021. The Poynting flux is a minimal contribution of the total power, as expected being $U_e \gg U_B$ in both cases. The bulk of the power is carried by relativistic electrons in model 1, while protons provides a comparable contribution only in model 2. This means that, if we relax the assumption of one cold proton per radiating electron, $\mathcal{L}_p$ can drastically decrease without a significant impact on $\mathcal{L}_{\rm jet}$. The jet radiates away less than 10% of its total power, meaning that the bulk of $\mathcal{L}_{\rm jet}$ can be used in the expansion of the radio structures. For the accretion disk luminosity, $\mathcal{L}_{\rm disk} \simeq 5 \times 10^{43}\,{\rm erg/s}$, estimated by Balasubramaniam et al. 2021 based on the $8 - 1000\,\mu{\rm m}$ fluxes in Kosmaczewski et al. 2020, the jet to disk luminosity ratio is in the range $\sim 0.1 - 1$. For a comparison, Ostorero et al. 2010 reported $\mathcal{L}_{\rm jet}/\mathcal{L}_{\rm disk} = 0.01 - 0.1$ for a sample of CSOs, while there are indications of higher ratios, $\sim 1 - 10$, in powerful blazars (Celotti and Ghisellini 2008).

5.2.3 1843+356

The poor statistics of the X-ray data did not allow us to characterize the X-ray properties of 1843+356. The source was selected for the study in view of the available X-ray observations and of the detection, though marginal, of a faint γ-ray counterpart ($\mathcal{L}_{0.1-1000\,\mathrm{GeV}} \simeq 2.3 \times 10^{45}\,\mathrm{erg/s}$ with a significance of $\sigma \simeq 3.3$, Principe et al. 2021). However, visual inspection of the XMM-*Newton* image unveiled the presence of a luminous X-ray source in the field. The source corresponds to the radio quasar B1843+357. We note that in literature the two sources have been sometimes mixed up, possibly inducing some confusion in the classification. Indeed, also in the major astronomical databases, the redshift of the QSO is not unique: for instance, NED[6] locates it at $z \simeq 0.765$, while SIMBAD[7] at $z \simeq 1.21$.

In Figure 5.5, we show the XMM-*Newton* image of 1843+356 field with the location of the putative γ-ray counterparts. The dashed lines are the position uncertainty countours at 68%, 95%, and 99% level of confidence. From the Figure, it is clear that the QSO is closer to the γ-ray best-fit position than the CSO. As discussed in 1.4.5, jetted QSOs can be γ-ray emitters when their jet is closely aligned to the line of sight (FSRQs). In view of this second source, we question the association of the γ-ray source with the CSO proposed by Principe et al. 2021.

[6] https://ned.ipac.caltech.edu
[7] http://simbad.u-strasbg.fr/simbad/

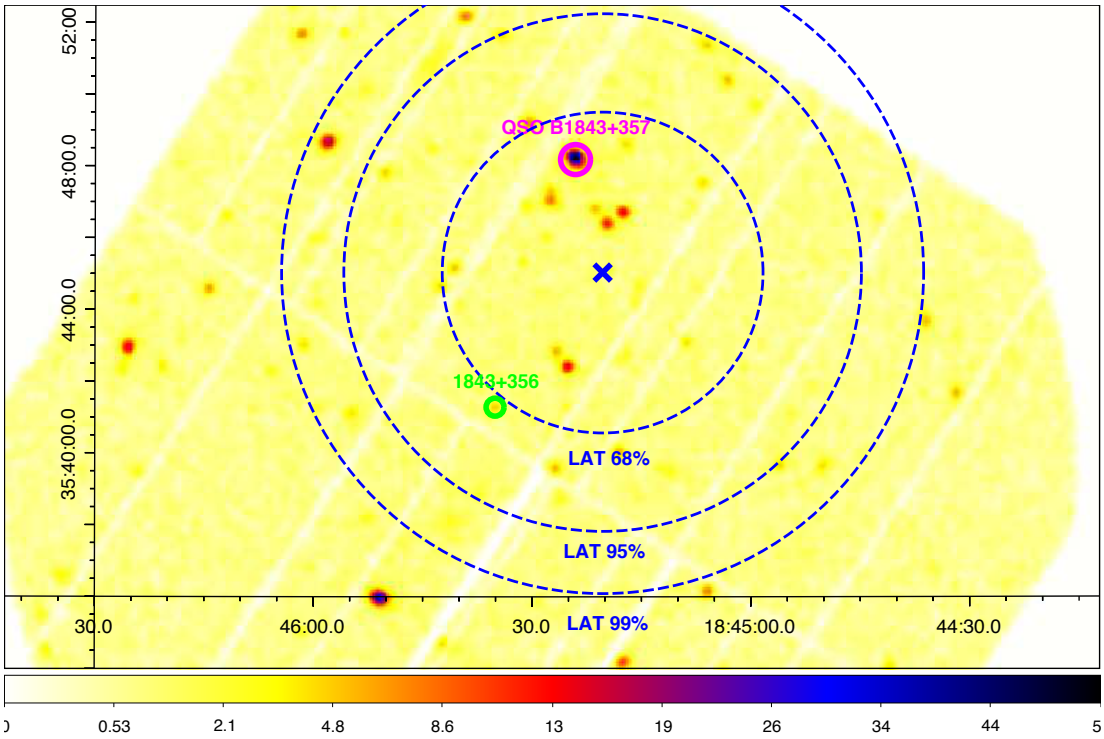

Figure 5.5: XMM-*Newton*/pn image of 1843+356 in the $0.7 - 4$ keV. The green circular region is 1843+356. The blue cross is the best-fit position of the γ-ray source obtained by Principe et al. 2021 and the blue dashed annuli regions are the confidence contours of this position at three different levels of confidence: 68%, 95% and 99%. The megenta circular region is the position of a field quasar (QSO B1843+357, $z \simeq 1.21$), which could be the real γ-rays emitter, instead of 1843+356.

Chapter 6

Conclusions and future prospects

The study of the class of CSOs is important to shed a light on the first phase in the evolution of the radio galaxies. The last twenty years have seen CSOs observations moving beyond the radio band. At high energies, XMM-*Newton* and *Chandra* observations allowed us to establish CSOs as a class of X-ray emitters and to derive their basic properties (e.g. luminosities, spectral models, etc.) as well as those of their environments (intrinsic absorption, co-spatial diffuse gas). X-ray emission is expected from both the AGN and the radio structures (jets and lobes).

However, due to their compact nature and the limited X-ray photon statistics, the nature of the X-ray emission of CSOs remains currently still uncertain, and yet crucial to make predictions on the fate of the expanding source and on its impact on the host galaxy.

In this thesis work, we addressed this open question by investigating the high-energy emission of a small sample of CSOs. The three studied targets have been selected in view of their good X-ray coverage among those CSOs which have been also detected in the γ-ray band by *Fermi*/LAT. The latter choice was motivated by the fact that the γ-ray window allows us to place constraints on the non-thermal high-energy contribution.

In the first part of the study, we investigated the X-ray properties of the sources, through X-ray imaging and spectral analysis of the available *Chandra*, XMM-*Newton* and *Swift* data. Moreover, for two of the three sources, 1718-649 and 1146+596, we obtained *NuSTAR* observations, which allowed us to investigate for the first time their spectra up to ~ 20 keV.

In the second part, we performed a broadband study of the two sources with the best sampled datasets. The main results of the study can be summarised as follows:

- we found evidence for intrinsic absorbers with column densities in the range $N_H \simeq 0.1 - 3.5 \times 10^{22}\,\mathrm{cm}^{-2}$ This allowed us to place the three sources in the radio size-radio luminosity-N_H plot. Our sources do not confirm the separation between obscured/frustrated and unobscured/freely-expanding sources proposed by Sobolewska et al. 2019b. This does not necessarily rule out a role of dense ($N_H > 10^{23}\,\mathrm{cm}^{-2}$) medium in preventing the CSO expansion. In fact, it is

possible that the unobscured CSOs are not confined to a specific area of the plot, while instead obscured ones are. It is clear that increasing *NuSTAR* detections of heavily obscured CSOs can significantly help in placing stringent constraints on the role of the ambient medium in the radio source evolution;

- diffuse hot gas is detected in two of the three sources (1843+356 lacks the statistics to perform a detailed study). Interestingly, the spectral analysis of 1146+596 indicates the presence of two thermal components, and for 1718-649 Beuchert et al. 2018 claimed that it can be related to a photo-ionized gas by the central AGN (the warmest component) and a collisionally ionized gas by supernova remnants (the hottest one). However, we put forward an alternative explanation: the hottest component could be produced by shock generated by the expanding radio structure and the warmest component can be the interstellar gas typically found in elliptical galaxies;

- the emission of the central AGN could be modelled with a simple power law. For 1718-649, the broad ($0.3 - 19$ keV) spectrum basically confirmed, improving over the uncertainties, the spectral parameters obtained in the $0.3 - 10$ keV. For 1146+596 the *NuSTAR* data led to a substantial revision of the spectral parameters obtained by fitting the *Chandra* $0.3 - 7$ keV spectrum. The joint analysis also supports the detection of an iron line, previously reported by Balasubramaniam et al. 2021 based only on *Chandra* data;

- we used the improved constraints on the X-ray spectrum of 1718-649 to test the model presented in Sobolewska et al. 2021 of broadband (radio-to-γ-ray) SED. In the model, the high-energy emission is accounted for by the IC emission from the lobes. While the *NuSTAR* upper limit provides only loose constraints above 20 keV, we were able to confirm the need for an additional component to model the excess at energies lower than 4 keV. This would be the emission from a weak hot corona or inefficient accretion flow;

- we performed a first modelization of the SED of 1146+596 with a simple synchrotron-SSC jet model, showing that also in this case a scenario where both non-thermal jet emission and corona-disk emission contribute the high-energy output is favored;

- the inferred jet powers of 1718-649 and 1146+356 are in the range $\sim 0.2 - 6 \times 10^{43}$ erg/s, suggesting for both sources an evolution as low-power FRI-type radio galaxies. Note that, according to hydrodynamical simulations, such low-power jet could actually impact the host galaxy environment, because of a prolonged action, with respect to high-power jets, on the ISM while piercing their way out of the galaxy.

In the future, new observations of the sample sources are needed. In particular, longer *NuSTAR* pointings of 1718-649 are essential to understand the nature of the

energy break at $E_{\rm break} \simeq 6.6\,{\rm keV}$, either physical or instrumental. In addition, thanks to its high effective area, deep XMM-*Newton* observations of 1146+596 would provide important constraints on the nature of the multi-temperature gas. In addition, deeper XMM-*Newton* observations of 1843+356 would help to unveil the X-ray properties of the source, in order to verify its γ-ray loud nature. As discussed for 1718-649 and 1146+596, well constrained X-ray properties are essential to fully establish the broad-band emission of the source: consequently, they are fundamental to test reasonable SED models and find clues for γ-ray emission.

Finally, CSOs are interesting targets also for the future generation of X-ray telescopes, such as the *Advanced Telescope for High Energy Astrophysics* (*Athena*[1], planned launch launch in 2034). Thanks to its unparalleled sensitivity ($A_{eff} \simeq 0.25\,{\rm m}^2$ at 6 keV), it will be possible to detect also the faintest CSOs and properly characterize the X-ray emission for most of them.

In addition, the high-energy SED of 1718-649 peaks in the MeV range, making 1718-649 an ideal target for future MeV-band missions such as *All-sky Medium Energy Gamma-ray Observatory* (AMEGO[2]), which will fill the observational gap between the current generation of hard X-ray instruments (like *NuSTAR*) and the *Fermi*/LAT, and, consequently, provide essential constrains for SED models.

[1] `https://www.the-athena-x-ray-observatory.eu`
[2] `https://asd.gsfc.nasa.gov/amego/`

Appendix A

X-ray analysis

In this appendix, I summarize the main tables and plots obtained during the X-ray analysis, that are not shown in Chapter 4, in order to make the chapter more readable.

A.1 1718-649

All data are grouped at 20 counts per bin and the χ^2 fitting statistics is adopted, except for *Chandra* ObsID. 12849 and *Swift* data for which unbinned data and Cstat statistics were used. In each table, Col(1) is the model fit, Col(2) the observation ID, Col(3) the detector, Col(4) the energy range, Col(5) the intrinsic hydrogen column density, Col(6-7) the photon index and normalization of the power law emission component, Col(8-9) the temperature and normalization of the collisionally ionized thermal plasma, Col(10) the ratio of the χ^2 fitting statistics to degrees of freedom. In `Xspec` nomenclature, models tested are

(I) phabs×po

(II) phabs×zphabs×po

(III) phabs×(zphabs×po+mekal)

All the models include Galactic hydrogen column density $N_{H,\,\mathrm{Gal}} = 5.90 \times 10^{20}\,\mathrm{cm}^{-2}$ and thermal component assumes solar abundance.
The normalizations are photons/keV/cm^2/s at 1 keV for the power law component, and $10^{-14}\,(1+z)^2\,n_e n_H V/4\pi d_L^2$, assuming uniform ionized plasma with electron and H number densities n_e and n_H, respectively, and volume V, all in cgs units.

A.1.1 *Chandra*

Table A.1: *Chandra* best-fit parameters for the X-ray emission of the point-like central source in 1718-649

Model #	ObsID	det	energy range [keV]	**zphabs** $N_H\,[\times 10^{21}\,\mathrm{cm}^{-2}]$	**po** Γ	norm $[\times 10^{-4}]$	**mekal** kT [keV]	norm $[\times 10^{-5}]$	χ^2/d.o.f.
(1)	(2)	(3)	(4)	(5)	(6)	(7)	(8)	(9)	(10)
(II)	12849	ACIS-S	$0.3-7.0$	< 2.24	$1.59^{+0.38}_{-0.34}$	$0.78^{+0.36}_{-0.23}$	—	—	$82.6/131^{\dagger}$
(II)	16070	ACIS-S	$0.3-7.0$	$1.74^{+1.11}_{-1.02}$	$1.61^{+0.18}_{-0.17}$	$1.52^{+0.36}_{-0.28}$	—	—	40.4/45
(III)	16070	ACIS-S	$0.3-7.0$	$4.01^{+3.27}_{-2.78}$	$1.75^{+0.28}_{-0.25}$	$1.87^{+0.83}_{-1.37}$	< 1.88	< 2.74	38.3/43
(II)	16623	ACIS-S	$0.3-7.0$	$2.47^{+0.51}_{-0.47}$	$1.79^{+0.11}_{-0.10}$	$2.18^{+0.26}_{-0.23}$	—	—	98.3/100
(III)	16623	ACIS-S	$0.3-7.0$	$4.32^{+1.50}_{-1.27}$	$1.92^{+0.16}_{-0.14}$	$2.64^{+0.58}_{-0.43}$	$0.48^{+0.12}_{-0.11}$	$1.61^{+0.74}_{-0.86}$	89.1/98

Notes. †Due to the small available statistics, the Cstat fitting statistics was used to fit the ungroupped data. However, best-fit parameters of model (III) remains unconstrained. The spectrum of the central point-like source was extracted from a region of radius 2.5″ centered on the source centroid.

Table A.2: *Chandra* best-fit parameters for the extended X-ray emission in 1718-649

Model	ObsID	det	energy range	**zphabs**	**po**		**mekal**		χ^2/d.o.f.
#			[keV]	N_H $[\times 10^{21}\,\mathrm{cm}^{-2}]$	Γ	norm $[\times 10^{-4}]$	kT [keV]	norm $[\times 10^{-5}]$	
(1)	(2)	(3)	(4)	(5)	(6)	(7)	(8)	(9)	(10)
(II)	12849	ACIS-S	$0.3-7.0$	< 1.64	$1.64^{+0.36}_{-0.25}$	$0.87^{+0.36}_{-0.18}$	—	—	106.9/144
(II)	16070	ACIS-S	$0.3-7.0$	$2.06^{+0.87}_{-0.79}$	$1.74^{+0.17}_{-0.16}$	$1.74^{+0.35}_{-0.27}$	—	—	47.9/49
(III)	16070	ACIS-S	$0.3-7.0$	$4.90^{+3.41}_{-2.53}$	$1.89^{+0.29}_{-0.25}$	$2.17^{+1.02}_{-0.60}$	$0.81^{+0.23}_{-0.17}$	$2.37^{+1.32}_{-1.43}$	40.2/47
(II)	16623	ACIS-S	$0.3-7.0$	$2.02^{+1.02}_{-0.43}$	$1.83^{+0.10}_{-0.10}$	$2.20^{+0.25}_{-0.22}$	—	—	110.8/115
(III)	16623	ACIS-S	$0.3-7.0$	$4.03^{+1.54}_{-1.27}$	$1.96^{+0.16}_{-0.15}$	$2.69^{+0.60}_{-0.44}$	$0.49^{+0.10}_{-0.10}$	$2.14^{+0.86}_{-0.99}$	97.6/113

Notes. [†]Due to the small available statistics, the Cstat fitting statistics was used to fit the ungroupped data. However, best-fit parameters of model (III) remains unconstrained. The spectrum for the extended X-ray emission of the source was extracted from a region of radius 15″ centered on the source centroid.

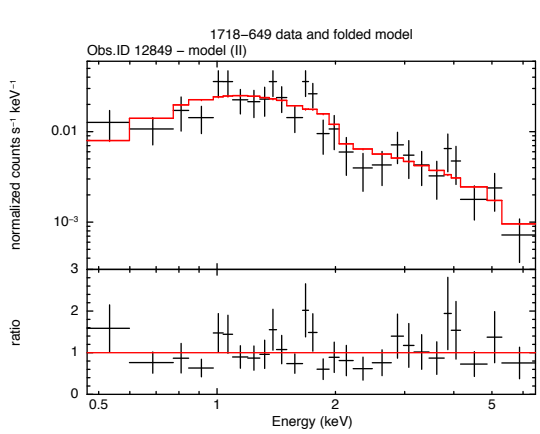

(a) Cstat/d.o.f. = 82.6/131

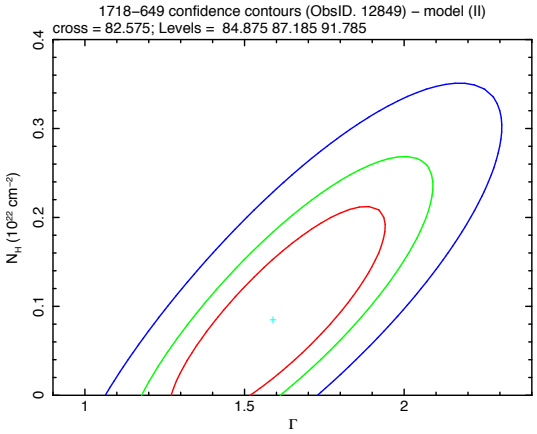

(b)

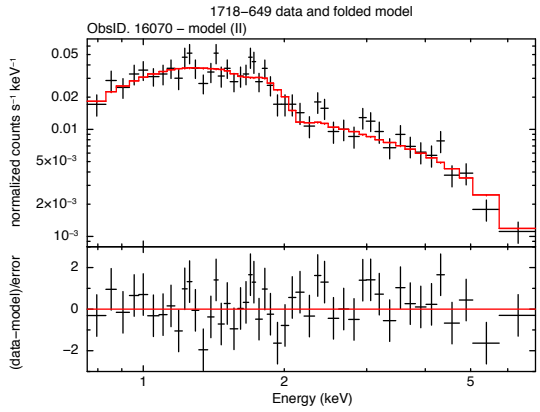

(c) $\chi^2/d.o.f. = 40.4/4$

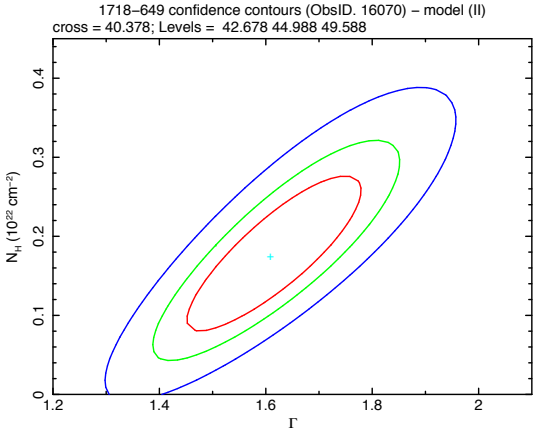

(d)

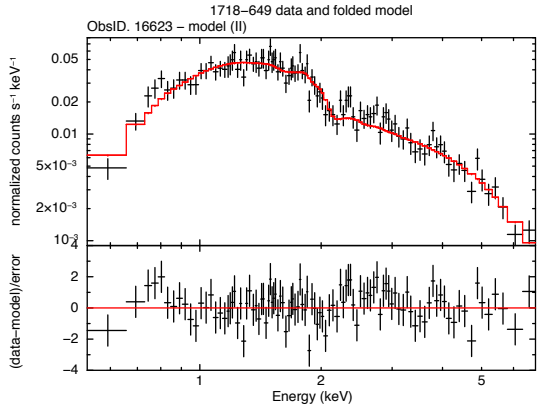

(e) $\chi^2/d.o.f. = 98.3/100$

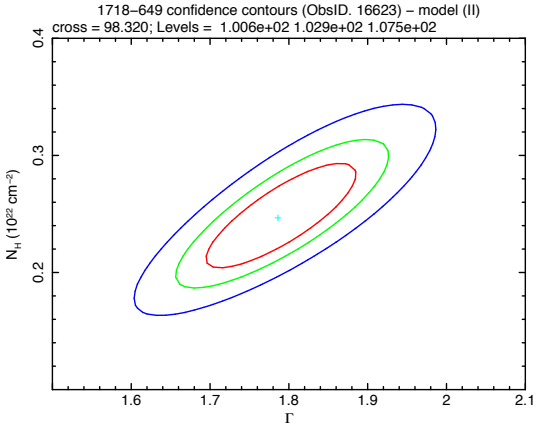

(f)

Figure A.1: 1718-649. For each *Chandra*/ACIS observation, *left panels* show the spectrum fitted with model II in the $0.3 - 7.0$ keV energy range, whereas *right panels* show the confidence contours of 1σ in red, 2σ in green, and 3σ in blue on the two degenerate parameters (N_H and Γ). The cross in cyan represents the values of the best-fit parameters. Spectra are extracted from a circular region of radius $2.5''$ centered on the source centroid. To make spectra clearer, data are also graphically rebinned.

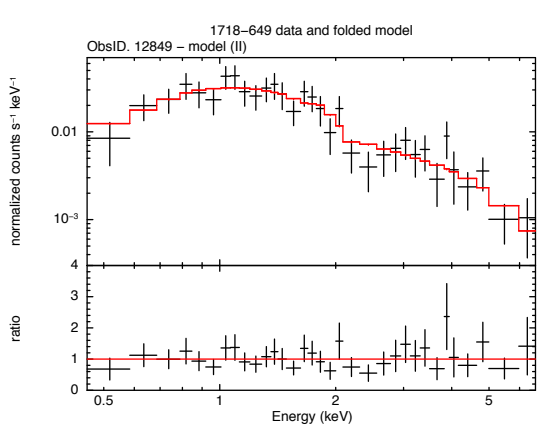

(a) Cstat/d.o.f. = 106.9/144

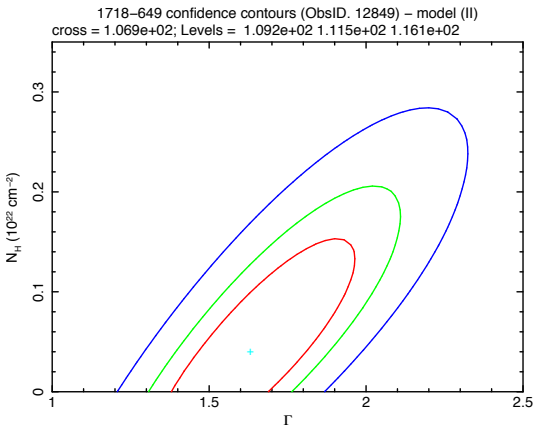

(b)

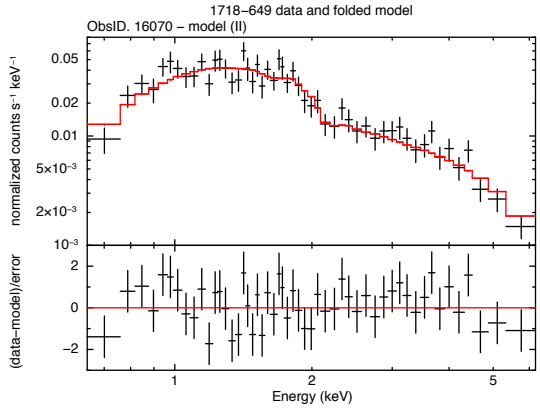

(c) $\chi^2/d.o.f. = 47.9/49$

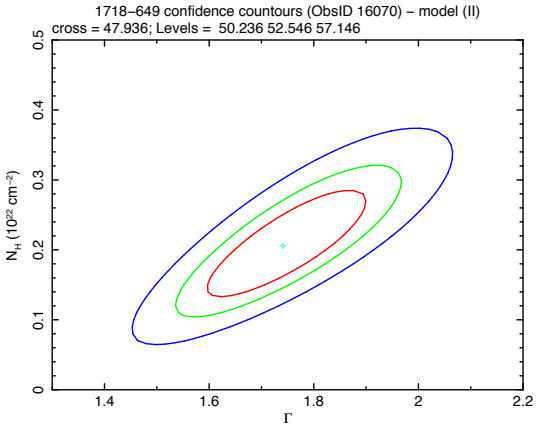

(d)

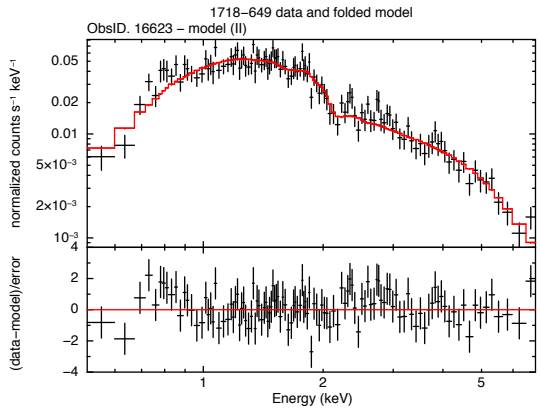

(e) $\chi^2/d.o.f. = 110.8/115$

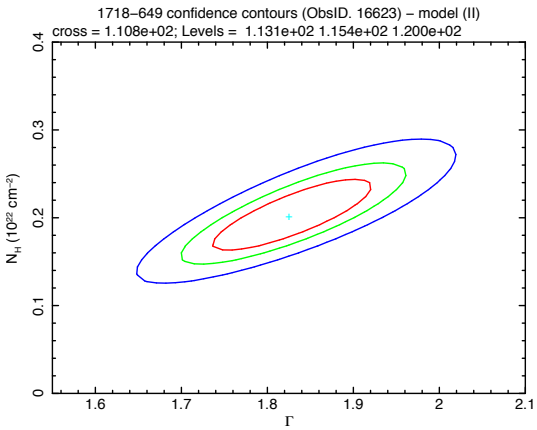

(f)

Figure A.2: 1718-649. For each *Chandra*/ACIS-S observation, *left panels* show the spectrum fitted with model II in the $0.3 - 7.0$ keV energy range, whereas *right panels* show the confidence contours of 1σ in red, 2σ in green, and 3σ in blue on the two degenerate parameters (N_H and Γ). The cross in cyan represents the values of the best-fit parameters. Spectra are extracted from a circular region of radius $15''$ centered on the source centroid. o make spectra clearer, data are also graphically rebinned.

A.1.2 XMM-*Newton*

For all observations, the source spectrum was extracted from a region of radius 25″ centered on the source, with the exception of MOS spectra from ObsID. 0784530201: in this case a region of radius 20″ centered on the source was chosen in order to maximize the SNR. The XMM-*Newton*/pn best-fit parameters are also shown for comparison.

Table A.3: 1718-649 XMM-*Newton* best-fit parameters

Model	ObsID	det	energy range	**zphabs**	**po**		**mekal**		χ^2/d.o.f.
#			[keV]	N_H $[\times 10^{21}\,\mathrm{cm}^{-2}]$	Γ	norm $[\times 10^{-4}]$	kT [keV]	norm $[\times 10^{-5}]$	
(1)	(2)	(3)	(4)	(5)	(6)	(7)	(8)	(9)	(10)
(II)	0784530201	pn	$0.3-9.5$	$0.82^{+0.30}_{-0.28}$	$1.80^{+0.12}_{-0.11}$	$1.06^{+0.12}_{-0.11}$	—	—	117.3/94
		MOS1	$0.3-10.0$	< 0.75	$1.44^{+0.18}_{-0.12}$	$0.74^{+0.15}_{-0.09}$	—	—	32.4/30
		MOS2	$0.3-10.0$	< 0.98	$1.61^{+0.17}_{-0.16}$	$0.93^{+0.17}_{-0.14}$	—	—	59.4/43
(III)	0784530201	pn	$0.3-9.5$	$0.67^{+0.38}_{-0.35}$	$1.61^{+0.13}_{-0.13}$	$0.83^{+0.13}_{-0.11}$	$0.83^{+0.19}_{-0.13}$	$1.71^{+0.55}_{-0.55}$	87.8/92
		MOS1	$0.3-10.0$	< 4.27	$1.36^{+0.25}_{-0.20}$	$0.68^{+0.28}_{-0.15}$	$0.59^{+0.16}_{-0.14}$	$1.82^{+1.19}_{-0.88}$	19.8/28
		MOS2	$0.3-10.0$	< 2.11	$1.52^{+0.20}_{-0.19}$	$0.83^{+0.20}_{-0.16}$	$0.65^{+0.23}_{-0.31}$	$1.56^{+0.83}_{-0.78}$	48.2/41
(II)	0804520301	pn	$0.3-8.5$	$0.92^{+0.23}_{-0.22}$	$1.85^{+0.09}_{-0.09}$	$1.02^{+0.09}_{-0.08}$	—	—	173.9/169
		MOS1	$0.3-8.5$	$0.40^{+0.37}_{-0.34}$	$1.73^{+0.13}_{-0.12}$	$0.93^{+0.12}_{-0.11}$	—	—	74.3/67
		MOS2	$0.3-10.0$	$0.79^{+0.42}_{-0.39}$	$1.78^{+0.14}_{-0.13}$	$1.02^{+0.15}_{-0.13}$	—	—	77.1/66
(III)	0804520301	pn	$0.3-8.5$	$0.88^{+0.28}_{-0.26}$	$1.72^{+0.10}_{-0.10}$	$0.88^{+0.10}_{-0.09}$	$0.66^{+0.18}_{-0.11}$	$0.93^{+0.29}_{-0.30}$	146.6/167
		MOS1	$0.3-8.5$	$0.52^{+0.57}_{-0.43}$	$1.64^{+0.15}_{-0.14}$	$0.83^{+0.17}_{-0.12}$	$0.60^{0.22}_{-0.33}$	$1.03^{+0.54}_{-0.53}$	64.0/65
		MOS2	$0.3-10.0$	$1.06^{+0.77}_{-0.62}$	$1.65^{+0.16}_{-0.15}$	$0.87^{+0.16}_{-0.14}$	$0.68^{+0.18}_{-0.10}$	$1.61^{+0.60}_{-0.58}$	55.9/64

Continues in the next page

Continues from the previous page

Model #	ObsID	det	energy range	**zphabs**	**po**		**mekal**		χ^2/d.o.f.
			[keV]	N_H $[\times 10^{21}\,\mathrm{cm}^{-2}]$	Γ	norm $[\times 10^{-4}]$	kT [keV]	norm $[\times 10^{-5}]$	
(1)	(2)	(3)	(4)	(5)	(6)	(7)	(8)	(9)	(10)
(II)	0845110101	pn	$0.35-8.5$	$0.86^{+0.11}_{-0.11}$	$1.87^{+0.04}_{-0.04}$	$1.05^{+0.04}_{-0.04}$	—	—	666.6/482
		MOS1	$0.3-8.5$	$0.87^{+0.22}_{-0.21}$	$1.84^{+0.08}_{-0.07}$	$1.09^{+0.08}_{-0.07}$	—	—	186.9/170
		MOS2	$0.3-8.0$	$0.82^{+0.22}_{-0.21}$	$1.86^{+0.08}_{-0.07}$	$1.11^{+0.08}_{-0.08}$	—	—	210.1/169
(III)	0845110101	pn	$0.35-8.5$	$0.89^{+0.15}_{-0.14}$	$1.73^{+0.05}_{-0.05}$	$0.88^{+0.05}_{-0.05}$	$0.60^{+0.04}_{-0.05}$	$1.25^{+0.16}_{-0.16}$	477.7/480
		MOS1	$0.3-8.5$	$1.06^{+0.31}_{-0.28}$	$1.76^{+0.08}_{-0.08}$	$1.00^{+0.09}_{-0.08}$	$0.60^{+0.09}_{-0.11}$	$1.02^{+0.31}_{-0.31}$	156.3/168
		MOS2	$0.3-8.0$	$1.03^{+0.32}_{-0.29}$	$1.77^{+0.08}_{-0.08}$	$1.00^{+0.09}_{0.08}$	$0.59^{+0.08}_{-0.11}$	$1.17^{+0.32}_{-0.32}$	171.2/167

Ends from the previous page

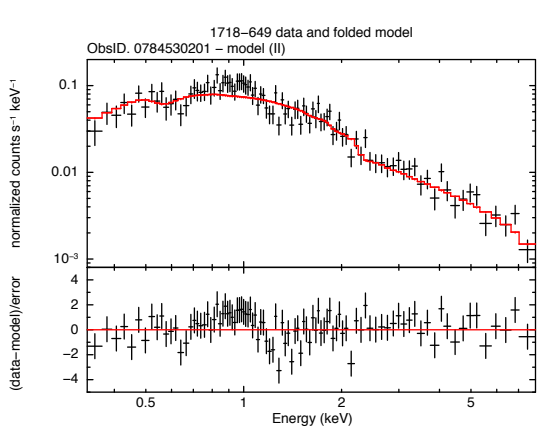

(a) χ^2/d.o.f. = 117.3/94

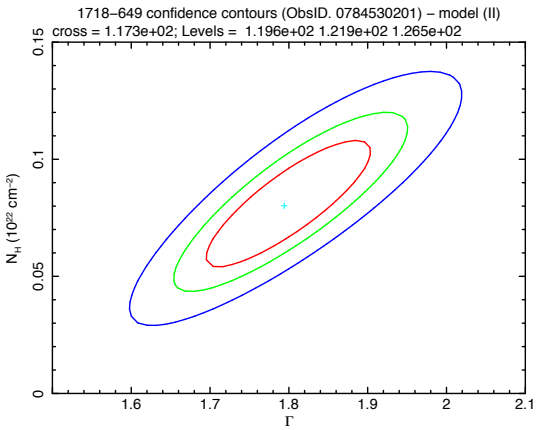

(b)

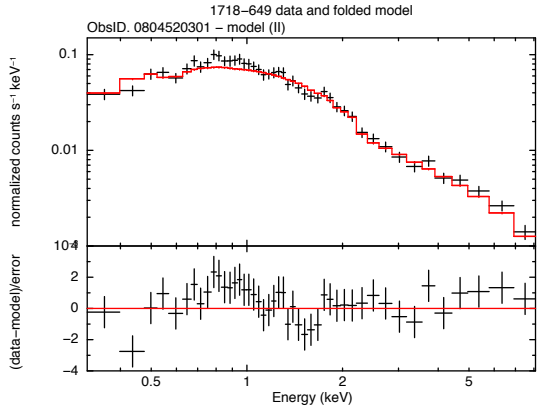

(c) χ^2/d.o.f. = 173.9/169

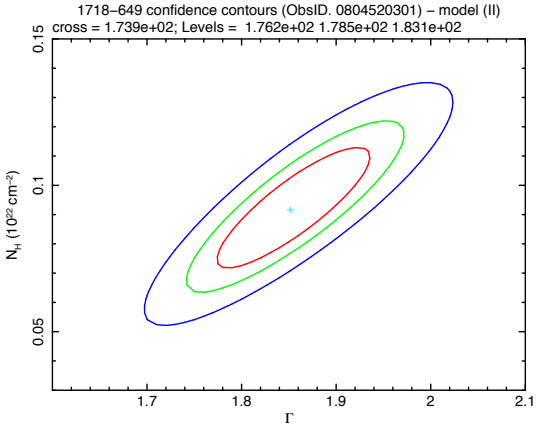

(d)

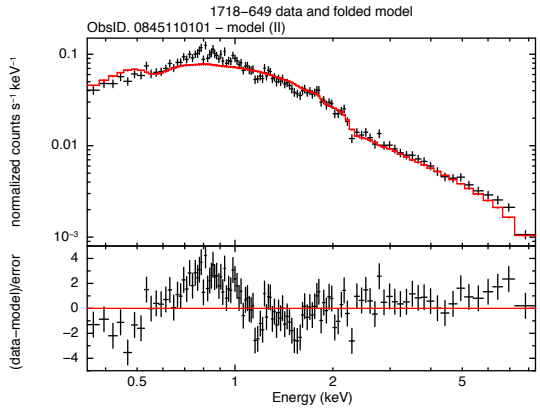

(e) χ^2/d.o.f. = 666.6/482

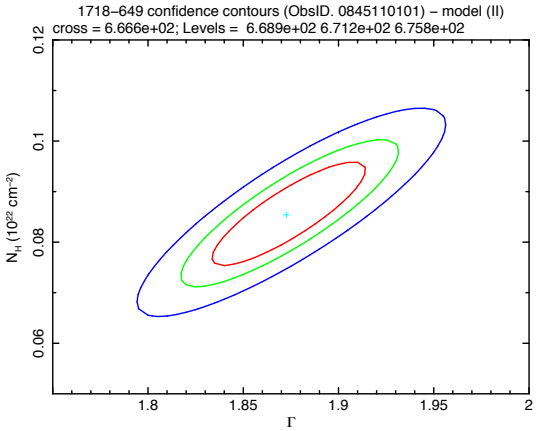

(f)

Figure A.3: 1718-649. For each XMM-*Newton*/pn observation, *left panels* show the spectrum fitted with model II in the energy ranges listed in Table A.3, whereas *right panels* show the confidence contours of 1σ in red, 2σ in green, and 3σ in blue on the two degenerate parameters (N_H and Γ). The cross in cyan represents the values of the best-fit parameters. To make spectra clearer, data are also graphically rebinned.

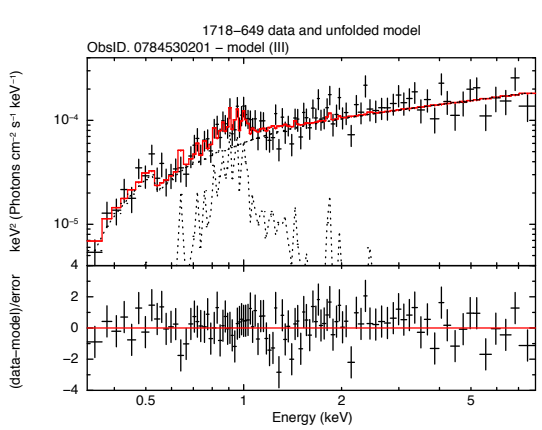

(a) χ^2/d.o.f. = 87.8/92

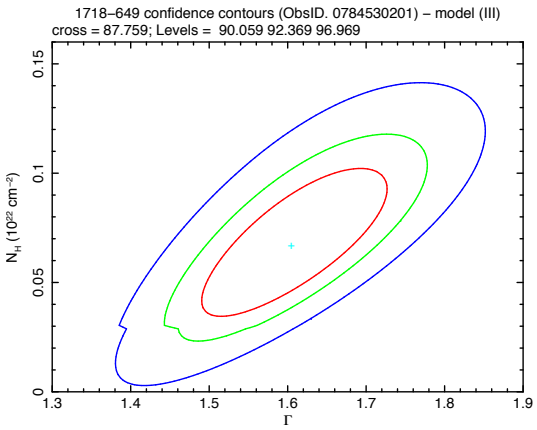

(b)

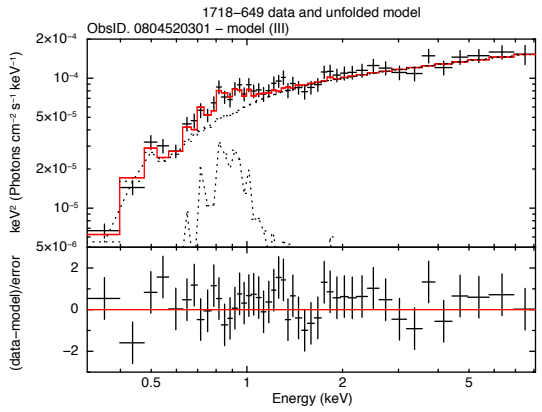

(c) χ^2/d.o.f. = 146.6/167

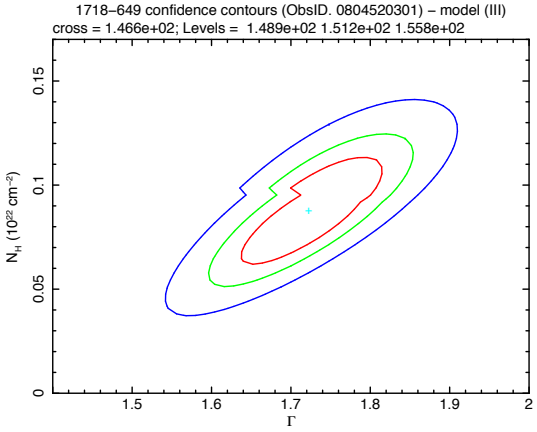

(d)

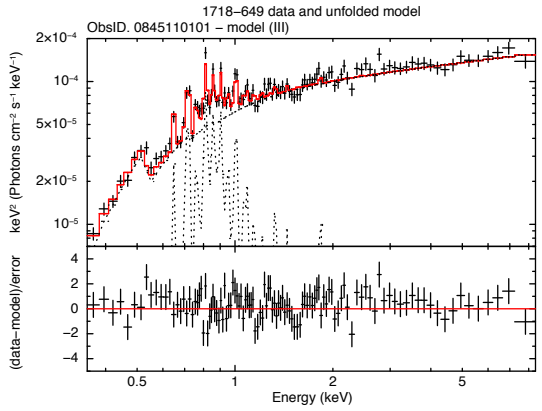

(e) χ^2/d.o.f. = 477.7/480

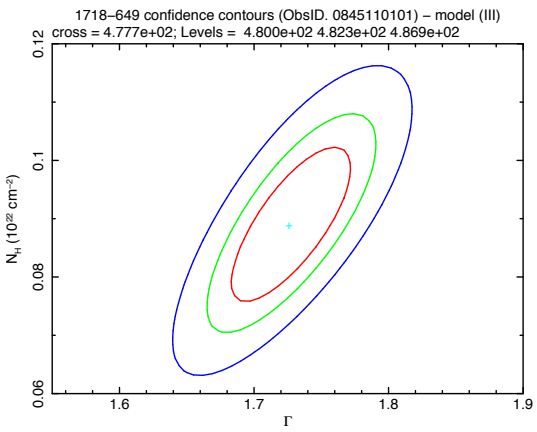

(f)

Figure A.4: 1718-649. For each XMM-*Newton*/pn observation, *left panels* show the spectrum fitted with model III in the energy ranges listed in Table A.3, whereas *right panels* show the confidence contours of 1σ in red, 2σ in green, and 3σ in blue on the two degenerate parameters (N_H and Γ). The cross in cyan represents the values of the best-fit parameters. To make spectra clearer, data are also graphically rebinned.

A.1.3 *NuSTAR*

For both instruments on-board *NuSTAR*, the source spectrum was extracted from a circular region of radius 30″ centered on the source.

Table A.4: 1718-649 *NuSTAR* best-fit parameters

Model #	ObsID	det	energy range [keV]	**zphabs** N_H $[\times 10^{21}\,\mathrm{cm}^{-2}]$	**po** Γ	norm $[\times 10^{-4}]$	**mekal** kT [keV]	norm $[\times 10^{-5}]$	χ^2/d.o.f.
(1)	(2)	(3)	(4)	(5)	(6)	(7)	(8)	(9)	(10)
(I)	60601020002	FPMA	$3.0-19.0$	—	$2.28^{+0.24}_{-0.23}$	$2.96^{+1.59}_{-1.06}$	—	—	11.9/17
		FPMB	$3.0-19.0$	—	$1.86^{+0.24}_{-0.24}$	$1.51^{+0.88}_{-0.57}$	—	—	7.6/18
(I)	60601020002_sim	FPMA	$3.0-19.0$	—	$2.08^{+0.17}_{-0.17}$	$2.06^{+0.82}_{-0.60}$	—	—	23.6/36
		FPMB	$3.0-19.0$	—	″	$2.27^{+0.84}_{-0.63}$	—	—	″

A.1.4 *Swift*

Table A.5: 1718-649 *Swift* best-fit parameters

Model #	ObsID	det	energy range [keV]	**zphabs** N_H $[\times 10^{21}\,\mathrm{cm}^{-2}]$	**po** Γ	norm $[\times 10^{-4}]$	**mekal** kT [keV]	norm $[\times 10^{-5}]$	Cstat/d.o.f.
(1)	(2)	(3)	(4)	(5)	(6)	(7)	(8)	(9)	(10)
(II)	00031815001	XRT	$0.3-6.5$	$3.95^{+4.10}_{-2.86}$	$2.50^{+0.96}_{-0.81}$	$2.48^{+3.68}_{-1.36}$	—	—	45.4/49
(II)	00031815004	XRT	$0.3-9.0$	< 1.98	$1.47^{+0.28}_{-0.26}$	$1.09^{+0.39}_{-0.28}$	—	—	123.3/195
(II)	00089109001	XRT	$0.3-9.5$	< 4.15	$1.58^{+0.70}_{-0.53}$	$1.03^{+1.15}_{-0.45}$	—	—	41.9/52

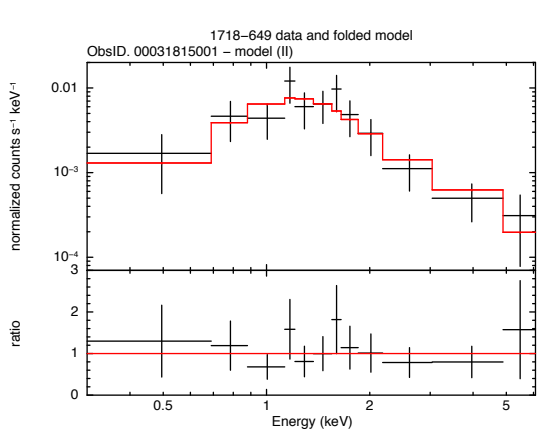

(a) Cstat/d.o.f. = 45.4/49

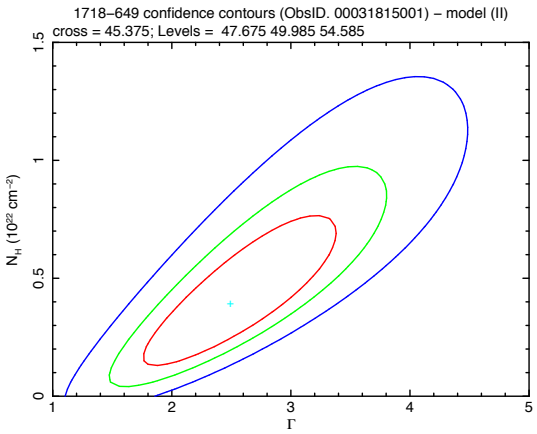

(b)

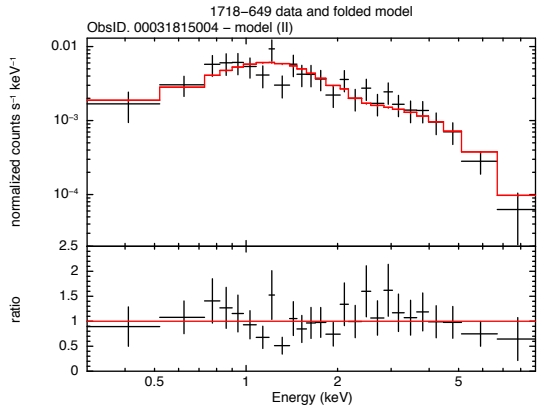

(c) Cstat/d.o.f. = 123.3/195

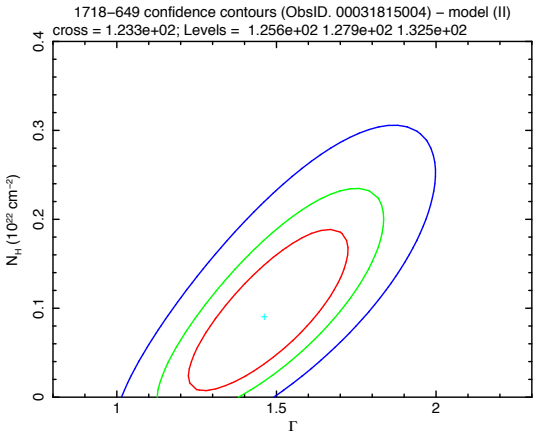

(d)

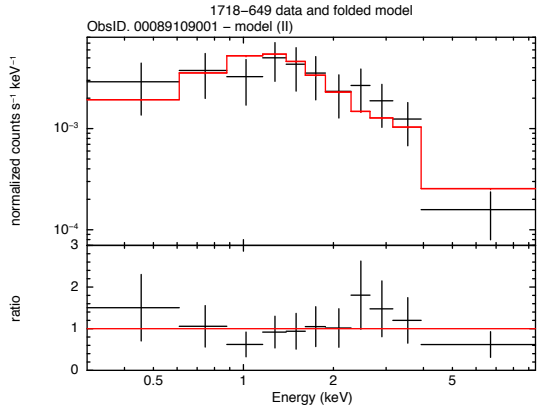

(e) Cstat/d.o.f. = 40.4/52

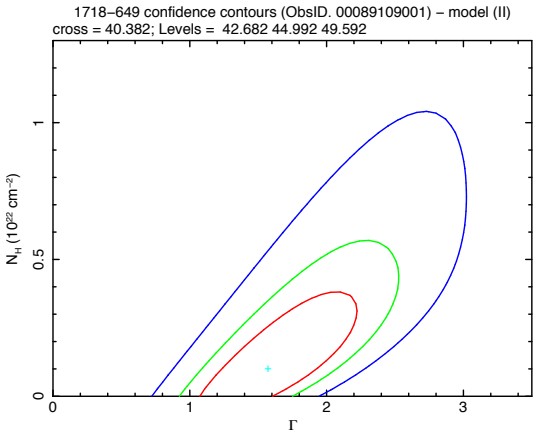

(f)

Figure A.5: 1718-649. For each *Swift*/XRT observation, *left panels* show the spectrum fitted with model II in the energy ranges listed in Table A.5, whereas *right panels* show the confidence contours of 1σ in red, 2σ in green, and 3σ in blue on the two degenerate parameters (N_H and Γ). The cross in cyan represents the values of the best-fit parameters. To make spectra clearer, data are also graphically rebinned.

A.2 1146+596

All data are grouped at 15 counts per bin and the χ^2 fitting statistics is adopted. In the table, Col(1) is the model fit, Col(2) the observation ID, Col(3) the detector, COl(4) the radius of the circular region used to extract the source spectrum, Col(5) the intrinsic hydrogen column density, Col(6-7) the photon index and normalization of the power law emission component, Col(8-9) the central energy and the normalization of the Gaussian component, Col(10-11) the temperature and normalization of the cold collisionally ionized thermal plasma, Col(12-13) the ones of the hot one, Col(14) the ratio of the χ^2 fitting statistics to degrees of freedom. In `Xspec` nomenclature, models tested are

(I) phabs×po

(II) phabs×zphabs×po

(IV) phabs×(zphabs×po+apec)

(V) phabs×(zphabs×(po+zgauss)+apec)

(VI) phabs×(zphabs×(po+zgauss)+apec+apec)

(VII) phabs×(zphabs×(po+zgauss)+apec+apec)

All the models include Galactic hydrogen column density $N_{H,\mathrm{Gal}} = 1.86 \times 10^{20}\,\mathrm{cm}^{-2}$ and thermal components assumes solar abundance.
The normalizations are photons/keV/cm^2/s at 1 keV for the power law components, $10^{-14}\,(1+z)^2\,n_e n_H V/4\pi d_L^2$, assuming uniform ionized plasma with electron and H number densities n_e and n_H, respectively, and volume V, all in cgs units, for the thermal component, and total number of photons/cm^2/s in the line, for the Gaussian component.

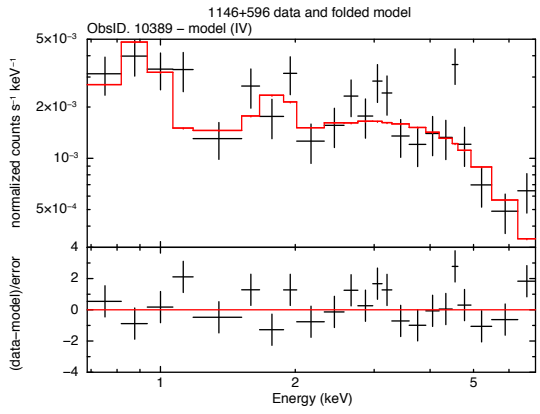

(a) χ^2/d.o.f. = 31.6/18

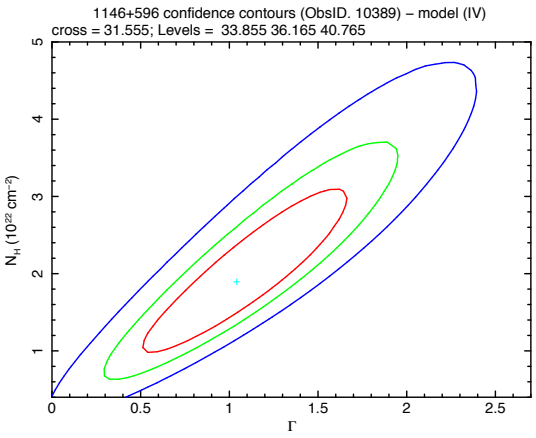

(b)

Table A.6: 1146+596 *Chandra*/ACIS-S and *NuSTAR* best-fit parameters

Model	ObsID	Det	Ext. Reg.	**zphabs**	**po**		**zgauss**		**apec**		**apec**		χ^2/d.o.f.
			[arcsec]	$N_H\left[\times10^{22}\,\mathrm{cm}^{-2}\right]$	Γ	norm $\left[\times10^{-5}\right]$	E_ℓ	norm $\left[\times10^{-6}\right]$	kT [keV]	norm $\left[\times10^{-6}\right]$	kT [keV]	norm $\left[\times10^{-6}\right]$	
(1)	(2)	(3)	(4)	(5)	(6)	(7)	(8)	(9)	(10)	(11)	(12)	(13)	(14)
(IV)	10389	ACIS-S	2.5	$1.90^{+1.32}_{-1.00}$	$1.05^{+0.67}_{-0.59}$	$1.88^{+3.37}_{-1.12}$	—	—	$0.84^{+0.17}_{-0.16}$	$2.70^{+0.82}_{-0.69}$	—	—	31.6/18
(IV)	10389	ACIS-S	2.5	$3.04^{+0.68}_{-0.55}$	1.70 (frozen)	$5.02^{+0.82}_{-0.76}$	—	—	$0.88^{+0.17}_{-0.15}$	$2.90^{+0.80}_{-0.70}$	—	—	34.1/19
(V)	10389	ACIS-S	2.5	$2.93^{+0.67}_{-0.56}$	1.70 (frozen)	$4.81^{+0.84}_{-0.78}$	$6.42^{+0.69}_{-0.09}$	$1.86^{+1.60}_{-1.37}$	$0.88^{+0.16}_{-0.15}$	$2.88^{+0.79}_{-0.70}$	—	—	28.6/17
(V)	10389	ACIS-S	10	$2.70^{+0.74}_{-0.52}$	1.70 (frozen)	$4.99^{+0.77}_{-0.76}$	$6.52^{+3.75}_{-0.99}$	$1.50^{+0.98}_{-0.11}$	$0.84^{+0.11}_{-0.13}$	$5.97^{+1.05}_{-0.94}$	—	—	36.8/27
(VI)	10389	ACIS-S	10	$2.93^{+0.77}_{-0.63}$	1.70 (frozen)	$5.17^{+0.82}_{-0.83}$	$6.54^{+0.46}_{-1.66}$	$1.49^{+1.65}_{-1.15}$	$0.31^{+0.16}_{-0.09}$	$6.13^{+2.70}_{-2.47}$	$1.12^{+0.25}_{-0.17}$	$5.18^{+2.30}_{-1.70}$	19.6/25
(I)	60601019002	FPMA	30	—	$1.83^{+0.37}_{-0.36}$	$5.98^{+5.93}_{-3.13}$	—	—	—	—	—	—	12.2/14
(I)	60601019002	FPMB	30	—	$2.01^{0.41}_{-0.41}$	$7.59^{+8.56}_{-4.25}$	—	—	—	—	—	—	14.8/12
(I)	60601019002_sim	FPMA	30	—	$1.91^{+0.27}_{-0.27}$	$6.97^{+4.69}_{-2.92}$	—	—	—	—	—	—	27.3/27
(I)	60601019002_sim	FPMB	30	—	"	"	—	—	—	—	—	—	"

Notes. (1) model fit, (2) observation ID, (3) detector name, (4) radius of the circular region used to extract the source spectrum, (5) the intrinsic hydrogen column density, (6-7) the photon index and normalization of the power law emission component, (8-9) the central energy and the normalization of the Gaussian component, (10-11) the temperature and normalization of the cold collisionally ionized thermal plasma, (12-13) those of the hot one, (14) the ratio of the χ^2 fitting statistics to degrees of freedom. *Chandra* data are fitted in the $0.3-7\,\mathrm{keV}$ energy range, whereas the *NuSTAR* one are in the $3-19\,\mathrm{keV}$. The model includes Galactic hydrogen column density $N_{H,\mathrm{Gal}} = 1.86\times10^{20}\,\mathrm{cm}^{-2}$ and thermal component assumes solar abundance. The normalizations are photons/keV/cm^2/s at 1 keV, for the power law component, $10^{-14}\,(1+z)^2\,n_e n_H V/4\pi d_L^2$, assuming uniform ionized plasma with electron and H number densities n_e and n_H, respectively, and volume V, all in cgs units, for the thermal component, and total number of photons/cm^2/s in the line, for the Gaussian component.

List of Constants and Units

Here I report the main physical constants and units used throughout this work. Values are listed in the metre-kilogram-second (mks) International System of Units (abbreviated SI, from the French *Système International*), even if the Gaussian System of Units (centimeter-gram-second, or cgs) is the commonly used in astrophysics. When applicable, standard error of the last digits are given in parentheses.

Name	Symbol	Value (mks)
Radian	1 rad	$180^\circ/\pi$
		57.2957795°
		$206264.80625''$
Degree	1°	0.01745329 radian
Arc second	$1''$	0.000004848 rad
Speed of light in vacuum	c	$2.99792458 \times 10^8\,\mathrm{m/s}$
Gravitational constant	G	$6.67408(31) \times 10^{-11}\,\mathrm{m^3/kg/s^2}$
Boltzmann constant	k	$1.380064852(79) \times 10^{-23}\,\mathrm{J/K}$
Planck constant	h	$6.626070040(81) \times 10^{-34}\,\mathrm{J\,s}$
Electron charge	e	$1.6022 \times 10^{-19}\,\mathrm{C}$
Electron mass	m_e	$9.10938356(11) \times 10^{-31}\,\mathrm{kg}$
		0.511 MeV
Proton mass	m_p	$1.672621898(21) \times 10^{-27}\,\mathrm{kg}$
		938.3 MeV
Thomson cross section	σ_T	$6.6524587158(91) \times 10^{-29}\,\mathrm{m^2}$
Solar mass	$\mathcal{M}_\odot$	$1.9891 \times 10^{30}\,\mathrm{kg}$
Electron volt	eV	$1.6021766208(98) \times 10^{-19}\,\mathrm{J}$
Jansky	Jy	$10^{-23}\,\mathrm{W/Hz/m^2}$
Parsec	pc	$3.0856776 \times 10^{16}\,\mathrm{m}$

Notes. Partially adapted from Cimatti, Fraternali, and Nipoti 2019.

Bibliography

Abdollahi, S. et al. (Mar. 2020). "Fermi Large Area Telescope Fourth Source Catalog". In: *Astrophysical Journal, Supplement* 247.1, 33, p. 33.

Aharonian, F. A. (Nov. 2000). "TeV gamma rays from BL Lac objects due to synchrotron radiation of extremely high energy protons". In: *New Astronomy* 5.7, pp. 377–395.

An, T. and W. A. Baan (Nov. 2012). "THE DYNAMIC EVOLUTION OF YOUNG EXTRAGALACTIC RADIO SOURCES". In: *The Astrophysical Journal* 760.1, p. 77.

Angioni, R. et al. (July 2019). "Gamma-ray emission in radio galaxies under the VLBI scope. I. Parsec-scale jet kinematics and high-energy properties of γ-ray-detected TANAMI radio galaxies". In: *Astronomy and Astrophysics* 627, A148, A148.

Antonucci, R. (1993). "Unified Models for Active Galactic Nuclei and Quasars". In: *Annual Review of Astronomy and Astrophysics* 31.1, pp. 473–521.

Arnaud, K. A. (Jan. 1996). "XSPEC: The First Ten Years". In: *Astronomical Data Analysis Software and Systems V*. Ed. by G. H. Jacoby and J. Barnes. Vol. 101. Astronomical Society of the Pacific Conference Series, p. 17.

Avni, Y. (Dec. 1976). "Energy spectra of X-ray clusters of galaxies." In: *Astrophysical Journal* 210, pp. 642–646.

Balasubramaniam, K. et al. (Nov. 2021). "X-Ray Emission of the γ-ray-loud Young Radio Galaxy NGC 3894". In: *The Astrophysical Journal* 922.1, p. 84. ISSN: 1538-4357.

Ballet, J. (Jan. 2003). "Pile-up on X-ray CCD instruments". In: *Advances in Space Research* 32.10, pp. 2077–2082.

Beck, R. and M. Krause (July 2005). "Revised equipartition and minimum energy formula for magnetic field strength estimates from radio synchrotron observations". In: *Astronomische Nachrichten* 326.6, pp. 414–427.

Beckmann, V. and C. R. Shrader (2012). *Active Galactic Nuclei*.

Beuchert, T. et al. (Apr. 2018). "Extended X-ray emission in PKS 1718-649". In: *Astronomy & Astrophysics* 612, p. L4. ISSN: 1432-0746.

Bicknell, G. V. and R. S. Sutherland (Mar. 2006). "Evolutionary models of powerful radio galaxies". In: *Astronomische Nachrichten* 327, pp. 235–240.

Bicknell, G. V. et al. (Jan. 2018). "Relativistic jet feedback – II. Relationship to gigahertz peak spectrum and compact steep spectrum radio galaxies". In: *Monthly Notices of the Royal Astronomical Society* 475.3, pp. 3493–3501. ISSN: 1365-2966.

Bicknell, G. V., M. A. Dopita, and C. P. O. O'Dea (Aug. 1997). "Unification of the Radio and Optical Properties of Gigahertz Peak Spectrum and Compact Steep-Spectrum Radio Sources". In: *Astrophysical Journal* 485.1, pp. 112–124.

Bicknell, G. V., C. J. Saxton, and R. S. Sutherland (Jan. 2003). "GPS and CSS Sources - Theory and Modelling". In: *Publications of the Astron. Soc. of Australia* 20.1, pp. 102–109.

Binney, J. and S. Tremaine (2008). *Galactic Dynamics: Second Edition*.

Blandford, R. D. and D. G. Payne (June 1982). "Hydromagnetic flows from accretion disks and the production of radio jets." In: *Monthly Notices of the RAS* 199, pp. 883–903.

Blandford, R. D. and R. L. Znajek (May 1977). "Electromagnetic extraction of energy from Kerr black holes." In: *Monthly Notices of the RAS* 179, pp. 433–456.

Boissay, Rozenn, Ricci, Claudio, and Paltani, Stéphane (2016). "A hard X-ray view of the soft excess in AGN". In: *A&A* 588, A70.

Böttcher, M. et al. (Apr. 2013). "LEPTONIC AND HADRONIC MODELING OFFERMI-DETECTED BLAZARS". In: *The Astrophysical Journal* 768.1, p. 54. ISSN: 1538-4357.

Burlon, D. et al. (Feb. 2011). "Three-year Swift-BAT Survey of Active Galactic Nuclei: Reconciling Theory and Observations?" In: *Astrophysical Journal* 728.1, p. 58.

Buttiglione, S. et al. (Jan. 2010). "An optical spectroscopic survey of the 3CR sample of radio galaxies with z< 0.3". In: *Astronomy and Astrophysics* 509, A6. ISSN: 1432-0746.

Cackett, E. M. et al. (Jan. 2014). "Modelling the broad Fe K_α reverberation in the AGN NGC 4151". In: *Monthly Notices of the Royal Astronomical Society* 438.4, pp. 2980–2994. ISSN: 0035-8711.

Callingham, J. R. et al. (Aug. 2015). "BROADBAND SPECTRAL MODELING OF THE EXTREME GIGAHERTZ-PEAKED SPECTRUM RADIO SOURCE PKS B0008-421". In: *The Astrophysical Journal* 809.2, p. 168. ISSN: 1538-4357.

Cappelluti, N. et al. (Feb. 2018). "Searching for the 3.5 keV Line in the Deep Fields with Chandra: The 10 Ms Observations". In: *Astrophysical Journal* 854.2, 179, p. 179.

Carter, C. et al. (Jan. 2003). "ChaRT: The Chandra Ray Tracer". In: *Astronomical Data Analysis Software and Systems XII*. Ed. by H. E. Payne, R. I. Jedrzejewski, and R. N. Hook. Vol. 295. Astronomical Society of the Pacific Conference Series, p. 477.

Carvalho, J. C. (Dec. 1994). "The age of GHz-peaked-spectrum radio sources." In: *Astronomy and Astrophysics* 292, pp. 392–394.

Carvalho, J. C. (Jan. 1998). "The evolution of GHz-peaked-spectrum radio sources". In: *Astronomy and Astrophysics* 329, pp. 845–852.

Cash, W. (Mar. 1979). "Parameter estimation in astronomy through application of the likelihood ratio." In: *The Astrophysical Journal* 228, pp. 939–947.

Celotti, A. and G. Ghisellini (Mar. 2008). "The power of blazar jets". In: *Monthly Notices of the RAS* 385.1, pp. 283–300.

Cimatti, A., F. Fraternali, and C. Nipoti (2019). *Introduction to Galaxy Formation and Evolution: From Primordial Gas to Present-Day Galaxies*. Cambridge University Press. ISBN: 9781107134768.

Condon, J. J. and J. J. Broderick (July 1988). "Radio Identification of UGC Galaxies: Starbursts and Monsters". In: *Astronomical Journal* 96, p. 30.

Crummy, J. et al. (Feb. 2006). "An explanation for the soft X-ray excess in active galactic nuclei". In: *Monthly Notices of the Royal Astronomical Society* 365.4, pp. 1067–1081. ISSN: 0035-8711.

Cutri, R. M. et al. (2003). *2MASS All Sky Catalog of point sources.*

Czerny, B. et al. (May 2009). "ACCRETION DISK MODEL OF SHORT-TIMESCALE INTERMITTENT ACTIVITY IN YOUNG RADIO SOURCES". In: *The Astrophysical Journal* 698.1, pp. 840–851. ISSN: 1538-4357.

Dallacasa, D. et al. (Nov. 2000). "High frequency peakers. I. The bright sample". In: *Astronomy and Astrophysics* 363, pp. 887–900.

Davis, J. E. et al. (2012). "Raytracing with MARX: x-ray observatory design, calibration, and support". In: *Space Telescopes and Instrumentation 2012: Ultraviolet to Gamma Ray*. Ed. by T. Takahashi, S. S. Murray, and J.-W. A. den Herder. Vol. 8443. International Society for Optics and Photonics. SPIE, pp. 375–386.

Davis, S. W. and A. Tchekhovskoy (Aug. 2020). "Magnetohydrodynamics Simulations of Active Galactic Nucleus Disks and Jets". In: *Annual Review of Astronomy and Astrophysics* 58.1, pp. 407–439. ISSN: 1545-4282.

de Kool, M. and M. C. Begelman (Oct. 1989). "Effects of Thermal Plasma on Self-absorbed Synchrotron Sources in Active Galactic Nuclei". In: *Astrophysical Journal* 345, p. 135.

De Marco, B. et al. (Oct. 2011). "PG 1211+143: probing high-frequency lags in a high-mass active galactic nucleus". In: *Monthly Notices of the Royal Astronomical Society: Letters* 417.1, pp. L98–L102. ISSN: 1745-3925.

de Vaucouleurs, G. et al. (1991). *Third Reference Catalogue of Bright Galaxies*.

de Vries, W. H., P. D. Barthel, and C. P. O'Dea (May 1997). "Radio spectra of Gigahertz Peaked Spectrum radio sources." In: *Astronomy and Astrophysics* 321, pp. 105–110.

De Young, D. S. (Apr. 1991). "The Deflection of Cosmic Jets". In: *Astrophysical Journal* 371, p. 69.

— (Jan. 1993). "The Evolution of Compact Steep Spectrum Sources". In: *Astrophysical Journal* 402, p. 95.

Dicken, D. et al. (Jan. 2012). "SPITZERMID-IR SPECTROSCOPY OF POWERFUL 2 JY AND 3CRR RADIO GALAXIES. I. EVIDENCE AGAINST A STRONG STARBURST-AGN CONNECTION IN RADIO-LOUD AGN". In: *The Astrophysical Journal* 745.2, p. 172. ISSN: 1538-4357.

Donato, D. et al. (Sept. 2001). "Hard X-ray properties of blazars". In: *Astronomy and Astrophysics* 375, pp. 739–751.

Einstein, A. (1916). "The Foundation of the General Theory of Relativity". In: *Annalen Phys.* 49.7. Ed. by J.-P. Hsu and D. Fine, pp. 769–822.

Elvis, M. et al. (Nov. 1994). "Atlas of Quasar Energy Distributions". In: *Astrophysical Journal, Supplement* 95, p. 1.

Emmanoulopoulos, D. et al. (Mar. 2014). "General relativistic modelling of the negative reverberation X-ray time delays in AGN". In: *Monthly Notices of the Royal Astronomical Society* 439.4, pp. 3931–3950. ISSN: 0035-8711.

Event Horizon Telescope Collaboration et al. (Apr. 2019). "First M87 Event Horizon Telescope Results. I. The Shadow of the Supermassive Black Hole". In: *Astrophysical Journal, Letters* 875.1, L1, p. L1.

Fabbiano, G. (2019). "X-Rays from Galaxies". In: *The Chandra X-ray Observatory*. Ed. by B. Wilkes and W. Tucker, pp. 7–1.

Fabian, A. C. et al. (Sept. 2000). "Broad Iron Lines in Active Galactic Nuclei". In: *Publications of the Astronomical Society of the Pacific* 112.775, pp. 1145–1161. ISSN: 1538-3873.

Fabian, A. C. et al. (May 2009). "Broad line emission from iron K- and L-shell transitions in the active galaxy 1H0707-495". In: *Nature* 459.7246, pp. 540–542.

Fabian, A. C. et al. (2015). *Properties of AGN coronae in the NuSTAR era*.

Fanaroff, B. L. and J. M. Riley (Apr. 1974). "The Morphology of Extragalactic Radio Sources of High and Low Luminosity". In: *Monthly Notices of the Royal Astronomical Society* 167.1, 31P–36P. ISSN: 0035-8711.

Fanti, C. (Feb. 2009). "Radio properties of CSSs and GPSs". In: *Astronomische Nachrichten* 330.2, pp. 120–127.

Fanti, C. et al. (Oct. 1995). "Are compact steep-spectrum sources young?" In: *Astronomy and Astrophysics* 302, p. 317.

Fanti, R. et al. (May 1990). "On the nature of compact steep spectrum radio sources." In: *Astronomy and Astrophysics* 231, pp. 333–346.

Ferrarese, L. and D. Merritt (Aug. 2000). "A Fundamental Relation between Supermassive Black Holes and Their Host Galaxies". In: *Astrophysical Journal, Letters* 539.1, pp. L9–L12.

Filippenko, A. V. (Feb. 1985). "New evidence for photoionization as the dominant excitation mechanism in liners." In: *Astrophysical Journal* 289, pp. 475–489.

Fisher, R. A. (1922). "On the Interpretation of χ^2 from Contingency Tables, and the Calculation of P". In: *Journal of the Royal Statistical Society* 85.1, pp. 87–94. ISSN: 09528385.

Floyd, D. J. E. et al. (Nov. 2004). "The host galaxies of luminous quasars". In: *Monthly Notices of the RAS* 355.1, pp. 196–220.

Fossati, G. et al. (Sept. 1998). "A unifying view of the spectral energy distributions of blazars". In: *Monthly Notices of the RAS* 299.2, pp. 433–448.

Frank, J., A. King, and D. Raine (2002). *Accretion Power in Astrophysics*. 3rd ed. Cambridge University Press.

Fritz, J., A. Franceschini, and E. Hatziminaoglou (Mar. 2006). "Revisiting the infrared spectra of active galactic nuclei with a new torus emission model". In: *Monthly Notices of the Royal Astronomical Society* 366.3, pp. 767–786. ISSN: 0035-8711.

Fruscione, A. et al. (June 2006). "CIAO: Chandra's data analysis system". In: *Society of Photo-Optical Instrumentation Engineers (SPIE) Conference Series*. Ed. by D. R. Silva

and R. E. Doxsey. Vol. 6270. Society of Photo-Optical Instrumentation Engineers (SPIE) Conference Series, p. 62701V.

Gaspari, M., F. Brighenti, and P. Temi (July 2012). "Mechanical AGN feedback: controlling the thermodynamical evolution of elliptical galaxies". In: *Monthly Notices of the RAS* 424.1, pp. 190–209.

Gaspari, M., M. Ruszkowski, and S. P. Oh (July 2013). "Chaotic cold accretion on to black holes". In: *Monthly Notices of the RAS* 432.4, pp. 3401–3422.

Gebhardt, K. et al. (Aug. 2000). "A Relationship between Nuclear Black Hole Mass and Galaxy Velocity Dispersion". In: *Astrophysical Journal, Letters* 539.1, pp. L13–L16.

George, I. M. and A. C. Fabian (Mar. 1991). "X-ray reflection from cold matter in Active Galactic Nuclei and X-ray binaries." In: *Monthly Notices of the RAS* 249, p. 352.

Giroletti, M. and A. Polatidis (Feb. 2009). "Samples and statistics of CSS and GPS sources". In: *Astronomische Nachrichten* 330.2, p. 193.

Gliozzi, M. and J. K. Williams (Oct. 2019). "The soft X-ray excess: NLS1s versus BLS1s". In: *Monthly Notices of the Royal Astronomical Society* 491.1, pp. 532–543. ISSN: 1365-2966.

Gonçalves, A. C. and M. Serote Roos (Jan. 2004). "The nuclear region of low luminosity flat radio spectrum sources. II. Emission-line spectra". In: *Astronomy and Astrophysics* 413, pp. 97–105.

González-Martin, O. et al. (Nov. 2009). "An X-ray view of 82 LINERs with Chandra and XMM-Newton data". In: *Astronomy and Astrophysics* 506.3, pp. 1107–1121.

Grandi, P. et al. (Apr. 2021). "Jet–Accretion System in the Nearby mJy Radio Galaxies". In: *The Astrophysical Journal* 911.1, p. 17. ISSN: 1538-4357.

Grimm, H. J. et al. (Jan. 2009). "An X-Ray Photometry System. I. Chandra ACIS". In: *Astrophysical Journal* 690.1, pp. 128–142.

Guainazzi, M. et al. (Jan. 2006). "A hard X-ray view of giga-hertz peaked spectrum radio galaxies". In: *Astronomy and Astrophysics* 446.1, pp. 87–96.

Hardcastle, M. and J. Croston (June 2020). "Radio galaxies and feedback from AGN jets". In: *New Astronomy Reviews* 88, p. 101539. ISSN: 1387-6473.

Harrison, C. (Sept. 2014). "Observational constraints on the influence of active galactic nuclei on the evolution of galaxies". PhD thesis. Durham University.

Harrison, F. A. et al. (Aug. 2010). "The Nuclear Spectroscopic Telescope Array (NuSTAR)". In: *arXiv e-prints*, arXiv:1008.1362, arXiv:1008.1362.

Hartman, R. C. et al. (July 1999). "The Third EGRET Catalog of High-Energy Gamma-Ray Sources". In: *Astrophysical Journal, Supplement* 123.1, pp. 79–202.

Harwood, J. J. et al. (May 2017). "FR II radio galaxies at low frequencies – II. Spectral ageing and source dynamics". In: *Monthly Notices of the Royal Astronomical Society* 469.1, pp. 639–655. ISSN: 0035-8711.

Heckman, T. M. and P. N. Best (Aug. 2014). "The Coevolution of Galaxies and Supermassive Black Holes: Insights from Surveys of the Contemporary Universe". In: *Annual Review of Astronomy and Astrophysics* 52, pp. 589–660.

HI4PI Collaboration et al. (2016). "HI4PI: a full-sky Hurvey based on EBHIS and GASS". In: *A&A* 594, A116.

Higgins, S. W., T. J. O'Brien, and J. S. Dunlop (Oct. 1999). "Structures produced by the collision of extragalactic jets with dense clouds". In: *Monthly Notices of the Royal Astronomical Society* 309.2, pp. 273–286. ISSN: 1365-2966.

Hönig, S. F. and M. Kishimoto (Nov. 2010). "The dusty heart of nearby active galaxies". In: *Astronomy & Astrophysics* 523, A27. ISSN: 1432-0746.

Hönig, S. F. and M. Kishimoto (Mar. 2017). "Dusty Winds in Active Galactic Nuclei: Reconciling Observations with Models". In: *The Astrophysical Journal* 838.2, p. L20. ISSN: 2041-8213.

Jamrozy, M. et al. (Apr. 2005). "Ageing analysis of the giant radio galaxy J1343+3758". In: *Astronomy and Astrophysics* 433.2, pp. 467–477.

Jeyakumar, S. et al. (Mar. 2005). "Jet propagation and the asymmetries of CSS radio sources". In: *Astronomy and Astrophysics* 432.3, pp. 823–833.

Kara, E. et al. (Dec. 2013). "The curious time lags of PG 1244+026: discovery of the iron K reverberation lag". In: *Monthly Notices of the Royal Astronomical Society: Letters* 439.1, pp. L26–L30. ISSN: 1745-3925.

Kara, E. et al. (Oct. 2016). "A global look at X-ray time lags in Seyfert galaxies". In: *Monthly Notices of the RAS* 462.1, pp. 511–531.

Kaspi, S. et al. (Aug. 2002). "The Ionized Gas and Nuclear Environment in NGC 3783. I. Time-averaged 900 KilosecondChandraGrating Spectroscopy". In: *The Astrophysical Journal* 574.2, pp. 643–662. ISSN: 1538-4357.

Kellermann, K. I. et al. (Oct. 1989). "VLA Observations of Objects in the Palomar Bright Quasar Survey". In: *Astronomical Journal* 98, p. 1195.

Kim, D.-W. (Nov. 1989). "Interstellar Matter in Early-Type Galaxies: Optical Observations". In: *Astrophysical Journal* 346, p. 653.

Kino, M. and K. Asano (Mar. 2011). "Mini-radio lobes in AGN core illumination and their hadronic gamma-ray afterlight". In: *Monthly Notices of the RAS* 412.1, pp. L20–L24.

Kormendy, J. and L. C. Ho (2013). "Coevolution (Or Not) of Supermassive Black Holes and Host Galaxies". In: *Annual Review of Astronomy and Astrophysics* 51.1, pp. 511–653.

Kormendy, J. and D. Richstone (Jan. 1995). "Inward Bound—The Search For Supermassive Black Holes In Galactic Nuclei". In: *Annual Review of Astronomy and Astrophysics* 33, p. 581.

Kosmaczewski, E. et al. (July 2020). "Mid-infrared Diagnostics of the Circumnuclear Environments of the Youngest Radio Galaxies". In: *Astrophysical Journal* 897.2, 164, p. 164.

Kunert-Bajraszewska, M. et al. (Nov. 2010). "A survey of low-luminosity compact sources and its implication for the evolution of radio-loud active galactic nuclei - I. Radio data". In: *Monthly Notices of the RAS* 408.4, pp. 2261–2278.

Laing, R. A. et al. (Jan. 1994). "Spectrophotometry of a Complete Sample of 3CR Radio Sources: Implications for Unified Models". In: *The Physics of Active Galaxies*. Ed. by G. V. Bicknell, M. A. Dopita, and P. J. Quinn. Vol. 54. Astronomical Society of the Pacific Conference Series, p. 201.

Lanzuisi, G. et al. (May 2016). "NuSTAR reveals the extreme properties of the super-Eddington accreting supermassive black hole in PG 1247+267". In: *Astronomy and Astrophysics* 590, A77, A77.

Lauberts, A. (1982). *Finding charts of ESO/Uppsala Catalogue objects*.

Liedahl, D. A., A. L. Osterheld, and W. H. Goldstein (Jan. 1995). "New Calculations of Fe L-Shell X-Ray Spectra in High-Temperature Plasmas". In: *Astrophysical Journal, Letters* 438, p. L115.

Maccagni, F. M. et al. (Nov. 2014). "What triggers a radio AGN?" In: *Astronomy & Astrophysics* 571, A67. ISSN: 1432-0746.

Magorrian, J. et al. (June 1998). "The Demography of Massive Dark Objects in Galaxy Centers". In: *Astronomical Journal* 115.6, pp. 2285–2305.

Mannheim, K. (Mar. 1993). "The proton blazar." In: *Astronomy and Astrophysics* 269, pp. 67–76.

Maraschi, L., G. Ghisellini, and A. Celotti (Sept. 1992). "A Jet Model for the Gamma-Ray–emitting Blazar 3C 279". In: *Astrophysical Journal, Letters* 397, p. L5.

Marscher, A. P. (Jan. 2005). "The Relationship between Radio and Higher-Frequency Emission in Active Galactic Nuclei". In: *Memorie della Società Astronomica Italiana* 76, p. 13.

Massaro, F., D. J. Thompson, and E. C. Ferrara (Dec. 2015). "The extragalactic gamma-ray sky in the Fermi era". In: *Astronomy and Astrophysics Reviews* 24, 2, p. 2.

Matthews, T. A., W. W. Morgan, and M. Schmidt (July 1964). "A Discussion of Galaxies Indentified with Radio Sources." In: *Astrophysical Journal* 140, p. 35.

Mattox, J. R. and J. F. Ormes (Dec. 2002). "The Final Catalog of EGRET Gamma-Ray Blazars". In: *American Astronomical Society Meeting Abstracts*. Vol. 201. American Astronomical Society Meeting Abstracts, p. 147.02.

McClintock, J. E. et al. (May 2011). "Measuring the spins of accreting black holes". In: *Classical and Quantum Gravity* 28.11, p. 114009. ISSN: 1361-6382.

Mewe, R., E. H. B. M. Gronenschild, and G. H. J. van den Oord (Nov. 1985). "Calculated X-radiation from optically thin plasmas. V." In: *Astronomy and Astrophysics, Supplement* 62, pp. 197–254.

Mewe, R., J. R. Lemen, and G. H. J. van den Oord (Sept. 1986). "Calculated X-radiation from optically thin plasmas. VI - Improved calculations for continuum emission and approximation formulae for nonrelativistic average Gaunt actors." In: *Astronomy and Astrophysics, Supplement* 65, pp. 511–536.

Meyer, F., B. F. Liu, and E. Meyer-Hofmeister (Feb. 2007). "Re-condensation from an ADAF into an inner disk: the intermediate state of black hole accretion?" In: *Astronomy and Astrophysics* 463.1, pp. 1–9.

Meyer, M. J. et al. (June 2004). "The HIPASS catalogue – I. Data presentation". In: *Monthly Notices of the Royal Astronomical Society* 350.4, pp. 1195–1209. ISSN: 0035-8711.

Migliori, G. et al. (Jan. 2014). "Jet Emission in Young Radio Sources: A Fermi Large Area Telescope Gamma-Ray View". In: *Astrophysical Journal* 780.2, 165, p. 165.

Migliori, G. et al. (Apr. 2016). "FIRST DETECTION IN GAMMA-RAYS OF A YOUNG RADIO GALAXY: FERMI -LAT OBSERVATIONS OF THE COMPACT SYMMETRIC OBJECT PKS 1718-649". In: *The Astrophysical Journal* 821.2, p. L31. ISSN: 2041-8213.

Miller, L., T. Turner, and J. Reeves (Mar. 2008). "An absorption origin for the X-ray spectral variability of MCG-6-30-15". In: *A&A* 483.

Misner, C. W., K. S. Thorne, and J. A. Wheeler (1973). *Gravitation*.

Morse, J. A. et al. (Sept. 1998). "Inclined Gas Disks in the Lenticular Seyfert Galaxy NGC 5252". In: *Astrophysical Journal* 505.1, pp. 159–173.

Mukherjee, D. et al. (June 2016). "Relativistic jet feedback in high-redshift galaxies – I. Dynamics". In: *Monthly Notices of the Royal Astronomical Society* 461.1, pp. 967–983. ISSN: 1365-2966.

— (Nov. 2017). "Erratum: Relativistic jet feedback in high-redshift galaxies I. Dynamics". In: *Monthly Notices of the RAS* 471.3, pp. 2790–2800.

Mukherjee, D. et al. (July 2018a). "Relativistic jet feedback – III. Feedback on gas discs". In: *Monthly Notices of the Royal Astronomical Society* 479.4, pp. 5544–5566. ISSN: 1365-2966.

Mukherjee, D. et al. (Jan. 2018b). "The jet–ISM interactions in IC 5063". In: *Monthly Notices of the Royal Astronomical Society* 476.1, pp. 80–95. ISSN: 1365-2966.

Müller, B. (June 2020). "Hydrodynamics of core-collapse supernovae and their progenitors". In: *Living Reviews in Computational Astrophysics* 6.1, 3, p. 3.

Murgia, M. (Jan. 2003). "Spectral Ages of CSOs and CSS Sources". In: *Publications of the Astron. Soc. of Australia* 20.1, pp. 19–24.

Nagai, H. et al. (Sept. 2006). "The Kinematic and Spectral Ages of the Compact Radio Source CTD 93". In: *Astrophysical Journal* 648.1, pp. 148–157.

Nandra, K. and K. A. Pounds (May 1994). "Ginga observations of the X-ray spectra of Seyfert galaxies". In: *Monthly Notices of the Royal Astronomical Society* 268.2, pp. 405–429. ISSN: 0035-8711.

Nandra, K. et al. (Nov. 2007). "An XMM-Newton survey of broad iron lines in Seyfert galaxies". In: *Monthly Notices of the RAS* 382.1, pp. 194–228.

Nenkova, M. et al. (Sept. 2008). "AGN Dusty Tori. II. Observational Implications of Clumpiness". In: *The Astrophysical Journal* 685.1, pp. 160–180.

Netzer, H. (2013). *The Physics and Evolution of Active Galactic Nuclei*. Cambridge University Press.

Netzer, H. et al. (May 2002). "The Density and Location of the X-Ray–absorbing Gas in NGC 3516". In: *The Astrophysical Journal* 571.1, pp. 256–264. ISSN: 1538-4357.

O'Dea, C. P., S. A. Baum, and C. Stanghellini (Oct. 1991). "What Are the Gigahertz Peaked-Spectrum Radio Sources?" In: *Astrophysical Journal* 380, p. 66.

O'Dea, C. P. (May 1998). "The Compact Steep-Spectrum and Gigahertz Peaked-Spectrum Radio Sources". In: *Publications of the ASP* 110.747, pp. 493–532.

O'Dea, C. P. and S. A. Baum (Jan. 1997). "Constraints on Radio Source Evolution from the Compact Steep Spectrum and GHz Peaked Spectrum Radio Sources". In: *Astronomical Journal* 113, pp. 148–161.

O'Dea, C. P. and D. J. Saikia (Mar. 2021). "Compact steep-spectrum and peaked-spectrum radio sources". In: *The Astronomy and Astrophysics Review* 29.1. ISSN: 1432-0754.

Orienti, M. (Feb. 2016). "Radio properties of Compact Steep Spectrum and GHz-Peaked Spectrum radio sources". In: *Astronomische Nachrichten* 337.1-2, pp. 9–17. ISSN: 0004-6337.

Orienti, M. and D. Dallacasa (July 2008). "Are young radio sources in equipartition?" In: *Astronomy & Astrophysics* 487.3, pp. 885–894. ISSN: 1432-0746.

Ostorero, L. et al. (May 2010). "X-RAY-EMITTING GHz-PEAKED-SPECTRUM GALAXIES: TESTING A DYNAMICAL-RADIATIVE MODEL WITH BROADBAND SPECTRA". In: *The Astrophysical Journal* 715.2, pp. 1071–1093. ISSN: 1538-4357.

Padovani, P. et al. (Aug. 2017). "Active galactic nuclei: what's in a name?" In: *Astronomy and Astrophysics Reviews* 25.1, 2, p. 2.

Pallavi, P. et al. (Jan. 2022). "Radio Spectra of Luminous, Heavily Obscured WISE-NVSS Selected Quasars". In: *arXiv e-prints*, arXiv:2201.07349, arXiv:2201.07349.

Panessa, F. et al. (2019). *The Origin of Radio Emission from Radio-Quiet AGN*.

Parma, P. et al. (Aug. 2007). "In search of dying radio sources in the local universe". In: *Astronomy and Astrophysics* 470.3, pp. 875–888.

Patil, P. et al. (June 2020). "High-resolution VLA Imaging of Obscured Quasars: Young Radio Jets Caught in a Dense ISM". In: *Astrophysical Journal* 896.1, 18, p. 18.

Peck, A. B. et al. (May 2000). "Redshifts and Neutral Hydrogen Observations of Compact Symmetric Objects in the COINS Sample". In: *Astrophysical Journal* 534.1, pp. 104–108.

Perlman, E. S. et al. (Aug. 2001). "Host Galaxies, Obscuration, and Nuclear Structure of Three Nearby Compact Symmetric Objects". In: *Astronomical Journal* 122.2, pp. 536–548.

Perucho, M. (Feb. 2016). "Radio source evolution". In: *Astronomische Nachrichten* 337.1-2, pp. 18–26. ISSN: 0004-6337.

Petrucci, P. O. et al. (Mar. 2018). "Testing warm Comptonization models for the origin of the soft X-ray excess in AGNs". In: *Astronomy and Astrophysics* 611, A59, A59.

Planck Collaboration et al. (2020). "Planck 2018 results - VI. Cosmological parameters". In: *A&A* 641, A6.

Polatidis, A. G. and J. E. Conway (2003). "Proper Motions in Compact Symmetric Objects". In: *Publications of the Astronomical Society of Australia* 20.1, pp. 69–74. ISSN: 1448-6083.

Principe, G. et al. (Mar. 2020). "NGC 3894: a young radio galaxy seen by Fermi-LAT". In: *Astronomy & Astrophysics* 635, A185. ISSN: 1432-0746.

Principe, G. et al. (Nov. 2021). "Gamma-ray emission from young radio galaxies and quasars". In: *Monthly Notices of the RAS* 507.3, pp. 4564–4583.

Read, A. M. et al. (Oct. 2011). "A new comprehensive 2D model of the point spread functions of the XMM-Newton EPIC telescopes: spurious source suppression and improved positional accuracy". In: *Astronomy and Astrophysics* 534, A34, A34.

Reynolds, C. S. and M. A. Nowak (Apr. 2003). "Fluorescent iron lines as a probe of astrophysical black hole systems". In: *Physics Reports* 377.6, pp. 389–466.

Ricci, C. (Dec. 2011). "Active Galactic Nuclei at hard X-ray energies: absorption, reflection and the unified model". eng. ID: unige: 19474. PhD thesis.

Richards, G. T. et al. (Oct. 2006). "Spectral Energy Distributions and Multiwavelength Selection of Type 1 Quasars". In: *Astrophysical Journal, Supplement* 166.2, pp. 470–497.

Risaliti, G. and M. Elvis (2004). "A Panchromatic View of AGN". In: *Astrophysics and Space Science Library*, pp. 187–224. ISSN: 0067-0057.

Saikia, D. J. et al. (Jan. 2003). "Symmetry Parameters of CSS Sources: Evidence of Fuelling?" In: *Publications of the Astron. Soc. of Australia* 20.1, pp. 50–56.

Schmidt, M. (Mar. 1963). "3C 273 : A Star-Like Object with Large Red-Shift". In: *Nature* 197.4872, p. 1040.

Seward, F. D. and P. A. Charles (2010). "X-ray emission and interaction with matter". In: *Exploring the X-ray Universe*. 2nd ed. Cambridge University Press, pp. 12–17.

Shakura, N. I. and R. A. Sunyaev (June 1973). "Reprint of 1973A&A....24..337S. Black holes in binary systems. Observational appearance." In: *Astronomy and Astrophysics* 500, pp. 33–51.

Siebenmorgen, R., F. Heymann, and A. Efstathiou (Nov. 2015). "Self-consistent two-phase AGN torus models". In: *Astronomy & Astrophysics* 583, A120. ISSN: 1432-0746.

Siemiginowska, A. (Feb. 2009). "X-ray emission from GPS and CSS sources". In: *Astronomische Nachrichten* 330.2-3, pp. 264–269. ISSN: 1521-3994.

Siemiginowska, A. et al. (2010). *Intermittent Activity of Jets in AGN*.

Siemiginowska, A. et al. (May 2016). "X-Ray Properties of the Youngest Radio Sources and Their Environments". In: *Astrophysical Journal* 823.1, 57, p. 57.

Sironi, L. and A. Spitkovsky (Mar. 2014). "Relativistic Reconnection: An Efficient Source of Non-thermal Particles". In: *Astrophysical Journal, Letters* 783.1, L21, p. L21.

Sironi, L., A. Spitkovsky, and J. Arons (July 2013). "The Maximum Energy of Accelerated Particles in Relativistic Collisionless Shocks". In: *Astrophysical Journal* 771.1, 54, p. 54.

Snellen, I. A. G. et al. (Dec. 2000). "On the evolution of young radio-loud AGN". In: *Monthly Notices of the Royal Astronomical Society* 319.2, pp. 445–456. ISSN: 1365-2966.

Sobolewska, M. A. and C. Done (Nov. 2006). "What is the origin of the soft excess in active galactic nuclei?" In: *Monthly Notices of the Royal Astronomical Society* 374.1, pp. 150–158. ISSN: 0035-8711.

Sobolewska, M. et al. (Oct. 2019a). "First Hard X-Ray Observation of a Compact Symmetric Object: A Broadband X-Ray Study of a Radio Galaxy OQ+208 with *NuSTAR* and *Chandra*". In: *Astrophysical Journal* 884.2, 166, p. 166.

— (Jan. 2019b). "The Impact of the Environment on the Early Stages of Radio Source Evolution". In: *Astrophysical Journal* 871.1, 71, p. 71.

Sobolewska, M. et al. (Nov. 2021). "The Origin of High Energy Emission in the Young Radio Source PKS 1718-649". In: *arXiv e-prints*, arXiv:2111.02611, arXiv:2111.02611.

Stalevski, M. et al. (Mar. 2016). "The dust covering factor in active galactic nuclei". In: *Monthly Notices of the Royal Astronomical Society* 458.3, pp. 2288–2302. ISSN: 1365-2966.

Stanghellini, C. et al. (Sept. 1993). "Optical CCD Imaging of GHz-peaked-Spectrum Radio Sources". In: *Astrophysical Journal, Supplement* 88, p. 1.

Stawarz, Ł. et al. (June 2008). "Evolution of and High-Energy Emission from GHz-Peaked Spectrum Sources". In: *The Astrophysical Journal* 680.2, pp. 911–925. ISSN: 1538-4357.

Stern, B. E. et al. (Aug. 1995). "On the Geometry of the X-Ray–Emitting Region in Seyfert Galaxies". In: *Astrophysical Journal, Letters* 449, p. L13.

Sutherland, R. S. and G. V. Bicknell (Aug. 2007). "Interaction of jets with the ISM of radio galaxies". In: *Astrophysics and Space Science* 311.1–3, pp. 293–303. ISSN: 1572-946X.

Tadhunter, C. (Aug. 2008). "An introduction to active galactic nuclei: Classification and unification". In: *New Astronomy Review* 52.6, pp. 227–239.

Taylor, G. B., J. M. Wrobel, and R. C. Vermeulen (May 1998). "Discovery of Twin Relativistic Jets in the Nearby E/S0 Galaxy NGC 3894". In: *Astrophysical Journal* 498.2, pp. 619–624.

Taylor, G. B. et al. (Sept. 2000). "Kinematic Age Estimates for Four Compact Symmetric Objects from the Pearson-Readhead Survey". In: *Astrophysical Journal* 541.1, pp. 112–119.

Tengstrand, O. et al. (Apr. 2009). "The X-ray view of giga-hertz peaked spectrum radio galaxies". In: *Astronomy & Astrophysics* 501.1, pp. 89–102. ISSN: 1432-0746.

Terashima, Y. and A. S. Wilson (Jan. 2003). "Chandra Snapshot Observations of Low-Luminosity Active Galactic Nuclei with a Compact Radio Source". In: *Astrophysical Journal* 583.1, pp. 145–158.

The *Fermi*/LAT collaboration et al. (Apr. 2020). "The Fourth Catalog of Active Galactic Nuclei Detected by the Fermi Large Area Telescope". In: *The Astrophysical Journal* 892.2, p. 105. ISSN: 1538-4357.

Tingay, S. J. et al. (June 1997). "The Nearest GHz Peaked-Spectrum Radio Galaxy, PKS 1718-649". In: *The Astronomical Journal* 113, pp. 2025–2030.

Tingay, S. J. et al. (Jan. 2015). "THE SPECTRAL VARIABILITY OF THE GHZ-PEAKED SPECTRUM RADIO SOURCE PKS 1718-649 AND A COMPARISON OF ABSORPTION MODELS". In: *The Astronomical Journal* 149.2, p. 74. ISSN: 1538-3881.

Tingay, S. J. and M. de Kool (2003). "An investigation of synchrotron self-absorption and free-free absorption models in explanation of the gigahertz-peaked spectrum of PKS 1718-649". In: *The Astronomical Journal* 126, pp. 723–733.

Tramacere, A. et al. (July 2009). "Swift observations of the very intense flaring activity of Mrk 421 during 2006. I. Phenomenological picture of electron acceleration and predictions for MeV/GeV emission". In: *Astronomy and Astrophysics* 501.3, pp. 879–898.

Tremblay, S. E. et al. (June 2016). "Compact symmetric objects and supermassive binary black holes in the VLBA Imaging and Polarimetry Survey". In: *Monthly Notices of the RAS* 459.1, pp. 820–840.

Trümper, J. and G. Hasinger (Jan. 2008). *The Universe in X-Rays*. ISBN: 978-3-540-34411-7.

Tsai, C. W. et al. (Nov. 2018). "Super-Eddington Accretion in the WISE-selected Extremely Luminous Infrared Galaxy W2246-0526". In: *Astrophysical Journal* 868.1, 15, p. 15.

Urry, C. M. (Jan. 2003). "The AGN Paradigm for Radio-Loud Objects". In: *Active Galactic Nuclei: From Central Engine to Host Galaxy*. Ed. by S. Collin, F. Combes, and I. Shlosman. Vol. 290. Astronomical Society of the Pacific Conference Series, p. 3.

Urry, C. M. and P. Padovani (Sept. 1995). "Unified Schemes for Radio-Loud Active Galactic Nuclei". In: *Publications of the ASP* 107, p. 803.

Uttley, P. et al. (Aug. 2014). "X-ray reverberation around accreting black holes". In: *Astronomy and Astrophysics Reviews* 22, 72, p. 72.

van Breugel, W., G. Miley, and T. Heckman (Jan. 1984). "Studies of kiloparsec-scale, steep-spectrum radio cores. I. VLA maps." In: *Astronomical Journal* 89, pp. 5–22.

van den Bosch, R. C. E. et al. (May 2015). "Hunting for Supermassive Black Holes in Nearby Galaxies With the Hobby-Eberly Telescope". In: *Astrophysical Journal, Supplement* 218.1, 10, p. 10.

Vermeulen, R. C. et al. (Mar. 1996). "Redshifts for Superluminal Candidates.II." In: *Astronomical Journal* 111, p. 1013.

Wagner, A. Y. and G. V. Bicknell (Jan. 2011). "RELATIVISTIC JET FEEDBACK IN EVOLVING GALAXIES". In: *The Astrophysical Journal* 728.1, p. 29. ISSN: 1538-4357.

Wiita, P. J. (Sept. 2004). "Jet Propagation Through Irregular Media and the Impact of Lobes on Galaxy Formation". In: *Astrophysics and Space Science* 293.1, pp. 235–245.

Wilkes, B. J. and M. Elvis (Dec. 1987). "Quasar Energy Distributions. I. Soft X-Ray Spectra of Quasars". In: *Astrophysical Journal* 323, p. 243.

Wilkinson, P. N. et al. (Sept. 1994). "Two-sided Ejection in Powerful Radio Sources: The Compact Symmetric Objects". In: *Astrophysical Journal, Letters* 432, p. L87.

Willett, K. et al. (Apr. 2010). "Spitzer mid-infrared spectroscopy of compact symmetric objects: What powers radio-loud active galactic nuclei?" In: *Astrophysical Journal* 713.

Wilson, A. S. and E. J. M. Colbert (Jan. 1995). "The Difference between Radio-loud and Radio-quiet Active Galaxies". In: *Astrophysical Journal* 438, p. 62.

Wójtowicz, A. et al. (Apr. 2020). "On the Jet Production Efficiency in a Sample of the Youngest Radio Galaxies". In: *The Astrophysical Journal* 892.2, p. 116. ISSN: 1538-4357.

Worrall, D. M. et al. (Feb. 1987). "X-Ray Studies of Quasars with the Einstein Observatory. IV. X-Ray Dependence on Radio Emission". In: *Astrophysical Journal* 313, p. 596.

Wright, E. L. (Dec. 2006). "A Cosmology Calculator for the World Wide Web". In: *Publications of the Astronomical Society of the Pacific* 118.850, pp. 1711–1715. ISSN: 1538-3873.

Wu, Q. (Aug. 2009). "OBSERVATIONAL EVIDENCE FOR YOUNG RADIO GALAXIES IS TRIGGERED BY ACCRETION DISK INSTABILITY". In: *The Astrophysical Journal* 701.2, pp. L95–L99. ISSN: 1538-4357.

Xu, W. et al. (Jan. 2016). "X-ray fluorescent lines from the Compton-thick AGN in M51". In: *Monthly Notices of the RAS* 455.1, pp. L26–L30.

Zamorani, G. et al. (Apr. 1981). "X-ray studies of quasars with the Einstein Observatory II." In: *Astrophysical Journal* 245, pp. 357–374.

Zappacosta, L. et al. (Mar. 2020). "The WISSH quasars project. VII. The impact of extreme radiative field in the accretion disc and X-ray corona interplay". In: *Astronomy and Astrophysics* 635, L5, p. L5.